VERA Observations of 43GHz SiO Masers toward a Symbiotic Star R Aquarii

Min, Cheulhong

Doctor of Philosophy

Department of Astronomical Science
School of Physical Sciences
SOKENDAI (The Graduate University for Advanced Studies)

VERA Observations of 43GHz SiO Masers toward a Symbiotic Star R Aquarii

Min, Cheulhong

Academic Advisors

Prof. Dr. Honma, Mareki
Dr. Shibata, Katsunori M.
Dr. Hirota, Tomoya

Department of Astronomical Science
School of Physical Sciences
The Graduated University for Advanced Studies (SOKENDAI)

2017

Abstract

Symbiotic stars are generally understood as interacting binary systems comprising a cool late-type star, which is a Red Giant Branch (RGB) or Asymptotic Giant Branch (AGB) star, and a hot compact companion, which is usually a White Dwarf (WD), surrounded by ionized nebulae. The interaction between the components presents a variety of astronomical phenomena that involve mass-loss and mass-transfer processes. In particular, the ionized nebulae are mostly found around D-type symbiotic stars, and a large proportion of those nebulae show a bipolar morphology. While the detailed mechanism has been longstanding topics of debate, the binary interaction is considered to play an important role in the formation mechanism. To acquire orbital parameters is indispensable to derive fundamental physical information for understanding various uncertain aspects of the formation mechanism. However, most of the known orbital parameters are limited to S-type symbiotic stars.

R Aquarii (R Aqr) is one of the well-known D-type symbiotic stars composed of a Mira variable and a WD companion. The characteristics of the system are the presence of bipolar jet-like features and the hour-glass-shape of two extended inner- and outer-bipolar nebulae. In addition, R Aqr is one of the symbiotic stars that exhibit circumstellar masers associated with the Mira variable. Several progresses were made in deriving orbital parameters for R Aqr, but the observations have not yielded consistent values for those parameters yet.

A radial velocity analysis has been widely used for determining orbital parameters of a binary system, but it cannot resolve the full parameters because of an inclination ambiguity. In order to disentangle the ambiguity, an astrometry observation is complementary to the radial velocity method. For the astrometry, SiO masers allow us to determine the accurate positions of the central star from their distributions with a high spatial resolution of VLBI observation. Combining the astrometry and the radial velocity analysis, the full orbital parameters can be derived without any ambiguity. Moreover, the VLBI observation of the SiO maser provide the kinematics of the inner region of the stellar atmosphere, and give implications for understanding the dynamics of the initial mass-loss process.

In this study, we have performed the VLBI Exploration of Radio Astrometry (VERA) observations of SiO masers toward the symbiotic star R Aqr from 2011 to 2014 to determine its reliable orbital parameters. We made long-period, multi-transitional observations of SiO masers with the phase-referencing VLBI technique, which provides absolute positional information as well as high-resolution images, for the first time for R Aqr

The SiO masers extended over an area of about 40 mas $\times$ 40 mas, forming clumpy, partial ring-like structure and predominantly occupying eastern portion of the shell. We determine the position of the Mira variable by fitting concentric circles to the observed SiO maser distributions for each epoch. Adopting previous VERA astrometry observations, we extended the time coverage of the astrometry to about 10 years for R Aqr. Moreover, we also conducted Nobeyama and Mopra single-dish observations of the SiO masers from 2002 to 2014 to trace the radial velocity variation of the Mira variable in R Aqr for a longer period of time. Complementing previous radial velocity data, we

covered about 85 years of radial velocities for R Aqr. Combining the astrometry and radial velocity data, we derive the full orbital parameters using a Markov Chain Monte Carlo (MCMC) method.

Comparing the orbital parameters with the VERA observations of SiO masers in R Aqr, we found that the global distribution of dominant SiO maser features is closely related to the orbital phase of R Aqr system due to the binary interaction. In our VERA observations, most of SiO maser components were detected in eastern hemisphere during the three stellar phases. Our orbital solution suggests that the dominant SiO maser region tends to appear in the direction of the WD companion with respect to the Mira variable. Besides, this tendency has been persistently observed through VLBI observations for over 20 yrs. Since the strong maser emission is preferentially observed in the region where the material density and velocity coherence are higher, the observed tendency indicates that high density of material properly concentrates in the direction of the companion, where the mass-transfer process may occur between the components.

Moreover, we newly obtained several stellar properties including the component masses of 1.55 $M_{\odot}$ for the Mira variable and 1.01 $M_{\odot}$ for WD companion, respectively. Applying the stellar masses to observed SiO maser distribution, the mass-transfer is likely to occur via the (wind) Roche-lobe overflow in R Aqr. The observed SiO maser region occupied over 70% of the Roche-lobe radius of 19.75 mas, and the material can effectively fill the Roche lobe with the assistance of the dust-driven winds. Applying a simple kinematic model, we define the inner boundary of the SiO maser region, where the radius and outflow velocity are $R_{\rm in} = 12$ and $V_{\rm in} = 7.7$ km s^{-1}, respectively. Moreover, we derive the outflow velocity at the Roche lobe radius of $V_{\rm out} = 12.2$ km s^{-1} for a logarithmic velocity gradient. Adopting the outflow velocities, the mass-loss rate of the Mira variable is as high as 4.1×10^{-5} M$_{\odot}$ yr^{-1} in R Aqr.

Finally, our orbital parameters imply that the formation mechanism of a bipolar nebula involves not only the binary interaction but also other processes in R Aqr. For the bipolar nebulae, the binary interaction is the most preferred mechanism. From the morphology and structure of the bipolar nebulae, several orbital parameters can be estimated based on theoretical studies. Comparing our orbital solution and the morphology of R Aqr nebulae, we found a misalignment between our orbital parameters and morphologically estimated values. Our result indicates that the binary interacting scenario alone cannot explain this discrepancy, and other processes, such as some effects of magnetic fields, are necessary to explain the misalignment.

Contents

List of Tables

List of Figures

Chapter 1

Introduction

1.1 Symbiotic Stars

The class of "Symbiotic star" was first introduced by Merill (1941), who presented peculiar spectra showing a combination of the continuum with molecular absorption features from the cool giant stars and emission lines from high-temperature ionized gasses. The explanation of this composite spectra would be considered as binaries containing two stars with different temperatures, both bright enough to contribute to the spectra. These stars are nowadays generally understood as interacting binary systems comprising of a cool late-type star and a hot compact companion surrounded by an ionized nebula. The late-type star is a red giant branch (RGB) or asymptotic giant branch (AGB) star, and the hot companion is usually a white dwarf (WD), in a few cases of a low-mass main-sequence star or a neutron star. Roughly 200 symbiotic stars are known in our Galaxy and Magellanic Cloud (catalog by Belczynski et al. 2000). According to other estimations, the total number of a symbiotic population might be from 3×10^3 (Allen 1984) up to 4×10^5 (Magrini et al. 2003) in our galaxy.

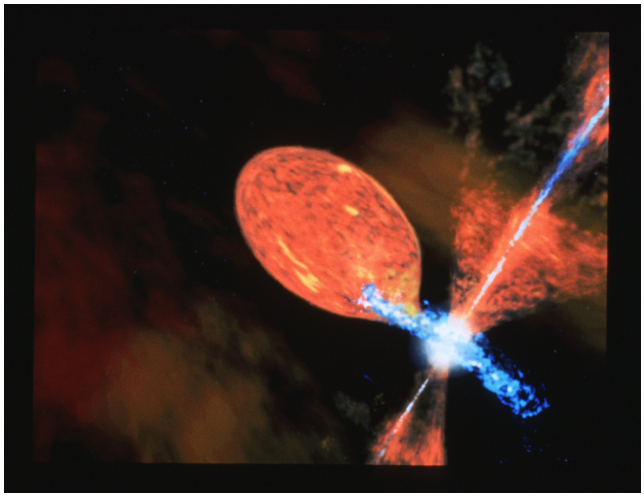

Figure 1.1: Artist's Impression of the Symbiotic Star, R Aquarii (credit by NASA/Dana Berry).

Interactions between the components in the symbiotic star play an important role in various astrophysical phenomena, such as the formation of an accretion disk, a collimating fast jet-like outflow, a nova-like thermonuclear outburst, and a photo-ionized nebula as illustrated in Figure 1.1. These symbiotic phenomena make them unique astrophysical laboratories for investigating a variety of astronomical processes of binary evolutions with important implications and applications. Moreover, studying the symbiotic stars give clues for better understanding a wide range of objects, such as Type Ia supernovae, post-AGB stars (e.g. Barium stars), planetary nebulae, soft X-ray sources, and cataclysmic binaries.

The definition of the symbiotic star has been crystallized after Kenyon (1986) described specific observational properties. Though Kenyon (1986) referred that the definition of the symbiotic star highly depends on the choice of prototype stars, the specific properties of original samples of prototypes were described as follows:

1. Irregular optical variability
2. The absorption features of a late-type giant star such as TiO bands and neutral metals
3. Prominent high ionization emission of recombination HI, HeI, HeII, and forbidden [OIII], [NIII] etc
4. A bright red continuum
5. A weak blue continuum
6. Usually found in planetary nebulae

Belczynski et al. (2000), who recently categorized the symbiotic stars, suggested that the classification criteria of symbiotic stars have following observational characteristics.

1. The presence of the absorption features of a late-type giant; in practice, these include (amongst others) TiO, H_2O, CO, CN, and VO bands, as well as CaI, CaII, FeI and NaI absorption lines
2. The presence of strong emission lines of HI and HeI and either
   - Emission lines of ions with an ionization potential of at least 35eV (e.g. [OIII]), or
   - An A-or F-type continuum with additional shell absorption lines from HI, HeI and singly-ionized metals
   - The latter corresponds to the appearance of a symbiotic star in outburst
3. The presence of the λ6825 (Raman scattering) emission features, even if no features of the cool star (e.g. TiO bands) are found

They also denoted that symbiotic stars are variables with timescales often exceeding a dozen years and that –as Kenyon very sensibly noted- “every known symbiotic star has, at one time or another, violated all the classification criteria invented”.

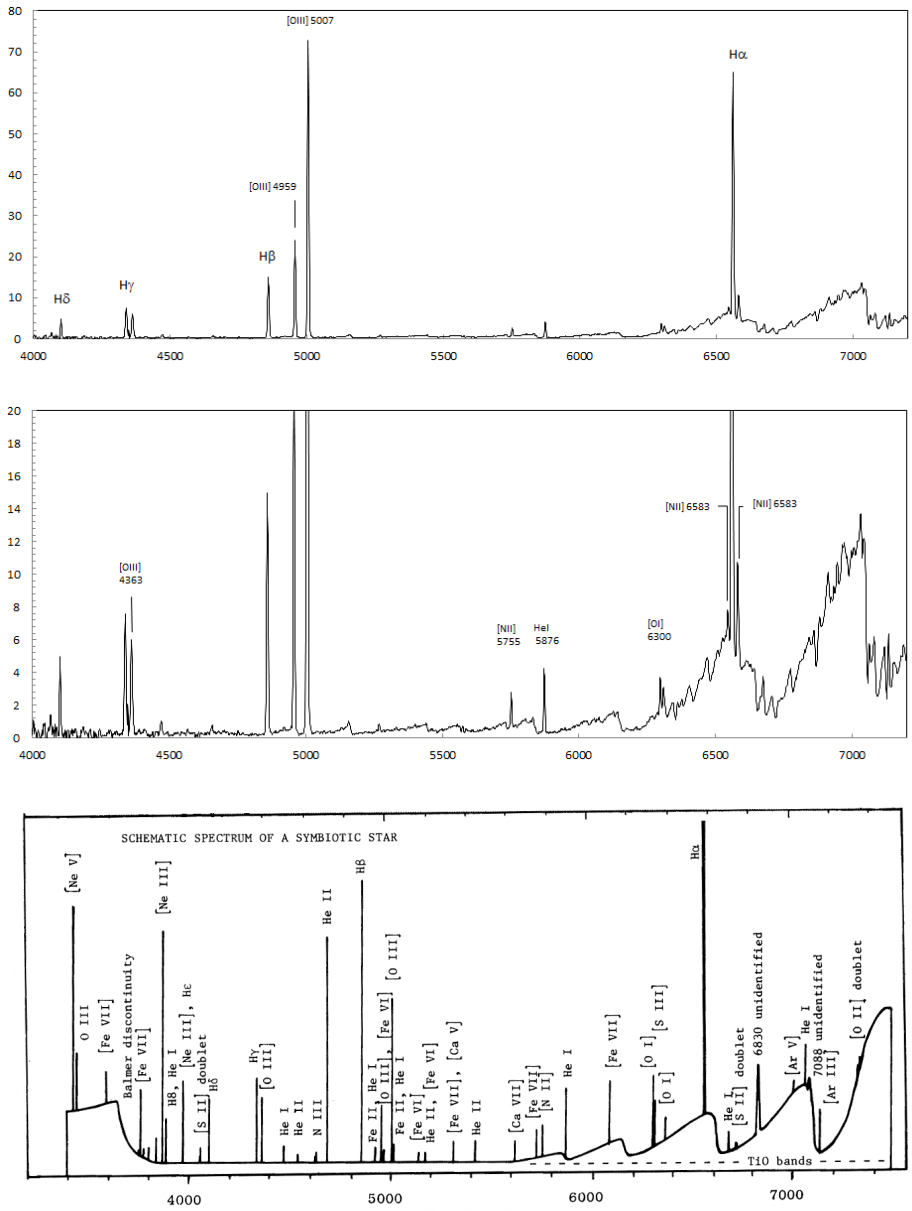

Figure 1.2: Optical spectra of symbiotic star with combination of cool giant's continuum with molecular absorption features and high ionized emissions. (Top,Middle) Optical spectra[1] of the symbiotic star, R Aquarii near minimum luminosity. (Bottom) Schematic spectrum of the symbiotic star.

[1]The data were released with the support by ARAS (Astronomical Ring for Access to Spectroscopy) http://www.astrosurf.com/aras/

1.1.1 Subclasses of Symbiotic stars

All symbiotic stars can be divided into several sub-classes. According to the hot companion's properties and outburst activities, there are three types of symbiotic stars: Recurrent novae, Symbiotic(Slow) novae, and Classical symbiotic stars. In addition, symbiotic stars can be classified into mainly two types of S(Stellar)-types and D(Dusty)-types based on the cool giant's properties.

Recurrent novae, Symbiotic(Slow) novae & Classical symbiotic stars
In the outburst phase, three types of symbiotic stars can be characterized based on the duration and spectroscopic changes(evolutions).

Recurrent novae and Symbiotic(Slow) novae are believed to be due to thermonuclear runaway on the accretion surface of the hot companion (WD), as in classical novae. They can be treated as a same subclass of nova, that shows no WD material enhancement (Kato 2002). However, the recurrent novae, as the name implies, repeat outbursts on the time scales from a few month to several-tens of year, and show a rapid decline in their light curves. They usually have a massive hot companion, over 1.1 $M_\odot$. While the symbiotic(slow) novae present a single and decade-long outburst. They contain a low to a medium mass of hot companion between 0.4 and 0.6 $M_\odot$.

Classical symbiotic stars are the most common in the symbiotic outburst, showing occasional eruptions on the timescale from months to years. However, their outburst mechanism is not clearly known (Mikołajewska 2011).

S-type and D-type Symbiotic stars
On the basis of infrared spectra in quiescent phase, there are mainly two types of symbiotic stars: S(Stellar)-type and D(Dusty)-type (Webster & Allen 1975). Figure 1.3 shows the difference between the S-type and D-type symbiotic stars in the infrared spectral energy distribution range between 1-4 μm.

The majority of symbiotic stars (about 80% of known symbiotic stars) belong to the S-type. They possess a star-like infrared continuum with modest mid-infrared excesses, which indicates a temperature of 2500-3500 K, and strong CO absorption bands. Besides their infrared spectra, they can be characterized by relative strengths of their forbidden and intercombination lines suggesting a high electron density of $N_e \sim 10^9$ cm^{-3} in nebulae ionized by a hot companion of T>75000 K. The S-type symbiotic stars generally have a normal RG star (spectral type of M) as a cool component. The known orbital periods of S-type symbiotic stars have a range between 200 and 1000 days.

The D-type symbiotic stars exhibit a warm dusty spectrum with high mid-infrared excesses, corresponding to a lower temperature about 800-1000 K, with H_2O and CO absorption bands. Since the D-type symbiotic stars contain a Mira variable as a cool component, they also called "symbiotic Miras". They have a lower electron nebula density of N_e $<10^6$ cm^{-3} and longer orbital periods of about >20 yrs than those of S-type symbiotic stars.

A small number of symbiotic stars are included as D'-type (or yellow) symbiotic star (Allen 1982). They show very red colors of dust emission in the far infrared spectrum which is typically lower temperatures than those observed in D-types. They are

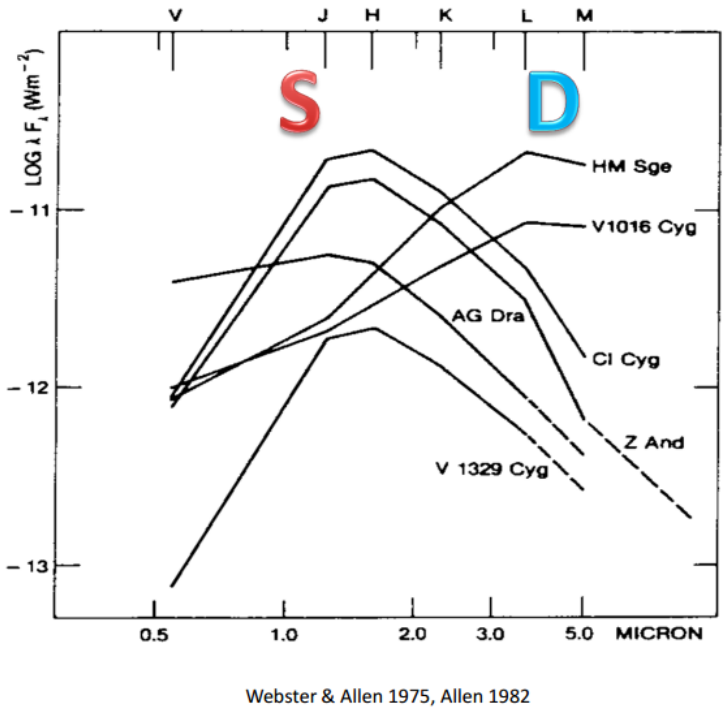

Figure 1.3: Spectrum differences between S-type and D-type symbiotic stars (Eiroa et al. 1982).

characterized by the cool component in which spectral type of F, G, K, or early R giants, in contrast to other symbiotic stars.

1.1.2 Symbiotic nebula

Large scale, extended and ionized nebulae are usually found around symbiotic stars. A comprehensive symbiotic nebula was compiled by Corradi et al. (1999,2000). Table 1.1 shows the resolved symbiotic nebulae with their brief properties.

An important characteristic is that most of the symbiotic nebulae are found around D-type symbiotic stars. These nebulae are more extended in D-type than S-type symbiotic stars and resemble planetary nebulae (PNe) in terms of morphology, spectra, exciting conditions and chemical abundances. Accordingly, those symbiotic nebulae were initially classified as PNe. After the character of symbiotic nebulae became obvious, a number of the misclassified PNe belonged to symbiotic stars, and the nature of symbiotic stars made them distinct objects formed in different stages of stellar evolution. Nevertheless, the fact that their morphology and kinematics are very similar to those of PNe tells us that similar dynamical processes are likely to occur in both classes of objects.

Another important characteristic of the symbiotic nebulae around D-type symbiotic stars is their wide variety of shapes. Many of symbiotic nebulae have an asymmetric morphology, and more than 40% show a bipolar morphology (Corradi et al. 2000). Since the underlying physics of the asymmetric morphology should be similar to those of PNe

Table 1.1: Resolved symbiotic nebulae with properties

Name	Type	Opt./Radio Size (")	Characteristic & Shape	V_{exp} (km s^{-1})
RX Pup	D	4 / 1	jet?, elliptical or spherical	>80
AS 201	D'	13 / -	circular	16
H 2-2	S	1.4 / -	elliptical?	
BI Cru	D	150 / -	bipolar (+jet?)	≤280
V417 Cen	D'	100 / -	bipolar	10
He 2–104	D	95 / -	bipolar + jet	6 - 240
He 2–147	D	5 / -	ring	100
SS 96	S	- / 0.17	axisymmetrical	
H 1–36	D	0.9–1.5 / 5	reflection nebula? / knotty	
RS Oph	S	- / 0.2	bipolar	
CH Cyg	S	32 / 1.5	jet + irregular	>65 (≫?)
HM Sge	D	30, 0.28 / 4	jet, irregular or bipolar?	>65
V1016 Cyg	D	20 / 4	elliptical or irregular	>30
HBV 475	S	0.4 / -	irregular	
AG Peg	S	8 / 60	irregular or elliptical, bipolar	-
R Aqr	D	120, 60 / <0.25	jet, bipolar	32, 55 to 250

in spite of different physical parameters, several scenarios have been proposed in order to explain this complex and varied morphology from the PNe formation mechanisms. However, there remains as elusive as ever. For the bipolar morphology, a widely accepted mechanism is a combination of a binary interaction and interacting wind model as shown in Figure 1.4.

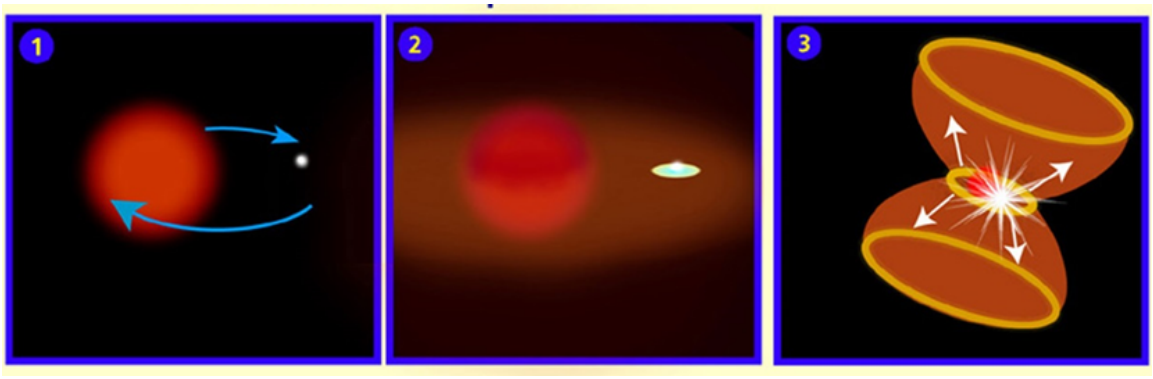

Figure 1.4: Formation scenario of the symbiotic nebula (created by NASA & ESA).

In symbiotic stars, a mass-losing giant star emanates a copious amount of material via stellar winds. A companion has influence on the wind material via Bondi-Hoyle-Lyttleton (BHL) wind accretion (Hoyle & Lyttleton 1939; Bondi & Hoyle 1944; Bondi 1952), Roche Lobe Overflow (RLOF) (Morris 1981,1987; Mastrodemos & Morris 1999; Soker 1994) wind Roche lobe Overflow (WRLOF) (Mohamed & Podsiadlowski 2007), or Gravitational focusing (de Val-Borro et al. 2009; Kim 2011; Kim & Taam 2012). This binary interaction produces slow winds (expanding velocity of 20-30 km s^{-1}) of

a circumbinary envelope, which shows a highly aspherical geometry. Hydrodynamic simulations have provided a detailed insight of the binary interacting geometry, which has an equatorial density enhancement in common. Most of the material strongly concentrates on the equatorial region, which corresponds to the orbital plane. Moreover, the slow winds generated on the orbital plane mainly form spiral structures (or arc-like structures depending on the viewing angle and the orbital inclination) with gravitational wakes breaking the spherical symmetry. Such spiral structures were found in several objects which have a binary nucleus (R Scl: Maercker et al. 2012, o Ceti: Ramstedt et al. 2014, IRC+10216(CW Leo): Decin et al. 2015). At the same moment, the companion accumulates some part of the material to form an accretion disk, and disk-driven bipolar jets (or collimated fast outflows) are possibly produced.

When enough(sufficient) mass concentrates on the companion's surface, a fast wind would be formed by a nova-like outburst expanding velocity of a hundred or thousand km s^{-1}. The fast wind catches up with the previous slower, denser winds, and compresses them into lobes above and below on opposite side of the dense equatorial region (Balick & Frank 2002). This formation stage is relevant to the scenario of the *Generalized Interacting Stellar Winds (GISW)* model, first proposed by Kwok et al. (1978).

The binary interaction is one of the main prerequisites for the formation mechanisms of a variety of symbiotic phenomena, and information of orbital parameters is necessary for further detail knowledge and modeling in symbiotic stars. To provide the orbital parameters can be applied to basic physical properties for a binary separation, period, component masses, which are relevant to a mass-loss and mass-transfer processes. Table 1.2 is the known orbital parameters of symbiotic stars so far (Belczyński et al 2000; Mikołajewska 2003). Although the orbital parameters are critical for the understanding of the symbiotic phenomena, only about a dozen of the known symbiotic stars currently have determined their orbits. Moreover, most of systems belong to S-type symbiotic stars, and fully known binary orbits are very rare with high uncertainties. Thus, determining orbital parameters for D-type symbiotic stars is a current issue and necessary to understanding the formation mechanism of symbiotic nebulae as well as various symbiotic phenomena.

1.2 Mira variables

Mira variables, named after their prototype of omicron Ceti (o Ceti), are a sub-class of Long Period Variables (LPVs). They are at a very late stage of low- and intermediate-mass stellar evolution located on the tip of the AGB phase in the Hertzsprung-Russell (H-R) diagram (Figure 1.5). They show a strong luminosity variation, larger than 2.5 and up to 10 magnitudes in the visual amplitude, due to stellar pulsations with changes in the opacity. The period of the variation and pulsation is typically between 100 and 1000 days. Typically, the masses for Mira variables are one to two solar masses. To this day the *"General Catalogue of Variable Stars"* lists more than 8000 Mira-type variables.

The schematic structure of the Mira variable is presented in Figure 1.6. In the AGB

Table 1.2: Known orbital parameters for symbiotic stars (Belczyński et al. 2000; Mikołajewska 2003)

Name	Type	$P_{\rm orb}$ (days)	$K_{\rm g}$ (km s^{-1})	q[4]	γ_0 (km s^{-1})	e	T_0 (JD[5])	$a_g \sin i$ ($R_\odot$)	$f(M)$ ($M_\odot$)
EG And	S	482.6	7.3		95	0	50804[3]	70	0.020
AX Per	S	680.8	7.5	2.5	116.5	0	45511.8	100	0.030
		682.1	7.8	2.3	-117.4	0	50964	105	0.033
BD Cam		596.21	8.5		22.3	0.09	42794[1]	99.7	0.037
V1261 Ori		642	7.5	3.0	79.7	0.07	46778[3]	95	0.028
BX Mon	S	1401	4.3	6.7	29.1	0.49	49530	104	0.0076
		1259	4.6		29.1	0.44	49680	103	0.0092
SY Mus	S	624.5	7.4		12.9	0	49082[3]	91	0.026
TX CVn	S	199	5.7		2.3	0.16	45195.25[1]	22	0.004
RW Hya	S	370.2	8.8		12.4	0	45071.6	65	0.026
		370.4	8.8		12.9	0	49512		0.026
BD21 3873	S	281.6	10.6		203.9	0	49087.3[3]	59	0.035
T CrB	S	227.57	23.9	0.6	27.8	0	47918.6	107	0.322
AG Dra	S	554	5.1		148.3	0	46366.4	56	0.008
		549	5.9		-147.2	0	50775	64	0.0115
KX TrA	S	1350	6.8	2.3	-123.7	0.29	51703	175	0.039
AE Ara	S	812	5.4	4	-15.7	0	50217	87	0.0133
RS Oph	S	455.7	16.7	0.35	40.2	0	50154.1[3]	150	0.221
V343 Ser		451.3	2.6		-5.63	0	50398[3]	23	0.0008
		450.5	2.7		-5.65	0.14	50575[1]	23.5	0.0009
FG Ser	S	650	8.3	2.8	71.2	0	48491	107	0.039
		633.5	6.9		73.3	0	51031	87	0.022
AR Pav	S	604.5	9.6	2.7	68.4	0	48139	115	0.055
		604.5	10.9	2.5	-68.3	0	48139	130	0.079
V443 Her	S	594	3.2		49.2	0	46007.7	39	0.002
		594	2.5		-55.5	0	50197	30	0.0010
FN Sgr	S	568.3	10.5	2.1	-53.7	0	50269	118	0.0689
BF Cyg	S	757.2	6.7	3.6	-3.75	0	51395	100	0.0239
CH Cyg	S	5700	4.9		57.7	0.47	45086	478	0.045
		756.0	2.6		60.6	0	46643.7	39	0.0014
		5292	4.8			0.06	45592[1]	500	0.060
CI Cyg	S	855.3	6.7	3	18.4	0	45241.8	114	0.027
		853.8	6.7		15.0	0.11	50426.4	112	0.026
V1329 Cyg	S	956.5	7.9	2.9	-23.1	0	51565	149	0.0481
CD43 14304	S	1448	4.4		27.6	0	45929[3]	126	0.013
		1442	4.6		27.5	0.22	45560[1]	128	0.014
AG Peg	S	816.5	5.3	4	15.9	0	31667.5	84	0.012
		818.2	5.4		15.9	0.11	46812	87	0.0135
Z And	S	758.8	6.8		1.8	0	45703.0	102	0.025
		758.8	6.7		-1.8	0	50260	102	0.024
CD27 8661		763.3	10.5		5.5	0	49280.5[3]	158	0.092

[1] T_0 - time of the passage through periastron
[2] Assumed from photometric ephemeris (eclipse)
[3] Time of maximum velocity
[4] Mass ratio of $q = M_g/M_h$
[5] Julian Date = 2400000 + JD

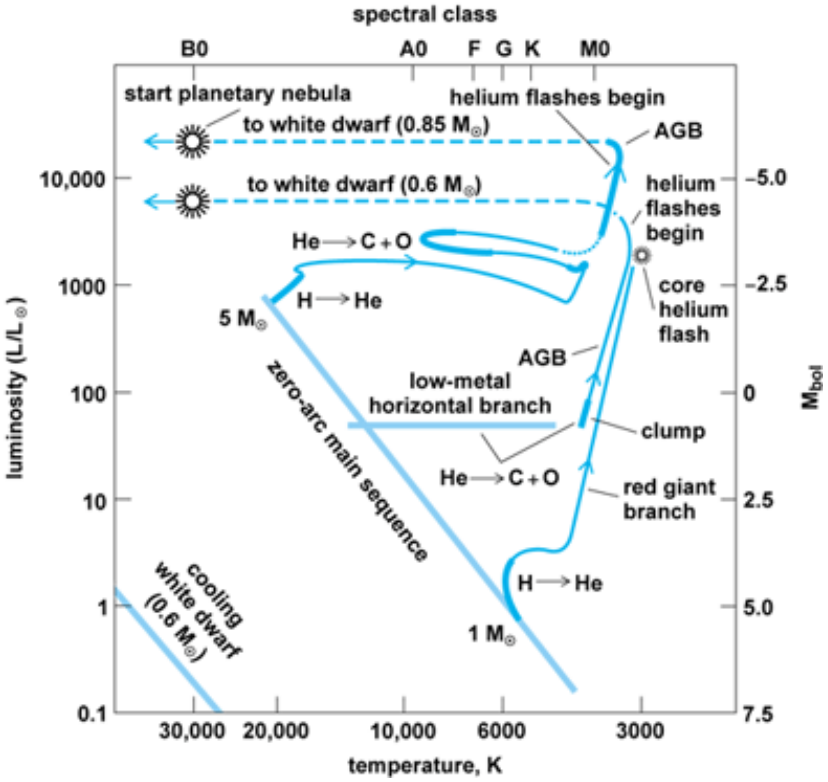

Figure 1.5: H-R diagram of evolution of low- and intermediate-mass stars. (After J. B. Kaler, Stars, W. H. Freeman, 1992, 1993, from work of I. Iben (1985))

phase, stars have an electron-degenerate core, consisting mostly of carbon and oxygen, surrounded by a nuclear burning of helium and hydrogen shells. In particular, convections between the core and the stellar envelope (called "dredge-up") occur in the AGB stage, and a stellar atmosphere would be abundant in various elements produced by nucleosynthesis. In addition, it is generally thought that AGB stars, including Mira variables, become unstable to produce radial pulsations. Shock waves induced by the pulsations bring material out to larger distances of the stellar atmosphere. The atmosphere of AGB stars expands to several hundreds of solar radii. Since an effective temperature of AGB stars is as low as 2500 K, the atmosphere enables to form(develop) a rich variation of molecule species. When the temperature is low enough, solid dust particles can condense at the further out region. Due to the highly extended atmosphere and a low surface gravity, in combination with a large amplitude pulsation, a large fraction of the mass drifts away through the strong stellar wind initiated by circumstellar dust formation. The greatly extended outer envelope becomes gravitationally unbound from the star and carries away mass with a mass-loss rate as high as 10^{-4} $M_\odot$ yr^{-1}.

According to the chemical composition of the stellar atmosphere, Mira variables divide into three spectral types, M-, S- and C-type, depending on the relative abundances of carbon and oxygen. Figure 1.7 shows the simple interrelationship along the three types of stars. As nucleo-synthesis (nuclear burning) and convection (dredge-up) progress, stars evolve into S- and C-type stars accompanied by the ratio of carbon and

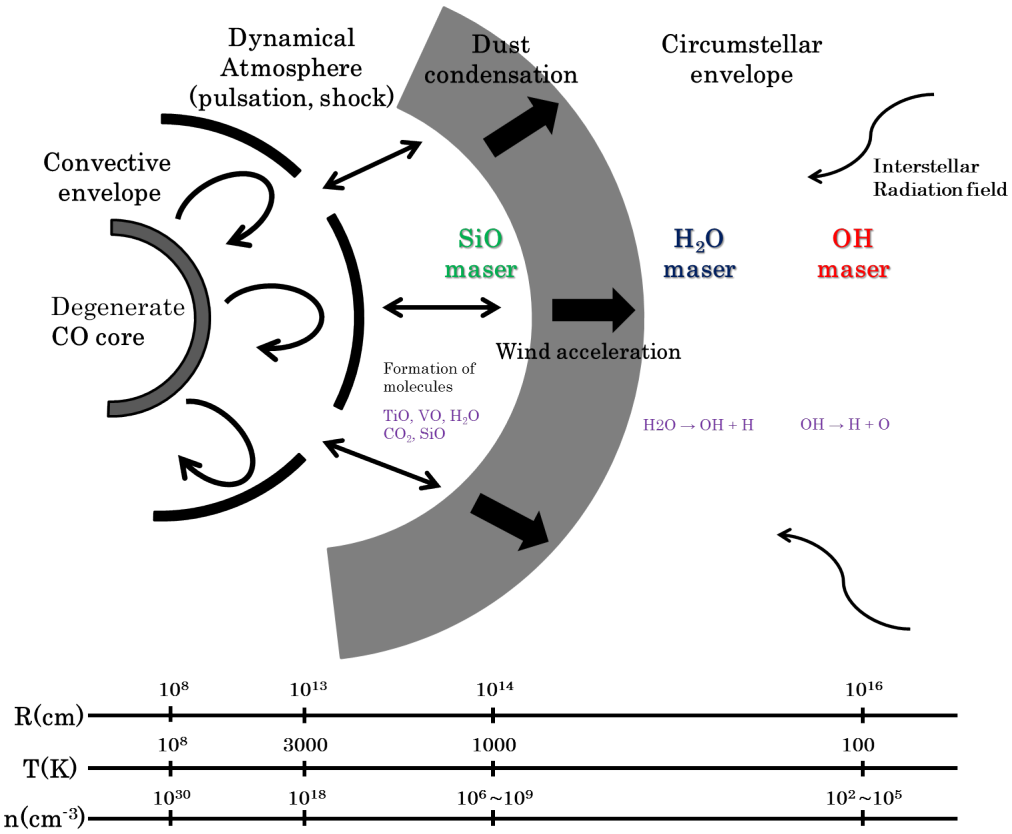

Figure 1.6: Schematic view (not to scale) of the structure in Mira variables. (Origin figure from Le Bertre T., 1997, "'Cool Stars Winds and Mass Loss: Observations", Lecture Notes in Physics, Springer, Vol. 497, p. 133)

oxygen changes. The changes of the ratio can be recognized by examination of their spectra.

When the ratio of C/O < 1, all carbons are bound in CO molecules, and the excess of oxygens is available for a formation of oxygen-bearing molecules and dust species such as amorphous aluminum oxide (Al_2O_3). This state is called M-type, also said to be an oxygen-rich star which is the largest class in Mira variables. They are characterized by TiO molecular absorption bands in the optical spectrum. Absorption bands due to VO and emission lines of Ca I also exist. In addition, they present strong near-infrared absorptions of H_2O and significant mid-infrared emissions of dust. The plentiful oxide molecules are also shown in radio wavelength as stellar masers such as SiO, H_2O and OH.

When the ratio of C/O ≈ 1, nearly all carbons and oxygens are bound in CO molecule, and less abundant elements are crucial for the molecular composition of the gas. Also, no abundant grain-forming material are available. This state takes place in S-type stars. The dominant feature is ZrO absorption bands in the optical spectrum. The presence of ZrO bands is often considered as a direct consequence of molecular equilibrium in the special circumstances where the atmospheric CO ratio is within

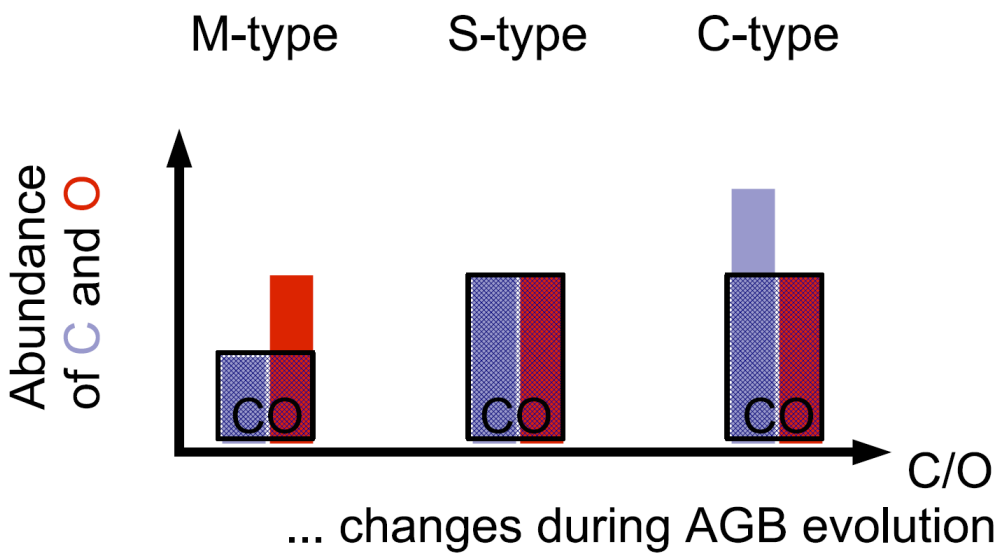

Figure 1.7: Interrelationship of M, S and C type of AGB stars. The relative abundances of carbon and oxygen lead to mainly three type of AGB cases. The excess of O (M-type) and C (C-type) is available for silicate grains (M-type) and carbon grains (C-type) respectively (Höfner 2009).

10% of unity (e.g. Scalo & Ross 1976). Sometimes, TiO absorption bands are strong as well. They show strong near-infrared CO absorptions and modest emissions from circumstellar dust at the infrared spectrum between 10 and 100 μm.

When the ratio of C/O $>$ 1, all oxygens are bound in CO molecules, and the excess carbon is mainly in form of hydrocarbon molecules and carbon-bearing species. This is C-type(or N-type) stars, also said to be a carbon-rich star. They show spectral features of molecules containing the carbon, such as CN, CH and C_2 and so on, in the optical spectrum. The abundant carbon molecules can be sometimes observed as a maser emission of HCN in those stars.

Similar to other variable stars, Mira variables are known to have a relationship between the pulsation period and luminosity, which is an important distance indicator for an old and intermediate-age population. Figure 1.8 shows the pulsation period and the K-band magnitude in which they have a significant correlation in the Mira variables. Large numbers of studies for determining the period-luminosity relationship have been carried out over the years (e.g. Feast et al. 1989; Hughes and Wood 1990; Groenewegen and de Jong 1994; Groenewegen and Whitelock 1996; van Leeuwen et al. 1997; Whitelock et al. 2000, 2008; Cioni et al. 2001; Feast 2004; Ita et al. 2004; Wang et al. 2010; Nakagawa et al. 2016). The nature of Mira variables and the period-luminosity relation has been uncertain, and the construction of the period-luminosity relation has been difficult since they have a large uncertainty in their luminosity due to distance measurement. Thus, accurate distance measurement toward Mira variables is necessary to provide their precise magnitude and promise to calibrate the accurate period-luminosity relation.

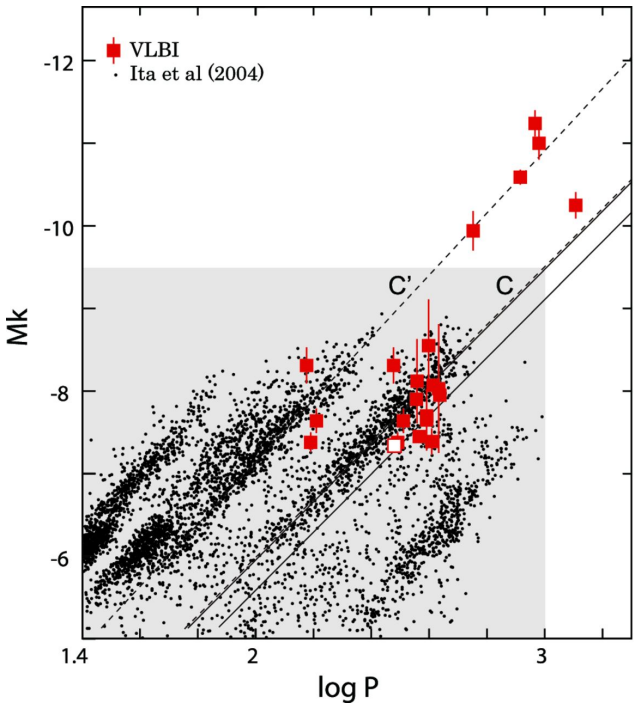

Figure 1.8: Example of the period-luminosity diagram (Nakagawa et al. 2016). The red squares are those measurements with VLBI astrometry. Dots are measurements of LPVs in the LMC and labels of C and C' correspond to the dashed lines at two sequences by Ita et al. (2004)

1.2.1 SiO masers in Mira variables

It is widely known that the extended circumstellar envelope of M-type (Oxygen rich) Mira variables shows one or more of three "classical" maser emissions: SiO, H_2O, and OH maser. These masers exist at different distances from the central star as shown in Figure 1.6. In addition, they play an important role in studying kinematics and dynamics of the stellar atmosphere from the inner to the outermost envelope.

SiO masers arise from rotational transitions of excited vibrational states with a high density ($> 10^9$ cm^{-3}). The characteristic temperature of the first excited vibrational level ($v = 1$), about 1800K, requires the region that is inside of the dust formation and wind acceleration point, distance about $3{\times}10^{13}$cm from the center of the star. The outer boundary of SiO masers is thought to be limited by the availability of the SiO in the gas phase before its condensation onto dust particles. This region between the photosphere and the dust formation point is sometimes termed as the extended atmosphere, where stellar pulsations, shocks, and localized mass ejections play a large role in governing(determining) the velocity field.

The first detection of SiO maser emissions was achieved by Snyder & Buhl (1974) toward a star-forming region of Orion A. Instantly, stellar SiO masers were discovered toward late-type stars by Thaddeus et al. (1974), Buhl et al. (1974) and Kaifu et al. (1975). Thereafter, thousands of late-type stars, including Mira variables, have been found to emit maser emissions in various SiO transitions.

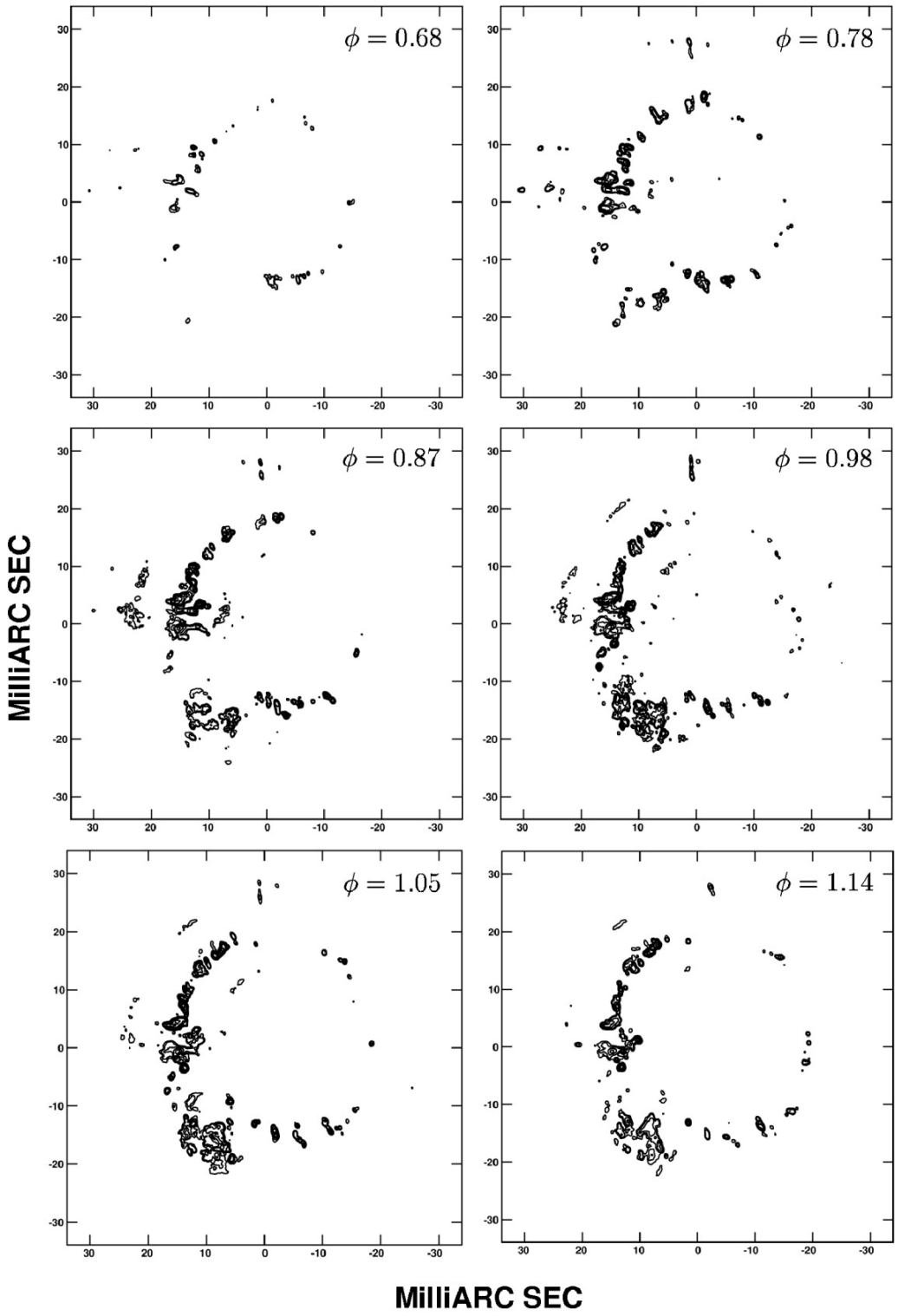

Figure 1.9: SiO v=1 J=1-0 maser emission toward the Mira variable TX Cam using VLBA observation. Each frame is displayed as an intensity contour plot with contour levels at -10, -5, -2, -1, 1, 2, 5, 10, 20, 40, 80, 100% of the frame peak intensity spaced at a phase interval of $\Delta\phi = \sim 0.1$ (Diamond & Kemball 2003)).

High resolution of Very Long Baseline Interferometry (VLBI) observations enables us to obtain spatial distributions of the SiO masers in the stellar atmosphere of the Mira variables. Several observations have verified that the spatial structure tends to show a clumpy and ring-like structure (e.g. Figure 1.9) located between 2 and 4 stellar radii, where the region from the stellar photosphere to the dust formation region (Diamond et al. 1994; Greenhill et al. 1995; Boboltz et al. 1997; Desmurs et al. 2000; Diamond and Kemball 2003; Yi et al. 2005; Cotton et al. 2004 references therein).

Monitoring and multi-transition observations of stellar SiO maser with VLBI also carried out to understand dynamics and kinematics of the stellar atmosphere for Mira variables. Along with theoretical studies, VLBI observations have demonstrated that the stellar atmosphere have complex motions of an expansion, contraction, rotation, asymmetric acceleration, and bipolar outflow with respect to the stellar pulsation (Gray & Humphreys 2000; Humphreys et al. 2002; Kemball et al. 2009; Assaf et al. 2011; Gonidakis et al. 2010, 2013). Therefore, these VLBI observations using SiO masers are a unique technique for studying complex processes occurring in the inner region of the envelope.

As other classical masers of OH and H_2O, an astrometry of SiO masers is available for Mira variables using the VLBI observation. One of essential in several applications of the astrometry is to obtain a distance using an annual (trigonometric) parallax measurement. The parallax is the basic and direct distance measurement without any other calibration or model dependence. By knowing the distance to the star, we can derive several physical parameters, such as an absolute luminosity, a stellar radius, physical scale of orbital separation with component masses and proper motions in actual velocities. For Mira variables, the distance measurement is a vital role in the period-luminosity relation. The classical masers of OH and H_2O have been successfully used for measuring the annual parallaxes in star forming regions and late-type stars e.g. comprehensive VLBI parallaxes are listed in Honma et al. (2012) and Reid et al. (2014). However, the parallax measurements of the SiO maser is rare and challenging, and only a few sources have been conducted (Orion KL: Kim et al. 2008; VY CMa: Zhang et al. 2012; R Aqr: Kamohara et al. 2010, Min et al. 2014). The interferometric phase coherence time is only in the order of dozens of seconds and there are very few available extragalactic sources for phase-referencing method at 43 GHz and higher frequencies in the observational and technical scheme. Moreover, typical lifetime of SiO maser components, which is both spatially and velocity coherent, is relatively short and they have complicated internal motions. These make it difficult to estimate the parallax by tracing the SiO maser components.

1.3 R Aquarii

R Aquarii (R Aqr) is one of the well-known symbiotic stars after the discovery by Harding (1816). R Aqr is known to be composed of a Mira variable as a cool late-type and a putative WD as a hot companion. The Mira variable is classified as a M-type (oxygen-rich) star showing an optical variation of over 5 magnitudes with a pulsation period of about 387 days.

R Aqr shows unique characteristics of (1) two extended inner & outer nebulae, (2) a bipolar jet-like feature, and (3) stellar maser emissions associated with the Mira variable. Numerous studies have been performed to examine those characteristics of symbiotic phenomena toward R Aqr in radio, infrared, optical, ultraviolet, and X-ray wavelength.

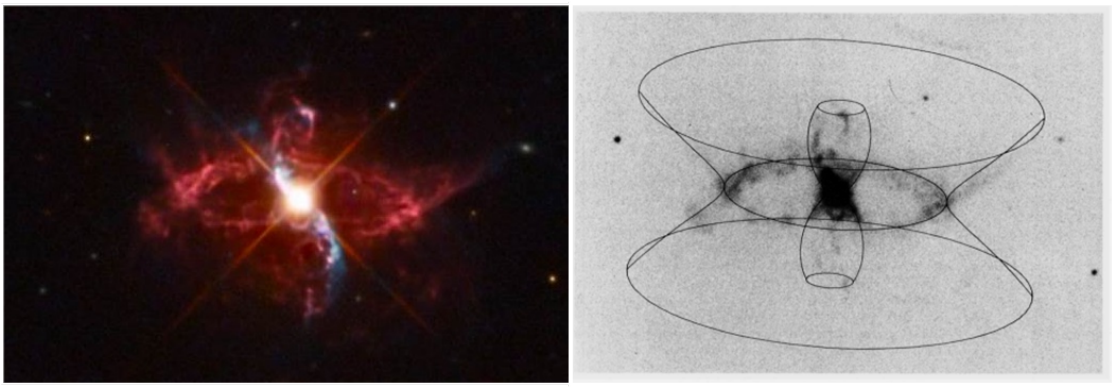

Figure 1.10: Images of the R Aqr nebulae. [Left] Optical image taken from Adam Block/Mount Lemmon SkyCenter/University of Arizona. [Right] Optical image overlapping the geometric structure of the inner & outer nebula (Solf & Ulrich 1985). North is up and East is left.

The extended inner & outer nebulae surrounding R Aqr, also known as Cederblad 211, were first discovered by Lampland (1923a, b). As shown in Figure 1.10, the outer nebula consists of two intersecting arc-shaped features of an equatorial dense region extending about 60 arcsec in the East and 70 arcsec in the West direction. The inner nebula looks like a wedge-shaped, extending about 30 arcsec in the North-South direction, nearly perpendicular to the outer nebula.

The outer nebula was considered to have an outward motion, which was firstly suspected by Hubble (1940, 1943) using the difference of images taken 17 years interval. The outward motion was confirmed by Baade (1943, 1944) using 16-years-apart optical plates. They inferred that the outer nebula was formed by a nova-like eruption approximately 600 years ago. Assuming a constant expansion, they deduced a kinematic distance of 260 pc for R Aqr.

Solf & Ulrich (1985) carried out an extensive study on the R Aqr nebulae using optical spectroscopic observations during 1982 to 1983. They showed that both inner and outer nebula have a same geometrical structure resembling a bipolar and hourglass-like shape. In addition, they introduced a simple(empirical) bipolar outflow model to describe the structure and expansion of the nebulae. Applying the model to the observations, both inner and outer nebula had a same bipolar axis oriented with a P.A. of 355 degrees and an inclination of 18 degrees with respect to the plane of the sky as shown in Figure 1.10. Expansion velocities on the equatorial regions were found to be 32 km s^{-1} for the inner nebula and 55 km s^{-1} for the outer nebula, respectively. Solf & Ulrich (1985) also suggested that both inner and outer nebulae are the result of two nova-like ejecting events, which were occurred approximately 185 and 640 years

ago. Assuming constant expansion velocities and proposed expansion ages, a kinematic distance is derived from 180 and 185 pc.

For the nova-like ejecting events on R Aqr, Yang et al. (2005) found historical records of two successive outbursts associated with R Aqr in A.D. 1073 and A.D. 1074. The outburst histories were also supported by a nitrate ion recorded in the Antarctic ice core (Tanabe & Motizuki 2012). Yang et al. (2005) suggested that these two records may provide astronomically meaningful constraints to the nebulae formation processes on R Aqr and symbiotic stars as well as the outburst models for other relative objects. In addition, they also derived a kinematic distance of 273 pc for R Aqr assuming the expansion velocity for the outer nebula from Solf and Ulrich (1985).

Recently, *Herschel*/PACS photometry observed a bright and extended central source with two opposing NE and SW arms in far-IR wavelength (Mayer et al. 2013). The arms reflected parts of the equatorial dense region of the outer nebula observed by Solf & Ulrich (1985). Two different wavelengths (70 μm and 160 μm) of PACS images provided that the arms are inclined by 77 degrees, which implies an elliptical structure of the equatorial dense region rather than circular. If the equatorial dense region of the outer nebula corresponds to the orbital plane, they inferred that the inclination of the binary orbit is also 77 degree with respect to the plane of sky.

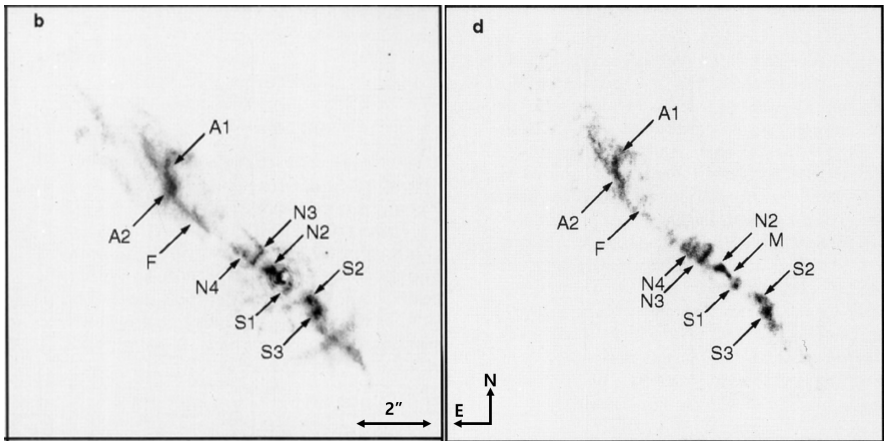

Figure 1.11: HST images of the jet and counter-jet of R Aqr (Paresce & Hack 1994). The binary is located at position of M in right figure. (Left) image taken by F190M (UV) filter (Right) image taken by F501N (optical) filter.

The most remarkable characteristic in R Aqr is the bipolar jet-like feature, probably powered by an accretion disk on the WD. The first detection of this feature was reported by Wallerstein and Greenstein (1980), who called the feature as "spike", in the northern portion of R Aqr. Subsequent VLA observations found the jet-like structure to extend about 6-10 arcsec in NE direction with a position angle of 22-24 degree from a central system (Sopka et al. 1982; Spergel et al. 1983). Further radio interferometry observations resolved the structure into (1) a series of knots for the NE jets, (2) a compact region of the central system and (3) SW jets, which are the counterpart of the NE jet. (Hollis et al. 1985, 1986, 1993; Kafatos et al. 1989; Hege et al. 1991). From the observations with different wavelengths, the jet was initially nonthermal radiation,

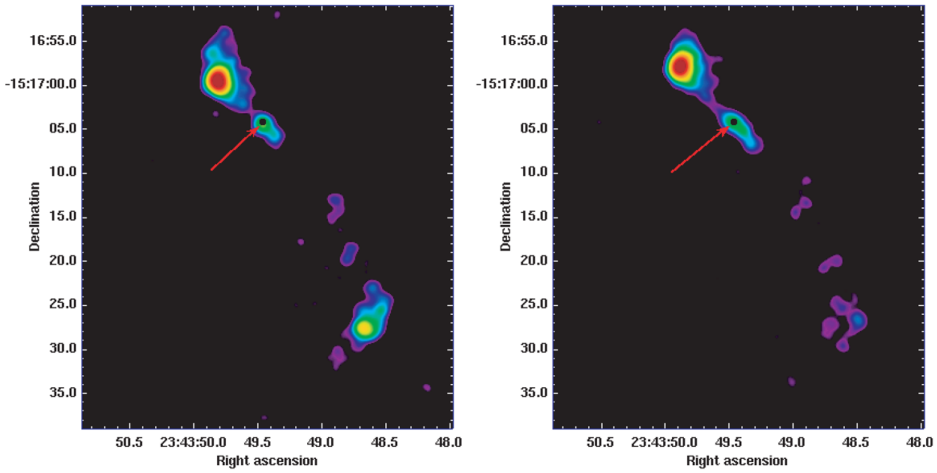

Figure 1.12: Chandra X-ray images of R Aqr jet (Kellogg et al. 2007). The images are taken at (Left) 2000.7 and (Right) 2004.0. The arrows point to the central R Aqr binary.

probably produced by a synchrotron emission, and become an optically thick thermal emission (Dougherty et al. 1995).

The Hubble Space Telescope (HST) also detected the jet-like feature in R Aqr as shown in Figure 1.11 (Paresce & Hack 1994). By comparing HST images taken with optical and UV filters, Paresce & Hack (1994) were able to identify a position of the central system, denoted as M. In addition, the jet was clearly shown as a narrow collimated stream tracing down to a distance ranging about 15 AU out to about 750 AU from the central system. The HST data provided that emissions of the jet were due to a shock driven through material left over from an earlier mass ejection and pre-ionized by a hot companion and/or an accretion disk.

In later Chandra X-ray images (Figure 1.12), the series of NE knots were not so well resolved as in the HST observations, but several large clumps were detected, corresponding to the NE jet, the central source observed in radio and HST. Furthermore, a next strongest SW jet feature was also detected in the X-ray image located at ∼30 arcsec with a P.A. of ∼211 degrees (Kellogg et al. 2001,2007). This SW jet had no counterpart of the radio and optical jet. Further UV spectroscopic observations suggested a bow shock model that have a shock speed of approximately 235-285 km s^{-1} and an inclination angle of about 10 and 35 degrees with the plane of the sky for the NE and SW jets, respectively (Nichols & Slavin 2009). Moreover, both jet features had similar physical parameters indicating a common origin and supporting a precessing accretion disk on the WD in R Aqr system.

Comparing two X-ray images, the central source had shown a morphological change and spectral characteristic between 2000 and 2004. The morphological difference indicated a new formation of a SW jet at the inner region of the central source. Contemporaneous VLA observations presented the spectral characteristic supporting a nonthermal, synchrotron emission from the new SW jet at the early stage of the jet development (Nichols et al. 2007).

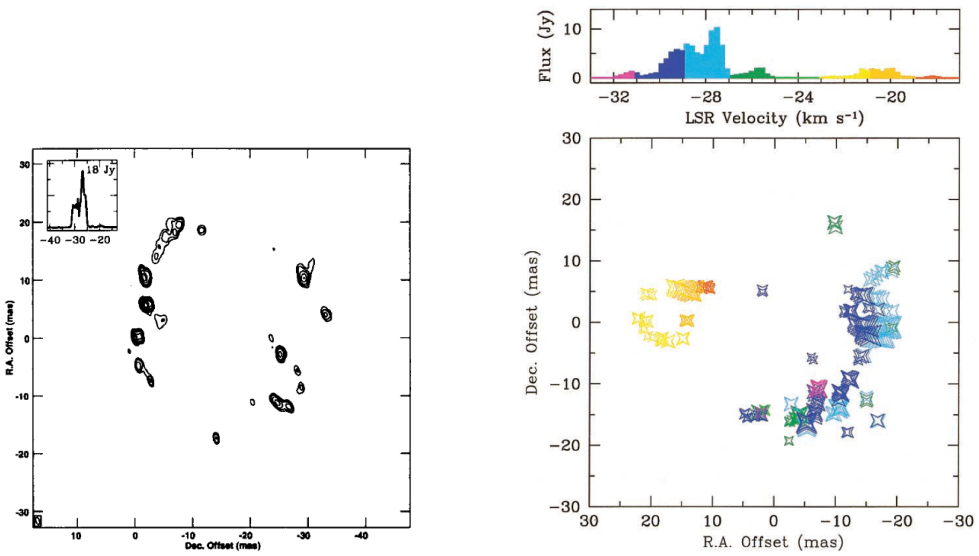

(a) (b)

Figure 1.13: VLBI observation images of R Aqr. (Left) VLBA observation image taken by Boboltz et al. (1997) (Right) VLBA observation suggesting differential rotation shell (Hollis et al. 2001)

R Aqr is one of the symbiotic stars to have circumstellar masers associated with the Mira variable. Since the first detection of a SiO maser toward R Aqr by Lépine et al. (1978), there have been several single-dish observational studies of 43/86/128 GHz SiO masers (Zuckerman 1979; Cohen & Ghigo 1980; Spencer et al. 1981; Martínez et al. 1988; Jewell et al. 1991; Schwarz et al. 1995; Cho et al. 1996; Alcolea et al. 1999; Pardo et al. 2004; Kang et al. 2006) as well as 22/321 GHz H_2O masers (Seaquist et al. 1995; Ivison et al 1994, 1998). Through the single-dish observations, the spectra of the SiO maser emission varied from one period to the next period, following the optical light curve with a phase lag of 0.1 to 0.2. This phase lag usually found in SiO masers for Mira variables, and indicated a possibility of a collisional maser pumping mechanism of the SiO maser emission.

The first high spatial resolution of VLBI observations was performed by Boboltz et al. (1997). They obtained four epochs of $v = 1$, $J = 1{-}0$ SiO maser distributions around the Mira variable in R Aqr (Left in Figure 1.13). The SiO maser distributions showed a ring-like structure with approximately 31 mas in radius, corresponding to about 3.4 AU assuming a distance of 220 pc. They argued that the SiO maser is located within 2-4 stellar radii, where the region is an outside of a stellar photosphere and inside of a circumstellar dust shell, similar to those of isolated AGB stars and Mira variables. In addition, they measured an averaged inward proper motion of $\sim$4 km s^{-1} for SiO maser components. Subsequent VLBA observations of SiO masers were performed by Hollis et al. (2001) and Cotton et al. (2004, 2006). Especially, Hollis et al. (2001) observed a velocity pattern implying a differential rotation in the SiO maser (Right in Figure 1.13). They suggested that the rotating maser shell has a rotational period between 8

to 34 years following a quasi-keplerian rotation as $v \propto (1/r^q)^{1/2}$, where $q \approx 1.09$.

In a precedent study with VERA, Kamohara et al. (2010) observed both $v = 1$ and $v = 2$ $J = 1 - 0$ SiO maser transitions simultaneously toward R Aqr. Assuming a position of the Mira variable from the SiO maser distribution, they measured a parallax of $\pi = 4.7 \pm 0.8$ mas, corresponding to a distance of 214^{+45}_{-32} pc with proper motions of $(\mu_{\rm RA}, \mu_{\rm Dec}) = (32.2 \pm 0.8, -29.5 \pm 0.7)$ mas yr^{-1} in the right ascension and declination, respectively. They also confirmed that both of the SiO maser transitions appeared in similar regions, but not exactly coincident within the spatial and spectral resolution. This result demonstrated that new theoretical studies are required for looking into the finer details of the maser emissions around Mira variables.

1.3.1 Orbital parameters for R Aquarii

Since the nature of symbiotic stars, there have been several attempts to define orbital parameters for R Aqr. However, its solution still has wide differences and large uncertainties. To date, the determination of the orbital parameter for R Aqr is a debatable issue.

Table 1.3: Summary of historical orbital parameters for R Aqr

	T_0 (JD)	Period (yr)	V_0 (km s^{-1})	e	ω (deg.)	$a \sin i$ (AU)
(1)	2429850	26.7	-42	0.5	265	22.7
(2)	2442100	44	-28.4	0.6	0	5.91
(3)	2442100	44		0.8	± 90	16.4 ± 0.5
(4)	2444349 ± 292	34.6 ± 1.2	-26.5 ± 0.3	0.52 ± 0.08	110.7 ± 18.4	3.5 ± 0.4
(5)	2444019 ± 728	43.6 ± 1.3	-24.9 ± 0.2	0.25 ± 0.07	106 ± 19	5.68 ± 0.85

(1) Merrill (1950) (2) Hinkle et al. (1989) (3) Hollis et al. (1997) (4) McIntosh & Rustan (2007) (5) Gromadzki & Mikołajewska (2009)

Table 1.3 is the summary of historical results of the orbital parameter analysis for R Aqr. The first orbital solution for R Aqr was reported by Merrill (1950), who used radial velocities of nebular emissions of [O III] and [Ne III] taken from 1920 to 1950. However, their solution was disproved by Jacobsen & Wallerstein (1975), who showed the nebular emissions did not vary periodically and not directly connected to the true orbital motion.

Willson et al. (1981) suggested an orbital period of ∼44 yr from the light curve of R Aqr. They found that the maximum brightness of the light curve had been depressed by over two magnitudes in comparison with the usual brightness between 1974 and 1980. A similar event was also discovered from 1928 to 1935. Willson et al. (1981) interpreted that the depressions of the light curve were attributed to the obscuration of the Mira variable by an extended accretion disk or dusty cloud around the companion. The orbital period of 44 yr for R Aqr was supported by later spectroscopic observations in the optical (Wallerstein 1986) and the infrared (Hinkle et al. 1989).

In an attempt to resolve the binary components of R Aqr, Hege et al. (1991) carried out speckle interferometry with a 1.8 nm bandpass centered on Hα (λ6563) in

October 1983. They obtained three components of a bright central component (C1) and relatively fainter components in NE (C2) and SW (C3) of the central component in a 45-mas-resolution image. The C1 was the brightest Hα source, probably arising from a hot companion and its accretion disk. The C2 was the weakest Hα components and corresponded to a radio jet-like feature observed by Hollis et al. (1986). On the other hand, the C3 had no radio counterpart, and the origin was unknown. They surmised that the C3 component might be associated with the Mira variable or another unidentified jet feature.

Another attempt to resolve the binary components was performed by Hollis et al. (1997), who simultaneously observed a 43 GHz of SiO maser emission with a 3.125 MHz bandpass and an adjacent lineless continuum emission with a 50 MHz bandpass using VLA. They were motivated to resolve the binary components because the SiO maser is associated with the Mira variable and the continuum comes from the HII region, presumably surrounding the hot companion/accretion disk. The position of the continuum was found to lie 55 ± 2 mas with a P.A. of 18 ± 2 degree relative to the position of the SiO maser measured by elliptical Gaussian fittings. With reasonable assumptions of the orbital period of 44 yr, they suggested a preliminary estimation of the orbital parameters. In addition, they argued that if these parameters are accurate, then the component C3 observed by Hege et al. (1991) is probably a knot of emission in the jet, rather than the Mira variable.

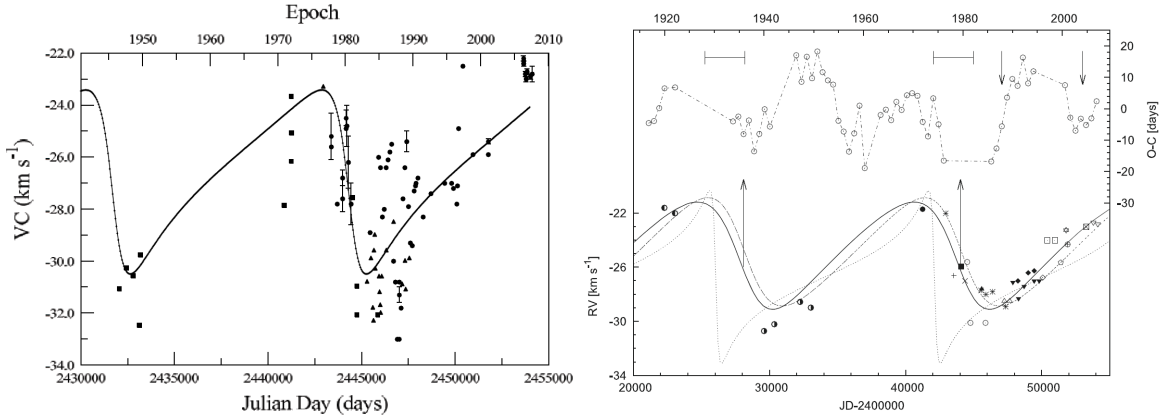

(a) McIntosh & Rustan (2007) (b) Gromadzki & Mikołajewska (2009)

Figure 1.14: The radial velocities and fitted orbital models for R Aqr.

Recently, McIntosh & Rustan (2007) collected an extensive, wide range of radial velocity data for R Aqr in visual, near-infrared and radio wavelength in a period between 1946 and 2007. As shown in Figure 1.14, they derived the orbital parameters from radial velocity analysis. However, the orbital period was 34.6 ± 1.2 yr, and their solution indicated a system mass function of $f(M) = 0.043\ M_{\odot}$ applying the inclination of 72 degree by Solf & Ulrich (1985). This mass is far less than assumed mass of the R Aqr system. To reduce and eliminate this problem, they suggested that the orbital inclination of the orbit is small of approximately 20 degrees.

Subsequently, Gromadzki & Mikołajewska (2009) complemented and reanalyzed the data collected by McIntosh and Rustan (2007) and obtained the orbital parameters of R Aqr as shown in Figure 1.14. Their solution was consistent with the previous orbital period by Willson et al. (1981) and indicated a reasonable system mass function of $f(M) = 0.096^{+0.042}_{-0.032}\ M_{\odot}$. Comparing the VLA observation by Hollis et al. (1997), their orbital parameters were consistent under the assumption of a distance lower than 200 pc. According to their orbital model, the last obscuration, called "Eclipse" event coincided with the predicted time from their orbital model.

1.4 VLBI astrometry

VLBI (Very Long Baseline Interferometry) is a technique which combines the radio emission simultaneously observed with several not-physical-connected radio telescopes. Distances between the telescopes of array range up to a few thousands of kilometers to achieve the high angular resolution in astronomy.

Special VLBI observational method called "phase-referencing" allows us to conduct precise astrometry of astronomical maser with accuracy much less than 1 mas. This method requires a reference source close to the target source (typically within a few degree separation) in order to compensate interferometric fringe(visibility) phase variations mainly caused by atmospheric fluctuations. Detail descriptions can be found in Thompson, Moran and Swenson (2001), Alef (1989), and Beasley and Conway (1995).

In interferometry observations, the phase Φ, which is given by the path-length difference of the signals from the different stations, contains the information about the position of the observed source. The output of a quasi-sinusoidal correlator response in an interferometry is expressed as $V = A \times \exp(i(\Phi_T - \Phi_M))$ for each antenna pair at frequency ν, where A is the visibility amplitude, Φ_T is the measured total phase and Φ_M is the modeled correlator phase. Since the correlator model phase has a limited accuracy, there exists residual phase error. This residual can be written as

$$\Phi_{resi} = \Phi_V + \Phi_{inst} + \Phi_{ant} + \Phi_{pos} + \Phi_{atmo} + \Phi_{iono} \tag{1.1}$$

where Φ_V is the visibility phase for extended source (visibility phase for the point source is zero), Φ_{inst} is the instrumental phase (effected by telescope path-length (cable) changes and so on), Φ_{ant} and Φ_{pos} are the error of the antenna and source positions, and Φ_{atmo} and Φ_{iono} are the phase error caused by the neutral atmosphere and ionosphere, respectively. If the target source is strong enough and its absolute position is not needed, these residual phases are generally corrected by using the source itself (global fringe-fitting and self-calibration).

For determining the position of the source, "phase-referencing" can be used to correct these phase errors by using the reference source closed to the target source. The concept of phase-referencing is that the target source phase can be corrected by interpolating the reference source phase. Considering the three measured phases, the reference (at time t_1) – target (at time t_2) – reference again (at time t_3) sequentially, the measured phases for the target and reference source will be

$$\Phi^{ref}_{resi}(t_1) = \Phi^{ref}_{V}(t_1) + \Phi^{ref}_{inst}(t_1) + \Phi^{ref}_{ant}(t_1) + \Phi^{ref}_{pos}(t_1) + \Phi^{ref}_{atmo}(t_1) + \Phi^{ref}_{iono}(t_1)$$

$$\Phi^{tar}_{resi}(t_2) = \Phi^{tar}_{V}(t_2) + \Phi^{tar}_{inst}(t_2) + \Phi^{tar}_{ant}(t_2) + \Phi^{tar}_{pos}(t_2) + \Phi^{tar}_{atmo}(t_2) + \Phi^{tar}_{iono}(t_2)$$

$$\Phi^{ref}_{resi}(t_3) = \Phi^{ref}_{V}(t_3) + \Phi^{ref}_{inst}(t_3) + \Phi^{ref}_{ant}(t_3) + \Phi^{ref}_{pos}(t_3) + \Phi^{ref}_{atmo}(t_3) + \Phi^{ref}_{iono}(t_3) \quad (1.2)$$

Then differencing the target and interpolated reference source phase, the difference phases will be

$$\begin{aligned}\Phi_{tar} - \widetilde{\Phi}_{ref} = (\Phi^{tar}_{V} - \widetilde{\Phi}^{ref}_{V}) + (\Phi^{tar}_{inst} - \widetilde{\Phi}^{ref}_{inst}) + \\ (\Phi^{tar}_{ant} - \widetilde{\Phi}^{ref}_{ant}) + (\Phi^{tar}_{pos} - \widetilde{\Phi}^{ref}_{pos}) + \\ (\Phi^{tar}_{atmo} - \widetilde{\Phi}^{ref}_{atmo}) + (\Phi^{tar}_{iono} - \widetilde{\Phi}^{ref}_{iono})\end{aligned} \quad (1.3)$$

where $\widetilde{\Phi}_{ref}$ is the interpolated phase at time t_2. Assuming that both the interpolated reference and target data are equally affected by the instrumental, atmospheric, ionospheric, antenna position error, and that the reference source is a point source (Φ^{ref}_{V}(reference visibility) or its structure is known, then, the phase difference between the reference and target source is obtained as follows.

$$\Phi_{tar} - \widetilde{\Phi}_{ref} = \Phi^{tar}_{V} + (\Phi^{tar}_{pos} - \widetilde{\Phi}^{ref}_{pos}) \quad (1.4)$$

Thus, phase-referenced phase difference only depends on the structure of target source Φ^{tar}_{V} and the difference in relative position between the reference and target source. This means that the result of phase-referenced difference contains only the information about the position of target source relative to the reference source (with the structure).

Sometimes the phase-referenced result contains the errors occurred by fluctuations of the total path length in the atmosphere and the interpolation error due to the time difference between two reference source scans. The VERA (VLBI Exploration of Radio Astrometry) has a dual beam system, and observes the target and reference source simultaneously, reducing these phase errors effectively.

1.4.1 VERA projects

The VERA (VLBI Exploration of Radio Astrometry) in NAOJ (National Astronomical Observatory of Japan) is a Japanese VLBI array aimed at obtaining 10 microarcsecond (10 μas) level accuracy of the parallax and proper motions for CH_3OH, H_2O and SiO maser sources using the phase-referencing VLBI observation (Honma et al. 2000).

The VERA array consists of four 20-m-diameter stations in Japanese archipelago located at Mizusawa (Iwate Prefecture), Iriki (Kagoshima Prefecture), Ogasawara (Tokyo), and Ishigaki-jima(Okinawa Prefecture), providing six baselines with the maximum length of 2270 km (Mizusawa to Ishigaki) and the minimum of 1019 km (Iriki to

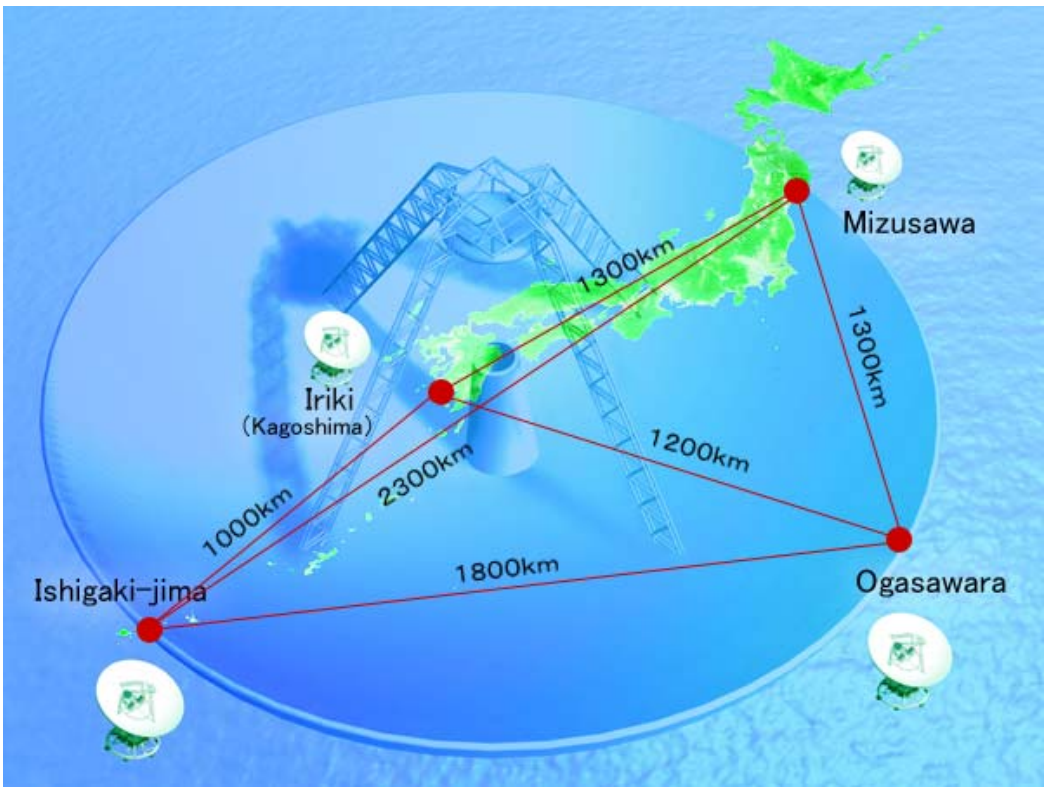

Figure 1.15: The arrangement of four VERA antennas

Ishigaki). The angular resolution given by the maximum baseline length is about 0.6 mas at 43 GHz.

The main sciences of VERA project are

1. to construct of 3-D Galaxy structure based on trigonometric parallax measurement and to reveal the distribution of Dark matter

2. to understand physical mechanism of outflows in star-forming regions and stellar envelopes

3. to understand physical mechanism of astronomical masers

4. to precisely calibrate the period-luminosity relation of Mira-type stars

5. to investigate structure and evolution of QSOs, AGNs and radio galaxies

Observing frequency bands are S, C, X, K, and Q-bands. The S-band (2 GHz) and X-band (8 GHz) are used for geodesy observations to determine baseline parameters, and C-band (6.7 GHz), K-band (22 GHz) and Q-band (43 GHz) are used for CH_3OH, H_2O and SiO maser observations, respectively.

VERA's unique dual-beam system can observe target sources and reference sources simultaneously within 2.2 degrees. As mentioned above, VLBI phase-referencing technique with a single-beam telescope significantly suffers from the fluctuation of the

atmosphere. However dual-beam observations with VERA effectively cancel out the atmospheric fluctuations. Therefore, VERA can measure relative positions of target source to reference sources with the highest accuracy. Usually, an extra-galactic AGN object is used as a phase calibrator, since an extra-galactic source does not have parallax and proper motions.

1.5 Aim of the present study

The aim of the present study is to determine reliable orbital parameters for a symbiotic star R Aqr.

The symbiotic star is a binary system showing various astrophysical phenomena, such as a jet-like outflow, a nova-like outburst, and an extended ionized nebula. These phenomena are closely related to binary interactions by a mass-loss and mass-transfer between the components. To acquire orbital parameters provides the fundamental physical information of the binary system for understanding and inspecting the symbiotic phenomena relevant to binary evolutions in theoretically and observationally. Especially, symbiotic nebulae are mostly found around D-type symbiotic stars. However, most of the systems of known orbital parameters are limited to S-type symbiotic stars.

Among the symbiotic stars, R Aqr is one of the well-known D-type symbiotic stars showing a variety of symbiotic phenomena. Several detection techniques have been used for determining their orbital parameters. Recently, a wide range of radial velocity data was accumulated to trace the orbital motion over 50 yrs. The radial velocity analysis is widely used for determining orbital parameters. Nevertheless, they still have a wide difference and a large uncertainty. Moreover, the only radial velocity method can not derive full orbital parameters because of an inclination ambiguity.

In order to disentangle the inclination ambiguity and derive full orbital parameters, an astrometry observation is complementary to the radial velocity method. For the astrometry, VLBI observations of SiO masers can address the astrometry to detect an accurate stellar position with a high spatial resolution. The stellar SiO masers around Mira variables are generally observed in the extended atmosphere which closed to the central star. In addition, the SiO masers tend to be formed in a ring-like structure precisely centered on the central star (Reid & Menten 1997, 2007). By tracing central positions of the SiO maser distributions, it is possible to measure the accurate astrometry for the Mira variable by the VLBI observation.

R Aqr is one of the symbiotic stars to have the stellar SiO maser associated with the Mira variable. In the present study, we conducted VLBI astrometry observations of SiO masers toward R Aqr. In addition, we also performed single-dish observations of SiO masers to trace a longer period of radial velocity variations. Combining the VLBI astrometry and radial velocity observations, we can determine full orbital parameters of R Aqr.

From the observations, we expect that the VLBI observation of SiO masers gives a kinematic information of the innermost region of the stellar atmosphere to understand the initial mass-loss process. In addition, the full orbital parameters provide the fundamental physical information of R Aqr as well as constraints on the mechanisms for

various symbiotic phenomena. Moreover, we also expect that the result will broaden the knowledge of late-stage of binary evolutions.

In the following chapters, we report results of monitoring observations of SiO masers toward the R Aqr system with VLBI and single-dish observations. In Chapter 2, we deal with the summary of the VERA, Nobeyama, and Mopra observations for VLBI and single-dish observations. Chapter 3 presents the results of the SiO maser observations for the astrometry and radial velocities and provides the orbital parameter analysis for R Aqr. Then, we devote to a detail discussions between the observational results and the symbiotic phenomena for the R Aqr system, in Chapter 4.

Chapter 2

Observations and Data analysis

2.1 VLBI observations

2.1.1 VERA observations

VLBI observations of $v = 1$ and $v = 2$ $J = 1 - 0$ SiO maser emissions toward R Aqr were performed using the four stations of VERA between October 2011 and June 2014. Rest frequencies of 43.122079 GHz and 42.820582 GHz were adopted for the $v = 1$ $J = 1 - 0$ and $v = 2$ $J = 1 - 0$ SiO maser transitions in the present study, respectively. VERA observations were done for a target source, R Aqr ($\alpha_{\rm J2000}$ = 23h43m49s.4616, $\delta_{\rm J2000} = -15°17'04".202$) and a phase-referencing source, J2348-1631 ($\alpha_{\rm J2000}$ = 23h48m02s.608532, $\delta_{\rm J2000} = -16°31'12".02226$) simultaneously using the VERA dual-beam system for the phase-referencing astrometry. The separation angle between the target and the reference source is about 1.6 degrees. A bright continuum source, 3C454.3, was also observed every 80 minutes for global fringe fitting and bandpass calibration. The instrumental delay differences between the two beams were measured in real time during the observation by the "horn-on-dish" method in which random signals from artificial noise sources injected into both beams are correlated at each station (Honma et al. 2008a).

The data were recorded onto magnetic tapes at a rate of 1024 Mbps with the VERA DIR2000 recording system, providing a total bandwidth of 256 MHz with 2-bit digitization. The 256 MHz bandwidth data were divided into 16 intermediate frequency (IF) channels (16 MHz each), and two of them were assigned to $v = 1$ $J = 1 - 0$ (IF2) and $v = 2$ $J = 1 - 0$ (IF1) SiO maser transitions for the target source, while others (IF3 - 16) were assigned to continuum for the reference source. Correlation processing was carried out on the Mitaka FX correlator located in NAOJ, Mitaka. For the maser source, the spectral channel spacing of the maser lines was set to be 31.25 kHz, yielding 512 spectral channels with a velocity resolution of $\sim$0.21 km s^{-1}.

In some of observations, SiO maser emissions were not detected because of system problems, bad weather conditions, and/or intrinsic property of SiO masers in AGB stars. Hence, we used the observational data of 16 epochs under relatively good conditions, with good weather, detectability of SiO maser emissions, and availability of full

Table 2.1: Summary of VERA observations

Obs.Code[1]	Date	Tsys[2] (K)	Beam$_{IF1}$[3] (mas×mas)	P.A.$_{IF1}$[3] (deg.)	Beam$_{IF2}$[4] (mas×mas)	P.A.$_{IF2}$[4] (deg.)
R11298C	2011-10-25	627.4	0.97×0.47	-25.68	1.05×0.45	-30.23
R12013A	2012-01-13	510.9	0.87×0.43	-18.84	0.92×0.45	-26.93
R12071A	2012-03-11	386.5	0.96×0.39	-20.56	0.97×0.39	-27.91
R12110B	2012-04-19	395.3	0.97×0.40	-28.26	0.92×0.41	-28.81
R12145C	2012-05-24	573.9	0.93×0.38	-28.14	1.05×0.35	-31.79
R12204B	2012-07-22	627.2	0.98×0.43	-26.89	1.05×0.40	-30.94
R13053A	2013-02-22	358.7	0.95×0.53	-21.61	0.96×0.52	-26.91
R13093B	2013-04-03	336.7	1.02×0.44	-28.17	0.95×0.40	-28.69
R13129B	2013-05-09	771.4	0.88×0.43	-27.50	0.92×0.40	-29.63
R13158D	2013-06-07	678.6	1.13×0.41	-27.33	1.30×0.41	-30.53
R13255A	2013-09-12	1103.0	0.99×0.39	-27.00	1.04×0.41	-27.68
R14026A	2014-01-26	374.4	0.94×0.45	-20.43	1.00×0.45	-20.34
R14051A	2014-02-20	268.7	1.04×0.44	-26.95	1.20×0.42	-30.16
R14086A	2014-03-27	314.3	1.02×0.42	-28.78	1.03×0.43	-29.50
R14116D	2014-04-26	527.1	0.87×0.48	-24.59	0.90×0.45	-24.56
R14164A	2014-06-13	1005.3	1.08×0.40	-32.70	1.13×0.40	-33.04

[1]Observation code indicating R(YY)(DOY)()
[2]Averaged system temperature of four stations
[3]Size and Position angle of synthesized beam for IF1 ($v = 2$ $J = 1 - 0$ SiO maser)
[4]Size and Position angle of synthesized beam for IF2 ($v = 1$ $J = 1 - 0$ SiO maser)

VERA stations in the present study. In Table 2.1, we give the summary of our VERA observations.

2.1.2 VERA data analysis

All the data analyses of VERA observations were performed using the Astronomical Image Processing System (AIPS) of National Radio Astronomy Observatory (NRAO) based on the standard VLBI data reduction procedure, consisting of the amplitude calibration, bandpass response, phase calibration, and imaging process. Through the AIPS processes, each calibration is performed by the individual program, called "task". The results of calibration steps are stored in the tables attached to the raw visibility data. The raw visibility data remain unaltered by the calibration steps until the one is satisfied that the best calibration in the tables is deliberately applied to the visibility data.

The data analysis steps were summarized in Figure 2.1, mainly made up of two processes of a single-beam and a dual-beam VLBI analysis. The amplitude calibrations for the target source (R Aqr) and the reference source (J2348-1631) were made independently using the system noise temperature measured during the whole observations based on the chopper-wheel method. The bandpass calibration was applied using auto-correlation data of a bright continuum source (3C454.3). Then, a modified delay-tracking model was also applied to the calibrated data for accurate astrometric

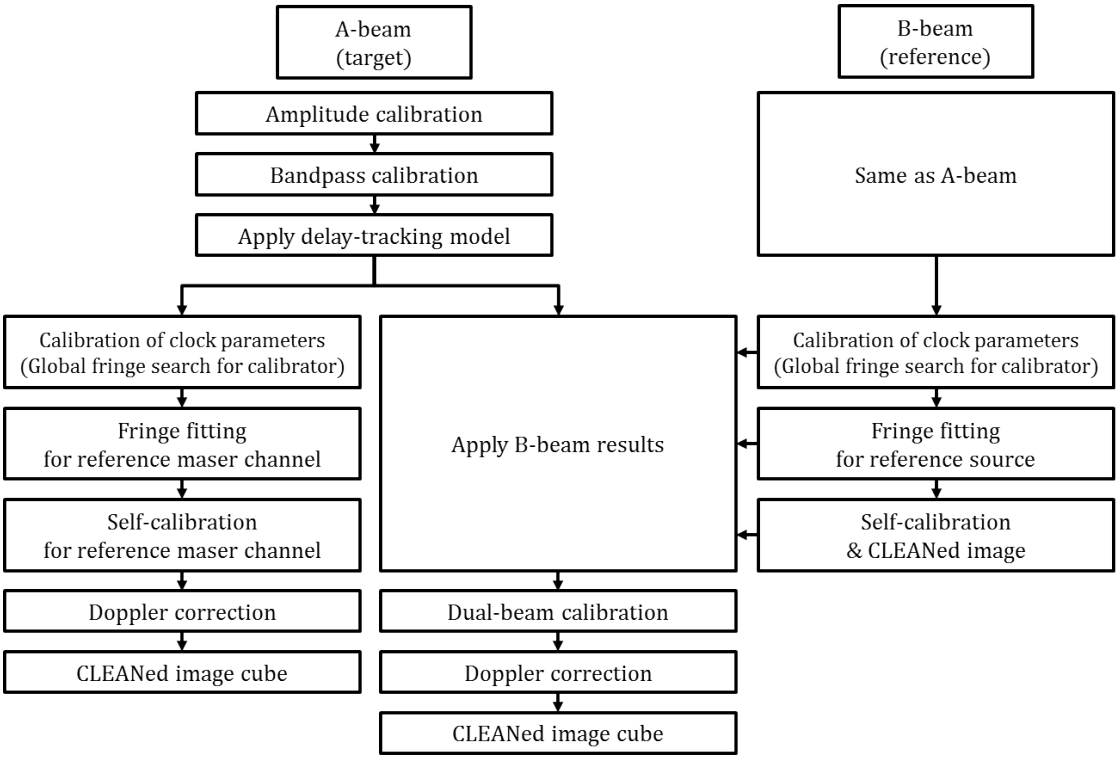

Figure 2.1: Procedures for VERA analysis in AIPS

measurements. Since the tracking model in the Mitaka FX correlator does not have sufficient accuracy, the new tracking model contains an estimation of the most recent Earth Orientation Parameters (EOP) and the tropospheric delay from GPS data at the each VERA stations (Honma et al. 2008b).

The single-beam VLBI analysis was used for the target source data to obtain overall distributions of the SiO maser emissions. A reference channel, which a bright and simple structure of maser component, was selected for a self-calibration. The solutions of the self-calibration were applied to all the other velocity channels of which the visibilities were phase-referenced to the reference maser component. After Doppler correction, CLEANed images were made covering the LSR velocities from -11 to -30 km s^{-1} consisting of 2048 pixels $\times$ 2048 pixels in size with a pixel spacing of 0.05 mas. All of the maser components were searched with a signal-to-noise ratio (SNR) higher than six as a detection criterion(threshold), and their positions were measured by two-dimensional elliptical Gaussian fitting. The selected maser components were considered as the real maser emissions if they exist in more than two adjacent velocity channels within the synthesized beam.

The single-beam VLBI analysis causes the loss of the absolute positional information. Therefore, the dual-beam VLBI analysis was also performed to obtain the absolute positions of the SiO maser emissions. The fringe fitting was made on the reference source to obtain the residual group delays and phase rates. The results of the fringe fitting were applied to the target source for phase referencing. The dual-beam calibration data were also requested to calibrate the altered delays and phases caused

by the instrumental delay differences between two beams. After Doppler correction, SiO maser images on the absolute coordinate system were obtained in the same manner as the single-beam analysis.

The target source data were divided into two maser transitions, and these data processes were independently worked on the $v = 1$ $J = 1 - 0$ and $v = 2$ $J = 1 - 0$ SiO maser transitions in the same way.

2.2 Single Dish observations

2.2.1 Nobeyama & Mopra observations

Single-dish observations of SiO maser emissions toward R Aqr were carried out using Nobeyama 45m telescope and Mopra 22m telescope.

The SiO maser observations by the Nobeyama 45m telescope were made from 2002 to 2012. The cooled SIS mixer receivers of S40 and S100, HEMT receivers of H40 and acousto-optical spectrometers (AOS) were used. The observations were summarized in Table 2.2. The 2048 velocity channels cover roughly between $-180 \sim +120$ km s^{-1} with a velocity resolution of 0.14 km s^{-1} for $v = 1$, $v = 2$ $J = 1 - 0$ SiO masers and between $-100 \sim +40$ km s^{-1} with a velocity resolution of 0.07 km s^{-1} for $v = 1$ $J = 2 - 1$ SiO maser transitions, respectively. Data reductions were performed using the reduction software of `NEWSTAR` developed by the Nobeyama Radio Observatory (Ikeda et al. 2001). Raw data were processed through (1) flagging out bad data, (2) integration, and (3) removing(subtracting) the baseline by emission-free channels with a least-squares fitting of a first-order polynomial.

Table 2.2: Summary of Nobeyama 45m telescope observations

Spectral lines	Periods	Epochs	N_{Ch}	Res. (km s^{-1})	Range (km s^{-1})
SiO (v=1 J=1−0)	2005/03∼2012/11	70	2048	0.14	$-180 \sim +120$
SiO (v=2 J=1−0)	2005/03∼2012/11	74	2048	0.14	$-180 \sim +120$
SiO (v=1 J=2−1)	2002/03∼2010/03	3	2048	0.07	$-100 \sim +40$

Additional single-dish observations were carried out using the Mopra 22m radio telescope of the Australia Telescope National Facility (ATNF). This observation is one of targets for the Mopra monitoring program, which observed 121 SiO maser sources including Long-period variables, semiregular variables, irregular variables, OH-IR stars, and the Orion. The Mopra monitoring program was published in the data catalogue by Indermuehle et al. (2013)[1]. The detailed observational information was reported in McIntosh & Indermuehle (2013). For R Aqr, the Mopra observed the $v = 1$ $J = 1-0$ and $v = 1$ $J = 2 - 1$ SiO maser transitions between 2008 and 2014. The observations were summarized in Table 2.3. The 4096 velocity channels cover roughly between $-400 \sim +500$ km s^{-1} with a velocity resolution of 0.23 km s^{-1} for $v = 1$ $J = 1 - 0$ SiO masers

[1]The data were released with the support by ATNF (http://www.narrabri.atnf.csiro.au/cgi-bin/obstools/siomaserdb.cgi)

and between $-240 \sim +230$ km s^{-1} with a velocity resolution of 0.12 km s^{-1} for $v = 1$ $J = 2-1$ SiO maser transitions, respectively. Among the observations, we excluded the data of 3 epochs (2011/02/16, 2011/02/14, 2011/09/06) for $v = 1$ $J = 1-0$ SiO maser observations and 3 epochs (2010/08/24, 2011/02/17, 2013/10/28) for $v = 1$ $J = 2-1$ SiO maser observations because of (1) a bad baseline (not well subtracted baseline with remaining sinusoidal pattern) and (2) very weak emission features due to system problems and/or bad weather conditions and/or their intrinsic properties.

Table 2.3: Summary of Mopra 22m telescope observations

Spectral lines	Periods	Epochs	N_{Ch}	Res. (km s^{-1})	Range (km s^{-1})
SiO (v=1 J=1−0)	2009/04∼2014/04	28	4096	0.23	$-400 \sim +500$
SiO (v=1 J=2−1)	2008/03∼2014/04	29	4096	0.12	$-240 \sim +230$

Chapter 3

Results

3.1 VERA observations

3.1.1 Spatial distributions of the SiO masers

The epochs of VERA observations toward R Aqr are presented in Figure 3.1 along with the optical light curve[1].

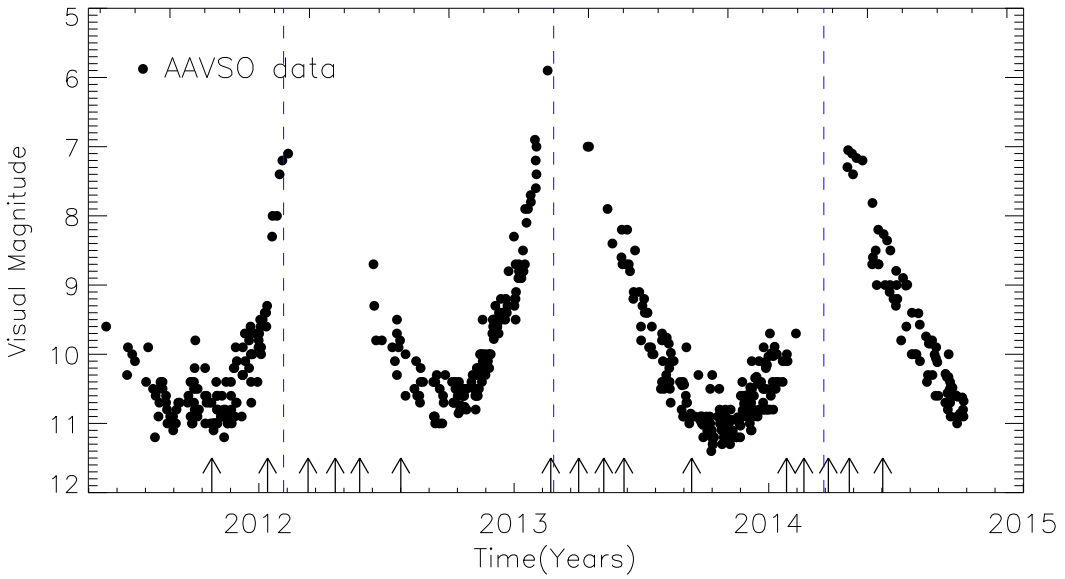

Figure 3.1: The epochs of VERA observations plotted on the optical light curve of R Aqr from AAVSO data from 2011 to 2015. Dashed lines indicate the maxima light curve, and upper arrows indicate the VERA observation epochs.

Our VERA observations covered the optical phase interval between $\phi = 0.74$ and $\phi = 3.22$ from 2011 to 2014. Note that we adopted the stellar pulsation ephemeris

[1]The optical data were supplied by the American Association of Variable Star Observers (AAVSO international Database)

derived by Gromadzki & Mikołajewska (2009) of

$$\mathrm{JD(max)} = 2416080 \pm 4 + 387.30 \pm 0.07 \times E \tag{3.1}$$

where JD(max) is the epoch of maximum light curve, 2415080±4 is the initial(reference) maximum epoch in Julian day, 387.30 ± 0.07 is the optical pulsational period in days, and E is the number of elapsed pulsation cycles.

Figure 3.2 shows the $v = 1$ $J = 1-0$ and $v = 2$ $J = 1-0$ SiO maser images and distributions ordered by epoch from top to bottom. The detected SiO maser components are tabulated in Appendix A.6. All the images are centered at the reference celestial coordinate of α_{J2000} = 23h43m49s.4616, $\delta_{\mathrm{J2000}} = -15°17'04".202$ in RA and Dec. Left images are the velocity integrated intensity images superposing two SiO maser transitions. Middle and right images are the LSR velocity distributions of the SiO maser components in the range between −12 and −30 km s^{-1}. Our VERA observation in the present study is the first long-period (covering three pulsation cycles), multi-transition SiO masers (both of $v = 1$ $J = 1 - 0$ and $v = 2$ $J = 1 - 0$ SiO maser transitions) and VLBI astrometry observation (providing the absolute positional information with high spatial resolution) toward the symbiotic star, R Aqr.

Overall SiO maser emission toward R Aqr extended around 40 mas × 40 mas in RA and Dec forming clumpy, sparse and partial ring (arc-like) structures as similar to the previous VLBI observations for AGB stars. They are commonly explained by tangential amplification (Diamond & Kemball 2003). However, the SiO maser components did not fill the whole of a circle, occupying several portions in the atmosphere. The strength and number of maser components increased near the optical maximum, while decreased and disappeared near the optical minimum. Superposing the $v = 1$ and $v = 2$ $J = 1-0$ SiO maser images showed that most predominant and brightest maser features located in similar regions but were rarely coincident.

Time variability of overall distributions can be divided into three patterns in our observations with respect to the stellar phase.

$\phi = 0.74 \sim 1.44$ (from 2011 to 2012): The SiO masers were located in mainly three parts confined to western, southern, and northern parts corresponding to the apex of a triangle. The Western part of the SiO masers shows a radially elongated distribution with relatively red shifted LSR velocities from −15 to −19 km s^{-1}. The dominant SiO masers were located in the north and northeast parts showing arc-like distributions with the LSR velocities from −20 to −24 km s^{-1}. In the last epoch of 2012 (R12204B; ϕ=1.44), $v = 2$ $J = 1 - 0$ SiO maser components split into two features, in which one might follow the outer motion of a pulsation shock front and the other moved to opposite direction following a gravitational infall (describing as split by Gonidakis et al. 2013). Moreover, the southern part of the SiO masers showed blue-shifted LSR velocities from −25 to −30 km s^{-1}, which maser components were relatively weaker than other features. They became weaker and disappeared in the last two epochs in 2012. Separations between the apex were ∼30 mas from north to south, ∼28 mas from north to west, and ∼28 mas from south to west parts, respectively.

ϕ = 1.99 $\sim$ 2.51 (in 2013): Most of SiO maser emissions dominated in the east to southern parts forming partial ring-like structures. Several weak emissions were detected in the western part having relatively red-shifted LSR velocities from -16 to -19 km s^{-1}. Dominant ring-like eastern parts of emissions took possession of almost 40% of a circle with LSR velocity range between -20 and -25 km s^{-1}. A few blue-shifted maser emissions were also detected in the southern part, as similar positions of the first pattern of the SiO maser distribution.

ϕ = 2.86 $\sim$ 3.22 (in 2014): The SiO masers were occupied in the north, east, and southern parts of the shells. The dominant maser emissions located in eastern and southern parts as similar as the second distribution pattern, but more sparsely distributed. These maser features seemed to persist along the pulsation cycles. The relatively red-shifted maser components (LSR velocity between -15 and -19 km s^{-1}) located in southeast part showing radially extended structures where the inner maser emissions were redder than outer emissions. Moreover, the eastern part of the SiO masers had relatively blue-shifted than southern part (between -20 and -23 km s^{-1}), and also showed the radially extended structure. Northern parts of the SiO masers had blue-shifted LSR velocities from -24 to -26 km s^{-1}, and newly appeared in comparison with the previous two observed patterns.

In several epochs, some groups of maser emissions showed radially extended structures with clear velocity gradient, so-called "spike-like" feature. These maser features came out in almost entire epochs, clearly seen in the third phase. Those spike-like structures are also seen in other AGB stars with high resolution VLBI observations (TX Cam: Yi et al. 2005; o Ceti: Cotton et al. 2006,2008; R Leo: Cotton et al. 2008; U Her: Cotton et al. 2008; IK Tau: Matsumoto et al. 2008), reflecting the dynamical motion of masing region.

The SiO maser emissions appeared to be random and no regular pattern over pulsation phases. No significant indication of a rotation shell reported by Hollis et al. (2001) is formed. However, most of the maser emissions concentrated on the East side of a semicircle, which might be affected by the companion of the binary system.

3.1.2 Concentric circular fitting

In order to characterize the SiO maser distribution, we performed a concentric circular fitting to the observed SiO maser components in each epoch. According to theoretical and observational studies for SiO maser emissions in AGB stars, the masers tend to form a ring-like distribution in different regions with respect to the masing conditions of the each maser transitions (Lockett & Elitzur 1992; Gray & Humphreys 2000; Gray et al. 2009; Yun & Park 2012). Particularly, the $v = 2$ $J = 1 - 0$ SiO maser usually occupies closer to the central star than the $v = 1$ $J = 1 - 0$ SiO maser transition, precisely centered on the central star (Desmurs et al. 2000; Reid & Menten 2007).

The concentric circle is the most simple model to describe the size of the SiO maser region, as well as the position of the central star from its radii and centers.

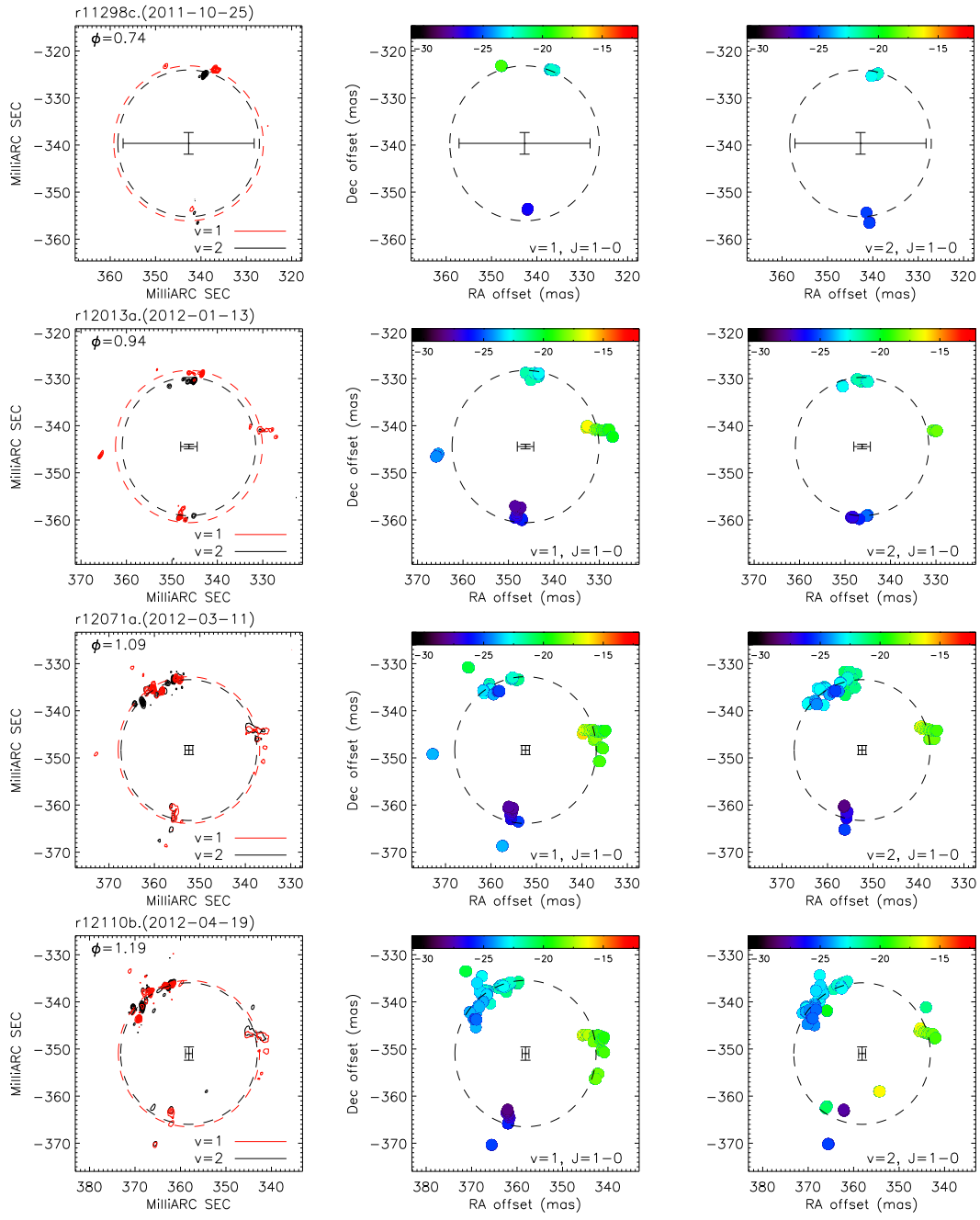

Figure 3.2: SiO maser emissions towards R Aqr. Dashed circles are the results of concentric circular fitting. Central positions and those uncertainties are also presented (Details in Chapter 3.1.2). [Left] Integrated intensity images of the $v = 1$, $J = 1 - 0$ (red) and $v = 2$, $J = 1 - 0$ (black) SiO maser emissions over the LSR velocity range of -31.5 to -12.0 km s^{-1}. Contour levels are 10, 20, 30, 40, 50, 60, 70, 80, 90 and 100% of the peak flux. [Middle] The LSR velocity map of the $v = 1$, $J = 1 - 0$ SiO maser components. [Right] The LSR velocity map of the $v = 2$, $J = 1 - 0$ SiO maser components. Velocity ranges are plotted on the top ranging from -31 to -12 km s^{-1}.

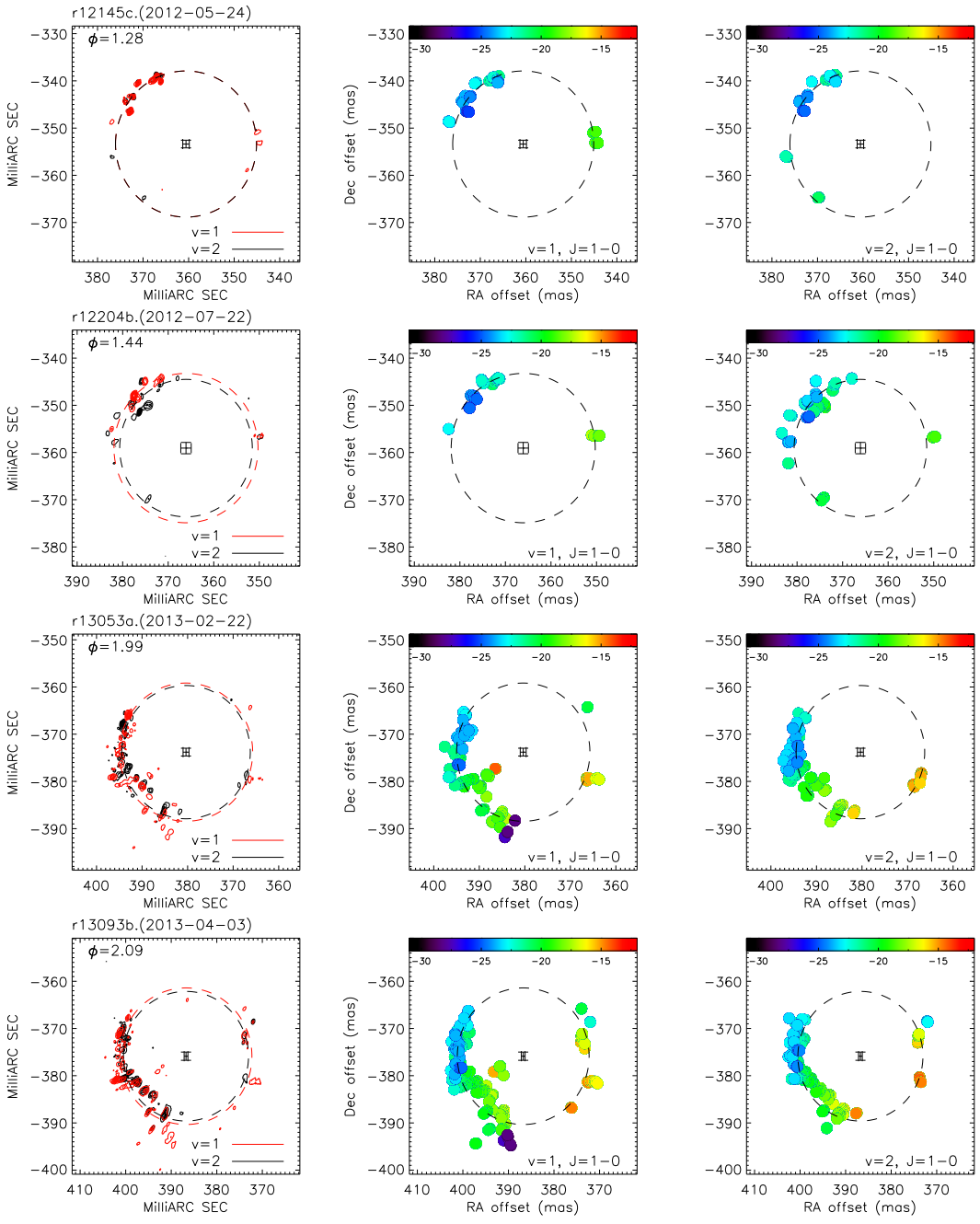

Figure 3.2: SiO maser emissions towards R Aqr. (Continued)

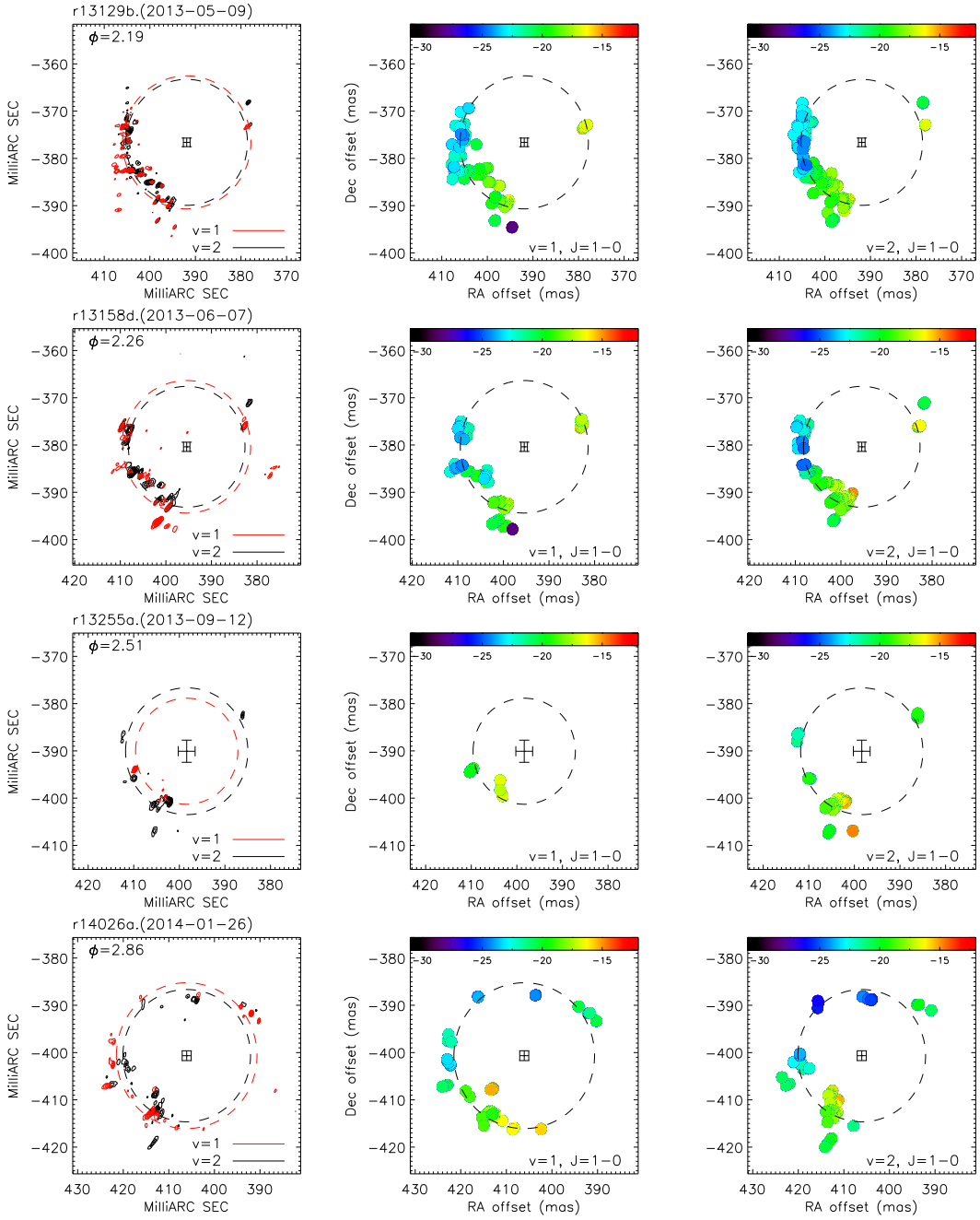

Figure 3.2: SiO maser emissions towards R Aqr. (Continued)

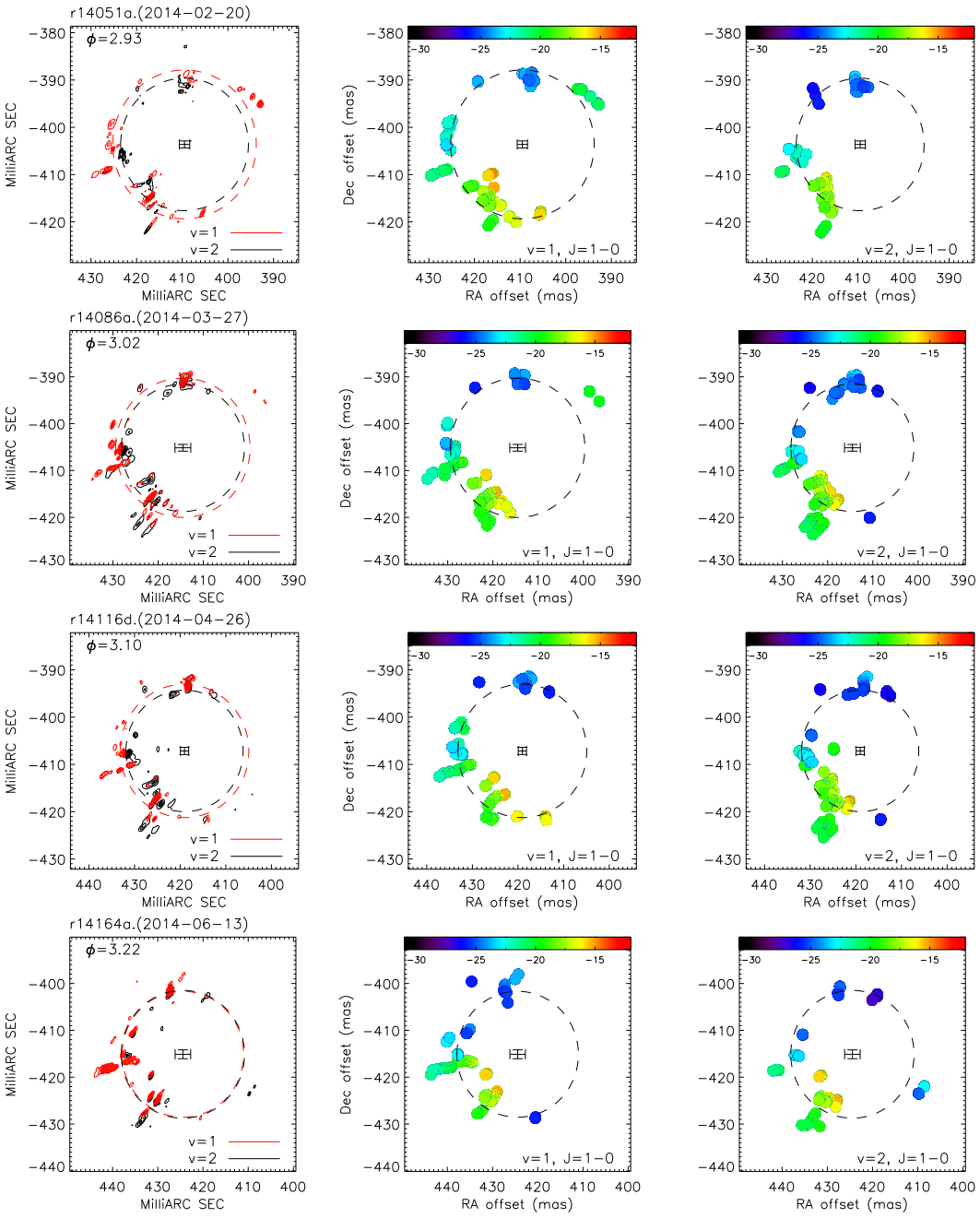

Figure 3.2: SiO maser emissions towards R Aqr. (Continued)

The changes of the radii provide overall behavior of the masing region, which is the innermost atmosphere of the Mira variable. In addition, the motion of the centers gives the astrometric information caused by an annual parallax, binary motion, and proper motion of the star.

The central position and the size with their uncertainties for the SiO maser rings were determined by a bootstrap method (Efron 1979; Efron & Tibshirani 1993). A Levenberg-Marquardt least-square minimization[2] (Markwardt 2009) was used as the optimization algorithm. The bootstrap is a computer-based resampling method, and can be applied to estimate model-based or model-independent parameters and uncertainties.

Through the bootstrap method, a synthetic data sample is generated from the original data set, which is the positions of the SiO maser components. The synthetic bootstrap sample turns out to be the same size with the original data by the replacement, i.e. one SiO maser position can be duplicated across the sample (one observation can occur multiple times, more than once). The ordering is not important for the replacement. Then, a least-square fitting is performed to obtain parameters which we are interested in. This process was repeated for 10^4 independent bootstrap samples, and we took the mean of the parameter values as the best value and the standard deviation as an uncertainty.

The results of the concentric circular fitting are presented in Figure 3.2 and summarized in Table 3.1. As a result, we measured the astrometry set for the Mira variable as well as the size of the SiO maser emitting regions from 2011 to 2014, totally 16 epochs. For two of results on 2011/10/25 (R11289C) and 2013/09/12 (R13255A), the fitting results are poorly constrained than other results because relatively fewer SiO maser components were detected. Those two epochs are a nearly stellar minimum phase in which SiO maser emissions are weaker than other epochs.

During the three years of observations, the positions of the Mira variable moved 81.73 mas to the East (linearly 31.06 mas yr^{-1}) and 75.48 mas to the South (linearly 28.69 mas yr^{-1}), respectively. The stellar motion contains mainly a proper motion and parallax motion. After extracting the parallax motion, the proper motion can be divided into a secular motion and a binary motion if there are no other effects. The change of the proper motion represents the binary motion, which can extract the binary parameters. We will deal with these astrometry parameters in Chapter 3.3.

The SiO maser components were distributed between 10 and 20 mas from the central position. For the size of circular fitting, the $v = 2$ $J = 1-0$ SiO maser radii were smaller than the $v = 1$ $J = 1 - 0$ SiO maser radii for the most of the epochs. The mean radius of the $v = 1$ $J = 1 - 0$ SiO maser ring was $\bar{R}_{v=1} = 14.81$ mas, and $v = 2$ $J = 1 - 0$ SiO maser ring was $\bar{R}_{v=2} = 14.10$ mas. This result indicates that the $v = 2$ $J = 1 - 0$ SiO maser region occupies the outside of $v = 1$ $J = 1 - 0$ SiO maser region, which is consistent with theoretical studies and other SiO maser observations for AGB stars by high-resolution VLBI observations. In addition, the difference of both masing regions indicates the different condition and property of the atmosphere providing implications

[2] a customized IDL (Interactive Data Language by Exelis Visual Information Solutions) routine `MPFIT` package was used

Table 3.1: Summary of the concentric circular fitting result of R Aqr

Obs.code[1]	ΔRA[2] (mas)	ΔDec[2] (mas)	$R_{v=1}$ (mas)	$R_{v=2}$ (mas)	Phase
R11298C	342.71 (14.44)	-339.63 (2.31)	16.47 (3.43)	15.59 (4.61)	0.74
R12013A	346.25 (1.81)	-344.42 (0.50)	16.15 (1.10)	14.67 (0.53)	0.94
R12071A	352.40 (0.84)	-348.34 (0.97)	15.56 (0.89)	14.94 (0.64)	1.09
R12110B	358.14 (0.76)	-350.97 (1.42)	15.52 (0.87)	15.02 (1.04)	1.19
R12145C	360.57 (0.72)	-353.38 (0.82)	15.48 (0.73)	15.48 (0.75)	1.28
R12204B	366.09 (1.14)	-359.07 (1.20)	15.82 (1.07)	14.56 (1.09)	1.44
R13053A	380.35 (0.65)	-373.80 (0.83)	14.64 (0.83)	14.11 (0.64)	1.99
R13093B	386.76 (0.42)	-375.87 (0.87)	14.47 (0.54)	13.73 (0.51)	2.10
R13129B	391.91 (0.73)	-376.61 (0.91)	14.07 (0.78)	13.33 (0.76)	2.19
R13158D	395.43 (0.70)	-380.37 (0.98)	14.02 (0.71)	12.79 (0.85)	2.26
R13255A	398.38 (1.84)	-390.07 (2.34)	11.22 (2.29)	13.41 (1.21)	2.51
R14026A	406.08 (0.99)	-400.66 (1.04)	15.43 (0.82)	14.00 (1.01)	2.86
R14051A	409.51 (1.14)	-403.62 (0.74)	15.73 (0.76)	14.00 (1.03)	2.93
R14086A	414.53 (1.75)	-405.14 (0.72)	14.86 (1.31)	13.59 (1.03)	3.02
R14116D	419.05 (0.90)	-407.15 (0.77)	14.10 (0.67)	12.84 (0.76)	3.10
R14164A	424.45 (1.72)	-415.11 (0.95)	13.44 (1.36)	13.63 (1.14)	3.22

[1]Observation code indicating R(YY)(DOY)
[2]Relative positions, origin of $\alpha_{\rm J2000}$ = 23h43m49s.4616, $\delta_{\rm J2000}$ = −15°17'04".202

to SiO maser theories (i.e. maser pumping mechanisms, properties and kinematic for masing gas conditions) in AGB stars.

Time variability of the fitted SiO maser sizes is shown in Figure 3.3. We can divide the variability into three patterns in our observations with respect to the stellar phase as same as the variability of overall SiO maser distribution in Chapter 3.1.1.

ϕ = 0.74 ∼ 1.44 Except for the first epoch of $\phi = 0.74$ (too poor fitting result with a large uncertainty), the size of the SiO maser rings varied differently in this phase. The $v = 1$ $J = 1 - 0$ SiO maser radii decreased, while the $v = 2$ $J = 1 - 0$ SiO maser radii increased from phase of 0.94 to 1.28. At the epoch of $\phi = 1.28$ (R12145C), both SiO maser radius were almost same, because those maser emissions located in the similar region. After then, the outer $v = 1$ $J = 1-0$ SiO maser radius started to increase, but the inner $v = 2$ $J = 1 - 0$ SiO maser radii decreased due to the split features, as described in previous Chapter 3.1.1. The overall size of the both SiO maser radii was slightly lager than that in the next two phases.

ϕ = 1.99 ∼ 2.51 During this phase, the radii of two transitions of the SiO masers showed a similar variation. The both SiO masers' radii showed a continuous decrease expect the last epoch of $\phi = 2.51$. In the last epoch, the SiO maser radii were poorly constrained because the maser emissions vanished at the stellar minimum. However, the inner $v = 2$ $J = 1 - 0$ SiO maser persevered in the last epoch of this phase, and seemed to expand in comparison to the previous epoch.

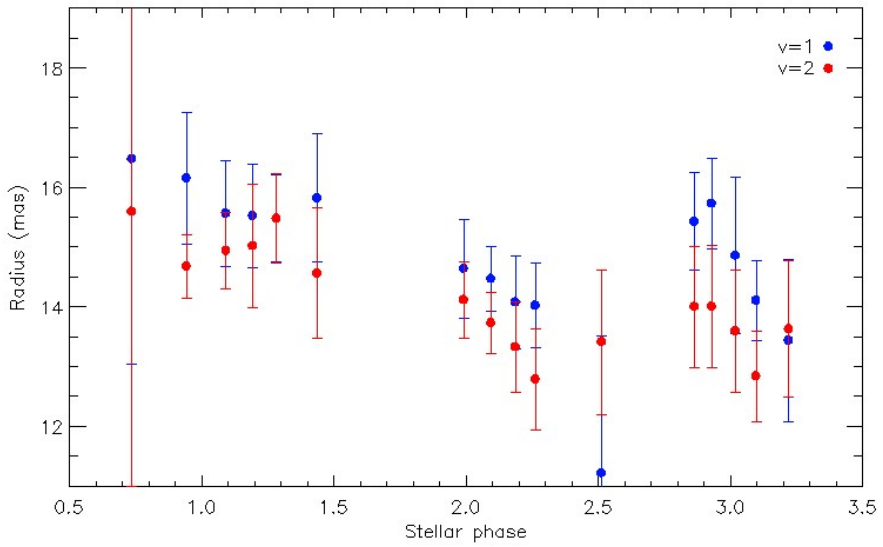

Figure 3.3: Time variations of the size of SiO maser region for R Aqr with respect to the stellar phase. Blue points are concentric radii for $v = 1$ $J = 1 - 0$ SiO masers, and red points are concentric radii for $v = 2$ $J = 1 - 0$ SiO masers.

Throughout this phase, the overall size of the both SiO maser radii was smaller than the other phases.

ϕ = 2.86 $\sim$ 3.22 During this phase, the elongated spike-like features made difficult to characterize the size of the maser region. Nevertheless, the SiO maser radii seemed to increase slightly toward the phase of $\phi = 2.93$, then started to decrease in both SiO maser transitions. At the last epoch of this phase ($\phi = 3.22$), the $v = 2$ $J = 1 - 0$ SiO maser radius showed the increment comparable to the size of the $v = 1$ $J = 1 - 0$ SiO maser radius within its uncertainty range. This behavior was similar to the previous cycle, and probably related to a propagation of a shock wave produced in the stellar atmosphere. Due to the spike-like features, overall size and motions of the both SiO masers were complex and dispersed in this phase.

The kinematic behavior of SiO maser region is believed to be attributed by a gravitational force and a propagation of shock waves produced by stellar pulsations. These effects can be detected in several SiO maser behaviors, such as an outflow and inflow (outward and inward motion), a split and ricocheted motion (Gonidakis et al. 2013). In our observations, we found the outflows and inflows from the variation of the SiO maser ring sizes. The inflows (inward motions) were detected in both SiO maser emissions across the whole cycles. However, the outflows (outward motions) were mostly detected in the $v = 2$ $J = 1 - 0$ SiO maser rings at different phases. Moreover, the split feature was also observed in the $v = 2$ $J = 1 - 0$ SiO maser emission at the first cycle. These motions of SiO masers provide significant implications for investigating properties and conditions of the stellar atmosphere around Mira variables.

3.2 Radial velocity of R Aqr

3.2.1 Previous radial velocity data of R Aqr

Recent radial velocity analysis for determining the orbital parameters of R Aqr was done by Gromadzki & Mikołajewska (2009). They reanalyzed and revised a variety of radial velocity data compiled by McIntosh & Rustan (2007) who collected the data from visual, near-IR and SiO maser observations. All of these spectral features are associated with the circumstellar envelope closed to the Mira variable in the R Aqr system. In addition, they reflect the motion of the Mira variable around the mass center of the system (Gromadzki & Mikołajewska 2009). In the present study, we adopted the radial velocity data from Gromadzki & Mikołajewska (2009) tabulated in Table 3.2 with several modifications as below:

1. Radial velocities of the visual wavelength data were restored to its original values.
2. Radial velocity data were averaged in 387 days corresponding to the stellar pulsation period of the Mira variable in R Aqr. The data, obtained at different wavelengths and stations, were averaged separately. The pulsation ephemeris was used from Gromadzki & Mikołajewska (2009), shown in Eq. 3.1.
3. Radial velocities from SiO masers were excluded between 1986 and 1988, 2001 and 2004.

For Mira variables, the radial velocities, measured by absorption lines in the blue-violet region of visual wavelengths, were necessary to be corrected for tracing true orbital motion. Typically, the correction value has been adopted between -5 and -10 km s^{-1} from the system velocity for R Aqr (Hinkle et al. 1984, 1989). Gromadzki & Mikołajewska (2009) adopted the correction value of -6 km s^{-1} (actual adopted value was -7.2 km s^{-1}). Moreover, Feast & Whitelock (2000), who investigate extensive radial velocities for oxygen-rich Mira variables, demonstrated that the radial velocity has a mean difference of -4.9 ± 0.6 km s^{-1} between SiO masers and visual wavelengths. To specify the correction value for visual radial velocities in R Aqr, we put those radial velocity data back and adopted its original(non-corrected) values. In addition, we set the correction value as a free parameter in the orbital parameter analysis in Chapter 3.3. The original values of the radial velocities in the visual wavelength is tabulated in Table A.4.1 of Appendix.

All radial velocities were averaged from observations at different wavelengths and stations in 387 days of the pulsation period of the Mira variable, separately. The different SiO maser transitions appear at the different region in the circumstellar envelope, and the velocity changes due to the orbital motion can be negligible in 387 days (Gromadzki & Mikołajewska 2009).

Radial velocities from SiO masers showed a peculiar variation from 1986 to 1988. During this period, Alcolea et al. (1999) reported the variation showing the velocity change up to 6 - 7 km s^{-1} with respect to the most stable velocity of -27.5 km s^{-1}. The variations accompanied the change in their spectral shapes (vanishing of mainly

strong peaks and appearing of new emission peaks at different velocities), not related to the pulsation phase.

Around the same period, VLA observations discovered a jet-like feature nearby the central system of R Aqr in NE direction (Kafatos et al. 1989). Multi-wavelength observations provided a negative spectral index indicating a nonthermal radiation for the jet-like feature produced by a synchrotron emission, which implies the early stage of jet mechanisms. Following MERLIN observations, this feature moved to NE direction further than before, and changed to a thermal radiation with increasing the radio flux by a factor of 2 (Dougherty et al. 1995). In addition, the UV continuum flux and emission line intensities also increased during this period by a factor of 2 - 3 (Meier & Kafatos 1995). Based on these results, Gromadzki & Mikołajewska (2009) suspected that the SiO maser emissions might be influenced by UV radiations due to increasing accretion activity around WD companion during the jet formation phase, and showed the peculiar variation in the radial velocity. This radial velocity variation was not related to the orbital motion. Therefore, we excluded the radial velocities from the SiO maser data between 1986 and 1988.

In this study, we also decided to exclude the radial velocities of SiO masers from 2001 to 2004. Chandra X-ray observations confirmed the morphological change in the central system of R Aqr suggesting a new jet formation in SW direction between 2001 and 2004 (Nichols et al. 2007). The new SW jet was also shown as a nonthermal radiation from contemporaneous multi-wavelength VLA observations, and the appearance of the new jet was probably synchrotron-powered jet with increasing accretion activity on the WD. Following the precedent speculation(presumption), the formation of new jet ejection might affect the shape of SiO maser spectra and cause the radial velocity variation which is not related to the orbital motion.

3.2.2 Radial velocities from Nobeyama & Mopra SiO maser observations

In order to trace a longer period of the radial velocity variation, supplementary radial velocity data were obtained from SiO maser observations of Nobeyama 45m telescope and Mopra 22m telescope.

The measurement of the radial velocities was used by the velocity centroid (V_C), which is the intensity-weighted first moment of the spectrum (McIntosh & Rustan 2007), given by

$$V_C = \frac{\sum_i v_{\mathrm{LSR},i} T_{a,i}}{\sum_i T_{a,i}} \tag{3.2}$$

where $v_{\mathrm{LSR},i}$ and $T_{a,i}$ are the local standard of rest velocity and the antenna temperatures (intensities) of each spectral channels, respectively. i is summed over the velocity interval along the emission, which is over the three times of r.m.s noise level. This method can derive the system velocity of the SiO maser region, simply and conveniently. The derived velocity can be regarded as a measurement of the average velocity of the masing gas. Moreover, the velocity centroid from SiO maser lines provides an

Table 3.2: Radial velocities of R Aqr from Gromadzki & Mikołajewska (2009)

JD	RV (km s^{-}1)	Spectral line	References
2422254.7	−14.40	Visual	(a)
2423039.0	−14.80	Visual	(a)
2429581.0	−23.50	Visual	(b)
2430336.0	−23.00	Visual	(b)
2432235.5	−21.60	Visual	(b)
2433019.3	−21.87	Visual	(b)
2441237.0	−14.50	Visual	(c)
2444509.0	−18.50	Visual	(d)
2444748.0	−23.00	Visual	(d)
2445862.0	−23.00	Visual	(d)
2442939.0	−22.00	Near-IR	(e)
2445535.0	−27.70	Near-IR	(e)
2445890.6	−28.00	Near-IR	(e)
2446378.5	−27.80	Near-IR	(e)
2447338.0	−28.90	Near-IR	(e)
2443371.0	−25.20	SiO (v=1, J=1−0)	(f)
2444078.0	−25.93	SiO (v=1, J=1−0)	(g), (h), (i)
2444356.0	−27.00	SiO (v=1, J=1−0)	(i)
2445574.5	−27.60	SiO (v=1, J=1−0)	(j), (k)
2447870.0	−27.10	SiO (v=1, J=1−0)	(l), (m)
2448283.0	−28.30	SiO (v=1, J=1−0)	(m)
2448696.0	−27.40	SiO (v=1, J=1−0)	(m)
2449435.0	−27.00	SiO (v=1, J=1−0)	(m)
2449804.0	−27.00	SiO (v=1, J=1−0)	(m)
2450068.8	−26.80	SiO (v=1, J=1−0)	(n)
2450407.0	−24.00	SiO (v=1, J=1−0)	(o)
2450948.0	−24.00	SiO (v=1, J=1−0)	(o)
2453784.3	−22.70	SiO (v=1, J=1−0)	(p)
2454112.0	−22.80	SiO (v=1, J=1−0)	(p)
2443684.5	−27.97	SiO (v=1, J=2−1)	(q)
2448240.0	−27.00	SiO (v=1, J=2−1)	(r)
2448998.4	−26.40	SiO (v=1, J=2−1)	(r)
2449439.0	−26.30	SiO (v=1, J=2−1)	(r)
2451390.4	−25.60	SiO (v=1, J=2−1)	(o), (s)
2451785.8	−23.20	SiO (v=1, J=2−1)	(s)

References : (a) Merrill (1935), (b) Merrill (1950), (c) Jacobsen & Wallerstein (1975), (d) Wallerstein (1986), (e) Hinkle et al. (1989), (f) Lepine et al. (1978), (g) Cohen & Ghigo (1980), (h) Spencer et al. (1981), (i) Lane (1982), (j) Cho et al. (1996), (k) Jewell et al. (1991), (l) Alcolea et al. (1999), (m) Pardo et al. (2004), (n) Boboltz et al. (1997), (o) Hollis et al. (2000), (p) McIntosh & Rustan (2007), (q) Zuckerman (1979), (r) Schwarz et al. (1995), (s) Kang et al. (2006)

accurate radial velocity and a good indicator of the system velocity for evolved stars (e.g. Jewell et al. 1991; Jiang et al. 1995; McIntosh 2006).

The radial velocity and associated uncertainty were determined by the bootstrap method. As similar as described in Chapter 3.1.2, we generated synthetic bootstrap samples from the original data set of the observed spectrum, independently. Then, the radial velocity was calculated for 10^4 different bootstrap samples. The mean and standard deviation were taken as a best value and uncertainty.

All radial velocities are assembled in Table A.5.1 and A.5.2 in Appendix. Applying modifications in the previous Chapter 3.2.1, we averaged the radial velocity data over 387 days corresponding to the stellar pulsation period. Data of different maser transitions and stations were treated separately. In Table 3.3, we present processed radial velocities for R Aqr from Nobeyama 45m telescope and Mopra 22m telescope.

In Figure 3.4, we plot all radial velocities of R Aqr along with previous data from

Table 3.3: Radial Velocities of R Aqr from Nobeyama & Mopra observations

Telescope	JD	RV (km s^{-1})[1]	Spectral lines	Note[2]
Nobeyama	2453482.0	−22.26 (0.48)	SiO (v=1 J=1−0)	
	2454101.1	−22.42 (0.21)	SiO (v=1 J=1−0)	
	2454513.7	−21.96 (0.18)	SiO (v=1 J=1−0)	
	2454941.7	−23.18 (0.19)	SiO (v=1 J=1−0)	N
	2455305.5	−22.70 (0.15)	SiO (v=1 J=1−0)	N
	2455662.0	−22.34 (0.23)	SiO (v=1 J=1−0)	N
	2456103.3	−21.54 (0.39)	SiO (v=1 J=1−0)	N
	2453482.0	−22.11 (0.50)	SiO (v=2 J=1−0)	
	2454101.1	−22.33 (0.25)	SiO (v=2 J=1−0)	
	2454513.7	−21.64 (0.19)	SiO (v=2 J=1−0)	
	2454941.7	−23.85 (0.18)	SiO (v=2 J=1−0)	N
	2455305.5	−23.65 (0.11)	SiO (v=2 J=1−0)	N
	2455665.0	−22.85 (0.20)	SiO (v=2 J=1−0)	N
	2456042.8	−21.51 (0.27)	SiO (v=2 J=1−0)	N
	2452379.4	−27.44 (0.23)	SiO (v=1 J=2−1)	N
	2455257.9	−21.76 (0.39)	SiO (v=1 J=2−1)	N
Mopra	2455025.7	−23.36 (0.67)	SiO (v=1 J=1−0)	N
	2455381.0	−23.10 (0.33)	SiO (v=1 J=1−0)	N
	2455807.6	−21.60 (0.55)	SiO (v=1 J=1−0)	N
	2456059.2	−22.09 (0.39)	SiO (v=1 J=1−0)	N
	2456508.9	−19.24 (0.39)	SiO (v=1 J=1−0)	
	2456763.5	−20.33 (0.73)	SiO (v=1 J=1−0)	
	2454548.6	−23.59 (0.35)	SiO (v=1 J=2−1)	N
	2454991.7	−23.16 (0.30)	SiO (v=1 J=2−1)	N
	2455373.5	−22.02 (0.32)	SiO (v=1 J=2−1)	N
	2455808.2	−22.17 (0.36)	SiO (v=1 J=2−1)	N
	2456081.7	−21.77 (0.44)	SiO (v=1 J=2−1)	N
	2456466.3	−19.13 (0.89)	SiO (v=1 J=2−1)	
	2456763.5	−19.83 (0.41)	SiO (v=1 J=2−1)	

[1] Uncertainties are $3 \times \sigma_{average}$

[2] Denoting "N" are not used for determining orbital parameters. See text in Chapter 3.2.2.

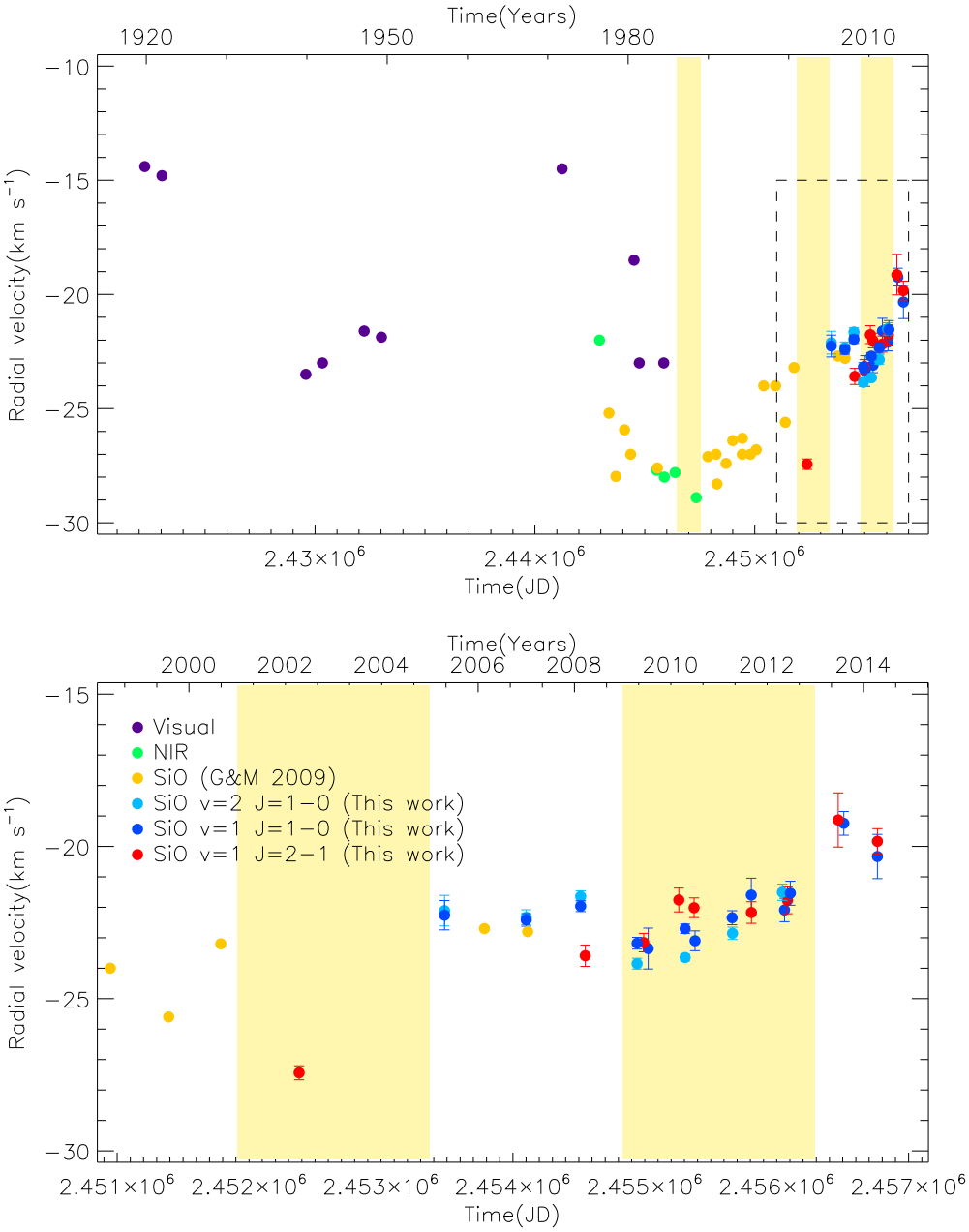

Figure 3.4: Radial velocities of R Aqr. Different colors represent different transitions of SiO masers and observations. The bottom figure is a close-up of Nobeyama and Mopra observations of dashed rectangular region in the upper figure. Three yellow regions are suspected to be affected by jet-ejecting events (see Text).

Gromadzki & Mikołajewska (2009). The period of the whole radial velocity data is from 1919 to 2014 covering ∼2 orbital cycles. Note that the radial velocities from visual data are not corrected in this figure, so they will shift a few km s^{-1} with respect to the other radial velocities. The range of the radial velocity variation is up to 10 km s^{-1} which mainly related with the orbital motion.

Three periods are marked by yellow in Figure 3.4. Two former periods are connected to the formations of jet-like feature reported by Katafos et al. (1989) and Nichols et al. (2007) between 1986 and 1988, 2001 and 2004. As described in the previous chapter, a radial velocity from Nobeyama observation of SiO $v = 1$ $J = 2 - 1$ (a red point at around 2003) came under these periods showing a large velocity difference of 4-5 km s^{-1} than previous and later observations. This difference was not caused by the orbital motion. Therefore, we excluded this data for determining orbital parameters because of mentioned modifications in the previous chapter.

For the third period (in the late of 2000s), we suspected another jet formation or change of accretion activity on the WD in R Aqr. From 1990 to 2014, radial velocities had gradually increased due to the orbital motion. However, we can see that radial velocities are significantly decreased about 2-3 km s^{-1}, that are not consistent with earlier measurements' trend, during the late of the 2000s. The variation is relatively small, but similar to the previous unusual radial velocity behaviors in the late 1980s reported by Alcolea et al. (1999) and early 2000s. In the SiO maser spectra, we also see the changes as shown in Figure 3.5. The main peak of spectra became weak, and the range of emissions was shifted toward redder wavelength, clearly confirmed in $v = 2$ $J = 1 - 0$ SiO maser spectra.

In the late of 2000s, there was no report of a new jet-ejection or change of accretion activity. Although the sudden spectra and radial velocity change might be caused by the internal(intrinsic) maser properties localized in the Mira variable, we could not rule out the possibility of a connection between the SiO maser change and new jet-ejection (and/or increasing accretion activity). Whatever the reason, this unusual variation is not related to the orbital motion. Hence, we also excluded the radial velocity data from 2008 to 2012 for determining the orbital parameters. The excluded radial velocity data are denoted in Table 3.3 as well.

3.3 Determination of orbital parameters for R Aqr

Combining astrometry data (Chapter 3.1) and radial velocity data (Chapter 3.2), we attempt to determine orbital parameters from three-dimensional motions toward R Aqr in this chapter.

For astrometry data, we complemented the positions of the Mira variable derived by Kamohara et al. (2010), who performed VERA observations of SiO masers toward R Aqr. They applied the circular fitting to the distribution of SiO masers, and obtained the eight positions of the Mira variable from 2004 to 2006. For the last two epochs of August and October 2006, the fittings were poor because of a small number of the SiO maser components and far from circular distribution. In addition, estimated positions of those epochs were not consistent with VLBA observations by Ragland et al. (2008)

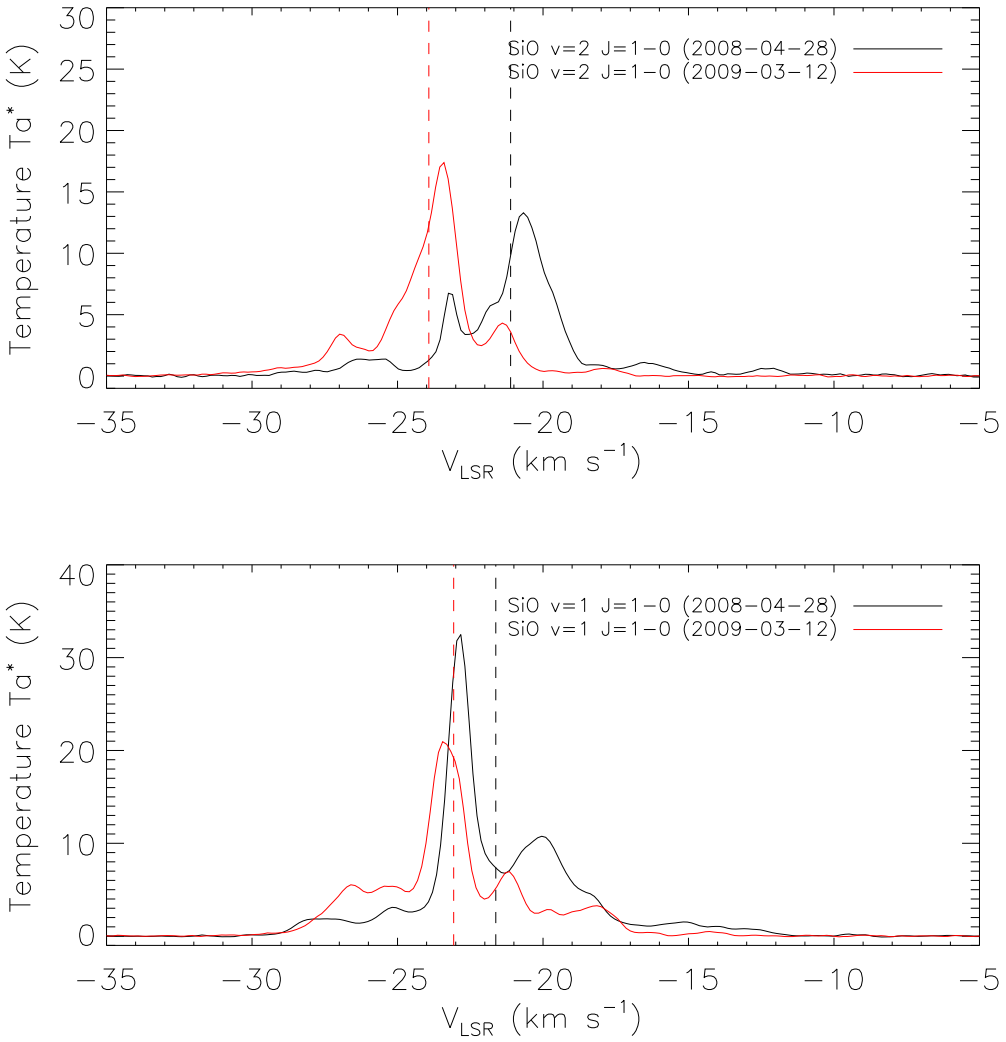

Figure 3.5: Comparison of SiO masers spectra by Nobeyama telescope between 2008 and 2009. Upper figure is the spectra of $v = 2$ $J = 1 - 0$ SiO maser, and bottom is the $v = 1$ $J = 1 - 0$ SiO maser emissions. Black lines are spectra obtained in 2008, and red lines are in 2009. Black and red dashed line are the derived(corresponding) velocity centroids.

who conducted SiO maser observations in September 2006. Therefore, we included only the six epochs for determining the orbital parameters presenting in Table 3.4 with $3\times\sigma$ uncertainties. The time gap between Kamohara et al. (2010) and the present study is about 6 years. Therefore, we can detect the proper motion changes due to the orbital motion.

Table 3.4: Positions of the Mira variable from previous VERA observations

Date	ΔRA[1] (mas)	ΔDec[1] (mas)	Reference
2004-12-23	135.30 (6.30)	−133.10 (2.10)	Kamohara et al. (2010)
2005-09-27	161.40 (0.75)	−154.90 (1.20)	Kamohara et al. (2010)
2005-11-23	164.50 (0.45)	−160.70 (0.75)	Kamohara et al. (2010)
2005-12-24	166.40 (0.45)	−162.40 (0.90)	Kamohara et al. (2010)
2006-02-14	172.70 (0.45)	−165.20 (0.75)	Kamohara et al. (2010)
2006-03-04	175.10 (0.45)	−165.70 (0.75)	Kamohara et al. (2010)

[1]Relative positions, origin of $\alpha_{\rm J2000}$ = 23h43m49s.4616, $\delta_{\rm J2000}$ = −15°17'04".202

Taking into account all assembled data, the astrometric data only covered about 10 yrs, which is much shorter than the radial velocity of ∼100 yrs. Even though a short period of astrometry are observed, the full orbital parameters can be revealed when radial velocity measurements cover a long time span over the orbital period of a system (Tuomi et al. 2009).

We derive the orbital parameters based on a Keplerian binary model, detail described in Appendix A.1, especially by equations A.1.15 and A.1.20. The model consists of total 13 parameters, seven of them describes binary motion (orbital period, eccentricity, longitude of periastron, semi-major axis, inclination, and longitude of ascending node), four are of secular motion (nominal positions, proper motions in RA and Dec direction), one is of the parallax, and one is of systemic velocity with an orbital variation. In addition, we also introduce 11 nuisance parameters in order to obtain the more reliable result. More details are described in Appendix.

A Bayesian framework using a Markov Chain Monte Carlo (MCMC) method was employed for quantifying the best-fit model parameters and their uncertainties. The MCMC method and their setting are described in Appendix A.2. In this study, we adopted an acceptance rate of 25%, which is recommended value for a multi-dimensional model (Gregory 2005b). In order to provide sufficiently dense samples of the posterior distributions, 3×10^7 MCMC chains were generated from the MCMC process. The first of 20% of samples were removed as a burn-in portion. We repeated the process several times and compared the resulting distributions to be sure that the chains are properly converged with good agreement in all the sequences.

The best-fit model parameter was measured by a maximum likelihood value, and the uncertainty of each parameter was determined by 68.26% of the Bayesian confidence interval, that contains the MCMC samples between the 15.87th and 84.14th percentile, from the posterior distributions. The posterior probability distributions of the model

parameters of the best-fit values and their uncertainties are shown in Figure 3.6, and we summarize the result in Table 3.5.

As a result, we provide the potential parameters of binary orbit toward the R Aqr system for the first time. All the orbital parameters, especially related to the radial velocity model, are well confined to short ranges of parameter spaces. Several parameters, related to the astrometry model, show wide ranges of confidence interval with asymmetric posterior probability distributions.

For the orbital parameters related to the radial velocity model, we obtain significantly different values from the recent radial velocity result by Gromadzki & Mikołajewska (2009). Especially, our analysis yields the longest orbital period of 46.2 yrs toward R Aqr, so far. The orbital period is constrained by the radial velocity variation, which is affected by complementary radial velocity data from Nobeyama and Mopra observation and the correction value for visual radial velocities, $RV_{vis.off}$.

The complementary radial velocities were plotted on the range between -22 and -19 km s^{-1} from 2011 to 2014. Along with those radial velocities, our analysis yields the correction value of $RV_{vis.off} = -5.29^{+0.65}_{-0.52}$ km s^{-1} for the visual radial velocity data. This value is consistent with the statistical result by Feast & Whitelock (2000), and smaller than adopted value by Gromadzki & Mikołajewska (2009). Both of the complementary radial velocity data and the correction value make a difference from the previous results in the parameters from the radial velocity model. Fig 3.9 shows the radial velocity variation with the best-fit orbital model. We can see that the radial motion follows the best-fit orbital model, and the residual of the radial velocity is less than 1 km s^{-1} even in the visual data.

From the astrometry model, we can extract the orbital inclination without any ambiguity. The orbital inclination, one of our interest orbital parameters, is estimated to be 68.6 degrees as the best-fit value. However, the reliable parameter range is still wide between 53 and 115 degrees with double peak structure in the posterior distribution. However, we can verify that R Aqr has the high inclination angle close to the edge-on orbit.

One of the newly constrained parameters is Longitude of ascending node, Ω, of $223.7^{+22.8}_{-38.1}$ degree. This parameter directly provides the orientation of the orbital axis on the plane of the sky. Our analysis results in a wide range in the parameter space, but indicates that the position angle of orbital axis is from 95 to 156 degree. Figure 3.8 shows the best-fit orbital motion with the position of the Mira variable subtracting the linear proper motion and parallax motion from the best-fit values listed in Table 3.5. The arrow indicates the orbital angular momentum vector corresponding to the orbital axis projected on the sky plane. The orbital plane is located in NE to SW direction perpendicular to the orbital axis. In the best-fit model, the Mira variable moves counter-clockwise and far away from the observer. The companion can be expected to locate at the directly opposite position with respect to the Mira variable along the center of mass.

The other astrometric parameters of nominal positions and proper motions in RA and Dec direction(coordinates) show significant asymmetries and wide ranges in the posterior probability distributions. Although the parallax is relatively well estimated

Table 3.5: The MCMC result of the model parameters

Parameters	Symbol	Best value	Median	68% C.I.
Periastron passage (yr)	T_0	1975.6	1976.3	$[1974.8, 1978.0]$
Orbital period (yr)	P	46.2	46.9	$[45.1, 49.2]$
Systemic velocity (km s^{-1})	V_0	-24.2	-24.1	$[-24.4, -23.8]$
Eccentricity	e	0.245	0.252	$[0.194, 0.315]$
Longitude of periastron (deg.)	ω	70.6	78.2	$[66.9, 91.8]$
Semi-major axis for Mira (AU)	a_{Mira}	6.94	7.29	$[6.42, 8.98]$
Inclination (deg.)	i	68.6	77.2	$[53.1, 115.6]$
Longitude of ascending node (deg.)	Ω	223.7	220.7	$[185.6, 246.5]$
Initial position in RA (mas)	α_0	137.1	143.6	$[135.1, 155.5]$
Initial position in Dec (mas)	δ_0	-117.0	-118.8	$[-126.7, -106.9]$
Proper motion in RA (mas yr^{-1})	μ^*_α	31.6	31.1	$[28.7, 32.3]$
Proper motion in Dec (mas yr^{-1})	μ_δ	-29.2	-28.9	$[-30.4, -27.8]$
Parallax (mas)	π	3.97	3.88	$[3.41, 4.33]$
Extra noise for Astrometry in RA (mas)	s_{RA}	0.053	0.458	[0.168, 0.774]
Extra noise for Astrometry in Dec (mas)	s_{Dec}	0.978	1.280	[0.957, 1.661]
RV offset for RV in visual (km s^{-1})	$RV_{vis.off}$	-5.29	-5.23	[-5.82, -4.64]
Extra noise for RV in visual (km s^{-1})	s_{vis}	1.03	1.37	$[1.06, 1.85]$
Extra noise for RV in NIR (km s^{-1})	s_{NIR}	0.46	0.84	$[0.54, 1.38]$
Extra noise for RV in SiO (v=1 J=1-0)[1] (km s^{-1})	s_{SiO43}	0.85	0.90	$[0.73, 1.14]$
Extra noise for RV in SiO (v=1 J=2-1)[1] (km s^{-1})	s_{SiO86}	1.42	1.53	$[1.10, 2.24]$
Extra noise for RV in SiO (v=2 J=1-0)[2] (km s^{-1})	$s_{N.SiO42}$	0.02	0.25	$[0.07, 0.66]$
Extra noise for RV in SiO (v=1 J=1-0)[2] (km s^{-1})	$s_{N.SiO43}$	0.05	0.28	$[0.08, 0.70]$
Extra noise for RV in SiO (v=1 J=1-0)[3] (km s^{-1})	$s_{M.SiO43}$	0.04	0.78	$[0.25, 1.98]$
Extra noise for RV in SiO (v=1 J=2-1)[3] (km s^{-1})	$s_{M.SiO86}$	0.10	0.54	$[0.13, 1.64]$

[1]SiO maser data for Gromadzki & Mikołajewska (2009)
[2]SiO maser data for Nobeyama observations
[3]SiO maser data for Mopra observations

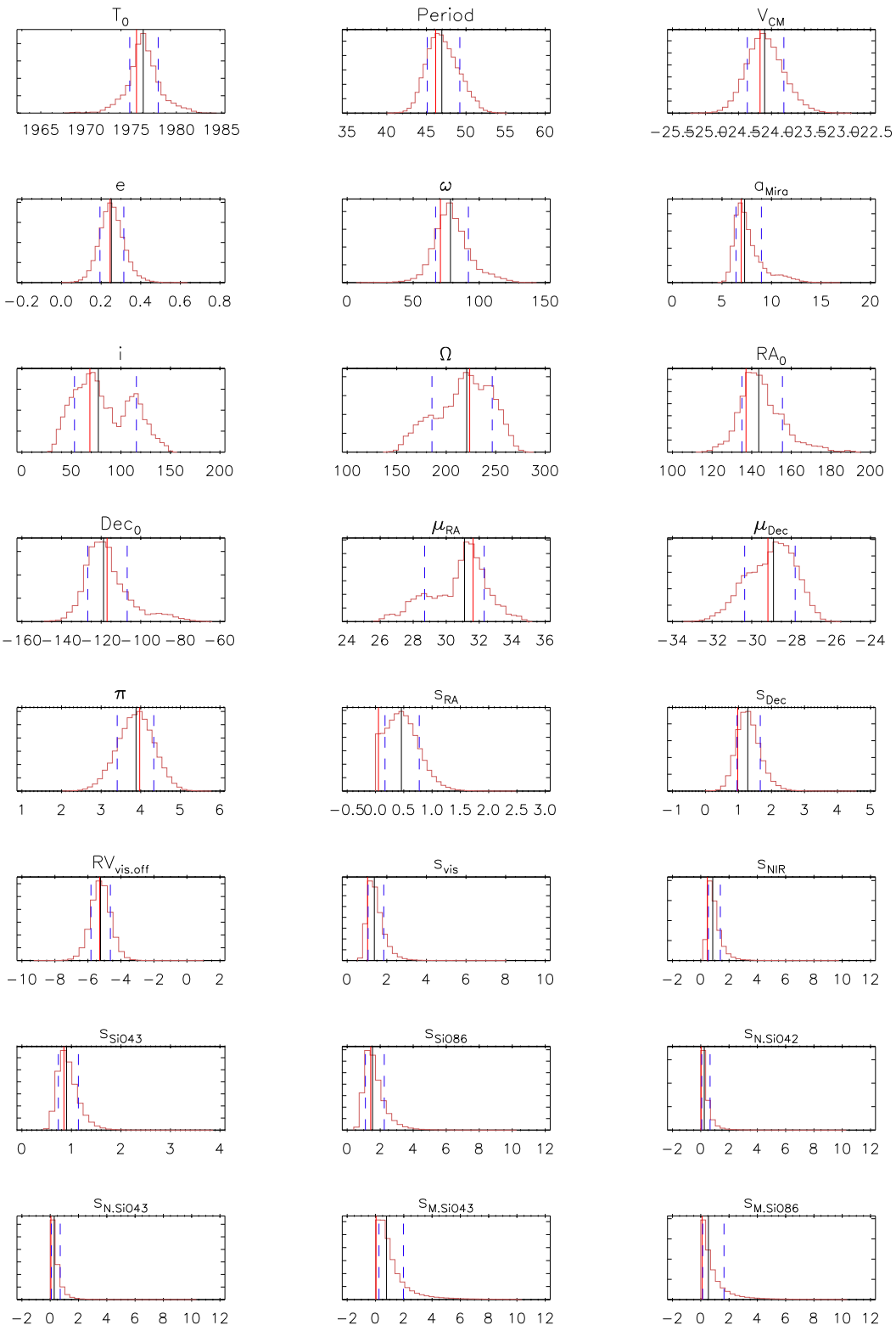

Figure 3.6: The posterior probability distributions of the MCMC analysis. In each panel, the red solid lines indicate the best-fit values, and the dashed lines indicate the range of 68% of confidence intervals.

to the posterior distribution as $3.97^{+0.36}_{-0.57}$ mas, that is a relatively small effect related to the binary model.

Figure 3.7 shows the astrometric positions of the Mira variable on the sky plane from 2004 to 2014 from the best-fit astrometry model. The undulating motion of the trajectory results from the parallactic movement caused by Earth-Sun motion and the reflected motion of the binary system.

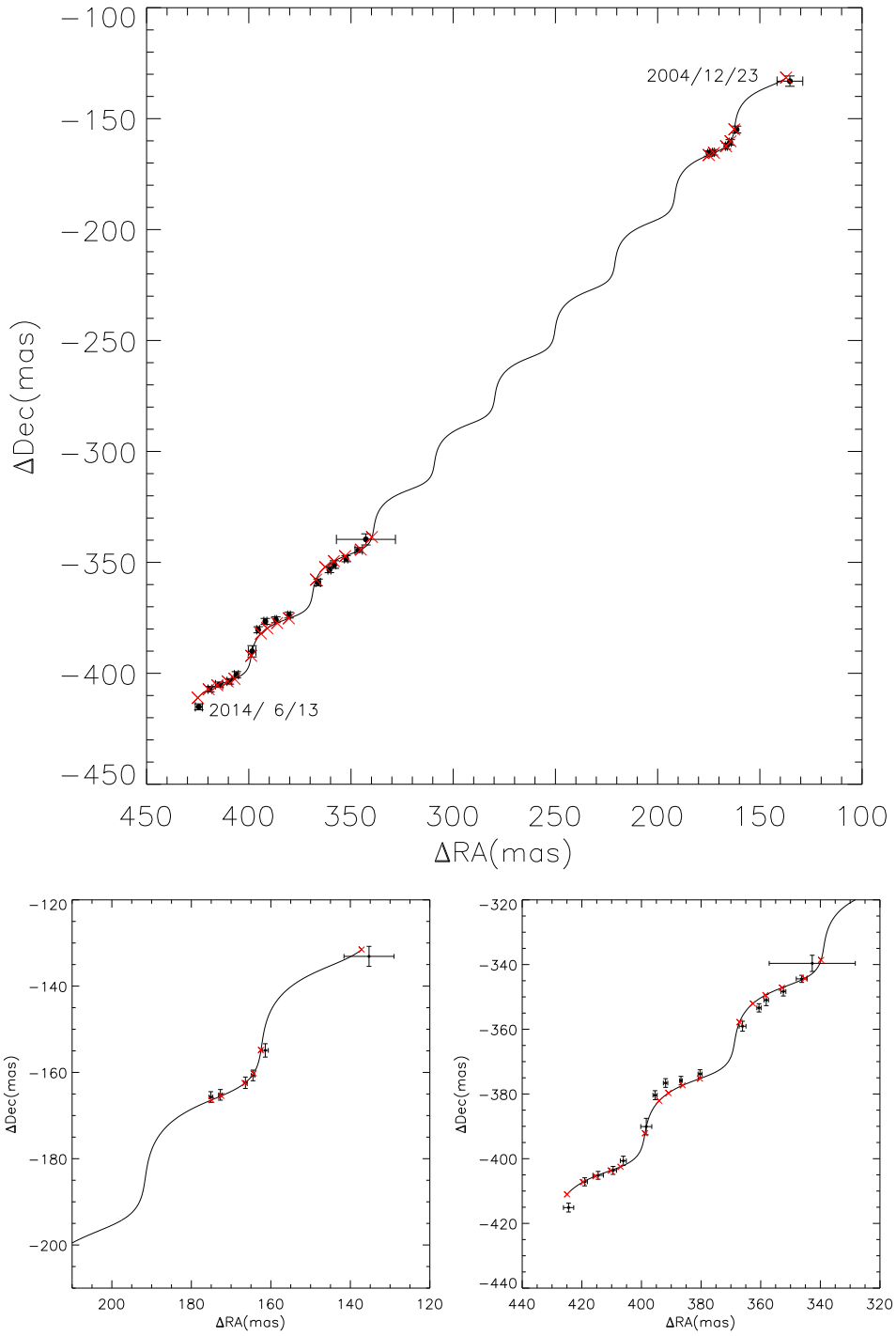

Figure 3.7: The astrometric motion for R Aqr in the sky plane with best-fit model. Upper figure is all range of astrometric points. Bottom left figure is the positions by Kamohara et al. (2010). Bottom right figure is the positions obtained in this study. Red crosses indicate the expected positions from the best-fit model

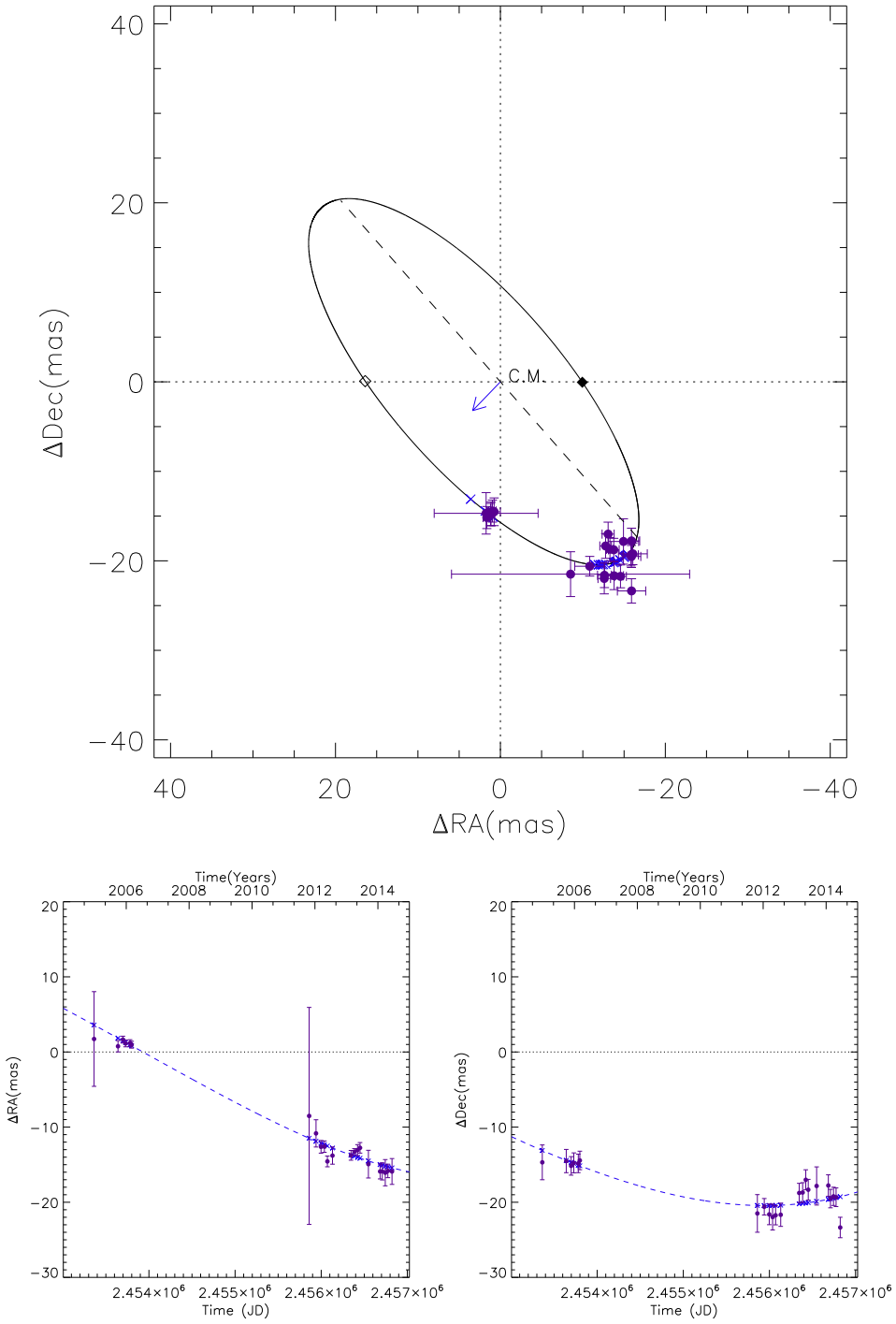

Figure 3.8: Upper figure presents the orbital motion with respect to the center of mass origin. The best-fit orbital motion (subtracting the parallax and linear proper motion) is presented by the solid line. The positions of the observed and expected Mira variable are also plotted by dots (with error bars) and blue crosses. The arrow indicates the orbital axis corresponding to the orbital angular momentum vector in the sky plane. The dashed line indicates the line of node. The diamonds are the periastron (filled diamond) and the apastron (open diamond) passages, respectively. Bottom figures are the orbital motion in RA direction (left) and Dec direction (right) with respect to the time.

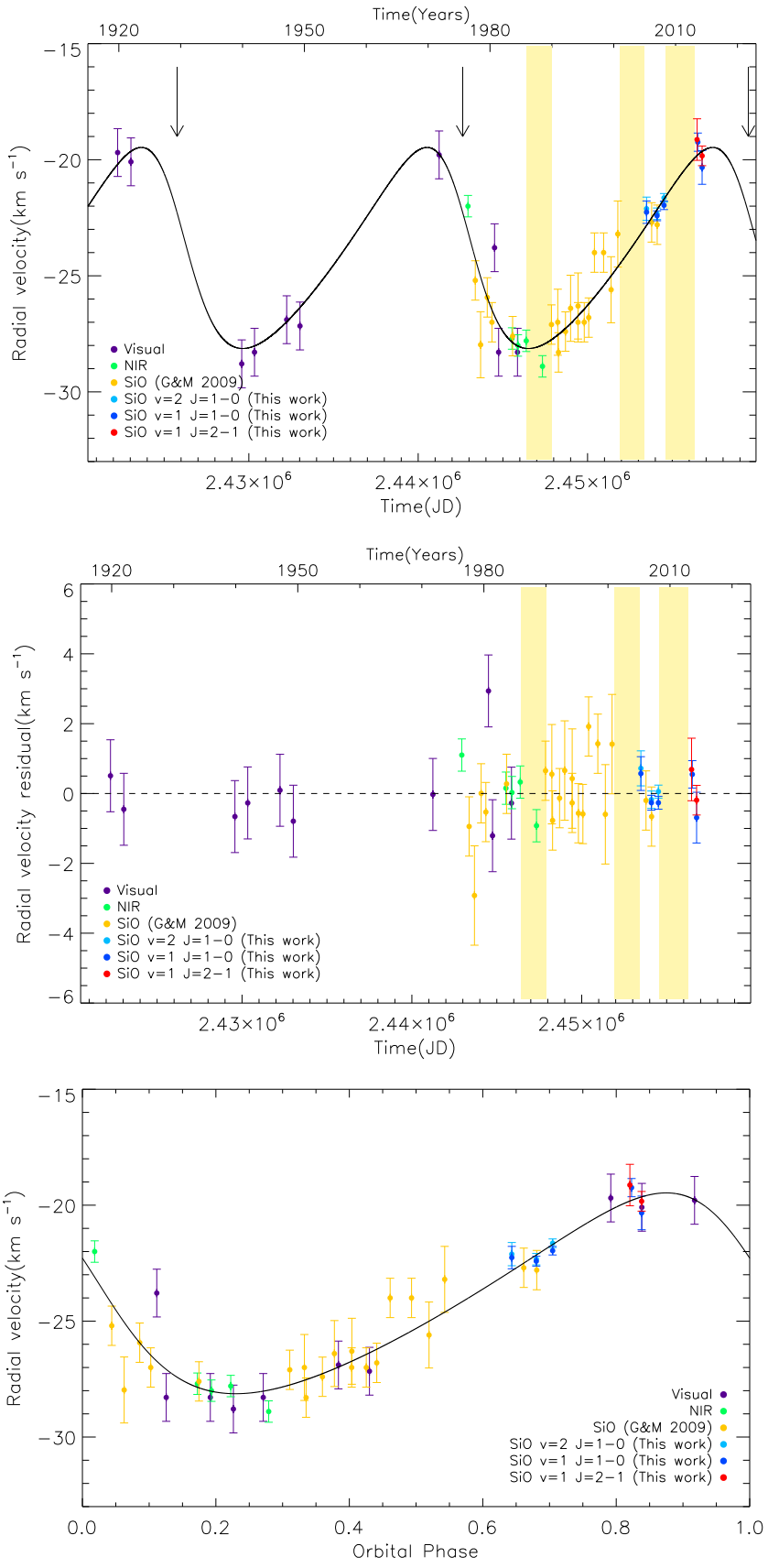

Figure 3.9: The radial velocity variation with the best-fit model. The different colors and the yellow regions are same as those in Figure 3.4. The arrows indicate the periastron passages.

Chapter 4

Discussions

We presented the global parameter estimation for R Aqr based on VLBI astrometry observations of SiO masers, and measured the full orbital parameters for the first time. In this chapter, we discuss the relation between the orbital motion and the phenomena in R Aqr.

4.1 SiO maser distributions in R Aqr

A ring-like distribution (circular structure) of the SiO masers is generally observed around AGB stars' atmosphere. The distribution is thought to arise from a spherical shell between a stellar photosphere and dust formation region. However, single and isolated AGB stars sometimes present a partial ring structure of SiO masers, not occupy a full circular region. The partial ring structure is caused by local phenomena, such as an anomalous density and velocity distribution due to a bulk rotating shell, localized(inhomogeneous) mass ejection, stellar activities, such as Hα flares (Rudnitskij 2008) or other peculiar properties, in the atmosphere.

The SiO masers around the Mira variable in R Aqr showed a partial ring-like (or arc-like) structure with predominant features during our VERA observations. In addition, we found that the SiO maser distributions show different characteristics at the same stellar phases. An inspection of the stellar phases of 1.09, 2.10 and 3.10 (those are the nearly same stellar phase), the distributions were significantly different as shown in Figure 3.2. This difference indicates that masing conditions vary greatly at every stellar phase, and the change of that conditions is caused by local phenomena in the stellar atmosphere. Every stellar phase, the condition for maintaining the maser emitting properties changes due to the local phenomena, and this is of particular importance for discussing the SiO maser emitting properties at each phase.

Nevertheless, we also found a global tendency of the SiO maser emissions in R Aqr. Figure 4.1 shows the distribution of the SiO masers components. Throughout our VERA observations, we can see that most of SiO maser components are detected in eastern hemispheres rather than western hemispheres.

If conditions on one side of the stellar atmosphere are more favorable for the maser emissions during several stellar phases, we can presume that the stronger side of the

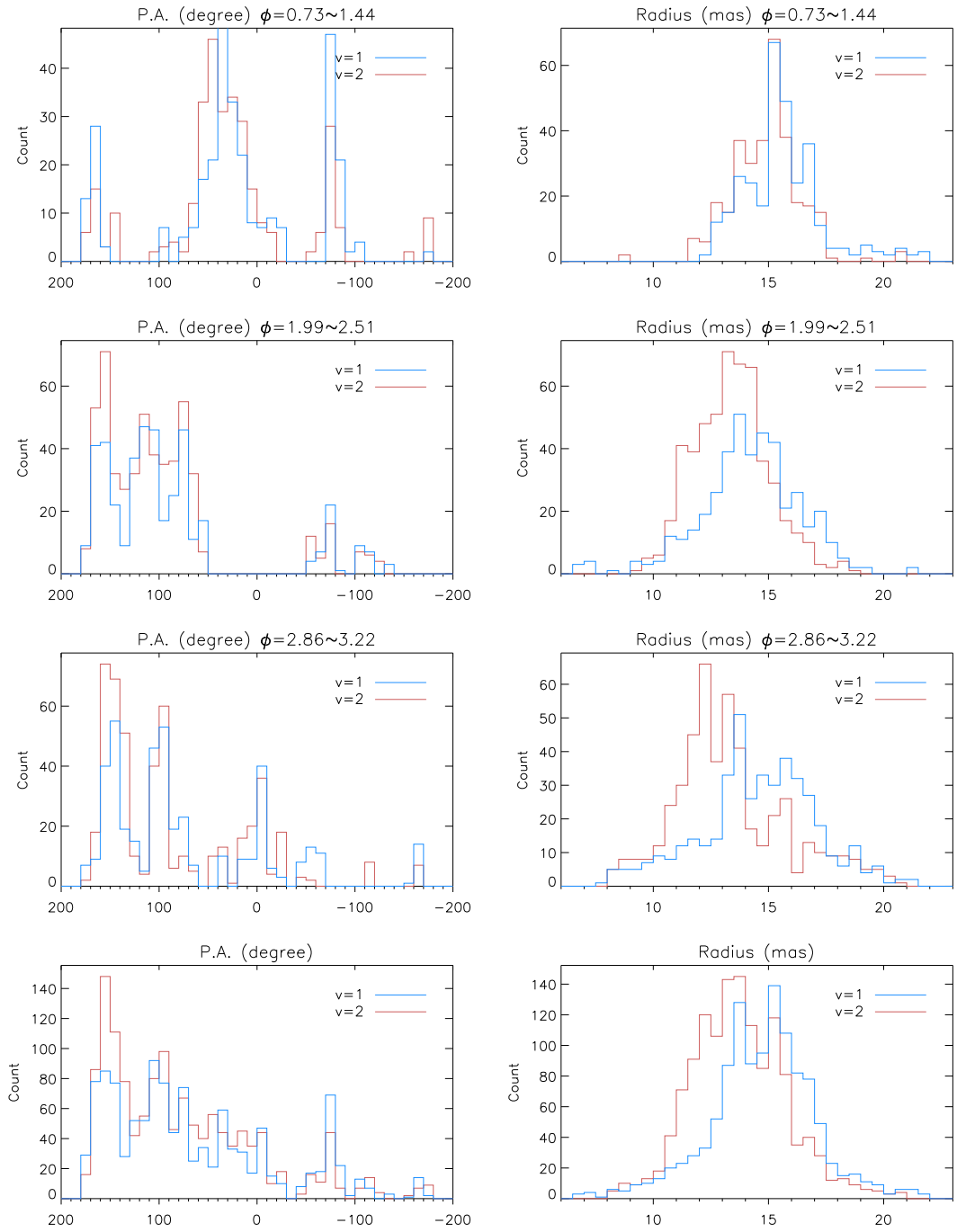

Figure 4.1: Histograms of the SiO maser distribution. Left is the distribution along the P.A., and right is the distribution along the radial direction. The blue indicate the $v = 1$ $J = 1 - 0$ SiO masers, and the red indicate the $v = 2$ $J = 1 - 0$ SiO masers.

SiO maser region is related to global phenomena rather than local phenomena. For R Aqr, one of the reasonable global phenomena is caused by the binary relevant to the orbital motion and the mass-transfer through the positional relationship between the components.

The maser emission is preferentially observed in directions along the line of sight, where the masing material density and velocity coherence are higher. In interacting binary systems, the high density of material properly concentrated along the line connected to the components, i.e. the line to the Lagrangian points of L_1, L_2 and L_3 where the mass-flow and mass-transfer took place. Therefore, the strong maser emission is expected in connection with the position of the companion.

Adopting our best-fit orbital model, the companion is thought to be located in NE direction with respect to the Mira variable in R Aqr during our observations. If the masing material density is enhanced by the location of the component, the observed tendency of maser distribution is favorable for our explanation.

Previous VLBI observations also showed that the SiO maser distribution tends to present an axially symmetric, partial ring- or arc-like SiO maser distributions dominated by the global structure in R Aqr. This tendency did not show the same pattern but had remained stable during more than 10 years.

Hollis et al. (2000,2001) suggested a rotating SiO maser shell with the symmetry axis oriented at a position angle of $-30/150$ degree using high-resolution VLBA observation in December 2000. From their observation, the dominant SiO maser lay in the west region of the shell. According to our orbital motion, the companion was located on the west with respect to the Mira variable at their observation epoch.

Cotton et al. (2004, 2006) also suggested the rotation of the SiO maser shell with the symmetry axis oriented at a position angle of $-10/170$ degree at two epochs in 2001, and 0/180 degree (150-180 degree) at one epoch in 2004. The VLBA observations detected several maser features, but the sector summed flux density indicated that the strongest features were located in western portions of the circular shell. According to our orbital motion, the companion was located on the northwest with respect to the Mira variable at their observation epochs.

The VERA observations by Kamohara et al. (2010) from 2004 to 2006 showed the partial ring-like structure of SiO maser distribution. Their distribution was mainly occupied in the northern part of the shell during their observations. According to our orbital motion, the companion was located in the north with respect to the Mira variable in their observation epoch of 2006.

On the other hands, Boboltz et al. (1997) observed the SiO maser around the Mira variable in R Aqr from 1995 to 1996 at four epochs. They detected a strong time-variability of the maser emission, and the dominant emission of the first epoch was located on the western side of the circular distribution. After six months later observation, the eastern side of maser emission appeared. According to our orbital motion, the companion was located on the southwest with respect to the Mira variable at their observation epochs. During their observation epochs, the binary orbit was nearly an apastron passage (predicted apastron passage is September 1998) where the distance between the Mira variable and the companion was the longest separation.

Therefore, the effect of the companion was relatively weaker than other observations, so that the SiO maser emission could also appear on the opposite side of the dominant hemisphere.

The characteristics of the SiO maser distributions is highly unpredictable along the stellar phase to phase, and within a phase. Our VERA observations found that the SiO maser distribution varies every stellar phase. This local variation of the spatial SiO maser emissions is responsible for the stellar properties. Moreover, R Aqr is a binary system with strong interaction between the components, so that the global tendency of the SiO maser distribution was found in our VERA observations. This global predominant masing tendency is surely related to the binarity which interacts the Mira variable with the component via the mass-transfer and/or mass-outflow process enhancing the masing material along the companion's direction.

4.2 Distance toward R Aqr

Previous distance measurements toward R Aqr have been mostly derived by three methods: (1) the nebula kinematics, (2) the Period-Luminosity relationship and (3) the parallax measurement through high precision astrometry. In Table 4.1, we summarize the historical distance measurements including the result of the present study.

Table 4.1: Historical distance measurements toward R Aqr

	Distance	Mehtods
Baade (1943)	260 pc	nebula kinematics
Solf & Ulrich (1985)	180, 185 pc	nebula kinematics
Yang et al. (2005)	273 pc	nebula kinematics
Whitelock et al. (2008)	250 pc	Period-Luminosity relation
ESA (1997)	197^{+323}_{-75} pc	Hipparcos parallax
Kamohara et al. (2010)	214^{+45}_{-32} pc	VERA parallax
Min et al. (2014)	218^{+12}_{-11} pc	VERA parallax
This study	252^{+42}_{-21} pc	VERA parallax

The kinematic distance measurements were deduced from expansion velocities and expansion ages of the inner and outer nebulae around R Aqr. Early efforts had estimated the kinematic distance with a large uncertainty due to a wide range of difference between the measured expansion velocities and the ambiguity of the expansion ages. Through recent discoveries of outburst records provided the accurate expansion age of the outer nebula (Yang et al. 2005; Tanabe & Motizuki 2012), the kinematic distance has a low accuracy as long as the formation and expansion model of the nebula is not well known.

Whitelock et al. (2008) established the Period-Luminosity relation using reanalyzed and revised Hipparcos parallaxes and VLBI parallax measurements with K-band magnitudes. By using their relation (in the case of the Oxygen-rich Mira variables), they derived the distance of 250 pc for R Aqr. However, the samples deriving the relation

is small, and it is necessary to obtain more accurate distance samples to confirm the relation.

Among the method, the parallax is the most accurate and direct method to obtain the distance without any models and assumptions. The first astrometric observation for the parallax measurement was introduced by Hipparcos satellite (ESA 1997) presenting the parallax of 5.07 ± 3.15 mas, which corresponds to the distance of 197^{+323}_{-75} pc. More precise parallax measurements were achieved by Kamohara et al. (2010) and Min et al. (2014) who used VERA astrometry observations of SiO masers around the Mira variable in R Aqr. Kamohara et al. (2010) regarded the stellar positions as the center of circular fitting of the SiO maser distributions, and estimated the annual parallax of $\pi = 4.7 \pm 0.8$ mas, corresponding to the distance of 214^{+45}_{-32} pc. Min et al. (2014) used the same data with Kamohara et al. (2010), but yielded the more precise parallax of $\pi = 4.59 \pm 0.24$ mas, corresponding to the distance of 218^{+12}_{-11} pc following one of SiO maser spots persistently found during the observations.

In this study, we estimated the parallax for R Aqr of $\pi = 3.97^{+0.36}_{-0.57}$ mas, corresponding to the distance of 252^{+42}_{-21} pc. Our result is slightly further and lower precision, but more reliable and reasonable than the previous VERA parallax measurements.

Firstly, we estimate the distance from the observation data of longer period than the previous measurements. Kamohara et al. (2010) and Min et al. (2014) covered the period of one or two years of astrometry data. However, we complemented three more years and covered about 10 yrs of astrometry than previous measurements.

Secondly, we take account of more reliable motion for deriving the distance. In previous studies, the motion of the maser source was assumed to be a combination of a linear proper motion and parallax motion. When we applied the same motion of Kamohara et al. (2010) and Min et al. (2014) to our observations, the parallax would yield $\pi = 3.46 \pm 0.48$, corresponding to the distance of 289^{+47}_{-35} pc, which is further than the previous results and this study.

On the other hand, we included a non-linear orbital motion, that makes somewhat difference in the parallax analysis. Adopting our orbital motion, a mean acceleration due to the orbital motion is 0.30 mas yr^{-2} ($a^*_\alpha = -0.25$ mas yr^{-2} and $a_\delta = 0.18$ mas yr^{-2}), and an additional linear motion is 2.80 mas yr^{-1} ($\mu^*_\alpha = -2.32$ mas yr^{-1} and $\mu_\delta = -1.58$ mas yr^{-1}) during the observational period of Kamohara et al. (2010) and Min et al. (2014). This non-linear orbital motion can not be negligible and influence even within one-year analysis for distance measurement toward R Aqr.

Finally, we derive the distance from a method of tracing stellar position instead of maser component. The method of tracing maser component is generally used for yielding a precise parallax measurement with a high spatial resolution of VLBI astrometry. However, this method is possible to yield faulty parallax measurement for SiO masers in R Aqr as well as AGB stars. When we follow a maser component to measure a parallax, the tracing maser component has to be unblended (simple structure) and consistently observed in the same position of the masing region. In other words, the tracing maser component is necessary to have a precondition of a maser persistence with both spatial and velocity coherence.

Through our observations, we have shown that the SiO maser distribution sig-

nificantly varies along the stellar phases because of local phenomena in the stellar atmosphere of Mira variable. Especially, the SiO maser components were forming and disappearing near the fiducial stellar phase of $\phi = 0.5$ (starts to form at >0.5 and disappears by approaching to <0.5). In addition, a typical lifetime of SiO maser components is a few month (around 200 days) in average (Gonidakis et al. 2010; McIntosh & Patriat 2010). Moreover, several SiO maser components are usually detected in one of velocity channels. Therefore, if we follow a different maser component, that is emitted in the different masing region, at a certain epoch, the derived parallax is surely different from the true parallax value. These indicate that the method of tracing SiO maser component is hard to apply to the distance measurement toward AGB stars for long term observations. To avoid the problem, several maser components should be traced to derive the parallax.

The observations of Min et al. (2014) was made within the stellar phase between ϕ =0.01 and 0.88. The spatial propensity of the SiO maser around the Mira variable in R Aqr probably changed around $\phi = 0.5$. They showed the velocity consistency throughout the observations, but weak spatial consistency among the traced maser components. That is, the tracing maser components are possibly emitted in different maser region. In addition, they traced only a one maser component, that persistently was observed, to estimate the parallax. For confident distance measurement, a number of components are necessary to derive the parallax measurement.

On the other hand, the method of tracing stellar positions, that is used in the present study, is no need to confirm the spatial and velocity coherence, and can trace longer period without the consideration of SiO maser's lifetime. There is an only disadvantage of the low positional precision for the tracing stellar position, that leads a lower precision of the distance measurement. Nonetheless, the method of tracing stellar position have a more reliability and provide a more reasonable result than that of tracing maser component for the SiO masers in AGB stars.

Other distance measurement method can be possible to apply to our observations. One possible method is a statistic method using proper motions of maser components. If spatial motions of maser components are isotropically random, the dispersion of the proper motion in the sky plane can be compared with the dispersion of the radial motion. Therefore, the distance can be estimated according to the below formula (Trumpler & Weaver 1953):

$$D = \sigma_\mu / \sigma_v \tag{4.1}$$

where σ_μ is the dispersion of the proper motion in the sky plane, and σ_v is the dispersion of the radial motion. Our VERA observations detected a number of SiO maser components as much as we can estimate the distance with the statistic method. We can expect to compare the distance between the statistic method and parallax measurement in the future study.

4.2.1 Stellar properties

Adopting our parallax measurement, we can derive several stellar properties of R Aqr. For the Mira variable, we calculated the absolute K-band magnitude of $M_{\rm K}$ =

$-8.02^{+0.19}_{-0.33}$ mag applying the apparent K-band magnitude of $m_{\rm K} = -1.02$ mag, obtained from SAAO (South African Astronomical Observatory) by Whitelock et al. (2000). Applying the pulsation period of 387.3 days, the absolute K-band magnitude is consistent with the most recent Period-Luminosity relation of $M_{\rm K} = -3.52 \log P + (1.09 \pm 0.14)$ by Nakagawa et al. (2016).

From the K-band magnitude, the luminosity and effective temperature can be derived based on following equations as function of color differences of $(m_{\rm J} - m_{\rm K})$ and $(m_{\rm H} - m_{\rm K})$. For the luminosity, we calculated the bolometric magnitude from the bolometric correction as the following equation by Whitelock et al. (2000):

$$\begin{aligned} BC_{\rm K} = 10.86 - 38.10(J-K) + 64.16(J-K)^2 \\ - 50.72(J-K)^3 + 19.48(J-K)^4 - 2.94(J-K)^5 \end{aligned} \tag{4.2}$$

where $BC_{\rm K}$ is the K-band bolometric correction and $(J - K)$ is the color difference of $(m_{\rm J} - m_{\rm K})$. Applying the J-band magnitude of $m_{\rm J} = 0.60$ mag obtained from SAAO (Whitelock et al. 2000), the bolometric correction would be $BC_{\rm K} = 3.25$ mag. From the bolometric correction, the absolute bolometric magnitude of star can be calculated by

$$M_{\rm bol,star} - M_K = BC_{\rm K} \tag{4.3}$$

Adopting the sun's absolute bolometric magnitude of $M_{\rm bol,\odot} = 4.74$ mag (Mamajek et al. 2015), we can yield the luminosity of the star as the following equation,

$$M_{\rm bol,\odot} - M_{\rm bol,star} = 2.5 \log L/L_\odot \tag{4.4}$$

From the above equation, the luminosity of the star was $\log L/L_\odot = 3.81^{+0.13}_{-0.07}$ or $L = 6413^{+2316}_{-1010} L_\odot$. The error caused by ignoring interstellar extinction is expected to be less than 0.1 mag, and the standard deviation of the above BC_K is $\sigma = 0.019$ mag. Therefore, the observational uncertainty for $(J - K)$ is expected to be around 0.05 mag, and the error of the luminosity is basically dominated by the error in distance measurements.

The effective temperature can be estimated by the equation (8) and (9) from Takeuti et al. (2013) of

$$\begin{aligned} (V-K) = 11((H-K) - 0.25) + 6 \\ T_{\rm eff} = -175((V-K) - 6) + 3400 \end{aligned} \tag{4.5}$$

where $(H - K)$ and $(V - K)$ are the color differences of $(m_{\rm H} - m_{\rm K})$ and $(m_{\rm V} - m_{\rm K})$, respectively. When we apply the H-band magnitude of $m_{\rm H} = -0.46$ mag obtained from SAAO (Whitelock et al. 2000), the effective temperature is $T_{\rm eff} = 2803$ K. The uncertainty of the effective temperature is approximately 100 K, or 3% (Takeuti et al. 2013). The effective temperature of 2800 K is well in agreement with previous SED analysis (Contini & Formiggini 2003; Meier & Kafatos 1995; Anandarao & Pottasch 1986). The luminosity of R Aqr was typically known about 4500 $L_\odot$ (Takeuti et al. 2013; Mayer et al. 2013; Wittkowski et al. 2016). However, the derived luminosity of the Mira variable becomes larger because our distance measurement is further than previous measurements.

Together with the luminosity and effective temperature, the stellar radius can be calculated by the Stefan-Boltzmann law of $L = 4\pi R^2 \sigma T_{\rm eff}^4$. Simply, we rewrite the equation in convenient units:

$$\log\left(\frac{R}{R_\odot}\right) = 0.5\log\left(\frac{L}{L_\odot}\right) - 2\log\left(\frac{T_{\rm eff}}{T_{\rm eff,\odot}}\right) \tag{4.6}$$

When we adopt the effective temperature of the Sun, $T_{\rm eff,\odot} = 5772$ K (Mamajek et al. 2015), the stellar radius would be $\log(R/R_\odot) = 2.53^{+0.07}_{-0.04}$ or $R = 339^{+57}_{-28} R_\odot$ corresponding to the angular diameter of $12.54^{+2.09}_{-1.03}$ mas with our distance measurement. Previous studies have shown that the near-IR of K-band is not contaminated much by molecular bands and that it provides a good estimate of the angular diameter of continuum-forming layers (Wittkowski et al. 2016). Comparing with the near-IR of K-band interferometry observations toward the R Aqr system, the angular diameter of the Mira variable have been provided from 11 to 18 mas (van Belle et al. 1997; Mennesson et al. 2002; Millan-Gabet et al. 2005; Ragland et al. 2008; Wittkowski et al. 2016). We can confirm that the derived stellar radius comes under the observational results.

Using the derived stellar radius, we can estimate the mass of the Mira variable in R Aqr. Generally, pulsating AGB stars have a relationship between the mean density (related to the mass and radius) and the pulsation period (e.g., Cox 1980):

$$Q = P\sqrt{\bar{\rho}/\bar{\rho_\odot}} \tag{4.7}$$

where P is the pulsation period, $\bar{\rho}$ is the mean density, and Q is the *pulsation constant*. We rewrite above relation in convenient unit:

$$\log\left(\frac{M}{M_\odot}\right) = 2\log Q - 2\log P + 3\log\left(\frac{R}{R_\odot}\right) \tag{4.8}$$

For the Mira variable in R Aqr, we adopted the pulsation constant of fundamental mode of $Q = 0.077 \pm 0.010$ (Takeuti et al. 2013). As a result, we obtained the mass of Mira variable of $1.55 \pm 0.75\ M_\odot$ using the pulsation period of 387.3 ± 0.07 days and $\log(R/R_\odot) = 2.53 \pm 0.06$ for simply estimating the error.

Moreover, we can also derive the component mass using the orbital parameters from our MCMC analysis. The Kepler's third law gives the mass function of

$$f'(M) = \frac{(M_{\rm WD})^3}{(M_{\rm WD} + M_{\rm Mira})^2} = \frac{4\pi^2}{G}\frac{a_{\rm Mira}^3}{P_{\rm orb}^2} = 0.157^{+0.158}_{-0.032} \tag{4.9}$$

where $M_{\rm WD}$ and $M_{\rm Mira}$ is the masses of the Mira variable and the WD companion, respectively.

Figure 4.2 shows the permitted mass of the WD companion when the Mira variable has a plausible mass range between 0.8 and 2.1 $M_\odot$. Applying the derived Mira's mass of 1.55 $M_\odot$, we obtained the WD mass of $1.01^{+0.39}_{-0.10}\ M_\odot$. When the mass of Mira variable over the 1.64 $M_\odot$, the upper limit of WD mass get closer to the Chandrasekhar limit of 1.44 $M_\odot$. Therefore, the possible masses of the component would have a range between $0.80 - 1.64\ M_\odot$ for the Mira variable, and $0.64 - 1.44\ M_\odot$ for the WD companion, respectively.

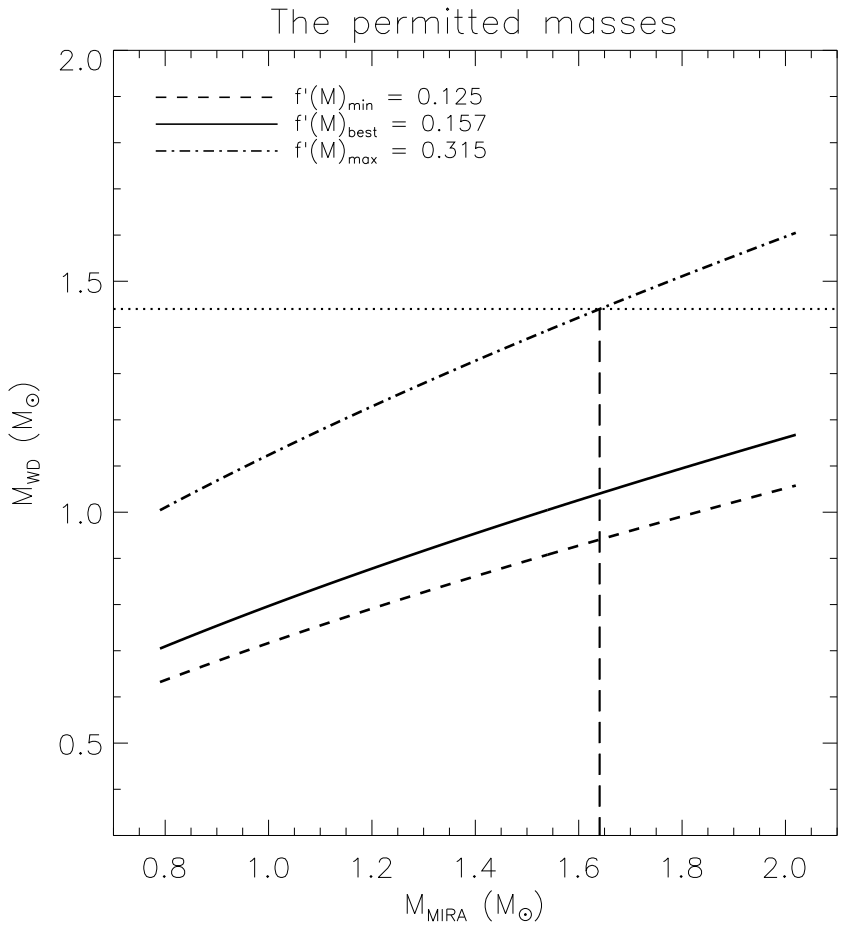

Figure 4.2: The permitted mass range of the R Aqr components. The x-axis is the mass range for the Mira variable, and the y-axis is the mass range for the WD companion. The horizontal dotted line indicates the Chandrasekhar mass limit. The vertical long dashed line is the upper limit of the Mira variable (see text).

4.3 Relations of the orbit & symbiotic phenomena

4.3.1 Mass transfer process

The symbiotic phenomena in R Aqr, such as a presence of bipolar nebulae and jet-like features, are formed by an effective mass-transfer of binary interaction from the Mira variable to the companion star. However, how the mass-transfer is not well known and not completely understood. We discuss the possible process of the mass transfer according to the new orbital parameters and the SiO maser observations.

Our VERA observations of the SiO masers provide a hypothesis that the mass transfer is possibly occurred via (wind) Roche lobe overflow. An effective Roche lobe radius depends on the orbital separation and the mass ratio. Approximated formula by Eggleton (1983) is

$$\frac{R_{\rm RL}}{a} = \frac{0.49q^{2/3}}{0.6q^{2/3} + \ln\left(1 + q^{1/3}\right)} \tag{4.10}$$

where $R_{\rm RL}$ is the Roche lobe radius, $q = M_{\rm Mira}/M_{\rm WD}$ is the mass ratio and a is the orbital separation. We derived the mass ration of $q = 1.53$, and the separation is $a = a_{\rm Mira}(1+q) = 11.46$ AU. Then, the effective Roche lobe radius is $R_{\rm RL} = 4.77$ AU, corresponding to an angular size of 18.96 mas at the distance of 252 pc.

Figure 4.1 shows distributions of the radial distance for SiO maser. The mean masing shell located at the radius of 14.81 mas for $v = 1$ $J = 1-0$ SiO maser transition and 14.10 mas for $v = 2$ $J = 1-0$ SiO maser transition covering from a few mas to 22 mas, where the maser shells reach to the effective Roche lobe radius $R_{\rm RL}$.

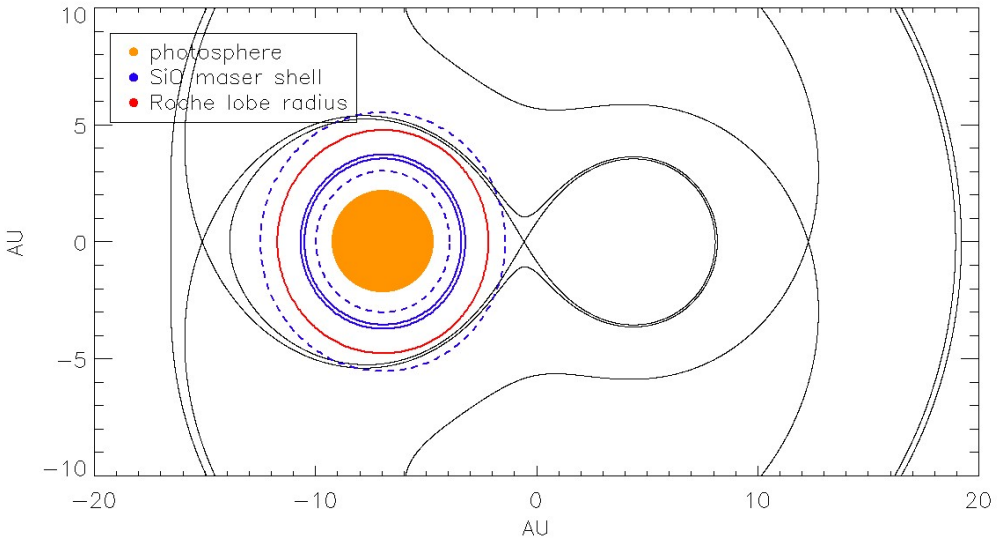

Figure 4.3: Representation of Roche equipotential (black) of R Aqr for a mass ratio of 1.26. The red circle is the effective Roche lobe circle, the Blue circle is the SiO maser region, and Orange circle is assumed photosphere.

Figure 4.3 presents the equipotential surface with the effective Roche lobe radius and the location of the SiO maser shells. According to the binary potential, the mean SiO maser shells correspond to the physical scale of 3.73 and 3.55 AU with our distance measurement, where the shells reach around 74-78% of its Roche lobe radius. Several maser components are detected on closed to the Roche lobe radius, indicating that the material possibly fills the Roche lobe and transfers to the companion through the Lagrangian point.

Moreover, radiation pressured dust-driven winds can overcome the pulsating region and central gravitational force, and efficiently fill the Roche lobe. The dust-driven winds occur beyond the dust formation region, where a temperature is sufficiently low to allow for dust condensation. If the dust region is comparable to the Roche lobe radius, the material can effectively fill the Roche lobe, and transfer to the companion through the Lagrangian point.

For oxygen-rich AGB stars, the dust-driven wind is thought to be caused by scattering on micron-sized Fe-free and Mg-rich silicate dust grains, such as forsterite (Mg_2SiO_4) and enstatite ($MgSiO_3$) or corundum (Al_2O_3) (Höfner 2008). The Al_2O_3 is one of can-

didate dust grains for starting dust-driven winds, condensing at distances closer than about 2 stellar radii where a gravitationally bound shell as part of the extended atmospheric layers. When the grains reach sizes large enough to drive the wind (about 0.1-1 micron), the outflow is triggered and both mass-loss rates and wind velocities increase.

For R Aqr, infrared interferometry observations provided that the Al_2O_3 dust grain occupied at the shell radius from 21 to 27 mas (Zhao-Geisler et al. 2012). Comparing with our VERA observations, the dust shell is located in smaller or co-existing with the SiO maser region and close as large as the Roche lobe radius. If the dust shell is responsible for triggering the outflow, the material can more effectively fill the Roche lobe with increasing the mass loss rate and activate mass-transfer to the companion efficiently.

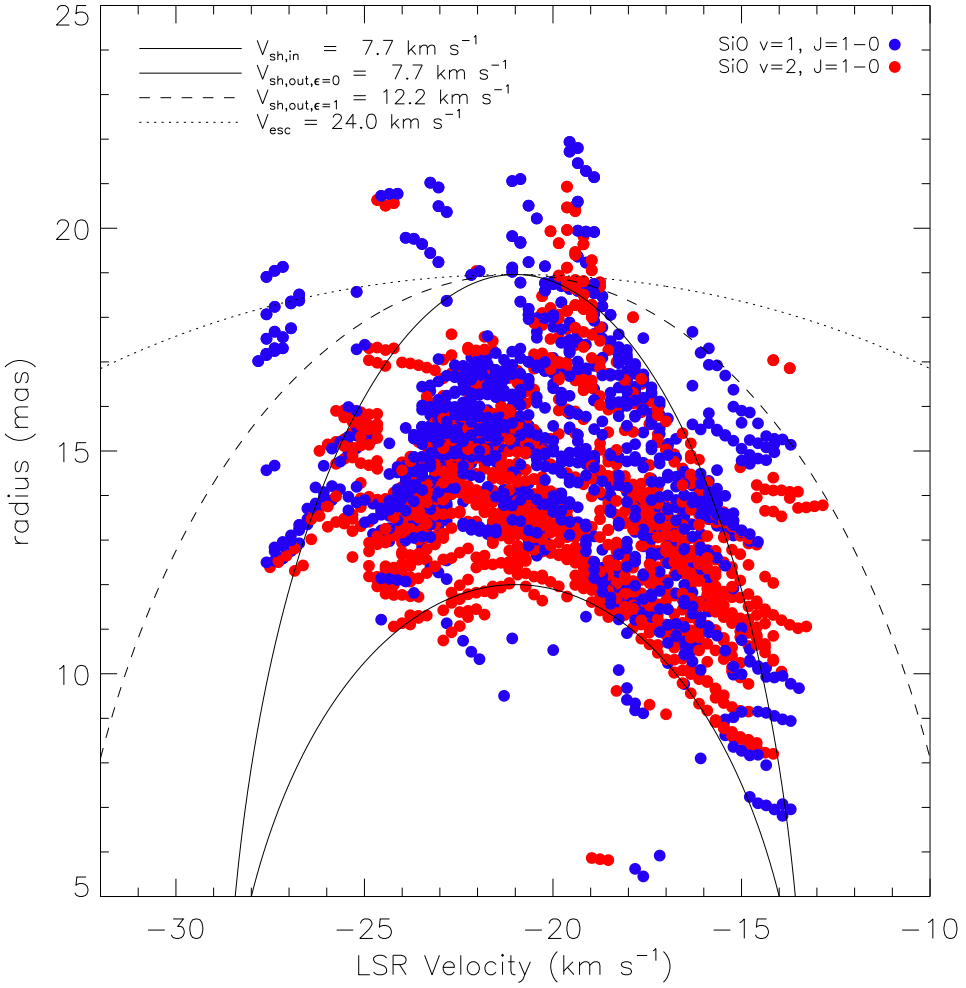

Figure 4.4: Distribution of the SiO maser distances from the center (radius) versus their LSR velocities. The different maser transitions are denoted by different colors. The curves represent the models at the inner boundary of the SiO maser shell and at the outer boundary of the Roche-lobe radius using a constant velocity expansion (solid lines), a logarithmic velocity gradient (dashed line) and an escape velocity (dotted line).

To characterize the kinematics of the SiO maser region, we apply a simple model of a spherical and uniformly expanding thin shell, proposed by Reid et al. (1977). The model often used in the case of SiO maser kinematics in AGB stars (Wittkowski et al. 2007; Chen & Shen 2008). In this model, the distance from the central star varies with the velocity according to

$$\left(\frac{r}{r_{sh}}\right)^2 + \left(\frac{v - v_*}{v_{sh}}\right)^2 = 1 \tag{4.11}$$

where r is the radial distance from the center, r_{sh} is the radius of the shell, v is the observed velocity of the SiO maser components v_* is the LSR stellar velocity and v_{sh} is the expansion velocity of the shell. The parameters of r_{sh} and v_{sh} are adjusted to fit the observed data.

Figure 4.4 shows the distribution of the radial distances against the LSR velocities of the SiO maser components. SiO masers show complex distributions, probably overlapped with a number of velocity structures along the masing region. We found that most of the maser features appear to have velocity gradients lying closer to the center at the higher velocity channels (blue- and red-shifted spectra). These features indicate the continuously ejected material, somewhat suffering the acceleration due to the shock (pulsation) propagation and dust-driven outflow, or deceleration due to the stellar gravitation.

Adopting the stellar velocity of $v_* = -21$ km s^{-1} from the radial velocity provided by Nobeyama and Mopra observations, we define the inner boundary of the SiO maser region, where the radius and velocity are $R_{\rm in} = 12$ mas and $V_{\rm in} = 7.7$ km s^{-1}, respectively. However, the outer boundary is not clearly confined because of several extended maser components.

Taking into account the Roche lobe radius, we expect that the matters are supplied by dust-driven winds and fill the Roche lobe. Moreover, theoretical studies of AGB star's atmosphere with SiO maser emission often use the Sobolev or Large Velocity Gradient (LVG) approximation (Lockett & Elitzur 1992; Bujarrabal 1994; Doel et al. 1995; Humphreys et al. 2002). The LVG approximation assumes a large velocity gradient across the SiO maser region, thus producing large Doppler shifts that serve to disconnect a region of velocity coherence from the surrounding medium (Bujarrabal 1994). The radial expanding velocity field in the maser region can be characterized by the logarithmic velocity gradient, ϵ given by

$$\epsilon = \frac{\mathrm{d}\ln v}{\mathrm{d}\ln r} = \frac{r}{v}\frac{\mathrm{d}v}{\mathrm{d}r} \tag{4.12}$$

When $\epsilon = 0$, the shell is expanding at a constant velocity, $\epsilon = 1$ is the case that the radial velocity is proportional to the distance r. The SiO maser numerical simulations (e.g. Lockett & Elitzur 1992; Bujarrabal 1994; Doel et al. 1995) usually use $\epsilon = 1$. A value larger than 1 indicates that the outflow is accelerated faster with an increase of distance r. Other values for the velocity gradient and their effect on various maser species are discussed by Chapman & Cohen (1985, 1986).

Adopting the logarithmic velocity gradient, the outflow velocity at the Roche lobe radius is $V_{\rm out} = 7.7$ and 12.2 km s^{-1} for $\epsilon = 0$ and 1, respectively. For comparison,

the escape velocity derived for the 1.55 $M_{\odot}$ central Mira variable, is $V_{\rm esc}$ = 23.98 km s^{-1} corresponding the velocity gradient of ϵ = 2.48. In Figure 4.4, we display the models for the inner and outer boundary of the SiO maser region along with the data. From the comparisons of SiO maser data with the model, most of SiO maser components are bound inside the constant expansion model, and the outer components have higher velocities than inner region. The masing gas does not exceed the escape velocity, indicating that the material is gravitationally bound to the central star, but affected by the dust-driven wind to fill the Roche lobe.

From the expanding velocity at a given radius, we simply expect the mass-loss rate with a uniform expanding spherical shell

$$\begin{aligned} \dot{M}_{\rm Loss} &= 4\pi r^2 \rho(r) v(r) \\ &= 1.12 \times 10^{-5} \left(\frac{r}{5{\rm AU}} \right)^2 \left(\frac{\rho}{10^{-17}{\rm kg\ cm^{-3}}} \right) \left(\frac{v(r)}{10{\rm km\ s^{-1}}} \right) {\rm M_{\odot} } yr^{-1} \end{aligned} \tag{4.13}$$

According to Khouri et al. (2016), the number density is as low as 10^{10} cm^{-3} at the distance of R = 4.63 AU for R Aqr. Typical number density in the SiO maser region and pulsation region is $n(\mathrm{H_2}) = 10^8 - 10^{10}$ cm^{-3} (Doel et al. 1995; Humphreys et al. 1996). Large number density in R Aqr can be deduced from the mass loss rate of 2.62 and 4.14 $\times 10^{-5}$ M$_{\odot}$ yr^{-1} for the velocity of $V_{\rm out}$ = 7.7 and 12.6 km s^{-1} at the Roche lobe radius, respectively.

4.3.2 Symbiotic nebulae in R Aqr

Most of the symbiotic nebulae are found around D-type symbiotic stars, and a large population of those nebulae shows a bipolar morphology. For the bipolar morphology, the most preference explanation is a binary interaction, since aspherical shape could naturally arise from the existence of a binary companion. Several studies have proposed the formation processes of the bipolar nebula with an equatorial dense region and bipolar outflows in symbiotic stars as well as planetary nebulae in binary cores. A matter of first importance between bipolar nebulae and orbital parameters is that the equatorial dense region is identical to the orbital plane. In the same sense of the word, the bipolar axis is identical to the orbital axis, equivalently.

The symbiotic star R Aqr is surrounded by two inner and outer nebulae, presumably linked to possible two nova-like outbursts. The seminal work of Solf & Ulrich (1985) presented that the both nebulae show hourglass-like bipolar structures with a prominent equatorial dense region. From the spectroscopic analysis, the nebulae have a common bipolar axis inclined at 18 degrees with respect to the plane of the sky, and an apparent position angle of that polar axis is about 355 degree. According to binary interacting bipolar nebula scenarios, these values are connected with orbital parameters, i.e. the orbital axis and apparent position angle of that axis indicate the orbital inclination, i, and the position angle of the node, Ω. Therefore, Solf & Ulrich (1985) predicted the orbital inclination of 72 degrees and the position angle of node of 85/265

degree. Afterward, Mayer et al. (2013) suggested the orbital inclination of 77 degrees from *Herschel* observations.

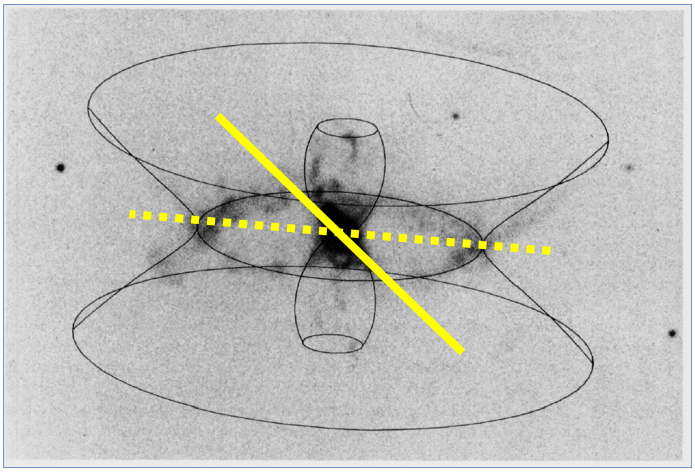

Figure 4.5: Symbiotic nebulae in R Aqr with the orientations of the orbital planes. The yellow dashed line represents the expected orientation of the orbital plane from the nebula morphology. The yellow line is the orientation of the orbital plane from our orbital model.

From our orbital analysis, the orbital plane is inclined at 68.6 degrees and oriented in NE-SW direction with the P.A. of the orbital axis to be about 134 degrees (the P.A. of orbital plane is 44/224 degree). Figure 4.5 denotes the morphological indication of the orbital plane by dotted line (characterized by Solf & Ulrich (1985) corresponding to the P.A. of 85/265 degree) and the expected orbital plane from our analysis by the solid line (corresponding to the P.A. of 44/224 degree). We can see that the morphological expectation of orbital plane is significantly different with our orbital parameters. This discrepancy between the nebula morphology and our orbital parameters indicates that the formation process does not favor the binary interacting bipolar nebula scenario, and the symbiotic nebula requires more advanced or complex processes to be formed in the R Aqr system.

In order to explain this misalignment, other possible process is to involve magnetic fields. The effects of magnetic fields on the stellar outflow have been also proposed to form the bipolar nebula morphology with the equatorial density enhancement whereby binary system produces the distinct aspherical shape (e.g. Pascoli 1987; Chevalier & Luo 1994; Gracía-Segura 1997; Tout & Regös 2003; Nordhaus & Blackman 2006; Gracía-Segura et al. 1999; Gracía-Segura & López 2000; Frank & Blackman 2004). Blackman et al. (2001a, b) suggested that a strong dipole magnetic field can constrain a bipolar outflow and an equatorial dense torus around the central star. Moreover, the magnetic field can produce multi-polar outflow with the different (misaligned) magnetic axis to the rotation axis of the central star. Moreover, polarimetric observations of SiO masers indicate that evolved stars have a specific magnetic field throughout the circumstellar envelope to possibly produce the aspherical shape of planetary nebulae (Vlemmings et al. 2005; Kemball et al. 2009).

For R Aqr, the WD companion has a strong magnetic field between 10^8 and 10^9 G (Hollis & Koupelis 2000). Nichols et al. (2007) also suspected that R Aqr is likely a magnetic symbiotic star to be similar to Intermediate Polars for the WD companion which has a strong magnetic field typically over 10^6 G (Warner 1995). In addition, Boboltz (1998) provided the polarization observations that SiO masers are significantly polarized implying a magnetic field strength from 13 to 46 G for the Mira variable in R Aqr. If the formation of nebulae is affected by magnetic fields from the central system, the circumbinary structure of outflows can possibly produce the equatorial dense region misaligned to the orbital plane. Moreover, the WD processes with a specific angle, the effect from the companion is more complex to the formation of symbiotic nebula structure. By considering the effects of the magnetic fields in R Aqr, the misalignment between the nebula morphology and true orbital parameter can be explained. In addition, this discrepancy between the nebula morphology and the true orbital plane in R Aqr is one of possible precursor for a multi-polar structure of planetary nebulae.

The discussion on the relationship between the orbital parameters and the circumstellar structure can apply to other related objects.

Mira AB (o Ceti) is a binary system, composed of the Mira A, a prototype of Mira variables, and the Mira B, a putative WD or recently considered as a somewhat F-type main-sequence star. The astrometric set of photometric observations provided the orbital parameters of Mira AB, that have an orbital period of 498 years, an inclination of 112 degrees (nearly edge-on), and a line of node of about 139 degrees (Prieur et al. 2002). Recent ALMA observations resolved the components in Mira AB, and supported the orbital parameters predicted by Prieur et al. (2002).

The structure of outflows around Mira AB showed several spiral arc-like structures extended in NE-SW direction, indicating that the binary interacting outflows confined to the orbital plane (Ramstedt et al. 2014). According to the binary interacting scenario, the spiral structure is identical to the orbital plane, and the spiral arcs are expected to be found in the edge-on orbit. For the spiral arc structure, the direction of the extending arc structure is parallel to the orbital plane when the binary is an edge-on orbit.

Figure 4.5 denotes the morphological indication of the orbital plane by the dotted line, which follows the direction of the spiral arcs (corresponding to the P.A. of ∼26/206 degree), and the orbital plane from the orbital parameters by the solid line (corresponding to the P.A. of 139/319 degree). As similar to the situation of R Aqr, the discrepancy between the outflow morphology and orbital parameters is also found in Mira AB, which does not favor the binary interacting scenario and requires advanced processes. However, Mira AB exhibits an exceptionally high space velocity, so that the shape of the environment is in a more complex situation, interacting the outflows with its companion, bipolar jets, and the interstellar medium.

Such misalignment of the orbital axis with the circumstellar structure is also found in binary Young Stellar Objects. Several observations provided direct evidence of the misalignment between the axis of circumstellar medium and the binary orbital axis (HK Tau: Jensen & Akeson 2014; V2434 Ori: Williams et al. 2014; AS 205: Salyk

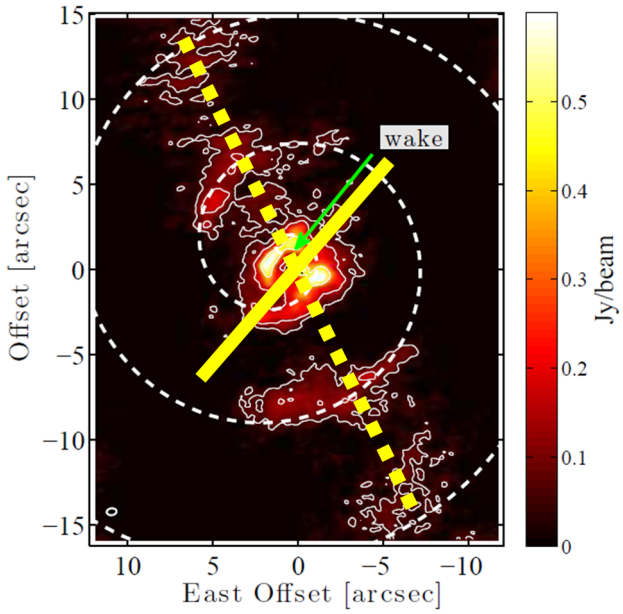

Figure 4.6: Spiral arcs in Mira AB (Ramstedt et al. 2014) with orbital orientation. White dashed line represents the spiral windings. The yellow dashed line is the direction of the spiral arcs. The yellow solid line is the orientation of the orbital plane.

et al. 2014). Moreover, several studies also provided the misalignment between the stellar spin axis and exoplanet's orbital axis (Albrecht et al. 2012 and reference therein; Winn et al. 2011;). These results indicate that the stellar properties can be affected by the circumstellar structures. Although the evolution stage in YSOs and symbiotic stars are quite different, the study of formation mechanisms and processes for those misalignments give implications to the nebulae and orbital parameter misalignment in R Aqr.

The formation mechanism for the bipolar morphology of nebulae is still matter of debate. For R Aqr, we showed the misalignment between the orbital plane and morphological indication of the bipolar shape for the symbiotic nebula. The binary interacting scenario alone cannot explain this misalignment, which is discrepancy and inconsistency between the true orbital plane and expected orbital plane from the nebula structure. This misalignment has been also found in other binary systems. In order to explain this misalignment, more advanced and complex processes are required to describe the bipolar symbiotic nebula. Effects of the magnetic fields can be involved to produce the aspherical shape, and the combination of both magnetic fields and binary interactions might be a possible explanation. Moreover, the misalignment in R Aqr is one of possible precursor for the multi-polar structure of the planetary nebula.

Chapter 5

Conclusions and Future prospects

In this study, we performed VERA observations of SiO masers to determine reliable orbital parameters of the symbiotic star R Aqr. Our observations provided the high resolution of SiO maser images with absolute positional information around the Mira variable in R Aqr from 2011 to 2014 for the first time. The SiO masers extended over an area of about 40 mas $\times$ 40 mas, forming clumpy, partial ring-like structure. Strong and dominant SiO maser emissions were located on eastern hemisphere of the shell in all of epochs. For the astrometry, we determined the positions of the Mira variable from the SiO maser distributions at 16 sessions. Adopting previous VERA astrometry observations, we covered about 10 yrs of a time baseline for astrometry data. For the radial velocity, we complemented previous radial velocity data with additional data from Nobeyama and Mopra single-dish observations, covering about 85 yrs of a time baseline. To estimate orbital parameters, we employed a Markov Chain Monte Carlo (MCMC) method to jointly fit the astrometry and radial velocity data. As a result, we obtain the full orbital parameters of the R Aqr system with several constraints for the first time.

Throughout the observations and analyses, we found several results related to the binary motion and the phenomena in R Aqr.

1. The global dominant SiO maser emissions are closely related to the orbital phase of R Aqr due to the binary interaction. During three stellar phases, most of SiO maser components were detected in eastern hemisphere rather than the western side. Comparing with our orbital motion, dominant SiO maser region tends to appear in the direction along the Mira variable and the WD companion. This tendency had been also observed in previous VLBI observations for over 20 yrs. Therefore, we conclude that high density of masing material properly concentrated in the direction of the components, where the mass–transfer process may occur between the components.

2. From our analysis, several stellar properties were derived, including the component masses of 1.55 $M_{\odot}$ for the Mira variable and 1.01 $M_{\odot}$ for WD companion, respectively. Applying the stellar properties to observed SiO maser distribution, the mass-transfer is likely to occur via the (wind) Roche-lobe overflow in R Aqr.

Our observations showed that the SiO maser region occupied over 70% of the Roche-lobe radius, and several maser components were detected near the Roche-lobe radius. The dust-driven winds possibly assist the material to fill the Roche-lobe accompanying an increase the mass-loss rate. To characterize the SiO maser region, we applied a simple kinematic model. From the model and observations, we defined the inner boundary of the SiO maser region, where the radius and outflow velocity are $R_{\rm in} = 12$ mas and $V_{\rm in} = 7.7$ km s^{-1}, respectively. Moreover, we derived the outflow velocity at the Roche lobe radius of $V_{\rm out} = 7.7$ and 12.2 km s^{-1} for a constant expanding velocity and a logarithmic velocity gradient, respectively. Comparing the model and observations, most of SiO maser components are bound inside the constant expansion model, and the outer components have higher velocities than inner region. Adopting the outflow velocities, the mass-loss rate of the Mira variable is as high as 4.2×10^{-5} M$_\odot$ yr^{-1} in R Aqr.

3. The formation of bipolar nebulae requires more complex processes in R Aqr. For bipolar nebulae, a binary interaction is the most preference explanation. In addition, several orbital parameters can be estimated from their morphology of the R Aqr nebulae. Comparing the nebula morphology with our orbital parameters, we found the misalignment between the true orbital parameters and morphological expected orbital parameters. Our result indicates that the only binary interacting scenario cannot explain the discrepancy, and more advanced processes are required, such as effects of magnetic fields, to explain the misalignment. Such misalignments also found in other related and distinct evolutionary state of objects. The studies of those systems can provide constraints for the formation of bipolar nebulae mechanisms in R Aqr.

To determine more reliable orbital parameters, analyzing the longer period of the astrometry is required. For previous astrometry data, we can employ the Hipparcos astrometry result for R Aqr. Moreover, the Gaia satellite, launched in 2013, is an ongoing astrometric program that is expected to measure accurate positional information for R Aqr in the future. The duration of the Gaia mission is about 5 yrs, and we can expect the improvement of the phase coverage of the orbital motion by increasing the number of data points. For very bright stars, such as nearby Mira variables, a Japanese satellite Nano-JASMINE will also carry out a powerful and promising observation to increase the data points.

Moreover, high resolution of VLBI observations of the SiO masers in late-type stars can provide the information of the innermost region of the circumstellar envelope. Our VERA monitoring observations provide gross kinematic properties of the SiO maser region by different maser transitions over several pulsation cycles. Comparing with different transitions of the SiO maser emissions also give implications to the pumping mechanisms, which is also a subject of debate.

Bibliography

Albrecht, S., Winn, J. N., Johnson, J. A., et al. 2012, ApJ, 757, 18

Alcolea, J., Pardo, J. R., Bujarrabal, V., et al. 1999, A&AS, 139, 461

Alef, W. 1989, NATO Advanced Science Institutes (ASI) Series C, 283, 261

Allen, D. A. 1982, IAU Colloq. 70: The Nature of Symbiotic Stars, 95, 27

Allen, D. A. 1984, Proceedings of the Astronomical Society of Australia, 5, 369

Anandarao, B. G., & Pottasch, S. R. 1986, A&A, 162, 167

Assaf, K. A., Diamond, P. J., Richards, A. M. S., & Gray, M. D. 2011, MNRAS, 415, 1083

Baade, W. A. 1943, Ann. Report Dir. Mt. Wilson Obs., 1942-1943, p.17

Baade, W. A. 1944, Ann. Report Dir. Mt. Wilson Obs., 1943-1944, p.12

Balick, B., & Frank, A. 2002, ARA&A, 40, 439

Beasley, A. J., & Conway, J. E. 1995, Very Long Baseline Interferometry and the VLBA, 82, 327

Belczyński, K., Mikołajewska, J., Munari, U., Ivison, R. J., & Friedjung, M. 2000, A&AS, 146, 407

Blackman, E. G., Frank, A., Markiel, J. A., Thomas, J. H., & Van Horn, H. M. 2001a, Nature, 409, 485

Blackman, E. G., Frank, A., & Welch, C. 2001b, ApJ, 546, 288

Boboltz, D. A., Diamond, P. J., & Kemball, A. J. 1997, ApJL, 487, L147

Boboltz, D. A., Jr. 1997, Ph.D. Thesis, 4866

Bondi, H., & Hoyle, F. 1944, MNRAS, 104, 273

Bondi, H. 1952, MNRAS, 112, 195

Bowen, G. H. 1988, ApJ, 329, 299

Buhl, D., Snyder, L. E., Lovas, F. J., & Johnson, D. R. 1974, ApJL, 192, L97

Bujarrabal, V. 1994, A&A, 285, 953

Bujarrabal, V., Mikołajewska, J., Alcolea, J., & Quintana-Lacaci, G. 2010, A&A, 516, A19

Catanzarite, J. H. 2010, arXiv:1008.3416

Chapman, J. M., & Cohen, R. J. 1985, MNRAS, 212, 375

Chapman, J. M., & Cohen, R. J. 1986, MNRAS, 220, 513

Chen, X., & Shen, Z.-Q. 2008, ApJ, 681, 1574-1583

Chevalier, R. A., & Luo, D. 1994, ApJ, 421, 225

Cho, S.-H., Kaifu, N., & Ukita, N. 1996, A&AS, 115, 117

Cioni, M.-R. L., Marquette, J.-B., Loup, C., et al. 2001, A&A, 377, 945

Cohen, N. L., & Ghigo, F. D. 1980, AJ, 85, 451

Contini, M., & Formiggini, L. 2003, MNRAS, 339, 148

Corradi, R. L. M., Brandi, E., Ferrer, O. E., & Schwarz, H. E. 1999, A&A, 343, 841

Corradi, R. L. M., Livio, M., Schwarz, H. E., & Munari, U. 2000, Asymmetrical Planetary Nebulae II: From Origins to Microstructures, 199, 175

Corradi, R. L. M. 2003, Symbiotic Stars Probing Stellar Evolution, 303, 393

Cotton, W. D., Mennesson, B., Diamond, P. J., et al. 2004, A&A, 414, 275

Cotton, W. D., Vlemmings, W., Mennesson, B., et al. 2006, A&A, 456, 339

Cotton, W. D., Perrin, G., & Lopez, B. 2008, A&A, 477, 853

Cotton, W. D., Ragland, S., Pluzhnik, E. A., et al. 2009, ApJS, 185, 574

Cotton, W. D., Ragland, S., Pluzhnik, E., et al. 2009, ApJ, 704, 170

Cotton, W. D., Ragland, S., Pluzhnik, E. A., et al. 2010, ApJS, 187, 107

Cotton, W. D., Ragland, S., Pluzhnik, E. A., et al. 2010, ApJS, 188, 506

Crepp, J. R., Johnson, J. A., Fischer, D. A., et al. 2012, ApJ, 751, 97

Decin, L., Richards, A. M. S., Neufeld, D., et al. 2015, A&A, 574, A5

Desmurs, J. F., Bujarrabal, V., Colomer, F., & Alcolea, J. 2000, A&A, 360, 189

de Val-Borro, M., Karovska, M., & Sasselov, D. 2009, ApJ, 700, 1148

Diamond, P. J., Kemball, A. J., Junor, W., et al. 1994, ApJL, 430, L61

Diamond, P. J., & Kemball, A. J. 2003, ApJ, 599, 1372

Doel, R. C., Gray, M. D., Humphreys, E. M. L., Braithwaite, M. F., & Field, D. 1995, A&A, 302, 797

Dougherty, S. M., Bode, M. F., Lloyd, H. M., Davis, R. J., & Eyres, S. P. 1995, MNRAS, 272, 843

Eastman, J., Gaudi, B. S., & Agol, E. 2012, Astrophysics Source Code Library, ascl:1207.001

Efron, B., 1979, Ann. Statist., 7, 1

Efron, B., Tibshirani, R. J., 1993, An Introduction to the Bootstrap. Boca Raton, FL: Chapman & Hall.

Eggleton, P. P. 1983, ApJ, 268, 368

Eiroa, C., Hefele, H., & Qian, Z. Y. 1982, IAU Colloq. 70: The Nature of Symbiotic Stars, 95, 43

Feast, M. W. 1963, MNRAS, 125, 367

Feast, M. W., Glass, I. S., Whitelock, P. A., & Catchpole, R. M. 1989, MNRAS, 241, 375

Feast, M. W., & Whitelock, P. A. 2000, MNRAS, 317, 460

Feast, M. 2004, IAU Colloq. 193: Variable Stars in the Local Group, 310, 304

Ford, E. B. 2005, AJ, 129, 1706

Ford, E. B. 2006, ApJ, 642, 505

Frank, A., & Blackman, E. G. 2004, ApJ, 614, 737

García-Segura, G. 1997, ApJL, 489, L189

García-Segura, G., Langer, N., Różyczka, M., & Franco, J. 1999, ApJ, 517, 767

García-Segura, G., & López, J. A. 2000, ApJ, 544, 336

Gazak, J. Z., Johnson, J. A., Tonry, J., et al. 2012, Advances in Astronomy, 2012, 697967

Gonidakis, I., Diamond, P. J., & Kemball, A. J. 2010, MNRAS, 406, 395

Gonidakis, I., Diamond, P. J., & Kemball, A. J. 2013, MNRAS, 433, 3133

Gray, M. D., & Humphreys, E. M. L. 2000, New Astron., 5, 155

Gray, M. D., Wittkowski, M., Scholz, M., et al. 2009, MNRAS, 394, 51

Greenhill, L. J., Colomer, F., Moran, J. M., et al. 1995, ApJ, 449, 365

Gregory, P. C. 2005a, Bayesian Logical Data Analysis for the Physical Sciences: A Comparative Approach with 'Mathematica' Support. Edited by P. C. Gregory. ISBN 0 521 84150 X (hardback); QA279.5.G74 2005 519.5'42 – dc22; 200445930. Published by Cambridge University Press, Cambridge, UK, 2005.,

Gregory, P. C. 2005b, ApJ, 631, 1198

Gregory, P. C. 2007a, MNRAS, 374, 1321

Gregory, P. C. 2007b, MNRAS, 381, 1607

Gregory, P. C. 2011, MNRAS, 410, 94

Groenewegen, M. A. T., & de Jong, T. 1994, A&A, 283, 463

Groenewegen, M. A. T., & Whitelock, P. A. 1996, MNRAS, 281, 1347

Gromadzki, M., & Mikołajewska, J. 2009, A&A, 495, 931

Harding, K. 1816, Zs. Ap. 1, 449

Hastings, W. K., 1970, Biometrika, 57, 97

Hege, E. K., Allen, C. K., & Cocke, W. J. 1991, ApJ, 381, 543

Hinkle, K. H., Scharlach, W. W. G., & Hall, D. N. B. 1984, ApJS, 56, 1

Hinkle, K. H., Wilson, T. D., Scharlach, W. W. G., & Fekel, F. C. 1989, AJ, 98, 1820

Höfner, S. 2009, Cosmic Dust - Near and Far, 414, 3

Höfner, S., Bladh, S., Aringer, B., & Ahuja, R. 2016, A&A, 594, A108

Hollis, J. M., Kafatos, M., Michalitsianos, A. G., & McAlister, H. A. 1985, ApJ, 289, 765

Hollis, J. M., Michalitsianos, A. G., Kafatos, M., Wright, M. C. H., & Welch, W. J. 1986, ApJL, 309, L53

Hollis, J. M., & Koupelis, T. 2000, ApJ, 528, 418

Hollis, J. M., & Michalitsianos, A. G. 1993, ApJ, 411, 235

Hollis, J. M., Pedelty, J. A., & Lyon, R. G. 1997, ApJL, 482, L85

Hollis, J. M., Pedelty, J. A., Forster, J. R., et al. 2000, ApJL, 543, L81

Hollis, J. M., Boboltz, D. A., Pedelty, J. A., White, S. M., & Forster, J. R. 2001, ApJL, 559, L37

Honma, M., Kawaguchi, N., & Sasao, T. 2000, Proc. SPIE, 4015, 624

Honma, M., Kijima, M., Suda, H., et al. 2008a, PASJ, 60, 935

Honma, M., Tamura, Y., & Reid, M. J. 2008b, PASJ, 60, 951

Honma, M., Hirota, T., Jike, T., et al. 2010, Publications of the National Astronomical Observatory of Japan, 13, 57

Honma, M., Nagayama, T., Ando, K., et al. 2012, PASJ, 64, 136

Hoyle, F., & Lyttleton, R. A. 1939, Proceedings of the Cambridge Philosophical Society, 35, 405

Hubble, E. P. 1940, Ann. Report Dir. Mt. Wilson Obs., 1939-1940, p.19

Hubble, E. P. 1943, Ann. Report Dir. Mt. Wilson Obs., 1942-1943, p.17

Hughes, S. M. G., & Wood, P. R. 1990, AJ, 99, 784

Humphreys, E. M. L., Gray, M. D., Yates, J. A., et al. 1996, MNRAS, 282, 1359

Humphreys, E. M. L., Gray, M. D., Yates, J. A., et al. 2002, A&A, 386, 256

Iben, I., Jr. 1985, QJRAS, 26, 1

Indrmuehle, B., Edwards, P., Brooks, K., & Urquhart, J., 2013, The Mopra SiO Maser Catalogue. v1. CSIRO. Data Collection DOI: 10.4225/08/521A8EF38E042

Ikeda, M., Nishiyama, K., Ohishi, M., & Tatematsu, K. 2001, Astronomical Data Analysis Software and Systems X, 238, 522

Ita, Y., Tanabé, T., Matsunaga, N., et al. 2004, MNRAS, 347, 720

Ivison, R. J., Seaquist, E. R., & Hall, P. J. 1994, MNRAS, 269, 218

Ivison, R. J., Yates, J. A., & Hall, P. J. 1998, MNRAS, 295, 813

Jacobsen, T. S., & Wallerstein, G. 1975, PASP, 87, 269

Jensen, E. L. N., & Akeson, R. 2014, Nature, 511, 567

Jewell, P. R., Snyder, L. E., Walmsley, C. M., Wilson, T. L., & Gensheimer, P. D. 1991, A&A, 242, 211

Jiang, B. W., Deguchi, S., Izumiura, H., Nakada, Y., & Yamamura, I. 1995, PASJ, 47, 815

Kafatos, M., Hollis, J. M., Yusef-Zadeh, F., Michalitsianos, A. G., & Elitzur, M. 1989, ApJ, 346, 991

Kaifu, N., Buhl, D., & Snyder, L. E. 1975, ApJ, 195, 359

Kamohara, R., Bujarrabal, V., Honma, M., et al. 2010, A&A, 510, A69

Kang, J., Cho, S.-H., Kim, H.-G., et al. 2006, ApJS, 165, 360

Kapur, J., 1989, Maximum-Entropy Models in Science and Engineering. Wiley

Kato, M. 2002, The Physics of Cataclysmic Variables and Related Objects, 261, 595

Kellogg, E., Pedelty, J. A., & Lyon, R. G. 2001, ApJL, 563, L151

Kellogg, E., Anderson, C., Korreck, K., et al. 2007, ApJ, 664, 1079

Kemball, A. J., Diamond, P. J., Gonidakis, I., et al. 2009, ApJ, 698, 1721

Kenyon, S. J., 1986, The Symbiotic Stars (Cambridge: Cambridge Univ. press)

Kenyon, S. J. 2001, The Starry Universe; The Cecilia Payne-Gaposchkin Century, 19, 123

Khouri, T., Vlemmings, W. H. T., Ramstedt, S., et al. 2016, MNRAS, 463, L74

Kim, M. K., Hirota, T., Honma, M., et al. 2008, PASJ, 60, 991

Kim, H. 2011, ApJ, 739, 102

Kim, H., & Taam, R. E. 2012, ApJ, 759, 59

Kohoutek, L. 1987, Ap&SS, 131, 781

Kwok, S., Purton, C. R., & Fitzgerald, P. M. 1978, ApJL, 219, L125

Kwok, S. 2003, Symbiotic Stars Probing Stellar Evolution, 303, 428

Lampland, C. O. 1923a PAAS, 4, 319

Lampland, C. O. 1923b PAAS, 4, 369

Lane, A. P. 1982, Ph.D. Thesis,

Lepine, J. R. D., Scalise, E., Jr., & Le Squeren, A. M. 1978, ApJ, 225, 869

Livio, M. 2004, Baltic Astronomy, 13, 273

Liu, M. C., Fischer, D. A., Graham, J. R., et al. 2002, ApJ, 571, 519

Lockett, P., & Elitzur, M. 1992, ApJ, 399, 704

López, J. A., Escalante, K., & Riesgo-Tirado, H. 2004, Revista Mexicana de Astronomia y Astrofisica Conference Series, 20, 226

Maercker, M., Mohamed, S., Vlemmings, W. H. T., et al. 2012, Nature, 490, 232

Magrini, L., Corradi, R. L. M., & Munari, U. 2003, Symbiotic Stars Probing Stellar Evolution, 303, 539

Mamajek, E. E., Torres, G., Prsa, A., et al. 2015, arXiv:1510.06262

Markwardt, C. B. 2009, Astronomical Data Analysis Software and Systems XVIII, 411, 251

Martinez, A., Bujarrabal, V., & Alcolea, J. 1988, A&AS, 74, 273

Mastrodemos, N., & Morris, M. 1999, ApJ, 523, 357

Matsumoto, N., Omodaka, T., Imai, H., et al. 2008, PASJ, 60, 1039

Mayer, A., Jorissen, A., Kerschbaum, F., et al. 2013, A&A, 549, A69

Meier, S. R., & Kafatos, M. 1995, ApJ, 451, 359

McIntosh, G. C. 2006, AJ, 132, 1046

McIntosh, G. C., & Rustan, G. 2007, AJ, 134, 2113

McIntosh, G. C., & Patriat, R. 2010, PASP, 122, 1187

McIntosh, G., & Indermuehle, B. 2013, AJ, 145, 131

Merrill, P. W. 1935, ApJ, 81, 312

Merrill, P. W., 1941, PAAS, 10, 168

Merrill, P. W. 1950, ApJ, 112, 514

Metropolis, N., Rosenbluth, A. W., Rosenbluth, M. N., Teller, A. H., & Teller, E. 1953, JChPh, 21, 1087

Mikòlajewska, J. 2000, Asymmetrical Planetary Nebulae II: From Origins to Microstructures, 199, 431

Mikołajewska, J. 2003, Symbiotic Stars Probing Stellar Evolution, 303, 9

Mikołajewska, J. 2007, Baltic Astronomy, 16, 1

Mikołajewska, J. 2008, RS Ophiuchi (2006) and the Recurrent Nova Phenomenon, 401, 42

Mikołajewska J. 2011, in Physics of Accreting Compact Binaries, ed. D. Nogami, Universal Academy Press, Inc., in press (arXiv:1011.5657)

Min, C., Matsumoto, N., Kim, M. K., et al. 2014, PASJ, 66, 38

Morris, M. 1981, ApJ, 249, 572

Morris, M. 1987, PASP, 99, 1115

Nagayama, T., Kobayashi, H., Omodaka, T., et al. 2015, PASJ, 67, 65

Nakagawa, A., Kurayama, T., Matsui, M., et al. 2016, PASJ, 68, 78

Nichols, J. S., DePasquale, J., Kellogg, E., et al. 2007, ApJ, 660, 651

Nichols, J., & Slavin, J. D. 2009, ApJ, 699, 902

Nordhaus, J., & Blackman, E. G. 2006, MNRAS, 370, 2004

Paresce, F., & Hack, W. 1994, A&A, 287, 154

Pardo, J. R., Alcolea, J., Bujarrabal, V., et al. 2004, A&A, 424, 145

Pascoli, G. 1987, A&A, 180, 191

Prieur, J. L., Aristidi, E., Lopez, B., et al. 2002, ApJS, 139, 249

Ragland, S., Le Coroller, H., Pluzhnik, E., et al. 2008, ApJ, 679, 746-761

Ramstedt, S., Mohamed, S., Vlemmings, W. H. T., et al. 2014, A&A, 570, L14

Reid, M. J., Muhleman, D. O., Moran, J. M., Johnston, K. J., & Schwartz, P. R. 1977, ApJ, 214, 60

Reid, M. J., & Menten, K. M. 2007, ApJ, 671, 2068

Reid, M. J., Menten, K. M., Brunthaler, A., et al. 2014, ApJ, 783, 130

Roberts, G. O., Gelman, A., & Gilks, W. R. 1997, Ann. Appl. Probability, 7, 110

Rudnitskij, G. M. 2008, Journal of Physical Studies, 12, 1301

Salyk, C., Pontoppidan, K., Corder, S., et al. 2014, ApJ, 792, 68

Scalo, J. M., & Ross, J. E. 1976, A&A, 48, 219

Schmid, H. M., Kaufer, A., Camenzind, M., et al. 2001, A&A, 377, 206

Schwarz, H. E., Nyman, L.-A., Seaquist, E. R., & Ivison, R. J. 1995, A&A, 303, 833

Seaquist, E. R., Ivison, R. J., & Hall, P. J. 1995, MNRAS, 276, 867

Seidelmann, P. K. 1992, Explanatory Supplement to the Astronomical Almanac. A revision to the Explanatory Supplement to the Astronomical Ephemeris and the American Ephemeris and Nautical Almanac., by Seidelmann, P. K.. University Science Books, Mill Valley, CA (USA), 1992, 780 p., ISBN 0-935702-68-7,,

Snyder, L. E., & Buhl, D. 1974, ApJL, 189, L31

Sokoloski, J. L., Bildsten, L., & Ho, W. C. G. 2001, MNRAS, 326, 553

Soker, N. 1994, MNRAS, 270, 774

Solf, J., & Ulrich, H. 1985, A&A, 148, 274

Sopka, R. J., Herbig, G., Kafatos, M., & Michalitsianos, A. G. 1982, ApJL, 258, L35

Spencer, J. H., Schwartz, P. R., Winnberg, A., et al. 1981, AJ, 86, 392

Spergel, D. N., Giuliani, J. L., Jr., & Knapp, G. R. 1983, ApJ, 275, 330

Takeuti, M., Nakagawa, A., Kurayama, T., & Honma, M. 2013, PASJ, 65, 60

Tanabe, K., & Motizuki, Y. 2012, Mem. Soc. Astron. Ital., 83, 840

Thaddeus, P., Mather, J., Davis, J. H., & Blair, G. N. 1974, ApJL, 192, L33

Thompson, A. R., Moran, J. M., & Swenson, G. W., Jr. 2001, "Interferometry and synthesis in radio astronomy by A. Richard Thompson, James M. Moran, and George W. Swenson, Jr. 2nd ed. New York

Tout, C. A., & Regos, E. 2003, 3D Stellar Evolution, 293, 100

Trumpler, R. J., & Weaver, H. F. 1953, Statistical astronomy, Dover Books on Astronomy and Space Topics, New York: Dover Publications

Tuomi, M., Kotiranta, S., & Kaasalainen, M. 2009, A&A, 494, 769

van de Kamp, P. 1960, JRASC, 54, 275

van de Kamp, P. 1967, Principles of Astrometry, W. H. Freeman and Company, San Francisco and London, p. 41

van Leeuwen, F., Feast, M. W., Whitelock, P. A., & Yudin, B. (ESA) 1997, MNRAS, 287, 955

Vlemmings, W. H. T., van Langevelde, H. J., & Diamond, P. J. 2005, A&A, 434, 1029

Vlemmings, W. H. T., Ramstedt, S., O'Gorman, E., et al. 2015, A&A, 577, L4

Wallerstein, G., & Greenstein, J. L. 1980, PASP, 92, 275

Wallerstein, G. 1986, PASP, 98, 118

Warner, B. 1995, Cambridge Astrophysics Series, 28,

Webster, B. L., & Allen, D. A. 1975, MNRAS, 171, 171

Williams, J. P., Mann, R. K., Di Francesco, J., et al. 2014, ApJ, 796, 120

Willson, L. A., Garnavich, P., & Mattei, J. A. 1981, Information Bulletin on Variable Stars, 1961, 1

Winn, J. N., Albrecht, S., Johnson, J. A., et al. 2011, ApJL, 741, L1

Wittkowski, M., Boboltz, D. A., Ohnaka, K., Driebe, T., & Scholz, M. 2007, A&A, 470, 191

Wittkowski, M., Chiavassa, A., Freytag, B., et al. 2016, A&A, 587, A12

Whitelock, P., Marang, F., & Feast, M. 2000, MNRAS, 319, 728

Whitelock, P., & Feast, M. 2000, MNRAS, 319, 759

Whitelock, P. A., Feast, M. W., van Loon, J. T., & Zijlstra, A. A. 2003, MNRAS, 342, 86

Whitelock, P. A., Feast, M. W., & van Leeuwen, F. 2008, MNRAS, 386, 313

Yang, H.-J., Park, M.-G., Cho, S.-H., & Park, C. 2005, A&A, 435, 207

Yi, J., Booth, R. S., Conway, J. E., & Diamond, P. J. 2005, A&A, 432, 531

Yun, Y. J., & Park, Y.-S. 2012, A&A, 545, A136

Zhang, B., Reid, M. J., Menten, K. M., & Zheng, X. W. 2012, ApJ, 744, 23

Zhao-Geisler, R., Quirrenbach, A., Köhler, R., & Lopez, B. 2012, A&A, 545, A56

Zuckerman, B. 1979, ApJ, 230, 442

Appendix

A.1 Geometry of Keplerian orbit

Stars in binary system are affected by each other through gravitational interaction and they orbit around the common center of mass. The orbital motion of binary system can be described using Kepler's equation, which derives the position and velocity of a star as function of time. In a different way, orbital parameters, called "Keplerian elements", can more generally describe the geometry of the binary orbit. In this section, we describe the geometry of Keplerian orbit in the sky coordinate system using the "Keplerian elements".

Note that Keplerian orbit assumes that isolated systems are treated in an inertial coordinate system, and also that two bodies are spherical with uniform density, which allows us to treat them as a point mass (particle). Then, the force acting on the two bodies is only the gravitational attraction between them along the line joining the centers of the two bodies.

At first, we begin with necessary definitions and conventions to explain the geometry (Catanzarite et al. 2010):

1. Reference direction : Along the line of sight from the observer to the barycenter of the binary system. The radial motion (radial velocity) of the star is projected on the this direction.

2. Sky plane: The plane orthogonal to the reference direction containing the apparent orbit.

3. Orbit plane: The plane containing the true orbit.

4. Observational frame (reference frame): A Left-handed Cartesian coordinate system of $\boldsymbol{r} = (X, Y, Z)$ which XY plane correspond to the sky plane. The system is tangential to the celestial sphere.

5. $+X$: Direction along North corresponding to declination (Dec).

6. $+Y$: Direction along East corresponding to right ascension (RA).

7. $+Z$: Direction along the reference direction.

8. Line of nodes: The intersection between the sky plane and orbit plane
9. Ascending / Descending node: The point on the line of nodes at which the star crosses the sky plane moving away from the observer / approaching to the observer. The positive (maximum) radial velocity at the ascending node, and the negative (minimum) radial velocity at the descending node.
10. Periastron / Apastron: the closest / farthest position to the barycenter in the orbit plane.

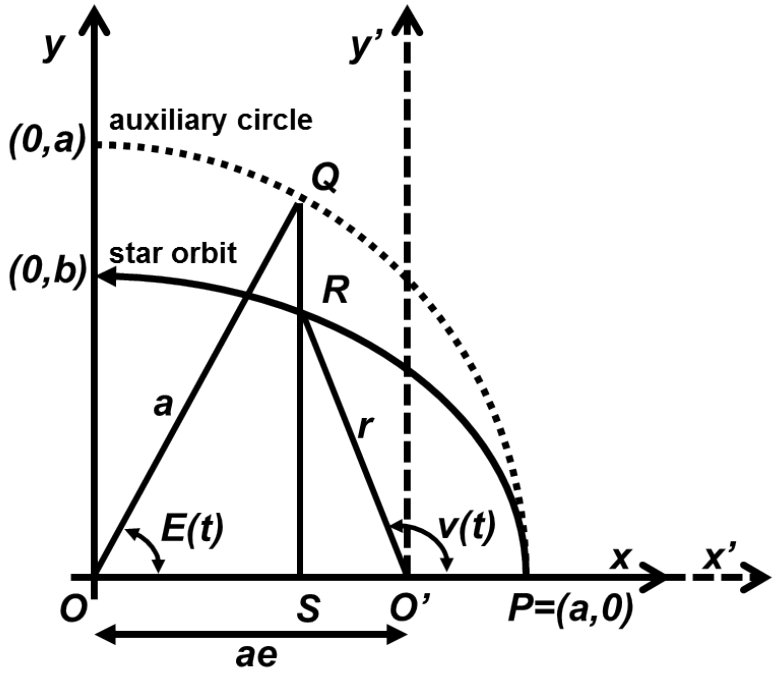

Figure A.1.1: Graphical representation for the Keplerian orbit of ellipse.

Starting out to describe the geometry of orbit with the general formula for an ellipse in Cartesian coordinate on the basis of Kepler's first law (which can be derived from two-body equation of motion).

$$\frac{x^2}{a^2} + \frac{y^2}{b^2} = 1 \tag{A.1.1}$$

where a is the *semi-major axis* and $b = a\sqrt{1-e^2}$ is the *semi-minor axis*, and e is the *eccentricity*. As seen in Figure A.1.1, if we assume that the right focus O' is the center of mass origin for the orbit, the true orbit of ellipse is expressed by a shifted coordination, as called *elliptical rectangular* coordinate, and polar coordinate as follows:

$$\begin{cases} x' = & x - ae = & a(\cos E - e) = & r\cos\nu \\ y' = & y = & a\sqrt{1-e^2}\sin E = & r\sin\nu \\ z' = & z = & 0 & \end{cases} \tag{A.1.2}$$

where the angle E is the *eccentric anomaly*, and ν is the *true anomaly* denoted in Figure A.1.1 respectively. The radial distance r also expressed through

$$r = \frac{a(1-e^2)}{1+e\cos\nu} = a(1-e\cos E) \tag{A.1.3}$$

Note that the relationship between the *eccentric anomaly* of E and *true anomaly* of ν is

$$\begin{aligned} \cos\nu &= \frac{\cos E - e}{1-e\cos E} \\ \sin\nu &= \sqrt{1-e^2}\frac{\sin E}{1-e\cos E} \\ \tan\frac{\nu}{2} &= \sqrt{\frac{1+e}{1-e}}\tan\frac{E}{2} \end{aligned} \tag{A.1.4}$$

Then, the motion of true orbit is described by *"Kepler's equation"* specifying the position angle of the star as a function of time as

$$E(t) - e\sin E(t) = M = \frac{2\pi}{P}(t-T_0) \tag{A.1.5}$$

where P is the *orbital period*, T_0 is the *periastron passage* of a specific epoch, and M is the *mean anomaly*, which is the angular distance from the *periastron passage*. The *mean anomaly* is determined directly from observations once the orbital period and the periastron passage have been determined. However, the equation can not be solved analytically, but should be solved numerically.

To describe the motion of the true orbit in the observational frame, three angle parameters are necessary to transform into new coordinate system of $\boldsymbol{r} = (X, Y, Z)$. A depiction of the true orbit from the perspective of the observer is presented in Figure A.1.2. Note that a sequence of rotations can be possibly selected in different ways, but a particular choice and order make the angles particular names and meanings using the following convention.

The true orbit has new coordinates rotating with the three Euler angles, termed of *the argument (longitude) of periastron* ω, *inclination* i, and *the longitude of the ascending node* Ω around the x-axis and z-axis. Rotation around the x and z-axis by an angle of ϕ can be described by the rotating matrix as

$$\mathbf{P}_x(\phi) = \begin{pmatrix} 1 & 0 & 0 \\ 0 & \cos\phi & -\sin\phi \\ 0 & \sin\phi & \cos\phi \end{pmatrix}$$

$$\mathbf{P}_z(\phi) = \begin{pmatrix} \cos\phi & -\sin\phi & 0 \\ \sin\phi & \cos\phi & 0 \\ 0 & 0 & 1 \end{pmatrix}$$

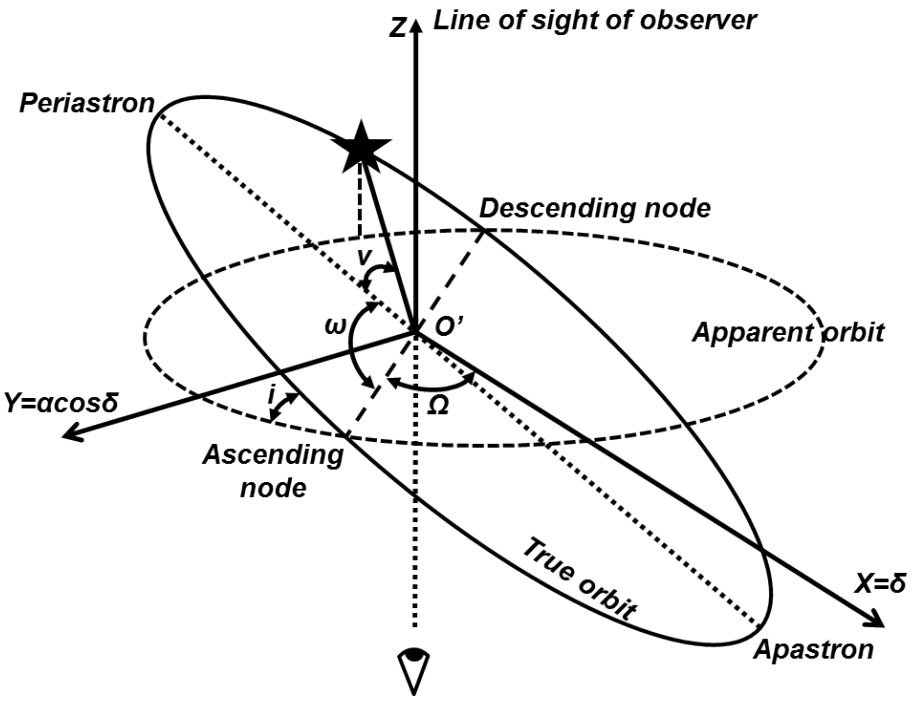

Figure A.1.2: Graphical representation for the Keplerian orbit of ellipse in the observational frame.

For describing the true orbit in observational frame coordinates, three rotations of ω, i, and Ω are carried out as follows:

$$\begin{pmatrix} X \\ Y \\ Z \end{pmatrix} = \mathbf{P}_z(\Omega)\mathbf{P}_x(i)\mathbf{P}_z(\omega) \begin{pmatrix} x' \\ y' \\ z' \end{pmatrix} = \mathbf{P} \begin{pmatrix} x' \\ y' \\ z' \end{pmatrix} \tag{A.1.6}$$

where $\mathbf{P}$ is explicitly

$$\mathbf{P} = \begin{pmatrix} \cos\omega\cos\Omega - \sin\omega\sin\Omega\cos i & -\sin\omega\cos\Omega - \cos\omega\sin\Omega\cos i & \sin\Omega\sin i \\ \cos\omega\sin\Omega + \sin\omega\cos\Omega\cos i & -\sin\omega\sin\Omega + \cos\omega\cos\Omega\cos i & -\cos\Omega\sin i \\ \sin\omega\sin i & \cos\omega\sin i & \cos i \end{pmatrix} \tag{A.1.7}$$

Note that the order of rotations are (1) rotation the true orbit of ellipse by ω about z-axis where the ascending node lies on the positive x-axis, (2) rotation (1) by i about x-axis in alignment with the reference direction, and (3) rotation the (2) by Ω about z-axis where x-axis correspond to the meridian direction to North.

For simply, we introduce the Thiele-Innes constants of A,B,C,F,G,H which are

related with the rotation matrix defined as:

$$\begin{aligned} A &= +\cos\omega\cos\Omega - \sin\omega\sin\Omega\cos i \\ B &= +\cos\omega\sin\Omega + \sin\omega\cos\Omega\cos i \\ C &= +\sin\omega\sin i \\ F &= -\sin\omega\cos\Omega - \cos\omega\sin\Omega\cos i \\ G &= -\sin\omega\sin\Omega + \cos\omega\cos\Omega\cos i \\ H &= +\cos\omega\sin i \end{aligned} \tag{A.1.8}$$

Then, the rotation matrix can be re-written as follows:

$$\mathbf{P} = \begin{pmatrix} A & F & \sin\Omega\sin i \\ B & G & -\cos\Omega\sin i \\ C & H & \cos i \end{pmatrix} \tag{A.1.9}$$

So, the motion of the Keplerian orbit (the position of the star with the Keplerian orbit) can be expressed in the observational frame as simply follows:

$$\begin{aligned} X &= Ax' + Fy' \\ Y &= Bx' + Gy' \\ Z &= Cx' + Hy' \end{aligned} \tag{A.1.10}$$

Therefore, the seven parameters called "Keplerian elements" for describing the geometry of the true orbit are :

a: Semi-major axis of true ellipse – specifying the size of orbit.

e: Eccentricity – specifying the shape of the ellipse.

i: Inclination – The angle between the sky plane and the orbit plane. The inclination is defined as positive when the star is moving away from us at the nodal point (measured at ascending node where orbit passes upward through the reference frame). Note that $i = 0°$ corresponds to a face-on, $i = 90°$ corresponds to a edge-on, clockwise orbit. $0° < i < 90°$ is direct, prograde motion (counter-clockwise; North to East), and $90° < i < 180°$ is retrograde (clockwise; North to west) motion.

Ω: The longitude of the ascending (approaching) node – The angle in the sky plane from the reference coordinate (e.g. north direction) to the ascending node.

ω: The argument (longitude) of periastron (the closest approach position) – the angle difference between the ascending node and the point of periastron measured in the orbit plane.

T_0: The epoch of periastron passage.

P: Orbital period; Alternatively mean motion of $n = 360/P$ or $\mu = 2\pi/P$ and orbital frequency of $f = 1/P$ can be used.

A.1.1 Radial Velocity model

In what follows, the radial velocity variation of star can be derived from the geometry of true orbit. The radial velocity is the projection of the stellar velocity along the reference direction of Z expressed by

$$V_{rad} = V_Z + V_0 \tag{A.1.11}$$

where V_0 is *the system velocity* of the binary system along the line of sight direction, and V_Z is the time derivative of Z direction of the motion of the true orbit of

$$V_Z = \frac{\partial Z}{\partial t} = C\frac{\partial x'}{\partial t} + H\frac{\partial y'}{\partial t} \tag{A.1.12}$$

We can evaluate the time derivatives of x' and y' with differentiating *"Kepler's equation"* of

$$\begin{aligned} \frac{\partial E}{\partial t} &= \frac{2\pi}{P}\frac{1}{1 - e\cos E} \\ \frac{\partial x'}{\partial t} &= -a\sin E\frac{\partial E}{\partial t} \\ \frac{\partial y'}{\partial t} &= a\sqrt{1-e^2}\frac{\partial E}{\partial t} \end{aligned} \tag{A.1.13}$$

So that, we can obtain the radial velocity model of the star of

$$V_{rad} = \frac{2\pi a\sin i}{P\sqrt{1-e^2}}\left(\frac{-\sqrt{1-e^2}\sin\omega\sin E + \cos\omega\cos E}{1 - e\cos E}\right) + V_0 \tag{A.1.14}$$

Applying the relation between the *eccentric anomaly* E and *true anomaly* ν, the radial velocity model can be generally expresses by

$$V_{rad} = K[\cos(\nu + \omega) + e\cos\omega] + V_0 \tag{A.1.15}$$

where K is the semi-amplitude of the radial velocity variation, expressed by

$$K = \frac{2\pi a\sin i}{P\sqrt{1-e^2}} \tag{A.1.16}$$

To describe radial velocity variation, the six parameters (*semi-major axis* a, *eccentricity* e, *inclination* i, *argument of periastron* ω, *the epoch of periastron passage*, and *orbital period* P as well as *system velocity* V_0) are necessary.

A.1.2 Astrometry model

Considering that astrometric positions of a single star are taken relative to the reference frame where the reference is the tracking center or a standard star, the time series of motion is a combination of two motions, proper motion and parallactic motion (parallax), and other spurious accelerations are rarely included. Then the motion of star can be expressed as follows (excluding spurious accelerations):

$$\begin{aligned} \Delta\alpha\cos\delta &= \alpha_0 + \mu_\alpha^*(t-t_0) + \pi P_\alpha \\ \Delta\delta &= \delta_0 + \mu_\delta(t-t_0) + \pi P_\delta \end{aligned} \tag{A.1.17}$$

where (α_0,δ_0) are *the initial(fiducial, nominal) positions* at t_0, (μ_α^*,μ_δ) are *the linear proper motions* for right ascension and declination respectively, π is the *parallax*, and (P_α, P_δ) are the parallax factors, which are sinusoidal functions of the parallactic ellipse for a certain time in right ascension and declination due to the motion of the Earth around the Sun. Parallax factors are computed as follows (Seidelmann 1992):

$$\begin{aligned} P_\alpha &= X_\odot \sin\alpha_\star - Y_\odot \cos\alpha_\star \\ P_\delta &= X_\odot \cos\alpha_\star \sin\delta_\star + Y_\odot \sin\alpha_\star \sin\delta_\star - Z_\odot \cos\delta_\star \end{aligned} \tag{A.1.18}$$

where $(X_\odot, Y_\odot, Z_\odot)$ are the Cartesian components in equatorial coordinates of the Earth relative to the barycenter of the solar system at the time of observation as available from NASA Jet Propulsion Laboratory Solar System ephimerides (e.g. JPL ephemeris DE405 or HORIZONS; linearly interpolating to find exact values corresponding to the time of the astrometric observations), and $(\alpha_\star, \delta_\star)$ are the position of the target (the nominal position - position of tracking center in this study) in right ascension and declination respectively.

Alternatively, the parallax factor can be derived by following formula (van de Kamp 1960, 1967)

$$\begin{aligned} P_\alpha &= \cos\varepsilon\cos\alpha_\star \sin\odot - \sin\alpha_\star\cos\odot \\ P_\delta &= (\sin\varepsilon\cos\delta_\star - \cos\varepsilon\sin\alpha_\star\sin\delta_\star)\sin\odot - \cos\alpha_\star\sin\delta_\star\cos\odot \end{aligned} \tag{A.1.19}$$

where $\varepsilon = 23°26'$ is the obliquity of the ecliptic, and $\odot$ is the Sun's true longitude.

In the case of binary system, the astrometric motion is also affected by binary motion around the center of mass. Therefore, the astrometry model for binary system can be finally described as follows:

$$\begin{aligned} X_{RA} = \Delta\alpha\cos\delta &= \alpha_0 + \mu_\alpha^*(t-t_0) + \pi P_\alpha + Q_\alpha \\ Y_{Dec} = \Delta\delta &= \delta_0 + \mu_\delta(t-t_0) + \pi P_\delta + Q_\delta \end{aligned} \tag{A.1.20}$$

where $(Q_\alpha, Q_\delta) = (Y, X) = (Bx' + Gy', Ax' + Fy')$ are the binary motion described in previous section.

For describing astrometric motion in the reference frame (photocentric or tracking center), the 12 parameters of *semi-major axis* a, *eccentricity* e, *inclination* i, *longitude of the ascending node* Ω, *argument of periastron* ω, *the epoch of periastron passage*, and *orbital period* P as well as *the initial(fiducial, nominal) positions* (α_0,δ_0), *the linear proper motions* (μ_α^*,μ_δ), and *parallax* π are necessary.

A.2 Bayesian Inference and Markov Chain Monte Carlo (MCMC) method

A wide range of astrophysical problems are amenable to a Bayesian analysis, and a method of Markov Chain Monte Carlo (MCMC) technique within the Bayesian analysis is a convenient and effective way for estimating the model parameters, model selections(comparisons) and prediction. This method has been successfully used for characterizing orbital parameters using radial velocity, transit and astrometry analysis (Ford 2005, 2006; Gregory 2005b, 2007a, 2007b; Eastman et al. 2012, references therein; Gazak et al. 2012, references therein; and others).

There are several advantages using the MCMC method compared with other methods (Ford 2005; Gregory 2005a).

One major advantage of the MCMC method is its efficiency. Traditional estimation methods, such as least-square methods, need a good initial value to get best-fit model parameters. In addition, it is necessary to repeat calculations for solving a complex and time-consuming nonlinear minimization problem. Especially, measurement for orbital parameters has been based on the use of nonlinear least square methods that typically require a good initial guess for the parameter values. There remains a problem to carry out several analyses with certain indications of a periodic signal obtained such as a periodogram. However, the MCMC method is capable of efficiently exploring all regions of parameter space without a good initial guess, and there is no need to carry out a separate search for an orbital period. Moreover, most techniques, that are less sensitive to local minima, are less efficient than the MCMC method for complex systems, which have a large number of free parameters. Calculating longer Markov chain is the relatively simple task and computationally more efficient than other techniques. In this sense, the MCMC method is particularly useful for high-dimensional parameter spaces. This advantage is particularly important for long-period and multi-component systems, where there are multiple free parameters that can be traded off against each other to obtain similarly good fits.

Another major advantage is that the MCMC method gives the full marginal posterior distributions, not just the maximum a posterior (MAP) values and a Gaussian approximation of their uncertainties, for each model parameter.By using the knowledge of the posterior distributions, we can assess reasonable model parameters and uncertainties, and directly obtain comprehensive information on any other derived quantities.

The other major advantage is flexibility. With the Bayesian approach to data analysis, we can incorporate prior knowledge, and obtain extensive posterior distributions about model parameters and derived quantities. The results can be updated to account for additional observations and alternative information by means of priors on a data and models. By using new information, either belief or experimental evidence, we can acquire more balanced results for a particular problem. For example, incorporating prior information can mitigate the effect of a small sample size. Importantly, the use of the prior evidence is achieved in a theoretically sound and principled way. Furthermore, a much broader variety of models can be applied, including those with multi-level structures, different measurement scales, and different testing items. Using

the MCMC method with the Bayesian approach, we can easily handle these complex model with its parameters.

In the following section, we introduce the Bayesian analysis with MCMC method to estimate orbital parameters and application to our observations of science interest.

A.2.1 Bayes theorem

A Bayesian inference interprets the concept of probability as a measure of belief in or a state of knowledge concerning a given hypothesis. As evidence accumulates, the degree of belief in a hypothesis should either increase or decrease. The Bayesian inference uses a numerical estimate of the degree of belief in a hypothesis before evidence has been observed (the prior probability) and calculates a numerical estimate of the degree of belief in the hypothesis after evidence has been observed (the posterior probability), sometimes repeatedly as new evidence becomes available.

In a Bayesian approach, the Bayesian inference can be derived from the basic algebra of the probability theory, and the Bayes' theorem can be expressed as

$$p(\theta, D) = p(D \mid \theta)p(\theta) = p(\theta \mid D)p(D)$$

$$p(\theta \mid D) = \frac{p(D \mid \theta)p(\theta)}{p(D)} \tag{A.2.1}$$

where θ is a set of model parameters, D is observational data, $p(\theta \mid D)$ is a posterior probability, $p(D \mid \theta)$ is called a likelihood representing the conditional probability of the observational data given the model parameters, $p(\theta)$ is a prior probability reflected the background knowledge of model parameters, and $p(D) = \int p(D \mid \theta)p(\theta)d\theta$ is a function as a normalizing constant.

This Bayesian inference has an advantage of quantifying rigorous uncertainties in the model parameters since all Bayesian inference are based on the posterior probability distributions. Moreover, a variety of information and observations are able to be included in the prior and the likelihood, thus the posterior distribution can be updated as a new knowledge called a Bayesian learning (or updating).

A.2.2 Metropolis-Hasting Markov Chain Monte Carlo method

For parameter estimation, the MCMC technique iteratively changes the parameter values until the likelihood is a global optimum. The term of Markov Chain implies that the current state of random variables during the iteration has a property that the past and future states are independent as shown in below equation.

$$p(X_{n+1} \mid X_1, X_2, ..., X_n) = p(X_{n+1} \mid X_n) \tag{A.2.2}$$

In the equation, X_n are the random variables, and $p(X_{n+1} \mid X_n)$ is the transition probability (or transition kernel) of obtaining X_{n+1} given from X_n, which is assumed to be time independent. Thus, in the Markov chain, the random variable at the next step depends only on the current step. The Markov Chain Monte Carlo method makes

use of Markov Chains to construct a stochastic process that samples a target density distribution.

There are several methods to construct the Markov chains; one of the methods is the Metropolis-Hasting algorithm(Metropolis et al. 1953; Hastings 1970), and summarized as below.

1. An initial set of model parameters, θ_0, is generated from the prior distribution.

2. A new set of parameters, θ_j, is generated from the proposal distribution, $q(\theta_i \mid \theta_j)$, at the i-th (current) set of parameters. In this step, the proposal distribution is usually a Gaussian(normal) distributions centered at θ_i. A uniform distribution is also available.

3. At the same time, a random variable, u, is selected in a uniform distribution of $[U(0,1)]$ (between 0 and 1).

4. Evaluate a Metropolis ratio of r that is written as:

$$r = \frac{p(\theta_j \mid D)q(\theta_i \mid \theta_j)}{p(\theta_i \mid D)q(\theta_j \mid \theta_i)} = \frac{p(D \mid \theta_j)p(\theta_j)q(\theta_i \mid \theta_j)}{p(D \mid \theta_i)p(\theta_i)q(\theta_j \mid \theta_i)} \tag{A.2.3}$$

5. The new proposal set of j-th parameters is accepted as a next chain of $i+1$ parameters if the ratio is $r \geq 1$, that the new proposal set produces a better state than current. Otherwise, the new proposal set is also accepted if r is grater than selected random variable u ($r \geq u$). When the ratio is $r < u$, the set of j-th parameters is rejected, and the current set is kept. This accept-rejection probability α is written as

$$\alpha(\theta_j \mid \theta_i) = \min[r, 1] \tag{A.2.4}$$

6. After updating the set of parameters, the series of steps of 2 - 5 are repeated as much as possible to construct the Markov chains.

The Gaussian proposal distribution of

$$q(\theta_i \mid \theta_j) = \frac{1}{\sqrt{2\pi\beta^2}} \exp\left\{-\frac{(\theta_i - \theta_j)^2}{2\beta^2}\right\} \tag{A.2.5}$$

are sampled from the area surrounding the current set of parameters, and the proposals is symmetric where $q(\theta_i \mid \theta_j) = q(\theta_j \mid \theta_i)$. Therefore, the Metropolis ratio is simplified as $r = p(D \mid \theta_j)/p(D \mid \theta_i)$ when the prior distribution is uniform for all the model parameters.

In the early stage of iterations, the Markov chains converge into a stationary parameter space with a significant probability independently regardless of what the initial set of parameters. That early period is called the "burn-in", which iterations are generally discarded as the posterior at the first 10-20% of the total iterations.

The acceptance rate, which the ratio of accepted chains to total chains, is a barometer of the quality of sampling processes. A proper rate is relevant to the step-size (β) of the proposal distributions. For the Gaussian proposal distribution, its variance determines the step-size and the acceptance rate. When the variance is large, the acceptance rate will decrease (with the large step-size). On the contrary, the acceptance rate will be increased when the variance is small (with the small step-size). In this case, it requires many samples to obtain an equilibrium set of samples. The variance can be adjusted during the chain iterations in order to determine the efficient acceptance rate. Technically, changing any one of the step sizes destroys the Markov property, so that we must discard the previous states in the Markov chain for inference, and a new chain must be begun (Ford 2006).

Based on empirical studies, Robert et al. (1997) recommend the acceptance rate to be about 25% for a high-dimensional model and to about 50% for a one or two-dimensional model (Ford 2005; Gregory 2005b).

A.2.3 Choice of prior

The prior refers to the knowledge, that is obtained earlier using different data or methods, about the parameters. For evaluating the posterior with a global likelihood, the choice of prior model is an important part of the Bayesian analysis with a significant effect on the result.

For the Bayesian analysis, any model parameters can be allocated to prior probability density in one of three forms:

1. fixed value
2. defined mathematic function
3. range combining with a specific functional form

When the prior knowledge for the model parameters does not exist, two priors are generally used: the **uniform prior** and the **Jeffreys prior**.

Uniform prior For a *location parameter*, which is either a positive or negative quantity depending on our choice of origin, we desire that the prior is invariant to a shift in location within the parameter space. This imply that

$$p(\theta)d\theta = p(\theta+\delta)d(\theta+\delta) = p(\theta+\delta)d(\theta) \tag{A.2.6}$$

where δ is a constant shift. This leads to the **uniform prior** of

$$p(\theta) = \text{constant} = \frac{H(\theta-\theta_{\min})H(\theta_{\max}-\theta)}{\theta_{\max}-\theta_{\min}} = \frac{1}{\theta_{\max}-\theta_{\min}} \tag{A.2.7}$$

where $\theta_{\min}$ and $\theta_{\max}$ are upper and lower prior boundary of the parameter, and $H(x)$ is the Heaviside step function. If parameter is bounded, it is suitable for model selection problems. Otherwise, the uniform prior is usable in parameter estimation problem.

Jeffreys prior For a *scale parameter*, which can always have a positive quantity in several decade irrespective of our choice of origin, we desire to assign equal prior per decade (scale invariance) along the parameter space by a factor of λ,

$$p(\theta)d\theta = p(\lambda\theta)d(\lambda\theta) = \lambda p(\lambda\theta)d(\theta) \tag{A.2.8}$$

which is solved by the **Jeffreys prior** of

$$p(\theta) = \frac{\text{constant}}{\theta} = \frac{H(\theta-\theta_{\min})H(\theta_{\max}-\theta)}{\theta \ln \frac{\theta_{\max}}{\theta_{\min}}} = \frac{1}{\theta \ln \frac{\theta_{\max}}{\theta_{\min}}} \tag{A.2.9}$$

The uniform prior would be inappropriate for the scale parameter, because of the fact that it would assign high probability in a higher decade of parameter space than a lower decade.

If the lower prior boundary is equal to zero, the denominator of Jeffreys prior can not be calculated. In this case, the **modified Jeffreys prior** is used as follows:

$$p(\theta) = \frac{H(\theta-\theta_{\min})H(\theta_{\max}-\theta)}{(\theta+\theta_0) \ln \frac{(\theta_{\max}+\theta_0)}{\theta_0}} = \frac{1}{(\theta+\theta_0) \ln \frac{(\theta_{\max}+\theta_0)}{\theta_0}} \tag{A.2.10}$$

where θ_0 is the *knee* of the prior that the prior is approximately uniform when $\theta \ll \theta_0$, and it approaches a Jeffreys prior when $\theta \gg \theta_0$.

A.2.4 Setting in this paper

First of all, some data did not have their measurement errors (or uncertainties), especially for radial velocity data. Also, the measured data perturbations can probably incorporate a variety of different and potentially unknown physical effects. To alleviate these problems, we introduce a nuisance parameter (extra noise parameter), s, for the data sets.

When we set the measured data value of d_i for i-th instant of time t_i, this measured data can be represented by the following equation (Gregory 2005),

$$d_i = f_{model,i} + e_i + e_0 \tag{A.2.11}$$

where $f_{model,i}$ is the true value by the model prediction, e_i is the known measurement error and e_0 is any real signal in the data, which cannot be explained by the model prediction (unknown noise term).

Generally, nature is more complicate than our understanding from explainable models. By including the extra noise terms, the positive noise value indicates a possible signal which is unexplainable effect in the data and model.

The extra noise terms can be the results of an undetected companion in a system (e.g. a third component in assumed binary system) in both radial velocity and astrometry. For the radial velocity, irregularities on the stellar surface cause intrinsic anomalies in the star's spectrum, such as "stellar jitter" effect. For the astrometry, the extra noise terms are remained due to a lack of detail understanding of a SiO maser region in a

stellar atmosphere. Unexpected perturbations, such as anisotropic pulsations, cause the variation in the stellar positions from the SiO maser distribution. Such effects are included in the extra noise parameters in this analysis.

In the absence of detailed knowledge of the effective noise distribution, other than that it has a finite variance, the maximum entropy principle tells us that a Gaussian distribution has maximum information-theoretic entropy, equivalent to minimum bias or prejudice with respect to the missing information. In addtion, the Gaussian distribution would be the most conservative choice (Kapur 1989; Gregory 2005). If we assume that the noise terms are uncorrelated and drawn from a Gaussian distribution with zero mean and variance of s, the expectation by the model of $f_{model,i}$ is unchanged. However, the distribution of residuals $d_i - f_{model,i}$ can be characterized by a Gaussian with a variance of $\sigma_i^2 + s^2$ (Ford 2006).

For the analysis, we expect to get a benefit from the nuisance parameter. Adopting the nuisance parameter in the model, the MCMC method can explore the parameter space more quickly when the Markov chain is started far from the best-fit solution (Ford 2006). In addition, the procedure of integrating out nuisance parameters is called *Marginalization*, and Marginalizing the nuisance parameter has the desirable effect of treating anything in the data, leading to the most conservative estimates of model parameters (Gregory 2011).

To estimate a proper characterization of model parameters with their uncertainties, we use here a Markov Chain (MCMC) method with Metropolis-Hastings algorithm. The orbital parameters describing three dimensional motion are $\theta_{\rm Orb} = (T_0,\ P,\ V_0,\ e,\ \omega,\ a_{Mira},\ i,\ \Omega,\ \alpha_0,\ \delta_0,\ \mu_\alpha^*,\ \mu_\delta,\ \pi)$, and the nuisance parameters are $\theta_{\rm s} = (s_{RA},\ s_{Dec},\ RV_{vis.off},\ s_{vis},\ s_{NIR},\ s_{SiO43},\ s_{SiO86},\ s_{N.SiO42},\ s_{N.SiO43},\ s_{M.SiO43},\ s_{M.SiO86})$ where $RV_{vis.off}$ is the additional radial velocity offset for visual data as correction (see Chapter 3.2.1). This parameter is systematic error, deterministic, but *a priori* unknown alteration. The whole parameters and its priors (the prior for each parameter is independent of the prior for any other parameter) adopted in this study is provided in Table A.2.1. For the extra noise parameters, we employed modified Jeffreys priors with a knee of s_0 = 1 km s^{-1} for radial velocities and 1 mas for astrometry.

Given collected N measurements with an independent Gaussian distribution of errors, the likelihood function $p(D \mid \theta) = \mathcal{L}$ is a product of N Gaussians defined as :

$$\mathcal{L} = \prod_i^N \frac{1}{\sqrt{2\pi(\sigma_i^2 + s^2)}} \exp\left(-\frac{(d_i - f_{model,i})^2}{2(\sigma_i^2 + s^2)}\right) \tag{A.2.12}$$

In this paper, we take the natural logarithm to both side of likelihood function (Log

Table A.2.1: Model parameters used in this study

Parameters	Symbol	Boundary	Prior Type
Periastron passage (yr)	T_0	[1950,1990]	Uniform
Orbital period (yr)	P	[0,40000]	Jeffreys
Systemic velocity (km s^{-1})	V_0	[-35,-15]	Uniform
Eccentricity	e	[0,1)	Uniform
Longitude of periastron (deg.)	ω	[0,360)	Uniform
Semi-major axis for Mira (AU)	a_{Mira}	[0,20]	Jeffreys
Inclination (deg.)	i	[0,180)	Uniform
Longitude of ascending node (deg.)	Ω	[0,360)	Uniform
Initial position in RA (mas)	α_0	[0,500]	Uniform
Initial position in Dec (mas)	δ_0	[-500,0]	Uniform
Proper motion in RA (mas yr^{-1})	μ^*_α	[-50,50]	Uniform
Proper motion in Dec (mas yr^{-1})	μ_δ	[-50,50]	Uniform
Parallax (mas)	π	[0, 10]	Jeffreys
Extra noise for Astrometry in RA (mas)	s_{RA}	[0,10]	mod. Jeffreys
Extra noise for Astrometry in Dec (mas)	s_{Dec}	[0,10]	mod. Jeffreys
RV offset for RV in visual (km s^{-1})	$RV_{vis.off}$	[-20,20]	Uniform
Extra noise for RV in visual (km s^{-1})	s_{vis}	[0,10]	mod. Jeffreys
Extra noise for RV in NIR (km s^{-1})	s_{NIR}	[0,10]	mod. Jeffreys
Extra noise for RV in SiO (v=1 J=1-0)[1] (km s^{-1})	s_{SiO43}	[0,10]	mod. Jeffreys
Extra noise for RV in SiO (v=1 J=2-1)[1] (km s^{-1})	s_{SiO86}	[0,10]	mod. Jeffreys
Extra noise for RV in SiO (v=2 J=1-0)[2] (km s^{-1})	$s_{N.SiO42}$	[0,10]	mod. Jeffreys
Extra noise for RV in SiO (v=1 J=1-0)[2] (km s^{-1})	$s_{N.SiO43}$	[0,10]	mod. Jeffreys
Extra noise for RV in SiO (v=1 J=1-0)[3] (km s^{-1})	$s_{M.SiO43}$	[0,10]	mod. Jeffreys
Extra noise for RV in SiO (v=1 J=2-1)[3] (km s^{-1})	$s_{M.SiO86}$	[0,10]	mod. Jeffreys

[1]SiO maser data for Gromadzki & Mikołajewska (2009)
[2]SiO maser data for Nobeyama observations
[3]SiO maser data for Mopra observations

Likelihood) for increasing computation speed. The Log Likelihood is expressed as:

$$\begin{aligned}\mathcal{LL} &= -\sum_i^{N_{RV}} \ln\sqrt{2\pi(\sigma_{RV,i}^2+s_{RV}^2)} - \frac{1}{2}\sum_i^{N_{RV}}\left[\frac{\Delta RV_i{}^2}{\sigma_{RV,i}^2+s_{RV}^2}\right] \\ &\quad -\sum_j^{N_{AST}}\left[\ln\sqrt{2\pi(\sigma_{RA,j}^2+s_{RA}^2)}+\ln\sqrt{2\pi(\sigma_{Dec,j}^2+s_{Dec}^2)}\right] \\ &\quad -\frac{1}{2}\sum_j^{N_{AST}}\left[\frac{\Delta RA_j{}^2}{\sigma_{RA,j}^2+s_{RA}^2}+\frac{\Delta Dec_j{}^2}{\sigma_{Dec,j}^2+s_{Dec}^2}\right] \end{aligned} \tag{A.2.13}$$

where N_{RV} and N_{AST} are the number of radial velocity and astrometry observations, $\sigma_{RV,i}$, $\sigma_{RA,j}$, $\sigma_{Dec,j}$ are the individual radial velocity and astrometry uncertainties, $\Delta RV_i = RV_i - RV_{model,i}$ is the difference between i-th radial velocity data and model-derived radial velocity value, $\Delta(RA_j, Dec_j) = (RA_j, Dec_j) - (RA_{model,j}, Dec_{model,j})$ are also the difference between measured i-th astrometric position and model-derived astrometry position in the RA(north) and Dec(east) direction, respectively.

Before the main MCMC process, a test chain is examined to determine an optimal step size (β) in the model parameters as a trial state. In order to ensure efficient convergence, we generate the test chain in accordance with the procedure outlined by Ford (2006). Through the procedure, a step size is periodically adjusted until the expected acceptance rate within a threshold (adopting 5% of the acceptance rate as the threshold; Ford 2005). For our main science chains, we follow the MCMC procedure described in Appendix A.2.2 with the previously determined step size.

A.3 Testing analysis for estimating orbital parameters with MCMC method

We developed the orbital parameter estimator using a MCMC technique based on a Bayesian inference. Even though our simulator is still early phases of development, we can acquire some initial result for applying other targets or sciences.

In this section, we provide independent analyses of orbital parameters with radial velocity and astrometry observations from the synthetic data and published data in order to validate the convergence, and performance of our program.

A.3.1 Application to mock data

First, we used simulated datasets of radial velocity and astrometric data to test the efficacy (convergence and accuracy) of the orbital parameters estimation derived by our analysis. For this simulation, we consider a similar situation with our observation, so that the radial velocity variation (motion on the line of sight) and the astrometric path (motion in the sky plane) of star comes from the one companion with respect to the photocenter (tracking center or reference position) following the models of Appendix A.1.1 and A.1.2.. Once radial velocity and astrometry was created, a Gaussian noise was added to each data point independently.

The Radial velocity data were made up of 40 points with 50-year time baseline, and the astrometry data were 20 points with 10-year time baseline.

The Gaussian noise with a center of 0 km s^{-1} and standard deviation of 0.5 km s^{-1} for radial velocities, and a center of 0 mas and standard deviation of 1.0 mas for astrometry data, for each RA and Dec separately, were added. The measurement uncertainties for a center of 0.5 km s^{-1} and standard deviation of 0.2 km s^{-1} for radial velocities, and a center of 1.0 mas and standard deviation of 0.2 mas for astrometry data, for each RA and Dec separately, were also included in the data set.

Figure A.3.1 shows the parameter posterior distributions, and Table A.3.1 shows the input parameters used to create the data set and the parameters estimated by our MCMC analysis for comparison. The estimated parameter values are the Maximum Likelihood Estimation (MLE) value and the median of the parameter probability distribution with 68% credible regions.

All the parameter values are in close agreement with the true values within credible intervals. The extra noise terms for the radial velocity and astrometry are closed to

the zero value, or less than the added noise ($s_{\rm RV} = 0.12$, $s_{\rm RA} = 0.03$ and $s_{\rm Dec} = 0.15$ respectively). This implies that the model estimated by the parameters is reasonable, and there is no additional signal in the present data set. From this test analysis, our analysis and result demonstrate potential and accuracy of orbital parameter estimation under ideal condition.

Table A.3.1: A comparison between input parameters of the mock data and parameters estimated with MCMC analysis.

Parameters	Input	Our analysis		
		Best value	Median	68% C.I.
Periastron passage (yr)	2000.0	2000.0	1999.9	[1999.2, 2000.6]
Orbital period (yr)	40.0	39.6	39.7	[39.3, 40.1]
Systemic velocity (km s^{-1})	-25.0	-25.0	-25.0	[-25.1, -24.9]
Eccentricity	0.30	0.32	0.32	[0.29, 0.35]
Longitude of periastron (deg.)	87.0	90.4	89.9	[83.5, 96.2]
Semi-major axis of a_1 (AU)	6.0	5.8	5.7	[5.5, 6.1]
Inclination (deg.)	72.0	81.5	83.4	[69.7, 98.3]
Longitude of ascending node (deg.)	90.0	88.7	88.0	[81.0, 94.4]
Initial position in RA (mas)	0.0	1.0	0.9	[-1.8, 3.6]
Initial position in Dec (mas)	0.0	2.2	2.3	[-3.8, 9.1]
Proper motion in RA (mas yr^{-1})	25.0	25.0	24.9	[24.6, 25.3]
Proper motion in Dec (mas yr^{-1})	-25.0	-25.7	-25.8	[-27.0, -24.7]
Parallax [mas]	4.50	4.6	4.5	[4.2, 4.8]
Extra noise for RA position (mas)	-	0.03	0.30	[0.08, 0.65]
Extra noise for Dec position (mas)	-	0.15	0.28	[0.08, 0.60]
Extra noise for RV (km s^{-1})	-	0.12	0.17	[0.05, 0.33]

A.3.2 Case study: HR7672 - Crepp et al. (2012)

To assure and convince our analysis for further confirmation, we carried out the orbital parameter estimation toward a real observed data which is already verified.

Among the candidates of observed data, HR7672 is adopted, because all the parameters (including nuisance parameters) can be examined. Some other targets of references did not report and introduce all parameters as those of result.

HR7672 (15 Sge, GI 779, HD190406) is a G0V type star having a companion directly imaged by Liu et al. (2002). Tracing radial velocity trend have been started since 1987, covering a 24-year time baseline for the primary star, HR7672A. The companion, HR7672B, has been imaged relative to the primary star, totally 6 epochs covering a 10-year time baseline. Crepp et al. (2012) found the orbital parameters using the MCMC method jointly analyzing the radial velocity and astrometry measurements. All the radial velocities and astrometry data with their measurement uncertainties are listed in Table 1 and Table 5 from Crepp et al. (2012).

Adopting all available data, the orbital parameters were estimated by the MCMC method as the same manner of Crepp et al. (2012). The 8 physical parameters (orbital period, eccentricity, inclination, longitude of periastron, longitude of ascending node,

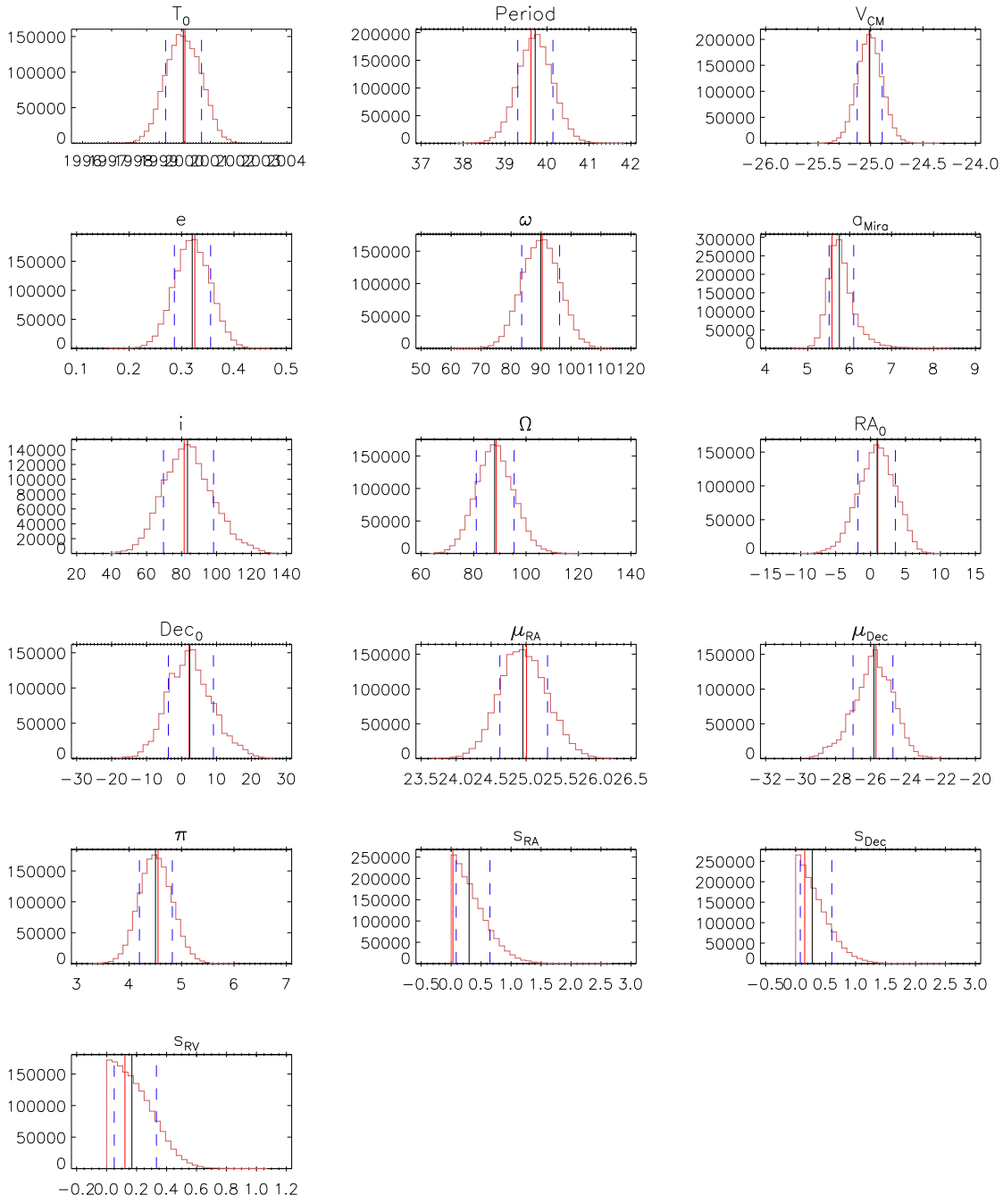

Figure A.3.1: The posterior probability distributions for the simulated data using our MCMC analysis. In each panels, the red solid lines indicate the best-fit values, the black lines indicate the median values, and the dashed lines indicate the range of 68% of confidence intervals of parameter distributions.

periastron passage, and companion mass) are used as variables, and the 13 parameters (6 RV instrument offsets and 7 RV jitter terms) are also included as nuisance parameters. Note that Crepp et al. probably included the system velocity parameters (V_0) for radial velocity model, but they did not introduce it in the MCMC analysis. Therefore, we also included the system velocity as the physical parameters to the analysis.

Specifically, we fixed the parallax of Hipparcos distance, $\pi = 56.28(\pm 0.35)$ mas, and primary mass of $1.08(\pm 0.04) M_{\odot}$ for the orbital parameters (If we took account of the parallax and primary mass as the parameters, the best-fit value is extremely changed. Therefore, Crepp et al. drew random parallax and mass values from a normal distribution centered on the each known values (the width also matched with measurement error), and combined with the MCMC chains.).

We ran the MCMC analysis for 10^7 samples with early 20% of burn-in, and acceptance rate of 25%. Uniform priors were defined for each parameter. The result of the best-fit parameter values with their confidence intervals (CI) are summarized in Table A.3.2, along with Crepp et al. (2012) for comparison.

Table A.3.2: Orbital parameters for HR7672

Parameters	Crepp et al. Values (68% CI)	Our analysis Best values (68% CI)
Periastron passage (yr)	2014.6 [2014.5–2014.7]	2014.5 [2014.1-2015.0]
Orbital period (yr)	73.3 [70.4-75.5]	79.7 [65.4-85.5]
Systemic velocity (km s^{-1})	(Unknown)	391.8 [345.9-404.8]
Eccentricity	0.50 [0.49–0.51]	0.52 [0.49-0.54]
Longitude of periastron (deg.)	259 [257–261]	256.1 [249.2-266.6]
HR7672B Mass (M_J)	68.7 [65.6-71.1]	71.4 [68.8-72.6]
Inclination (deg.)	97.3 [96.8–97.7]	97.3 [96.8-97.8]
Longitude of ascending node (deg.)	61.0 [60.6–61.3]	151.0 [150.6-151.3]
RV $\mathrm{Offset}_{6,\mathrm{Lick}}$ (m s^{-1})	0	0
RV $\mathrm{Offset}_{8,\mathrm{Lick}}$ (m s^{-1})	28.4 [21.5-33.9]	36.6 [22.2-43.2]
RV $\mathrm{Offset}_{18,\mathrm{Lick}}$ (m s^{-1})	38.8 [30.2-46.0]	45.4 [27.1-59.5]
RV $\mathrm{Offset}_{24,\mathrm{Lick}}$ (m s^{-1})	63.5 [52.1-72.9]	67.8 [50.0-82.5]
RV $\mathrm{Offset}_{39,\mathrm{Lick}}$ (m s^{-1})	46.9 [39.6-52.9]	53.4 [37.9-65.3]
RV $\mathrm{Offset}_{102,\mathrm{Keck}}$ (m s^{-1})	50.7 [42.6-57.5]	58.2 [39.6-70.9]
RV $\mathrm{Offset}_{130,\mathrm{Keck}}$ (m s^{-1})	65.0 [53.1-75.0]	67.0 [50.3-81.7]
RV $\mathrm{Jitter}_{6,\mathrm{Lick}}$ (m s^{-1})	24.3 [18.9-28.8]	19.0 [18.9-28.8]
RV $\mathrm{Jitter}_{8,\mathrm{Lick}}$ (m s^{-1})	9.8 [7.1-11.7]	9.4 [7.5-12.0]
RV $\mathrm{Jitter}_{18,\mathrm{Lick}}$ (m s^{-1})	8.5 [6.7-9.9]	7.7 [6.9-10.1]
RV $\mathrm{Jitter}_{24,\mathrm{Lick}}$ (m s^{-1})	9.2 [6.5-11.3]	7.0 [6.5-11.3]
RV $\mathrm{Jitter}_{39,\mathrm{Lick}}$ (m s^{-1})	9.3 [7.0-11.1]	8.0 [7.3-11.4]
RV $\mathrm{Jitter}_{102,\mathrm{Keck}}$ (m s^{-1})	7.1 [6.0-8.0]	6.7 [6.1-8.1]
RV $\mathrm{Jitter}_{130,\mathrm{Keck}}$ (m s^{-1})	5.6 [4.7-6.3]	5.1 [4.8-6.4]
Chi-square (χ^2)	-	168.54
Degree of freedom ($N_{obs.} - N_{par.}$)	-	160 (160)
Reduced chi-square $\sqrt{\chi^2_r}$	0.96	1.03 (1.03)

Our results are in good agreement with the orbital parameters found by Crepp et al. (2012) except the Longitude of ascending node Ω with exactly 90 degree difference.

This would come out when they define different geometric conventions of the reference coordinate of North and East direction and rotation angles in astrometry (described in Eq. A.1.6).

We find slightly larger secondary (HR7672B) mass and longer period parameters. These parameters are closely related to the radial velocity variation, and our radial velocity offsets differ from those in Crepp et al. (2012). However, our result shows also reliable orbital parameters comparing the chi-square value. The result of Crepp et al. (2012) was probably overestimated in the nuisance parameters of the RV jitter values which make the reduced chi-square below the unity. These RV jitter values are affected by the radial velocity analysis, and likely to be reflected to vary the orbital parameters.

Throughout our implementations from the MCMC analysis, we can show that our MCMC analysis is available to determine scientific interest, and can obtain a reasonable result.

A.4 Radial velocities in visual wavelength

In this study, the radial velocities have been adopted by several modifications to trace the true orbital motion of R Aqr. Especially, the data in visual wavelength are in special important for tracking a long period of orbital motion.

As we mentioned earlier in the text, it is necessary to correct the radial velocity in visual wavelength to trace the true orbital motion. The correction value have a range between -5 and -10 km s^{-1}. In order to specify the correction value for R Aqr, we took the original values of radial velocity in visual wavelength.

In the following table, we present the original values of radial velocities in visual wavelength from several works of literature. These values are averaged in 387 days, corresponding to the pulsation period of R Aqr, for determining orbital parameters in Chapter 3.3. The averaged values are also tabulated in Table 3.2.

Table A.4.1: Radial velocities for R Aqr in visual wavelength

Obs. JD	Obs. Date	Ori. RV	Aver. JD	Aver. RV	References
2422249.0	1919-10-17	-17.3			Merrill (1935)
2422251.0	1919-10-19	-16.3	2422254.7	-14.40	Merrill (1935)
2422264.0	1919-11-01	- 9.6			Merrill (1935)
2423039.0	1921-12-15	-14.8	2423039.0	-14.80	Merrill (1935)
2429542.0	1939-10-05	-24.0	2429581.0	-23.50	Merrill (1950)
2429620.0	1939-12-22	-23.0			Merrill (1950)
2430336.0	1941-12-07	-23.0	2430336.0	-23.00	Merrill (1950)
2432048.0	1946-08-15	-22.0	2432235.5	-21.60	Merrill (1950)
2432423.0	1947-08-25	-21.2			Merrill (1950)
2432779.0	1948-08-15	-21.5			Merrill (1950)
2433110.0	1949-07-12	-23.4	2433019.3	-21.87	Merrill (1950)
2433169.0	1949-09-09	-20.7			Merrill (1950)
2441237.0	1971-10-12	-14.63	2441237.0	-14.60	Jacobsen & Wallerstein (1975)
2444509.0	1980-09-26	-18.5	2444509.0	-18.50	Wallerstein (1986)
2444748.0	1981-05-23	-23.0	2444748.0	-23.00	Wallerstein (1986)
2445862.0	1984-06-10	-23.0	2445862.0	-23.00	Wallerstein (1986)

A.5 Radial velocities from single-dish observations

In this section, we present all the result of spectral analysis for deriving radial velocities from Mopra 22m and Nobeyama 45m telescope observations of SiO masers. The observational summary is described in Chapter 2.2, and the method is in Chapter 3.2.2. For determining orbital parameters, we excluded several epochs and averaged in 387 days of the stellar pulsation period. The averaged result is tabulated in Table 3.3, and more detail is also described in Chapter 3.2.2.

A.5.1 Mopra 22m observations

Table A.5.1: Radial Velocity of R Aqr from Mopra-22m

JD	Date	RV (km s$^-$1)	r.m.s (K)	V_{range} (km s$^-$1)	Spectral lines
2454941.5	2009-04-20	−23.894(0.246)	0.103	[−29.498, −17.787]	SiO (v=1, J=1−0)
2455109.9	2009-10-05	−22.816(0.374)	0.117	[−28.422, −16.710]	SiO (v=1, J=1−0)
2455215.8	2010-01-19	−22.815(0.308)	0.093	[−28.305, −12.376]	SiO (v=1, J=1−0)
2455271.5	2010-03-15	−23.126(0.275)	0.108	[−28.345, −16.868]	SiO (v=1, J=1−0)
2455299.7	2010-04-13	−23.290(0.272)	0.129	[−27.611, −17.774]	SiO (v=1, J=1−0)
2455363.4	2010-06-15	−23.417(0.255)	0.100	[−26.601, −17.233]	SiO (v=1, J=1−0)
2455399.4	2010-07-21	−23.265(0.304)	0.110	[−25.575, −17.846]	SiO (v=1, J=1−0)
2455433.2	2010-08-24	−23.366(0.262)	0.119	[−26.151, −18.655]	SiO (v=1, J=1−0)
2455491.0	2010-10-21	−22.551(0.366)	0.106	[−26.376, −16.069]	SiO (v=1, J=1−0)
2455573.8	2011-01-12	−22.971(0.388)	0.130	[−27.067, −16.760]	SiO (v=1, J=1−0)
2455687.5	2011-05-06	−22.649(0.491)	0.109	[−26.176, −17.745]	SiO (v=1, J=1−0)
2455757.2	2011-07-14	−21.523(0.483)	0.103	[−26.428, −17.763]	SiO (v=1, J=1−0)
2455789.2	2011-08-15	−20.972(0.452)	0.111	[−26.601, −17.701]	SiO (v=1, J=1−0)
2455847.1	2011-10-12	−21.317(0.433)	0.107	[−27.217, −16.910]	SiO (v=1, J=1−0)
2455867.0	2011-11-01	−21.479(0.415)	0.110	[−27.398, −16.388]	SiO (v=1, J=1−0)
2455897.8	2011-12-02	−21.654(0.435)	0.102	[−27.543, −16.767]	SiO (v=1, J=1−0)
2455991.5	2012-03-05	−22.115(0.282)	0.118	[−27.893, −15.713]	SiO (v=1, J=1−0)
2455991.6	2012-03-05	−22.184(0.281)	0.123	[−28.136, −15.956]	SiO (v=1, J=1−0)
2456019.5	2012-04-02	−22.127(0.221)	0.099	[−28.006, −15.826]	SiO (v=1, J=1−0)
2456234.0	2012-11-02	−21.929(0.238)	0.112	[−24.425, −15.992]	SiO (v=1, J=1−0)
2456414.4	2013-05-01	−20.120(0.259)	0.104	[−28.255, −13.734]	SiO (v=1, J=1−0)
2456518.2	2013-08-13	−18.987(0.206)	0.119	[−24.070, −15.170]	SiO (v=1, J=1−0)
2456594.0	2013-10-28	−18.621(0.206)	0.122	[−24.543, −14.705]	SiO (v=1, J=1−0)
2456750.5	2014-04-03	−20.271(0.330)	0.043	[−25.623, −14.849]	SiO (v=1, J=1−0)
2456776.5	2014-04-29	−20.396(0.353)	0.039	[−26.195, −14.719]	SiO (v=1, J=1−0)
JD	Date	RV (km s$^-$1)	r.m.s (K)	V_{range} (km s$^-$1)	Spectral lines
2454538.8	2008-03-13	−23.660(0.165)	0.543	[−26.328, −19.770]	SiO (v=1, J=2−1)
2454558.5	2008-04-02	−23.519(0.167)	0.239	[−26.462, −18.264]	SiO (v=1, J=2−1)
2454923.5	2009-04-02	−23.322(0.141)	0.333	[−27.794, −18.074]	SiO (v=1, J=2−1)
2454941.5	2009-04-20	−23.398(0.136)	0.247	[−27.897, −18.177]	SiO (v=1, J=2−1)
2455109.9	2009-10-05	−22.757(0.232)	0.271	[−27.969, −17.311]	SiO (v=1, J=2−1)
2455215.8	2010-01-19	−22.184(0.250)	0.196	[−27.607, −16.597]	SiO (v=1, J=2−1)
2455271.5	2010-03-16	−22.254(0.271)	0.264	[−26.526, −17.391]	SiO (v=1, J=2−1)
2455299.7	2010-04-13	−22.331(0.272)	0.238	[−26.816, −17.330]	SiO (v=1, J=2−1)
2455363.4	2010-06-15	−22.163(0.288)	0.222	[−26.507, −17.724]	SiO (v=1, J=2−1)
2455399.4	2010-07-21	−22.066(0.281)	0.207	[−26.442, −17.541]	SiO (v=1, J=2−1)
2455491.0	2010-10-21	−21.007(0.336)	0.282	[−24.211, −17.887]	SiO (v=1, J=2−1)
2455573.8	2011-01-12	−22.101(0.291)	0.412	[−24.886, −18.444]	SiO (v=1, J=2−1)
2455687.5	2011-05-06	−22.077(0.287)	0.184	[−25.521, −17.909]	SiO (v=1, J=2−1)
2455757.2	2011-07-14	−22.240(0.327)	0.144	[−24.729, −19.459]	SiO (v=1, J=2−1)
2455789.2	2011-08-15	−22.223(0.294)	0.168	[−24.884, −19.262]	SiO (v=1, J=2−1)
2455811.2	2011-09-06	−22.072(0.331)	0.210	[−24.385, −19.349]	SiO (v=1, J=2−1)
2455847.1	2011-10-12	−22.185(0.316)	0.184	[−25.035, −19.296]	SiO (v=1, J=2−1)
2455867.0	2011-11-01	−22.279(0.338)	0.218	[−25.096, −19.591]	SiO (v=1, J=2−1)
2455897.8	2011-12-02	−22.132(0.292)	0.188	[−25.014, −18.924]	SiO (v=1, J=2−1)

Radial Velocity of R Aqr from Mopra-22m (continued)

JD	Date	RV (km s$^-$1)	r.m.s (K)	V_{range} (km s$^-$1)	Spectral lines
2455991.6	2012-03-05	−22.048(0.291)	0.311	[−24.194, −19.626]	SiO (v=1, J=2−1)
2456019.5	2012-04-02	−21.685(0.245)	0.217	[−24.763, −18.439]	SiO (v=1, J=2−1)
2456234.0	2012-11-02	−21.580(0.222)	0.180	[−23.762, −17.554]	SiO (v=1, J=2−1)
2456414.4	2013-05-01	−20.731(0.559)	0.145	[−28.059, −15.060]	SiO (v=1, J=2−1)
2456518.2	2013-08-13	−17.532(0.199)	0.165	[−22.353, −14.858]	SiO (v=1, J=2−1)
2456750.5	2014-04-03	−19.791(0.207)	0.397	[−21.795, −16.642]	SiO (v=1, J=2−1)
2456776.5	2014-04-29	−19.875(0.181)	0.313	[−22.835, −16.629]	SiO (v=1, J=2−1)

A.5.2 Nobeyama 45m observations

Table A.5.2: Radial Velocity of R Aqr from Nobeyama-45m

JD	Date	RV (km s$^-$1)	r.m.s (K)	V_{range} (km s$^-$1)	Spectral lines
2453450.0	2005-03-20	−22.488(0.192)	0.119	[−25.681, −19.376]	SiO (v=1, J=1−0)
2453514.0	2005-05-23	−22.031(0.257)	0.124	[−25.300, −18.295]	SiO (v=1, J=1−0)
2454098.2	2006-12-28	−22.396(0.183)	0.146	[−27.726, −14.260]	SiO (v=1, J=1−0)
2454100.1	2006-12-30	−22.403(0.184)	0.110	[−27.725, −14.116]	SiO (v=1, J=1−0)
2454101.1	2006-12-31	−22.453(0.179)	0.132	[−27.868, −14.402]	SiO (v=1, J=1−0)
2454102.1	2007-01-01	−22.432(0.180)	0.111	[−27.867, −10.393]	SiO (v=1, J=1−0)
2454103.1	2007-01-02	−22.404(0.183)	0.120	[−27.724, −13.256]	SiO (v=1, J=1−0)
2454104.1	2007-01-03	−22.414(0.183)	0.108	[−27.582, −13.401]	SiO (v=1, J=1−0)
2454461.2	2007-12-26	−22.308(0.226)	0.148	[−30.406, −13.191]	SiO (v=1, J=1−0)
2454464.3	2007-12-29	−22.369(0.225)	0.262	[−30.548, −14.052]	SiO (v=1, J=1−0)
2454465.2	2007-12-30	−21.824(0.237)	0.294	[−27.886, −13.398]	SiO (v=1, J=1−0)
2454466.3	2007-12-31	−22.564(0.220)	0.296	[−30.383, −14.451]	SiO (v=1, J=1−0)
2454467.2	2008-01-01	−22.531(0.220)	0.147	[−31.370, +02.516]	SiO (v=1, J=1−0)
2454468.2	2008-01-02	−21.830(0.240)	0.103	[−30.483, −09.972]	SiO (v=1, J=1−0)
2454469.2	2008-01-03	−21.865(0.236)	0.206	[−29.909, −11.406]	SiO (v=1, J=1−0)
2454470.2	2008-01-04	−21.872(0.238)	0.146	[−30.052, −10.688]	SiO (v=1, J=1−0)
2454481.2	2008-01-15	−21.859(0.236)	0.272	[−29.721, −12.795]	SiO (v=1, J=1−0)
2454574.9	2008-04-18	−21.711(0.235)	0.126	[−28.534, −12.130]	SiO (v=1, J=1−0)
2454576.9	2008-04-20	−21.755(0.230)	0.104	[−28.949, −12.128]	SiO (v=1, J=1−0)
2454583.9	2008-04-27	−21.592(0.240)	0.100	[−28.664, −11.704]	SiO (v=1, J=1−0)
2454584.8	2008-04-28	−21.624(0.237)	0.064	[−28.941, −11.842]	SiO (v=1, J=1−0)
2454585.9	2008-04-29	−21.819(0.224)	0.078	[−29.497, −11.702]	SiO (v=1, J=1−0)
2454586.9	2008-04-30	−21.909(0.225)	0.134	[−29.079, −12.257]	SiO (v=1, J=1−0)
2454902.0	2009-03-11	−23.054(0.221)	0.078	[−29.613, −13.555]	SiO (v=1, J=1−0)
2454902.9	2009-03-12	−23.066(0.220)	0.051	[−29.898, −13.553]	SiO (v=1, J=1−0)
2454903.9	2009-03-13	−23.111(0.217)	0.061	[−29.324, −14.126]	SiO (v=1, J=1−0)
2454954.9	2009-05-03	−23.273(0.179)	0.083	[−29.425, −16.229]	SiO (v=1, J=1−0)
2454955.9	2009-05-04	−23.064(0.188)	0.092	[−29.281, −16.228]	SiO (v=1, J=1−0)
2454956.9	2009-05-05	−23.259(0.177)	0.089	[−29.710, −16.658]	SiO (v=1, J=1−0)
2454957.9	2009-05-06	−23.253(0.178)	0.209	[−28.276, −17.231]	SiO (v=1, J=1−0)
2454958.8	2009-05-07	−23.315(0.176)	0.307	[−28.275, −17.517]	SiO (v=1, J=1−0)
2454981.9	2009-05-30	−23.233(0.170)	0.103	[−28.855, −16.809]	SiO (v=1, J=1−0)
2455190.1	2009-12-24	−21.895(0.294)	0.305	[−27.290, −15.550]	SiO (v=1, J=1−0)
2455208.1	2010-01-11	−22.137(0.242)	0.059	[−29.959, −11.597]	SiO (v=1, J=1−0)
2455258.9	2010-03-03	−22.402(0.219)	0.062	[−31.506, −11.567]	SiO (v=1, J=1−0)
2455282.8	2010-03-27	−22.626(0.218)	0.124	[−30.605, −15.854]	SiO (v=1, J=1−0)
2455283.8	2010-03-28	−22.689(0.208)	0.170	[−29.833, −16.060]	SiO (v=1, J=1−0)
2455287.9	2010-04-01	−22.531(0.233)	0.502	[−26.741, −16.715]	SiO (v=1, J=1−0)
2455320.8	2010-05-04	−22.786(0.197)	0.071	[−29.862, +03.147]	SiO (v=1, J=1−0)
2455321.8	2010-05-05	−22.782(0.197)	0.076	[−29.718, −15.089]	SiO (v=1, J=1−0)
2455322.9	2010-05-06	−22.742(0.203)	0.069	[−30.147, +02.717]	SiO (v=1, J=1−0)
2455331.9	2010-05-15	−22.774(0.197)	0.087	[−27.979, −15.357]	SiO (v=1, J=1−0)
2455332.9	2010-05-16	−22.789(0.194)	0.095	[−28.982, −15.501]	SiO (v=1, J=1−0)
2455338.8	2010-05-22	−22.806(0.196)	0.060	[−27.425, −15.664]	SiO (v=1, J=1−0)
2455339.8	2010-05-23	−23.469(0.202)	0.347	[−26.278, −17.672]	SiO (v=1, J=1−0)
2455341.8	2010-05-25	−22.860(0.191)	0.102	[−26.707, −16.236]	SiO (v=1, J=1−0)
2455342.8	2010-05-26	−22.850(0.192)	0.141	[−26.420, −16.236]	SiO (v=1, J=1−0)

Radial Velocity of R Aqr from Nobeyama-45m (continued)

JD	Date	RV (km s$^-$1)	r.m.s (K)	V_{range} (km s$^-$1)	Spectral lines
2455343.8	2010-05-27	−22.900(0.185)	0.149	[−26.563, −16.666]	SiO (v=1, J=1−0)
2455344.8	2010-05-28	−22.921(0.183)	0.110	[−26.563, −16.523]	SiO (v=1, J=1−0)
2455595.0	2011-02-02	−22.495(0.283)	0.083	[−28.666, −15.612]	SiO (v=1, J=1−0)
2455596.0	2011-02-03	−22.504(0.284)	0.083	[−28.665, −15.467]	SiO (v=1, J=1−0)
2455597.0	2011-02-04	−22.495(0.288)	0.101	[−28.520, −15.896]	SiO (v=1, J=1−0)
2455598.0	2011-02-05	−22.465(0.291)	0.108	[−28.949, −15.608]	SiO (v=1, J=1−0)
2455603.2	2011-02-10	−22.510(0.289)	0.124	[−29.096, −15.898]	SiO (v=1, J=1−0)
2455613.0	2011-02-20	−22.456(0.302)	0.119	[−28.651, −16.028]	SiO (v=1, J=1−0)
2455614.0	2011-02-21	−22.445(0.305)	0.098	[−29.367, −16.170]	SiO (v=1, J=1−0)
2455623.9	2011-03-03	−22.477(0.311)	0.132	[−28.749, −15.839]	SiO (v=1, J=1−0)
2455630.9	2011-03-10	−22.474(0.309)	0.131	[−28.529, −16.253]	SiO (v=1, J=1−0)
2455684.9	2011-05-03	−22.376(0.331)	0.130	[−29.480, −16.284]	SiO (v=1, J=1−0)
2455685.9	2011-05-04	−22.359(0.338)	0.159	[−28.906, −16.714]	SiO (v=1, J=1−0)
2455686.8	2011-05-05	−22.364(0.335)	0.058	[−29.192, −15.996]	SiO (v=1, J=1−0)
2455687.8	2011-05-06	−22.357(0.338)	0.166	[−28.761, −16.569]	SiO (v=1, J=1−0)
2455699.8	2011-05-18	−22.239(0.350)	0.092	[−28.750, −16.127]	SiO (v=1, J=1−0)
2455700.8	2011-05-19	−22.216(0.351)	0.092	[−28.892, −16.270]	SiO (v=1, J=1−0)
2455701.8	2011-05-20	−22.267(0.352)	0.105	[−28.892, −16.987]	SiO (v=1, J=1−0)
2455935.2	2012-01-08	−21.348(0.331)	0.257	[−29.882, −15.538]	SiO (v=1, J=1−0)
2456016.0	2012-03-29	−21.609(0.312)	0.222	[−27.560, −15.681]	SiO (v=1, J=1−0)
2456056.7	2012-05-09	−21.700(0.167)	0.275	[−27.238, −15.494]	SiO (v=1, J=1−0)
2456237.3	2012-11-05	−21.306(0.173)	0.126	[−27.457, −14.975]	SiO (v=1, J=1−0)
JD	Date	RV (km s$^-$1)	r.m.s (K)	V_{range} (km s$^-$1)	Spectral lines
2453450.0	2005-03-20	−22.364(0.233)	0.112	[−26.527, −17.644]	SiO (v=2, J=1−0)
2453514.0	2005-05-23	−21.859(0.239)	0.146	[−24.743, −18.823]	SiO (v=2, J=1−0)
2454098.2	2006-12-28	−22.304(0.219)	0.144	[−29.379, −12.471]	SiO (v=2, J=1−0)
2454099.2	2006-12-29	−22.304(0.221)	0.142	[−29.379, −12.185]	SiO (v=2, J=1−0)
2454100.1	2006-12-30	−22.326(0.219)	0.102	[−29.237, −12.329]	SiO (v=2, J=1−0)
2454101.1	2006-12-31	−22.341(0.217)	0.121	[−29.811, −11.041]	SiO (v=2, J=1−0)
2454102.1	2007-01-01	−22.336(0.215)	0.095	[−29.526, −10.755]	SiO (v=2, J=1−0)
2454103.1	2007-01-02	−22.335(0.216)	0.106	[−29.670, −11.472]	SiO (v=2, J=1−0)
2454104.1	2007-01-03	−22.348(0.216)	0.091	[−29.812, −12.188]	SiO (v=2, J=1−0)
2454461.2	2007-12-26	−22.124(0.243)	0.115	[−30.733, −12.378]	SiO (v=2, J=1−0)
2454464.3	2007-12-29	−22.126(0.246)	0.229	[−29.015, −13.384]	SiO (v=2, J=1−0)
2454465.2	2007-12-30	−21.817(0.260)	0.254	[−28.810, −12.904]	SiO (v=2, J=1−0)
2454466.3	2007-12-31	−22.176(0.243)	0.246	[−28.873, −13.098]	SiO (v=2, J=1−0)
2454467.2	2008-01-01	−22.140(0.243)	0.116	[−29.719, −12.654]	SiO (v=2, J=1−0)
2454468.2	2008-01-02	−21.658(0.273)	0.086	[−28.685, −02.898]	SiO (v=2, J=1−0)
2454469.2	2008-01-03	−21.796(0.268)	0.183	[−28.686, −12.637]	SiO (v=2, J=1−0)
2454470.2	2008-01-04	−21.789(0.271)	0.124	[−28.687, −12.208]	SiO (v=2, J=1−0)
2454481.2	2008-01-15	−21.776(0.269)	0.245	[−28.517, −12.613]	SiO (v=2, J=1−0)
2454574.9	2008-04-18	−21.073(0.205)	0.140	[−28.396, −11.774]	SiO (v=2, J=1−0)
2454576.9	2008-04-20	−20.975(0.198)	0.109	[−28.542, −11.777]	SiO (v=2, J=1−0)
2454583.9	2008-04-27	−21.156(0.204)	0.115	[−28.552, −11.787]	SiO (v=2, J=1−0)
2454584.8	2008-04-28	−21.122(0.197)	0.071	[−29.127, −11.645]	SiO (v=2, J=1−0)
2454585.9	2008-04-29	−21.351(0.198)	0.076	[−29.128, −11.503]	SiO (v=2, J=1−0)
2454586.9	2008-04-30	−21.562(0.232)	0.121	[−27.824, −12.193]	SiO (v=2, J=1−0)
2454902.0	2009-03-11	−23.919(0.177)	0.061	[−31.286, −17.379]	SiO (v=2, J=1−0)
2454902.9	2009-03-12	−23.920(0.175)	0.048	[−31.288, −17.381]	SiO (v=2, J=1−0)
2454903.9	2009-03-13	−24.007(0.181)	0.053	[−53.352, −17.383]	SiO (v=2, J=1−0)
2454954.9	2009-05-03	−23.960(0.166)	0.074	[−29.677, −20.216]	SiO (v=2, J=1−0)
2454955.9	2009-05-04	−23.771(0.174)	0.072	[−29.678, −18.067]	SiO (v=2, J=1−0)
2454956.9	2009-05-05	−23.967(0.169)	0.073	[−29.679, −19.645]	SiO (v=2, J=1−0)
2454957.9	2009-05-06	−23.718(0.176)	0.183	[−28.247, −20.507]	SiO (v=2, J=1−0)
2454958.8	2009-05-07	−23.714(0.183)	0.294	[−25.956, −20.939]	SiO (v=2, J=1−0)
2454981.9	2009-05-30	−23.684(0.180)	0.092	[−28.429, −20.687]	SiO (v=2, J=1−0)
2455190.1	2009-12-24	−23.043(0.162)	0.300	[−25.809, −18.358]	SiO (v=2, J=1−0)
2455208.1	2010-01-11	−23.492(0.159)	0.043	[−29.726, −16.822]	SiO (v=2, J=1−0)
2455258.9	2010-03-03	−23.647(0.158)	0.053	[−29.425, −17.813]	SiO (v=2, J=1−0)
2455282.8	2010-03-27	−23.510(0.149)	0.100	[−25.945, −19.489]	SiO (v=2, J=1−0)
2455283.8	2010-03-28	−23.509(0.151)	0.166	[−26.203, −19.600]	SiO (v=2, J=1−0)
2455287.9	2010-04-01	−23.575(0.149)	0.509	[−25.237, −20.934]	SiO (v=2, J=1−0)

Radial Velocity of R Aqr from Nobeyama-45m (continued)

JD	Date	RV (km s$^-$1)	r.m.s (K)	V_{range} (km s$^-$1)	Spectral lines
2455320.8	2010-05-04	−23.643(0.148)	0.060	[−29.403, −18.367]	SiO (v=2, J=1−0)
2455321.8	2010-05-05	−23.646(0.147)	0.072	[−29.261, −18.655]	SiO (v=2, J=1−0)
2455322.9	2010-05-06	−23.599(0.152)	0.066	[−29.262, +01.996]	SiO (v=2, J=1−0)
2455331.9	2010-05-15	−23.627(0.147)	0.072	[−29.116, −18.366]	SiO (v=2, J=1−0)
2455332.9	2010-05-16	−23.628(0.147)	0.080	[−28.973, −18.653]	SiO (v=2, J=1−0)
2455338.8	2010-05-22	−23.683(0.146)	0.049	[−29.145, −18.536]	SiO (v=2, J=1−0)
2455339.8	2010-05-23	−24.546(0.205)	0.283	[−53.212, −20.400]	SiO (v=2, J=1−0)
2455341.8	2010-05-25	−23.718(0.144)	0.089	[−29.146, −19.111]	SiO (v=2, J=1−0)
2455342.8	2010-05-26	−23.713(0.145)	0.115	[−29.147, −18.824]	SiO (v=2, J=1−0)
2455343.8	2010-05-27	−23.726(0.143)	0.121	[−29.004, −19.112]	SiO (v=2, J=1−0)
2455344.8	2010-05-28	−23.724(0.144)	0.087	[−29.004, −19.256]	SiO (v=2, J=1−0)
2455595.0	2011-02-02	−23.371(0.201)	0.063	[−28.747, −16.703]	SiO (v=2, J=1−0)
2455596.0	2011-02-03	−23.369(0.202)	0.079	[−28.892, −16.705]	SiO (v=2, J=1−0)
2455597.0	2011-02-04	−23.375(0.202)	0.105	[−28.750, −16.993]	SiO (v=2, J=1−0)
2455598.0	2011-02-05	−23.379(0.202)	0.106	[−28.752, −17.139]	SiO (v=2, J=1−0)
2455603.2	2011-02-10	−23.402(0.201)	0.112	[−28.768, −16.724]	SiO (v=2, J=1−0)
2455613.0	2011-02-20	−23.387(0.204)	0.110	[−28.932, −16.602]	SiO (v=2, J=1−0)
2455623.9	2011-03-03	−23.130(0.276)	0.143	[−25.587, −17.262]	SiO (v=2, J=1−0)
2455630.9	2011-03-10	−23.335(0.227)	0.125	[−28.878, −16.834]	SiO (v=2, J=1−0)
2455684.9	2011-05-03	−22.610(0.319)	0.125	[−28.549, −16.935]	SiO (v=2, J=1−0)
2455685.9	2011-05-04	−22.596(0.325)	0.167	[−28.550, −16.937]	SiO (v=2, J=1−0)
2455686.8	2011-05-05	−22.603(0.321)	0.055	[−29.268, −16.938]	SiO (v=2, J=1−0)
2455687.8	2011-05-06	−22.451(0.329)	0.180	[−28.553, −16.940]	SiO (v=2, J=1−0)
2455699.8	2011-05-18	−22.396(0.332)	0.088	[−28.848, −16.951]	SiO (v=2, J=1−0)
2455700.8	2011-05-19	−22.365(0.331)	0.081	[−28.849, −16.809]	SiO (v=2, J=1−0)
2455701.8	2011-05-20	−22.314(0.335)	0.095	[−28.706, −17.096]	SiO (v=2, J=1−0)
2455935.2	2012-01-08	−21.584(0.199)	0.248	[−27.060, −15.444]	SiO (v=2, J=1−0)
2455978.9	2012-02-21	−21.446(0.273)	0.370	[−26.148, −15.466]	SiO (v=2, J=1−0)
2455998.1	2012-03-11	−21.562(0.268)	0.171	[−27.469, −15.505]	SiO (v=2, J=1−0)
2456015.9	2012-03-29	−21.950(0.271)	0.138	[−27.808, −15.417]	SiO (v=2, J=1−0)
2456016.8	2012-03-30	−21.658(0.271)	0.146	[−27.082, −15.546]	SiO (v=2, J=1−0)
2456018.9	2012-04-01	−21.673(0.269)	0.099	[−27.513, −15.550]	SiO (v=2, J=1−0)
2456019.8	2012-04-02	−21.671(0.269)	0.125	[−27.515, −15.552]	SiO (v=2, J=1−0)
2456056.7	2012-05-09	−21.418(0.163)	0.447	[−24.549, −15.526]	SiO (v=2, J=1−0)
2456237.3	2012-11-05	−20.672(0.201)	0.129	[−26.810, −14.762]	SiO (v=2, J=1−0)
JD	Date	RV (km s$^-$1)	r.m.s (K)	V_{range} (km s$^-$1)	Spectral lines
2452360.9	2002-03-27	−27.203(0.083)	0.509	[−28.228, −26.351]	SiO (v=1, J=2−1)
2452397.8	2002-05-03	−27.668(0.128)	0.155	[−32.190, −19.956]	SiO (v=1, J=2−1)
2455257.9	2010-03-02	−21.760(0.130)	0.257	[−26.084, −17.251]	SiO (v=1, J=2−1)

A.6 List of SiO maser components from VERA observations

In this section, we tabulate several parameters of selected SiO maser components from VERA observations toward R Aqr. Each column shows (1) the Local Standard of Rest (LSR) velocity of the channel map in a unit of km s^{-1}, (2) the peak intensity of the SiO maser spot in a unit of Jy beam^{-1} and (3) the position offsets and errors in RA and Dec direction with respect to the delay-tracking center of $\alpha_{\rm J2000}$ = 23h43m49s.4616, $\delta_{\rm J2000}$ = −15°17'04".202 in units of mas.

The positions and errors are given by the result of the AIPS task SAD, which performs to fit two-dimensional elliptical Gaussian model to the image by least-squares algorithm. The evaluated error is determined from theory based on the rms (signal free) of the image. This error is a formal error ($\sigma_{\rm for}$) due to the thermal noise, which is dominated by a receiver.

Note that the true positional error is expected to be dominated by systematic errors, $\sigma_{\rm sys}$ caused by several factors, such as the uncalibrated tropospheric zenith delay (residual of the wet zenith excess path), the structure of maser component, and the accuracy of antenna position of each station, and so on. The mainly dominated systematic error is contributed by the tropospheric zenith delay as large as 100μas in phase referencing VERA observation. (Honma et al. 2008b; Nakagawa et al. 2008; Honma et al. 2010; Nagayama et al. 2015). Other factors is one order of magnitude smaller than other factors.

We need to evaluate the true positional error more detail, but the total positional error is roughly $\sigma_{\rm tot} = \sqrt{\sigma_{\rm for}^2 + \sigma_{\rm sys}^2} = 0.2$ mas, when $\sigma_{\rm for}$ is about 0.1 mas and $\sigma_{\rm sys}$ is about 0.2 mas.

The observed SiO maser components in R11298C (2011-10-25)

SiO (v=1 J=1−0)				SiO (v=2 J=1−0)			
$V_{\rm LSR}$ (km s^{-1})	I (Jy beam^{-1})	ΔRA (mas)	ΔDec (mas)	$V_{\rm LSR}$ (km s^{-1})	I (Jy beam^{-1})	ΔRA (mas)	ΔDec (mas)
−18.04	0.91	347.77(0.04)	−323.23(0.04)	−20.51	0.63	339.24(0.04)	−325.10(0.08)
−18.26	0.69	347.89(0.05)	−323.14(0.06)	−20.72	1.45	339.33(0.03)	−325.08(0.04)
−20.65	0.68	337.13(0.05)	−323.99(0.05)	−20.94	4.05	339.31(0.01)	−325.01(0.02)
−20.87	1.29	337.11(0.03)	−323.91(0.03)	−21.16	1.54	339.30(0.03)	−325.03(0.04)
−21.08	1.28	336.13(0.03)	−324.13(0.04)	−21.38	1.26	339.17(0.06)	−324.99(0.06)
−21.08	4.29	337.01(0.01)	−323.90(0.01)	−21.60	1.09	338.84(0.04)	−324.75(0.05)
−21.30	1.24	336.16(0.03)	−324.16(0.03)	−22.04	0.63	340.29(0.05)	−325.35(0.07)
−21.30	1.92	336.92(0.02)	−323.92(0.02)	−24.45	0.54	340.69(0.05)	−356.42(0.08)
−21.52	1.51	336.64(0.03)	−324.03(0.03)	−24.66	0.54	340.68(0.06)	−356.49(0.09)
−21.74	1.04	336.57(0.04)	−324.08(0.04)	−24.66	0.64	341.40(0.05)	−354.35(0.06)
−21.95	0.58	336.10(0.04)	−324.14(0.04)	−24.88	0.54	340.78(0.04)	−356.56(0.07)
−21.95	0.62	336.71(0.03)	−324.04(0.05)				
−25.65	0.59	342.08(0.07)	−353.76(0.06)				
−25.86	0.51	342.00(0.07)	−353.51(0.07)				

The observed SiO maser components in R12013A (2012-01-13)

SiO (v=1 J=1−0)				SiO (v=2 J=1−0)			
$V_{\rm LSR}$ (km s^{-1})	I (Jy beam^{-1})	ΔRA (mas)	ΔDec (mas)	$V_{\rm LSR}$ (km s^{-1})	I (Jy beam^{-1})	ΔRA (mas)	ΔDec (mas)
−15.43	0.53	332.83(0.03)	−340.46(0.06)	−17.22	0.56	330.67(0.04)	−340.97(0.07)

The observed SiO maser components in R12013A (2012-01-13) - (continued)

SiO (v=1 J=1−0)				SiO (v=2 J=1−0)			
$V_{\rm LSR}$ (km s^{-1})	I (Jy beam^{-1})	ΔRA (mas)	ΔDec (mas)	$V_{\rm LSR}$ (km s^{-1})	I (Jy beam^{-1})	ΔRA (mas)	ΔDec (mas)
−15.65	0.62	332.76(0.03)	−340.14(0.06)	−17.44	0.49	330.39(0.04)	−341.07(0.08)
−15.87	0.51	332.60(0.03)	−340.07(0.07)	−17.66	0.56	330.07(0.05)	−341.18(0.07)
−16.95	0.58	330.92(0.03)	−340.90(0.07)	−17.88	0.62	329.77(0.04)	−341.08(0.04)
−17.17	0.59	330.65(0.04)	−340.71(0.10)	−20.07	1.40	346.37(0.03)	−330.60(0.03)
−17.39	0.72	330.38(0.03)	−340.84(0.08)	−20.29	2.26	346.45(0.02)	−330.65(0.02)
−17.61	0.73	330.06(0.03)	−340.93(0.06)	−20.50	1.90	346.42(0.03)	−330.63(0.03)
−17.82	0.69	329.69(0.03)	−340.98(0.06)	−20.72	1.79	345.64(0.04)	−330.57(0.03)
−18.04	0.73	329.34(0.04)	−340.93(0.05)	−20.94	3.05	345.15(0.02)	−330.48(0.02)
−18.26	0.64	328.98(0.04)	−340.94(0.04)	−20.94	1.56	345.60(0.03)	−330.45(0.04)
−18.47	0.50	328.55(0.06)	−340.86(0.05)	−20.94	1.77	347.46(0.03)	−330.16(0.03)
−18.69	0.82	328.12(0.03)	−340.90(0.04)	−21.16	5.27	345.20(0.02)	−330.45(0.01)
−18.91	0.75	327.85(0.03)	−340.82(0.04)	−21.16	1.65	347.25(0.06)	−330.09(0.04)
−19.13	0.85	327.13(0.03)	−342.39(0.03)	−21.38	8.56	345.19(0.01)	−330.43(0.01)
−19.34	0.54	327.00(0.06)	−342.33(0.05)	−21.60	4.13	345.13(0.02)	−330.45(0.02)
−20.65	0.66	343.50(0.04)	−329.65(0.04)	−21.82	1.19	344.95(0.05)	−330.71(0.07)
−20.65	0.99	346.20(0.03)	−328.85(0.03)	−21.82	1.82	350.63(0.04)	−331.52(0.04)
−20.86	0.91	345.03(0.05)	−329.06(0.04)	−22.04	1.52	350.48(0.04)	−331.69(0.05)
−20.86	1.21	346.23(0.04)	−328.76(0.03)	−23.13	0.60	344.98(0.05)	−358.93(0.05)
−21.08	0.88	345.16(0.05)	−328.91(0.05)	−23.35	0.95	345.06(0.03)	−359.09(0.04)
−21.08	0.96	346.21(0.06)	−328.79(0.04)	−23.57	1.24	345.18(0.03)	−359.12(0.03)
−21.30	0.81	343.34(0.04)	−329.34(0.04)	−23.79	1.34	345.26(0.02)	−359.12(0.03)
−21.30	0.92	345.08(0.04)	−330.34(0.03)	−24.01	0.81	345.32(0.04)	−359.14(0.05)
−21.52	1.50	343.40(0.02)	−329.11(0.03)	−25.32	0.70	346.86(0.05)	−359.82(0.07)
−21.52	0.70	344.23(0.04)	−328.81(0.04)	−25.54	0.79	348.29(0.04)	−359.55(0.05)
−21.73	4.73	343.35(0.01)	−328.94(0.01)	−25.54	0.61	348.68(0.04)	−359.44(0.05)
−21.95	2.09	343.32(0.01)	−328.84(0.02)	−25.76	2.43	348.44(0.02)	−359.47(0.02)
−22.17	0.48	343.35(0.04)	−328.92(0.06)	−25.98	2.17	348.39(0.02)	−359.42(0.02)
−23.04	0.90	365.43(0.03)	−345.95(0.05)	−26.19	0.60	348.33(0.05)	−359.28(0.07)
−23.25	0.93	365.61(0.03)	−346.24(0.06)				
−23.47	1.25	365.79(0.02)	−346.46(0.03)				
−23.69	1.16	365.90(0.02)	−346.55(0.03)				
−23.91	0.48	365.92(0.05)	−346.57(0.06)				
−24.99	0.63	347.04(0.04)	−360.04(0.05)				
−25.21	0.96	347.06(0.03)	−359.95(0.04)				
−25.43	0.74	347.06(0.05)	−359.72(0.04)				
−25.43	0.90	348.52(0.04)	−359.56(0.04)				
−25.65	2.19	348.28(0.02)	−359.49(0.02)				
−25.86	2.39	348.20(0.02)	−359.35(0.02)				
−26.08	1.33	348.13(0.02)	−358.97(0.03)				
−26.30	1.04	348.13(0.03)	−358.48(0.03)				
−26.51	0.69	347.91(0.04)	−358.03(0.04)				
−26.73	0.80	347.67(0.03)	−357.69(0.03)				
−26.95	0.82	347.49(0.04)	−357.47(0.03)				
−27.17	0.69	347.29(0.03)	−357.34(0.05)				
−27.38	0.43	348.56(0.04)	−357.05(0.05)				

The observed SiO maser components in R12071A (20012-03-11)

SiO (v=1 J=1−0)				SiO (v=2 J=1−0)			
$V_{\rm LSR}$ (km s^{-1})	I (Jy beam^{-1})	ΔRA (mas)	ΔDec (mas)	$V_{\rm LSR}$ (km s^{-1})	I (Jy beam^{-1})	ΔRA (mas)	ΔDec (mas)
−15.21	0.34	339.77 (0.03)	−344.86(0.08)	−15.47	0.57	339.67 (0.03)	−343.48(0.07)
−15.65	0.51	339.53 (0.03)	−344.08(0.07)	−15.69	0.85	339.57 (0.02)	−343.48(0.05)
−15.87	0.72	339.30 (0.02)	−344.06(0.04)	−15.91	0.78	339.10 (0.02)	−343.90(0.04)
−16.08	0.58	339.08 (0.03)	−344.02(0.05)	−15.91	0.92	339.41 (0.01)	−343.34(0.04)
−16.30	0.49	338.83 (0.03)	−344.07(0.05)	−16.13	1.09	339.03 (0.02)	−343.64(0.04)
−16.52	0.37	338.48 (0.04)	−344.17(0.07)	−16.35	0.87	338.78 (0.02)	−343.69(0.04)
−16.74	0.40	338.16 (0.04)	−344.14(0.06)	−16.56	0.85	338.51 (0.02)	−343.82(0.05)
−16.95	0.61	337.40 (0.03)	−346.16(0.04)	−16.78	0.55	337.65 (0.03)	−346.06(0.04)
−16.95	0.35	337.88 (0.05)	−344.16(0.06)	−16.78	0.93	338.23 (0.02)	−343.97(0.04)
−17.17	0.68	337.19 (0.02)	−346.07(0.03)	−17.00	0.99	337.55 (0.02)	−345.95(0.03)

The observed SiO maser components in R12071A (20012-03-11) - (continued)

SiO (v=1 J=1−0)				SiO (v=2 J=1−0)			
$V_{\rm LSR}$ (km s^{-1})	I (Jy beam^{-1})	ΔRA (mas)	ΔDec (mas)	$V_{\rm LSR}$ (km s^{-1})	I (Jy beam^{-1})	ΔRA (mas)	ΔDec (mas)
−17.17	0.42	337.50 (0.04)	−344.05(0.05)	−17.00	0.64	337.97 (0.03)	−343.86(0.08)
−17.39	0.43	336.86 (0.04)	−345.98(0.05)	−17.22	0.97	337.40 (0.02)	−345.93(0.03)
−17.39	0.63	337.08 (0.03)	−344.29(0.04)	−17.22	0.70	337.65 (0.03)	−344.00(0.05)
−17.60	0.39	335.27 (0.04)	−344.61(0.04)	−17.44	0.83	337.40 (0.02)	−344.03(0.04)
−17.60	0.52	335.81 (0.04)	−347.75(0.03)	−17.66	0.86	337.07 (0.02)	−344.24(0.04)
−17.60	0.77	336.76 (0.02)	−344.40(0.03)	−17.88	0.48	336.51 (0.02)	−345.97(0.04)
−17.82	0.55	335.61 (0.04)	−347.81(0.04)	−17.88	0.70	336.82 (0.03)	−344.22(0.03)
−17.82	0.45	336.28 (0.05)	−350.73(0.04)	−18.10	0.44	336.25 (0.04)	−344.22(0.05)
−17.82	0.84	336.45 (0.02)	−344.35(0.03)	−18.31	0.42	335.92 (0.05)	−344.18(0.06)
−18.04	0.38	335.36 (0.05)	−348.01(0.05)	−19.85	0.53	354.53 (0.03)	−333.10(0.06)
−18.04	0.54	336.01 (0.03)	−350.75(0.05)	−20.06	2.29	354.53 (0.01)	−333.21(0.02)
−18.04	0.84	336.08 (0.02)	−344.36(0.03)	−20.28	4.60	354.54 (0.01)	−333.28(0.02)
−18.26	0.75	335.72 (0.02)	−344.30(0.03)	−20.28	1.50	355.16 (0.02)	−335.38(0.03)
−18.47	0.71	335.41 (0.02)	−344.30(0.04)	−20.28	2.35	355.84 (0.02)	−333.57(0.02)
−18.69	0.55	335.12 (0.03)	−344.18(0.04)	−20.28	1.30	356.13 (0.03)	−336.71(0.03)
−18.91	0.33	334.81 (0.05)	−344.19(0.07)	−20.28	1.45	356.34 (0.03)	−331.75(0.03)
−19.34	0.48	364.86 (0.04)	−330.86(0.04)	−20.50	3.27	353.60 (0.02)	−332.20(0.04)
−19.56	0.33	365.11 (0.05)	−330.72(0.06)	−20.50	3.29	353.93 (0.02)	−335.06(0.04)
−19.99	0.85	354.44 (0.02)	−333.49(0.03)	−20.50	5.02	354.53 (0.01)	−333.33(0.02)
−20.21	1.99	354.37 (0.01)	−333.52(0.02)	−20.50	2.99	355.08 (0.02)	−331.70(0.04)
−20.43	2.48	354.26 (0.01)	−333.43(0.01)	−20.50	7.79	355.86 (0.01)	−333.41(0.02)
−20.65	1.76	354.21 (0.02)	−333.39(0.02)	−20.72	3.32	354.54 (0.02)	−333.35(0.02)
−20.65	1.14	355.62 (0.02)	−333.24(0.03)	−20.72	11.96	355.81 (0.00)	−333.40(0.01)
−20.86	1.25	353.96 (0.02)	−333.35(0.03)	−20.94	14.51	355.78 (0.01)	−333.39(0.01)
−20.86	1.98	355.33 (0.02)	−333.21(0.02)	−20.94	2.06	364.01 (0.03)	−338.24(0.05)
−20.86	0.93	360.34 (0.03)	−334.25(0.05)	−21.16	10.44	355.71 (0.01)	−333.38(0.01)
−21.08	3.22	355.28 (0.01)	−333.13(0.02)	−21.38	5.73	355.63 (0.02)	−333.29(0.02)
−21.08	1.30	360.32 (0.03)	−334.43(0.06)	−21.38	2.08	360.65 (0.03)	−334.91(0.04)
−21.30	3.48	355.26 (0.01)	−333.03(0.01)	−21.38	2.62	364.20 (0.02)	−338.60(0.03)
−21.30	2.01	360.32 (0.01)	−335.56(0.02)	−21.60	2.48	355.56 (0.03)	−333.00(0.04)
−21.30	2.45	360.40 (0.02)	−334.79(0.02)	−21.60	2.36	357.26 (0.04)	−334.00(0.04)
−21.51	2.14	355.25 (0.02)	−332.93(0.03)	−21.60	3.72	360.47 (0.03)	−335.16(0.04)
−21.51	4.80	360.37 (0.01)	−335.35(0.01)	−21.60	4.52	364.31 (0.02)	−338.50(0.03)
−21.73	7.36	360.32 (0.01)	−335.43(0.01)	−21.82	4.23	357.08 (0.02)	−334.04(0.02)
−21.95	4.23	360.26 (0.01)	−335.47(0.01)	−21.82	5.20	360.42 (0.02)	−335.25(0.02)
−22.17	2.22	360.19 (0.02)	−335.50(0.02)	−21.82	2.01	361.17 (0.03)	−335.16(0.05)
−22.17	1.09	361.32 (0.02)	−335.59(0.03)	−21.82	5.09	364.35 (0.02)	−338.49(0.02)
−22.38	0.80	359.99 (0.03)	−335.51(0.05)	−22.03	3.95	357.08 (0.02)	−334.11(0.02)
−22.38	0.58	361.50 (0.07)	−336.29(0.12)	−22.03	3.88	360.27 (0.01)	−335.33(0.02)
−22.38	1.67	361.66 (0.02)	−335.62(0.03)	−22.03	3.38	361.18 (0.02)	−335.36(0.02)
−22.60	1.61	361.65 (0.02)	−335.74(0.04)	−22.03	3.04	364.37 (0.02)	−338.55(0.02)
−22.82	0.76	359.45 (0.02)	−336.50(0.04)	−22.25	2.08	357.20 (0.02)	−334.18(0.02)
−22.82	0.88	361.72 (0.02)	−335.75(0.04)	−22.25	2.08	360.15 (0.02)	−335.42(0.03)
−22.82	0.52	372.75 (0.04)	−349.17(0.05)	−22.25	2.94	361.08 (0.01)	−335.43(0.01)
−23.04	0.45	357.42 (0.04)	−368.64(0.05)	−22.25	3.17	361.58 (0.01)	−335.51(0.02)
−23.04	1.12	359.43 (0.01)	−336.55(0.02)	−22.25	1.10	362.19 (0.02)	−335.29(0.06)
−23.04	0.54	372.88 (0.04)	−349.20(0.04)	−22.25	5.23	362.77 (0.01)	−337.84(0.01)
−23.25	0.40	357.54 (0.04)	−368.72(0.06)	−22.47	1.81	360.82 (0.02)	−338.80(0.04)
−23.25	0.68	359.40 (0.03)	−336.51(0.04)	−22.47	2.10	361.68 (0.03)	−335.48(0.03)
−23.47	0.97	358.59 (0.02)	−335.91(0.04)	−22.47	8.14	362.71 (0.01)	−337.96(0.01)
−23.69	2.53	358.46 (0.01)	−335.78(0.02)	−22.69	2.91	359.68 (0.02)	−336.34(0.04)
−23.90	4.05	358.41 (0.01)	−335.78(0.02)	−22.69	10.76	362.65 (0.01)	−338.06(0.01)
−24.12	3.39	358.35 (0.01)	−335.80(0.01)	−22.91	4.76	359.62 (0.01)	−336.48(0.02)
−24.34	2.01	358.23 (0.01)	−335.86(0.02)	−22.91	10.82	362.57 (0.01)	−338.18(0.01)
−24.56	1.09	358.13 (0.01)	−335.92(0.02)	−23.13	3.84	359.57 (0.01)	−336.55(0.02)
−24.77	0.39	353.99 (0.04)	−363.52(0.04)	−23.13	7.92	362.48 (0.01)	−338.36(0.01)
−24.77	0.31	358.15 (0.03)	−335.77(0.06)	−23.35	1.18	359.49 (0.03)	−336.55(0.05)
−25.21	0.96	355.62 (0.02)	−363.05(0.03)	−23.35	5.63	362.41 (0.01)	−338.56(0.01)
−25.43	1.42	355.60 (0.02)	−362.93(0.02)	−23.57	1.37	357.57 (0.01)	−335.85(0.03)
−25.64	0.95	355.58 (0.02)	−362.75(0.03)	−23.57	0.75	358.76 (0.02)	−336.00(0.04)
−25.86	0.63	355.74 (0.03)	−362.15(0.04)	−23.57	1.95	362.37 (0.01)	−338.66(0.02)
−26.08	0.95	355.64 (0.02)	−361.92(0.02)	−23.78	1.18	357.56 (0.01)	−335.86(0.02)
−26.29	1.14	355.47 (0.02)	−361.66(0.02)	−23.78	1.33	358.76 (0.01)	−336.01(0.03)

The observed SiO maser components in R12071A (20012-03-11) - (continued)

SiO (v=1 J=1−0)				SiO (v=2 J=1−0)			
$V_{\rm LSR}$ (km s^{-1})	I (Jy beam^{-1})	ΔRA (mas)	ΔDec (mas)	$V_{\rm LSR}$ (km s^{-1})	I (Jy beam^{-1})	ΔRA (mas)	ΔDec (mas)
−26.51	0.77	355.30 (0.03)	−361.37(0.04)	−24.00	1.20	358.67 (0.02)	−335.82(0.03)
−26.73	0.77	355.23 (0.03)	−360.95(0.03)	−24.22	0.54	356.32 (0.03)	−365.19(0.05)
−26.95	0.77	355.32 (0.03)	−360.75(0.03)	−24.22	0.93	358.37 (0.02)	−335.69(0.03)
−26.95	0.46	356.20 (0.03)	−360.65(0.05)	−24.44	0.85	356.28 (0.02)	−365.16(0.03)
−27.16	0.76	355.18 (0.02)	−360.61(0.03)	−24.44	0.93	358.28 (0.02)	−335.71(0.03)
−27.16	1.29	356.09 (0.02)	−360.40(0.02)	−24.66	0.90	356.31 (0.02)	−365.21(0.03)
−27.38	0.96	356.09 (0.02)	−360.32(0.02)	−24.66	0.42	358.26 (0.04)	−335.72(0.05)
				−24.88	0.43	356.16 (0.04)	−365.23(0.06)
				−25.32	0.76	355.82 (0.02)	−362.79(0.04)
				−25.53	1.20	355.82 (0.02)	−362.76(0.02)
				−25.75	0.60	355.84 (0.03)	−362.64(0.04)
				−26.19	0.42	355.84 (0.05)	−361.62(0.05)
				−26.41	0.42	355.56 (0.05)	−361.47(0.06)
				−27.07	0.38	356.44 (0.04)	−360.38(0.05)
				−27.29	0.86	356.35 (0.02)	−360.20(0.03)
				−27.50	0.45	356.29 (0.04)	−360.10(0.06)

The observed SiO maser components in R12110B (2012-04-19)

SiO (v=1 J=1−0)				SiO (v=2 J=1−0)			
$V_{\rm LSR}$ (km s^{-1})	I (Jy beam^{-1})	ΔRA (mas)	ΔDec (mas)	$V_{\rm LSR}$ (km s^{-1})	I (Jy beam^{-1})	ΔRA (mas)	ΔDec (mas)
−15.43	0.47	345.58 (0.03)	−347.11(0.05)	−15.47	0.73	345.54 (0.02)	−346.21(0.06)
−15.65	0.90	345.43 (0.02)	−346.99(0.03)	−15.47	0.46	354.41 (0.03)	−359.00(0.05)
−15.87	0.90	345.26 (0.02)	−347.04(0.03)	−15.69	1.15	345.36 (0.01)	−346.13(0.04)
−16.08	0.69	344.99 (0.03)	−346.99(0.04)	−15.69	0.51	354.24 (0.03)	−358.99(0.04)
−16.30	0.66	344.76 (0.03)	−347.01(0.04)	−15.91	0.92	345.18 (0.02)	−346.28(0.05)
−16.52	0.56	344.44 (0.03)	−347.02(0.04)	−15.91	0.43	345.33 (0.03)	−345.62(0.05)
−16.74	0.52	344.26 (0.04)	−347.06(0.05)	−16.13	0.77	344.94 (0.03)	−346.20(0.06)
−17.39	0.55	342.27 (0.03)	−355.22(0.04)	−16.35	0.80	344.58 (0.03)	−346.52(0.05)
−17.39	0.75	342.96 (0.02)	−347.19(0.03)	−16.56	0.95	344.37 (0.02)	−346.45(0.04)
−17.60	0.60	342.10 (0.04)	−355.28(0.05)	−16.78	0.60	344.07 (0.03)	−346.53(0.06)
−17.60	0.99	342.68 (0.02)	−347.14(0.03)	−17.00	0.48	343.73 (0.04)	−346.69(0.06)
−17.60	0.53	342.93 (0.04)	−356.33(0.04)	−17.22	0.48	343.45 (0.04)	−346.82(0.06)
−17.82	0.68	341.42 (0.03)	−350.40(0.04)	−17.44	0.85	343.07 (0.02)	−346.96(0.03)
−17.82	0.94	342.33 (0.02)	−347.08(0.03)	−17.66	0.67	342.76 (0.03)	−347.02(0.06)
−17.82	0.51	342.66 (0.05)	−356.34(0.03)	−17.88	0.64	342.19 (0.02)	−347.76(0.04)
−17.82	0.53	343.20 (0.03)	−348.45(0.03)	−17.88	0.71	342.49 (0.02)	−346.85(0.04)
−18.04	0.81	341.05 (0.03)	−350.51(0.03)	−18.10	0.73	341.96 (0.03)	−347.65(0.04)
−18.04	0.80	341.75 (0.02)	−348.02(0.02)	−18.75	0.40	365.85 (0.04)	−341.97(0.07)
−18.04	0.98	341.98 (0.02)	−347.11(0.03)	−18.97	0.54	365.83 (0.03)	−341.92(0.06)
−18.26	0.45	340.81 (0.04)	−350.71(0.06)	−19.19	0.68	365.84 (0.03)	−341.88(0.04)
−18.26	0.94	341.45 (0.02)	−347.90(0.04)	−19.41	0.47	365.89 (0.05)	−341.82(0.07)
−18.47	0.67	341.09 (0.03)	−347.93(0.05)	−19.85	0.50	365.88 (0.04)	−362.14(0.08)
−18.91	0.57	340.86 (0.03)	−347.49(0.04)	−20.07	1.01	366.03 (0.02)	−362.42(0.03)
−19.34	0.63	371.15 (0.03)	−333.48(0.04)	−20.28	1.00	344.12 (0.02)	−341.15(0.03)
−19.56	0.43	371.39 (0.05)	−333.49(0.06)	−20.28	1.05	361.88 (0.02)	−336.18(0.03)
−20.21	0.61	359.88 (0.05)	−336.17(0.06)	−20.28	0.84	366.17 (0.03)	−362.57(0.04)
−20.21	0.66	361.90 (0.04)	−336.43(0.03)	−20.50	1.63	344.05 (0.02)	−341.16(0.03)
−20.43	1.01	359.76 (0.03)	−336.01(0.04)	−20.50	4.59	361.88 (0.01)	−336.16(0.01)
−20.43	2.64	361.77 (0.01)	−336.36(0.01)	−20.72	9.29	361.87 (0.01)	−336.16(0.01)
−20.43	0.65	362.71 (0.04)	−336.26(0.03)	−20.72	1.48	362.70 (0.03)	−336.12(0.04)
−20.65	1.06	359.63 (0.03)	−335.72(0.04)	−20.94	10.57	361.84 (0.01)	−336.13(0.01)
−20.65	4.91	361.69 (0.01)	−336.31(0.01)	−21.16	8.05	361.81 (0.01)	−336.05(0.01)
−20.65	1.16	362.39 (0.03)	−337.89(0.03)	−21.16	2.70	364.38 (0.03)	−337.33(0.04)
−20.86	6.02	361.65 (0.01)	−336.25(0.01)	−21.38	4.56	361.62 (0.02)	−335.87(0.02)
−20.86	1.78	364.12 (0.02)	−337.06(0.03)	−21.38	2.68	362.42 (0.03)	−335.96(0.04)
−21.08	5.23	361.58 (0.02)	−336.14(0.01)	−21.38	3.81	363.60 (0.03)	−336.43(0.03)
−21.08	2.09	364.09 (0.03)	−337.04(0.04)	−21.38	2.48	367.06 (0.02)	−337.11(0.03)
−21.08	3.49	366.43 (0.02)	−337.58(0.02)	−21.38	3.75	370.41 (0.02)	−341.04(0.02)
−21.30	4.04	361.44 (0.02)	−335.99(0.02)	−21.60	2.39	361.44 (0.03)	−335.61(0.03)

The observed SiO maser components in R12110B (2012-04-19) - (continued)

SiO (v=1 J=1−0)				SiO (v=2 J=1−0)			
$V_{\rm LSR}$ (km s^{-1})	I (Jy beam^{-1})	ΔRA (mas)	ΔDec (mas)	$V_{\rm LSR}$ (km s^{-1})	I (Jy beam^{-1})	ΔRA (mas)	ΔDec (mas)
−21.30	2.69	363.65 (0.03)	−336.57(0.04)	−21.60	5.22	363.43 (0.02)	−336.48(0.02)
−21.30	6.01	366.44 (0.01)	−337.66(0.01)	−21.60	5.55	367.13 (0.01)	−337.32(0.02)
−21.52	2.44	361.44 (0.03)	−335.85(0.03)	−21.60	6.30	370.45 (0.01)	−341.01(0.01)
−21.52	5.17	363.50 (0.01)	−336.52(0.02)	−21.82	6.68	362.88 (0.01)	−336.62(0.01)
−21.52	6.80	366.53 (0.01)	−337.73(0.01)	−21.82	2.88	363.56 (0.02)	−336.46(0.02)
−21.52	1.87	367.20 (0.02)	−337.42(0.04)	−21.82	5.05	367.23 (0.02)	−337.37(0.02)
−21.73	1.64	362.68 (0.03)	−336.83(0.04)	−21.82	7.10	370.46 (0.01)	−341.03(0.01)
−21.73	5.96	363.38 (0.01)	−336.53(0.01)	−22.03	9.80	362.76 (0.01)	−336.83(0.01)
−21.73	1.70	365.88 (0.03)	−340.36(0.04)	−22.03	2.96	367.45 (0.03)	−334.37(0.02)
−21.73	2.92	366.48 (0.02)	−337.94(0.03)	−22.03	5.29	370.44 (0.02)	−341.11(0.02)
−21.73	3.42	366.97 (0.03)	−337.73(0.03)	−22.25	7.69	362.68 (0.01)	−337.01(0.01)
−21.95	4.70	363.13 (0.02)	−336.60(0.02)	−22.25	3.49	366.65 (0.01)	−338.27(0.03)
−21.95	4.16	366.54 (0.01)	−338.26(0.02)	−22.25	2.95	370.35 (0.03)	−341.24(0.03)
−21.95	2.03	367.73 (0.04)	−334.53(0.02)	−22.47	3.46	362.61 (0.01)	−337.18(0.02)
−22.17	2.67	363.00 (0.03)	−336.69(0.03)	−22.47	2.72	366.67 (0.01)	−338.35(0.02)
−22.17	4.32	366.55 (0.01)	−338.40(0.02)	−22.47	2.52	367.52 (0.02)	−339.89(0.03)
−22.17	2.25	367.72 (0.03)	−334.62(0.02)	−22.47	2.18	367.66 (0.01)	−339.24(0.02)
−22.17	2.52	368.05 (0.03)	−337.95(0.03)	−22.47	2.77	368.31 (0.01)	−337.52(0.02)
−22.38	4.37	366.61 (0.01)	−338.40(0.01)	−22.47	1.59	368.63 (0.03)	−340.37(0.03)
−22.38	2.10	367.87 (0.02)	−338.16(0.04)	−22.47	2.00	370.40 (0.02)	−341.37(0.02)
−22.38	2.42	368.24 (0.02)	−337.87(0.02)	−22.69	2.03	366.69 (0.02)	−338.23(0.03)
−22.60	3.66	366.64 (0.01)	−338.45(0.01)	−22.69	1.77	367.36 (0.02)	−336.51(0.03)
−22.60	2.17	367.87 (0.01)	−338.34(0.02)	−22.69	1.94	368.28 (0.02)	−337.65(0.04)
−22.60	1.71	368.24 (0.02)	−337.73(0.03)	−22.69	5.76	368.51 (0.01)	−340.59(0.01)
−22.82	2.28	366.66 (0.01)	−338.54(0.02)	−22.69	1.83	371.22 (0.02)	−342.37(0.03)
−22.82	1.17	367.44 (0.03)	−339.90(0.04)	−22.91	10.08	368.44 (0.01)	−340.77(0.01)
−22.82	1.30	368.49 (0.02)	−340.86(0.03)	−22.91	2.05	370.55 (0.04)	−342.11(0.04)
−22.82	1.16	368.77 (0.03)	−335.99(0.03)	−23.13	12.44	368.40 (0.00)	−340.92(0.01)
−23.04	1.24	367.58 (0.02)	−340.03(0.04)	−23.13	3.15	370.52 (0.02)	−342.14(0.03)
−23.04	1.04	368.47 (0.03)	−340.82(0.03)	−23.35	14.16	368.37 (0.00)	−341.08(0.00)
−23.04	0.89	368.94 (0.03)	−342.29(0.03)	−23.35	1.43	370.39 (0.03)	−342.07(0.03)
−23.04	0.81	369.08 (0.04)	−345.41(0.03)	−23.57	8.23	368.35 (0.01)	−341.35(0.01)
−23.04	1.87	370.38 (0.02)	−342.15(0.02)	−23.57	1.88	369.32 (0.02)	−343.39(0.03)
−23.25	0.89	368.33 (0.02)	−341.09(0.05)	−23.79	5.82	368.30 (0.01)	−341.65(0.02)
−23.25	2.38	369.54 (0.01)	−343.66(0.01)	−23.79	1.77	368.61 (0.03)	−344.97(0.03)
−23.25	1.53	370.40 (0.02)	−342.26(0.02)	−23.79	3.79	369.21 (0.01)	−343.40(0.02)
−23.47	4.93	369.36 (0.01)	−343.64(0.01)	−23.79	1.88	369.76 (0.03)	−341.69(0.03)
−23.69	11.21	369.20 (0.00)	−343.61(0.00)	−23.79	2.22	370.16 (0.02)	−344.74(0.03)
−23.91	8.50	369.12 (0.00)	−343.62(0.01)	−24.00	2.16	368.26 (0.01)	−341.68(0.01)
−24.12	0.90	365.58 (0.03)	−370.37(0.03)	−24.00	2.53	369.12 (0.01)	−343.48(0.01)
−24.12	4.12	369.04 (0.01)	−343.67(0.01)	−24.22	0.59	365.49 (0.03)	−370.18(0.04)
−24.34	1.24	365.59 (0.02)	−370.36(0.02)	−24.22	0.75	368.98 (0.03)	−343.48(0.03)
−24.34	1.17	368.94 (0.02)	−343.78(0.02)	−24.44	0.97	365.57 (0.02)	−370.09(0.03)
−24.56	0.84	365.60 (0.03)	−370.31(0.03)	−24.66	0.47	365.66 (0.04)	−370.19(0.05)
−24.99	0.69	362.02 (0.03)	−365.82(0.03)	−26.85	0.77	362.09 (0.03)	−363.16(0.03)
−25.21	1.30	361.98 (0.02)	−365.83(0.02)	−27.07	1.45	362.16 (0.01)	−362.97(0.02)
−25.43	0.85	362.00 (0.03)	−365.78(0.03)	−27.29	1.15	362.18 (0.02)	−362.84(0.02)
−26.08	0.39	361.60 (0.07)	−364.62(0.06)				
−26.30	0.43	361.81 (0.06)	−364.30(0.05)				
−26.51	0.63	361.87 (0.04)	−363.92(0.04)				
−26.73	1.35	361.84 (0.01)	−363.67(0.02)				
−26.73	0.86	362.35 (0.02)	−363.55(0.04)				
−26.95	2.89	362.08 (0.01)	−363.36(0.01)				
−27.16	3.26	362.11 (0.01)	−363.22(0.01)				
−27.38	1.43	362.13 (0.01)	−363.08(0.02)				
−27.60	0.39	362.07 (0.05)	−362.84(0.06)				

The observed SiO maser components in R12145C (2012-05-24)

SiO (v=1 J=1−0)				SiO (v=2 J=1−0)			
$V_{\rm LSR}$ (km s^{-1})	I (Jy beam^{-1})	ΔRA (mas)	ΔDec (mas)	$V_{\rm LSR}$ (km s^{-1})	I (Jy beam^{-1})	ΔRA (mas)	ΔDec (mas)
−17.82	0.54	344.78 (0.04)	−353.13(0.05)	−19.63	0.55	369.63 (0.04)	−364.71(0.06)
−18.04	0.69	344.40 (0.03)	−353.15(0.04)	−19.85	0.77	369.75 (0.03)	−364.71(0.04)
−18.04	0.60	345.22 (0.03)	−351.00(0.04)	−20.07	0.73	369.88 (0.03)	−364.76(0.05)
−18.26	0.54	344.15 (0.04)	−353.14(0.06)	−20.50	0.64	365.99 (0.05)	−338.88(0.05)
−18.26	0.78	344.85 (0.03)	−350.82(0.03)	−20.72	1.01	365.83 (0.03)	−338.99(0.04)
−18.47	0.50	344.66 (0.05)	−350.78(0.05)	−20.72	1.18	366.17 (0.03)	−338.69(0.03)
−20.43	0.75	365.91 (0.03)	−339.07(0.04)	−20.72	1.29	367.70 (0.03)	−339.84(0.03)
−20.43	0.72	367.88 (0.04)	−340.01(0.05)	−20.72	1.23	368.20 (0.04)	−339.78(0.05)
−20.65	1.13	365.92 (0.03)	−338.97(0.03)	−20.72	1.04	376.67 (0.04)	−356.18(0.04)
−20.65	1.76	368.01 (0.02)	−339.97(0.02)	−20.94	1.40	366.10 (0.05)	−338.71(0.04)
−20.86	2.50	367.75 (0.02)	−339.89(0.02)	−20.94	2.16	367.78 (0.03)	−339.67(0.03)
−21.08	2.77	367.56 (0.02)	−339.81(0.02)	−20.94	1.39	376.87 (0.04)	−356.10(0.04)
−21.30	3.54	367.18 (0.01)	−339.35(0.02)	−21.16	2.41	366.79 (0.02)	−339.00(0.03)
−21.52	4.03	367.11 (0.01)	−339.25(0.02)	−21.16	1.66	367.36 (0.03)	−339.31(0.08)
−21.52	1.79	370.86 (0.03)	−340.37(0.04)	−21.16	1.45	377.01 (0.03)	−355.96(0.04)
−21.73	3.08	367.12 (0.01)	−339.23(0.02)	−21.38	4.49	367.07 (0.01)	−339.01(0.02)
−21.73	3.12	371.05 (0.02)	−340.51(0.02)	−21.60	8.26	367.12 (0.01)	−338.96(0.01)
−21.95	3.68	371.14 (0.01)	−340.58(0.02)	−21.82	3.61	367.18 (0.01)	−338.92(0.02)
−22.17	1.02	366.30 (0.03)	−339.81(0.04)	−21.82	1.62	371.25 (0.03)	−340.18(0.04)
−22.17	2.20	371.21 (0.02)	−340.57(0.02)	−22.03	1.33	367.27 (0.03)	−338.89(0.04)
−22.17	1.05	376.67 (0.03)	−348.77(0.04)	−22.03	1.69	371.26 (0.03)	−340.19(0.03)
−22.17	1.04	376.98 (0.03)	−348.57(0.05)	−22.47	1.68	366.08 (0.02)	−340.00(0.03)
−22.38	1.39	366.27 (0.02)	−340.03(0.03)	−22.69	2.01	366.05 (0.02)	−340.07(0.02)
−22.38	0.95	376.81 (0.04)	−348.66(0.04)	−22.91	1.10	366.01 (0.03)	−340.17(0.04)
−22.60	2.49	366.10 (0.01)	−340.15(0.02)	−22.91	1.19	372.17 (0.03)	−342.95(0.04)
−22.60	1.09	374.09 (0.04)	−344.27(0.03)	−22.91	1.65	373.89 (0.03)	−344.14(0.03)
−22.82	3.61	366.07 (0.01)	−340.23(0.01)	−23.13	1.82	372.25 (0.02)	−343.18(0.03)
−22.82	1.43	373.86 (0.03)	−344.41(0.03)	−23.13	1.44	373.83 (0.03)	−344.28(0.03)
−23.04	2.68	366.07 (0.01)	−340.29(0.02)	−23.35	2.30	372.29 (0.02)	−343.37(0.02)
−23.04	1.16	372.12 (0.03)	−343.21(0.03)	−23.35	1.16	373.99 (0.04)	−344.45(0.03)
−23.04	1.89	373.81 (0.02)	−344.52(0.02)	−23.57	1.79	372.13 (0.02)	−343.50(0.02)
−23.25	1.13	366.16 (0.02)	−340.40(0.03)	−23.57	1.52	373.21 (0.02)	−346.33(0.03)
−23.25	2.21	372.13 (0.01)	−343.36(0.02)	−23.78	2.16	373.08 (0.01)	−346.37(0.02)
−23.25	2.11	372.72 (0.01)	−343.27(0.02)	−24.00	2.05	372.90 (0.02)	−346.34(0.02)
−23.25	1.05	373.32 (0.03)	−343.15(0.03)	−24.22	1.18	372.78 (0.02)	−346.39(0.03)
−23.25	1.51	373.79 (0.02)	−344.64(0.02)				
−23.47	2.31	372.27 (0.02)	−343.44(0.02)				
−23.47	2.23	373.14 (0.02)	−346.45(0.02)				
−23.69	1.73	372.29 (0.03)	−343.44(0.02)				
−23.69	3.30	372.99 (0.01)	−346.49(0.01)				
−23.90	7.30	372.87 (0.01)	−346.48(0.01)				
−24.12	3.97	372.75 (0.01)	−346.48(0.01)				
−24.34	2.18	372.64 (0.01)	−346.50(0.02)				
−24.56	0.76	372.49 (0.03)	−346.60(0.03)				

The observed SiO maser components in R12204B (2012-07-22)

SiO (v=1 J=1−0)				SiO (v=2 J=1−0)			
$V_{\rm LSR}$ (km s^{-1})	I (Jy beam^{-1})	ΔRA (mas)	ΔDec (mas)	$V_{\rm LSR}$ (km s^{-1})	I (Jy beam^{-1})	ΔRA (mas)	ΔDec (mas)
−16.74	0.52	351.07 (0.05)	−356.32(0.07)	−17.66	0.91	350.20 (0.03)	−356.79(0.04)
−17.17	0.45	350.49 (0.06)	−356.51(0.08)	−17.88	1.10	349.97 (0.02)	−356.64(0.03)
−17.60	0.58	349.57 (0.05)	−356.52(0.09)	−18.10	0.89	349.67 (0.04)	−356.68(0.04)
−17.82	0.46	349.35 (0.06)	−356.42(0.07)	−18.10	0.74	373.84 (0.04)	−350.42(0.04)
−20.43	0.66	372.85 (0.06)	−345.60(0.07)	−18.31	1.44	373.88 (0.02)	−350.20(0.03)
−20.65	0.77	372.48 (0.06)	−344.97(0.06)	−18.53	2.94	374.11 (0.02)	−350.20(0.02)
−20.86	1.21	372.03 (0.04)	−344.67(0.04)	−18.75	3.60	374.16 (0.02)	−350.07(0.01)
−21.08	1.45	371.79 (0.03)	−344.50(0.04)	−18.97	2.60	373.97 (0.01)	−349.88(0.02)
−21.30	1.46	371.27 (0.02)	−344.42(0.03)	−18.97	3.06	374.68 (0.01)	−350.01(0.02)
−21.30	1.83	371.71 (0.02)	−344.24(0.04)	−19.19	1.42	374.08 (0.02)	−369.54(0.04)
−21.30	1.42	374.95 (0.03)	−344.96(0.04)	−19.19	2.95	374.74 (0.02)	−349.92(0.02)

The observed SiO maser components in R12204B (2012-07-22) - (continued)

SiO (v=1 J=1−0)				SiO (v=2 J=1−0)			
$V_{\rm LSR}$ (km s^{-1})	I (Jy beam^{-1})	ΔRA (mas)	ΔDec (mas)	$V_{\rm LSR}$ (km s^{-1})	I (Jy beam^{-1})	ΔRA (mas)	ΔDec (mas)
−21.52	1.83	371.45 (0.02)	−344.28(0.04)	−19.41	2.03	374.26 (0.02)	−369.68(0.03)
−21.52	2.17	375.10 (0.02)	−344.96(0.03)	−19.41	2.05	374.83 (0.03)	−349.92(0.03)
−21.73	2.03	375.00 (0.02)	−345.21(0.03)	−19.63	1.42	374.40 (0.03)	−349.44(0.03)
−21.73	1.91	375.25 (0.02)	−344.56(0.03)	−19.63	2.13	374.41 (0.02)	−369.89(0.03)
−21.95	0.96	374.84 (0.03)	−345.35(0.05)	−19.63	1.55	375.27 (0.02)	−350.44(0.03)
−21.95	1.50	375.22 (0.02)	−344.77(0.03)	−19.85	1.46	374.66 (0.03)	−370.19(0.04)
−21.95	1.65	382.43 (0.02)	−355.02(0.03)	−19.85	1.83	375.39 (0.02)	−350.47(0.03)
−22.17	2.41	377.60 (0.02)	−347.92(0.03)	−19.85	0.96	376.19 (0.03)	−351.40(0.04)
−22.17	1.31	382.46 (0.03)	−355.00(0.04)	−20.07	1.33	372.10 (0.04)	−346.86(0.05)
−22.38	3.76	377.60 (0.01)	−347.91(0.02)	−20.07	1.25	375.55 (0.03)	−350.31(0.04)
−22.60	7.08	377.53 (0.01)	−347.89(0.01)	−20.07	4.32	376.27 (0.01)	−351.45(0.02)
−22.82	3.35	377.41 (0.01)	−348.01(0.02)	−20.28	1.64	372.24 (0.04)	−346.87(0.05)
−23.04	3.14	377.32 (0.01)	−348.12(0.02)	−20.28	9.94	376.29 (0.00)	−351.42(0.01)
−23.25	2.09	377.25 (0.02)	−348.21(0.03)	−20.50	17.00	376.30 (0.00)	−351.40(0.00)
−23.47	0.83	376.73 (0.04)	−348.67(0.03)	−20.72	10.17	376.31 (0.01)	−351.38(0.01)
−23.47	0.89	376.99 (0.04)	−347.98(0.03)	−20.72	2.53	381.83 (0.04)	−362.31(0.03)
−23.69	1.22	376.56 (0.03)	−348.77(0.03)	−20.94	3.37	371.91 (0.03)	−345.75(0.03)
−23.69	0.88	376.76 (0.03)	−348.12(0.03)	−20.94	3.46	376.32 (0.03)	−351.36(0.05)
−23.90	1.30	376.50 (0.03)	−348.72(0.04)	−20.94	2.47	381.96 (0.03)	−362.28(0.04)
−24.12	0.69	376.27 (0.05)	−348.71(0.07)	−21.16	2.63	371.67 (0.03)	−345.53(0.04)
−24.12	2.04	377.97 (0.02)	−350.50(0.03)	−21.16	2.97	378.20 (0.02)	−349.78(0.03)
−24.34	1.31	377.86 (0.02)	−350.62(0.03)	−21.38	2.65	371.53 (0.02)	−345.25(0.04)
				−21.38	2.67	378.33 (0.02)	−349.64(0.03)
				−21.38	2.86	381.22 (0.03)	−352.24(0.02)
				−21.60	2.01	367.97 (0.02)	−344.27(0.03)
				−21.60	1.87	375.90 (0.02)	−344.87(0.04)
				−21.60	1.67	378.36 (0.03)	−349.45(0.03)
				−21.60	2.28	381.44 (0.03)	−352.16(0.03)
				−21.60	1.93	383.29 (0.03)	−355.99(0.04)
				−21.82	2.26	367.95 (0.02)	−344.37(0.03)
				−21.82	5.19	375.90 (0.01)	−344.93(0.01)
				−21.82	1.48	381.70 (0.04)	−352.08(0.04)
				−21.82	2.25	383.36 (0.02)	−355.85(0.03)
				−22.03	5.12	375.89 (0.01)	−344.92(0.01)
				−22.25	1.92	375.86 (0.02)	−344.82(0.03)
				−22.25	2.94	377.64 (0.01)	−349.21(0.02)
				−22.47	1.37	375.98 (0.03)	−347.60(0.04)
				−22.47	4.75	377.64 (0.01)	−349.15(0.02)
				−22.47	1.33	381.95 (0.05)	−357.81(0.03)
				−22.69	1.02	375.79 (0.03)	−347.73(0.03)
				−22.69	3.28	377.64 (0.01)	−349.08(0.02)
				−22.69	2.48	381.86 (0.02)	−357.81(0.02)
				−22.91	0.80	375.72 (0.04)	−348.04(0.05)
				−22.91	1.30	377.68 (0.02)	−348.98(0.03)
				−22.91	2.00	381.74 (0.02)	−357.80(0.02)
				−23.13	0.85	375.69 (0.04)	−348.26(0.08)
				−23.13	0.99	381.39 (0.04)	−357.62(0.04)
				−23.35	0.78	377.89 (0.04)	−352.57(0.06)
				−23.57	1.23	377.63 (0.02)	−352.56(0.03)
				−23.78	1.75	377.50 (0.01)	−352.48(0.02)
				−24.00	1.69	377.41 (0.02)	−352.48(0.03)
				−24.22	1.01	377.36 (0.02)	−352.37(0.04)

The observed SiO maser components in R13053A (2013-02-22)

SiO (v=1 J=1−0)				SiO (v=2 J=1−0)			
$V_{\rm LSR}$ (km s^{-1})	I (Jy beam^{-1})	ΔRA (mas)	ΔDec (mas)	$V_{\rm LSR}$ (km s^{-1})	I (Jy beam^{-1})	ΔRA (mas)	ΔDec (mas)
−13.69	0.59	386.37 (0.04)	−377.29(0.07)	−13.50	0.58	366.98 (0.03)	−378.23(0.05)
−13.91	0.50	386.51 (0.04)	−377.28(0.06)	−13.72	1.30	367.03 (0.02)	−378.37(0.03)
−14.13	0.84	366.43 (0.03)	−379.31(0.04)	−13.94	1.82	367.04 (0.01)	−378.50(0.02)

The observed SiO maser components in R13053A (2013-02-22) - (continued)

SiO (v=1 J=1−0)				SiO (v=2 J=1−0)			
$V_{\rm LSR}$ (km s^{-1})	I (Jy beam^{-1})	ΔRA (mas)	ΔDec (mas)	$V_{\rm LSR}$ (km s^{-1})	I (Jy beam^{-1})	ΔRA (mas)	ΔDec (mas)
−14.35	1.38	366.38 (0.02)	−379.48(0.04)	−13.94	0.71	368.68 (0.03)	−380.65(0.05)
−14.56	1.12	366.33 (0.02)	−379.60(0.05)	−14.16	2.02	367.09 (0.01)	−378.63(0.02)
−14.78	0.60	366.34 (0.05)	−379.81(0.12)	−14.16	1.04	368.63 (0.03)	−380.78(0.05)
−15.00	0.61	365.74 (0.04)	−379.36(0.07)	−14.38	1.75	367.11 (0.01)	−378.76(0.03)
−15.87	0.59	364.37 (0.05)	−379.40(0.06)	−14.38	0.81	368.66 (0.03)	−380.86(0.06)
−16.08	0.54	364.06 (0.06)	−379.33(0.07)	−14.60	0.81	367.08 (0.03)	−378.95(0.06)
−16.30	0.57	363.66 (0.06)	−379.61(0.08)	−14.60	0.55	368.49 (0.05)	−381.15(0.08)
−16.52	0.60	384.18 (0.04)	−387.82(0.07)	−14.81	0.68	381.62 (0.04)	−386.18(0.05)
−16.74	1.18	384.95 (0.02)	−386.39(0.06)	−15.03	0.52	367.25 (0.04)	−380.32(0.07)
−16.95	2.31	385.01 (0.01)	−386.71(0.03)	−15.03	0.64	381.73 (0.04)	−386.41(0.05)
−17.17	2.98	385.08 (0.02)	−386.82(0.03)	−15.25	0.72	381.82 (0.05)	−386.50(0.06)
−17.17	1.67	386.99 (0.04)	−388.48(0.03)	−15.47	0.57	381.90 (0.04)	−386.77(0.06)
−17.39	3.08	385.38 (0.03)	−387.27(0.03)	−15.47	0.70	384.26 (0.03)	−384.98(0.06)
−17.39	1.59	387.17 (0.04)	−388.62(0.05)	−15.69	0.86	384.35 (0.03)	−385.02(0.05)
−17.39	3.32	388.40 (0.03)	−383.24(0.02)	−15.91	1.42	384.61 (0.02)	−385.03(0.03)
−17.61	5.18	385.73 (0.02)	−387.52(0.02)	−16.13	2.61	384.76 (0.01)	−385.12(0.02)
−17.61	3.52	387.19 (0.03)	−388.48(0.03)	−16.13	1.21	386.32 (0.03)	−387.35(0.05)
−17.61	3.40	387.99 (0.03)	−378.77(0.03)	−16.35	4.42	384.89 (0.01)	−385.23(0.02)
−17.61	7.35	389.61 (0.02)	−381.05(0.02)	−16.35	1.59	386.46 (0.02)	−387.32(0.05)
−17.82	4.65	385.88 (0.02)	−387.60(0.03)	−16.56	5.56	385.00 (0.01)	−385.41(0.02)
−17.82	4.14	387.93 (0.02)	−378.98(0.03)	−16.78	6.22	385.13 (0.02)	−385.66(0.03)
−17.82	4.78	388.40 (0.02)	−378.53(0.03)	−17.00	6.06	385.20 (0.02)	−385.92(0.03)
−17.82	8.33	389.76 (0.02)	−380.99(0.02)	−17.00	4.60	387.95 (0.03)	−381.75(0.03)
−18.04	3.78	386.04 (0.03)	−387.75(0.05)	−17.22	6.31	385.27 (0.02)	−386.17(0.03)
−18.04	3.56	388.36 (0.05)	−378.75(0.06)	−17.22	3.92	386.80 (0.03)	−388.38(0.04)
−18.04	6.50	389.69 (0.01)	−381.26(0.02)	−17.22	6.36	388.09 (0.02)	−381.87(0.03)
−18.04	7.08	390.17 (0.01)	−380.79(0.02)	−17.44	5.91	385.38 (0.02)	−386.43(0.03)
−18.26	3.37	385.42 (0.03)	−389.72(0.04)	−17.44	3.63	386.93 (0.03)	−388.51(0.04)
−18.26	4.54	389.90 (0.02)	−381.50(0.02)	−17.44	5.89	388.30 (0.03)	−381.98(0.03)
−18.26	5.81	390.36 (0.01)	−380.84(0.02)	−17.66	6.04	385.48 (0.02)	−386.67(0.03)
−18.47	2.62	385.40 (0.04)	−389.71(0.04)	−17.66	5.77	389.40 (0.02)	−380.24(0.03)
−18.47	5.17	391.21 (0.01)	−379.44(0.02)	−17.88	5.14	385.62 (0.02)	−386.92(0.03)
−18.69	5.96	391.33 (0.01)	−379.52(0.02)	−17.88	7.00	389.59 (0.02)	−380.49(0.02)
−18.91	2.36	388.96 (0.03)	−385.87(0.04)	−18.10	2.95	385.78 (0.02)	−387.14(0.05)
−18.91	4.34	391.49 (0.02)	−379.48(0.02)	−18.10	6.26	389.85 (0.02)	−380.69(0.02)
−18.91	1.72	393.31 (0.06)	−381.14(0.08)	−18.32	2.17	388.26 (0.03)	−379.27(0.04)
−19.13	4.09	389.18 (0.02)	−385.99(0.03)	−18.32	4.64	390.13 (0.02)	−380.92(0.02)
−19.13	2.37	392.33 (0.04)	−379.70(0.05)	−18.32	2.25	391.79 (0.02)	−383.03(0.03)
−19.34	5.43	389.45 (0.02)	−386.18(0.02)	−18.32	2.13	392.44 (0.03)	−381.33(0.04)
−19.34	3.61	392.71 (0.02)	−379.80(0.05)	−18.53	7.07	391.09 (0.01)	−379.19(0.02)
−19.56	4.18	389.62 (0.02)	−386.21(0.03)	−18.53	3.53	392.05 (0.02)	−382.98(0.03)
−19.56	2.56	393.22 (0.06)	−380.02(0.06)	−18.53	2.83	392.70 (0.02)	−381.27(0.04)
−19.56	2.57	394.13 (0.03)	−375.03(0.05)	−18.75	9.06	391.22 (0.01)	−379.21(0.02)
−19.78	2.78	366.28 (0.02)	−364.32(0.04)	−18.75	4.03	392.20 (0.02)	−383.04(0.03)
−19.78	3.31	393.82 (0.04)	−380.13(0.03)	−18.75	3.76	392.81 (0.02)	−381.31(0.03)
−19.78	2.78	394.37 (0.02)	−374.73(0.04)	−18.97	7.41	391.34 (0.01)	−379.22(0.02)
−20.00	3.00	366.20 (0.03)	−364.22(0.04)	−18.97	5.33	392.53 (0.02)	−376.71(0.03)
−20.00	2.33	394.37 (0.04)	−374.06(0.07)	−19.19	9.42	392.71 (0.02)	−376.84(0.02)
−20.00	3.09	394.38 (0.04)	−380.54(0.06)	−19.41	13.60	393.01 (0.02)	−377.04(0.02)
−20.21	5.96	394.78 (0.03)	−380.64(0.03)	−19.63	10.65	393.23 (0.02)	−377.12(0.04)
−20.43	4.55	395.00 (0.02)	−380.75(0.02)	−19.85	6.28	394.19 (0.03)	−374.52(0.04)
−20.43	6.57	395.25 (0.02)	−374.27(0.02)	−20.07	3.98	393.73 (0.03)	−377.88(0.04)
−20.43	3.55	396.04 (0.04)	−377.35(0.04)	−20.07	4.94	394.42 (0.03)	−374.18(0.04)
−20.65	7.06	395.41 (0.01)	−374.28(0.02)	−20.29	4.62	394.53 (0.04)	−378.70(0.04)
−20.65	5.14	395.41 (0.03)	−380.83(0.02)	−20.50	7.38	394.57 (0.03)	−378.56(0.04)
−20.65	3.54	396.51 (0.03)	−377.37(0.02)	−20.50	5.81	395.24 (0.04)	−376.76(0.06)
−20.86	3.76	394.96 (0.03)	−373.20(0.02)	−20.50	5.34	395.54 (0.04)	−379.93(0.05)
−20.86	2.75	395.70 (0.03)	−373.52(0.05)	−20.50	5.65	396.15 (0.03)	−378.03(0.04)
−20.86	10.35	396.24 (0.01)	−379.06(0.01)	−20.72	4.75	393.72 (0.03)	−370.49(0.04)
−20.86	3.00	397.61 (0.03)	−372.63(0.03)	−20.72	7.81	394.76 (0.03)	−378.56(0.03)
−21.08	5.21	394.23 (0.04)	−372.19(0.03)	−20.72	3.81	396.28 (0.05)	−377.81(0.07)
−21.08	11.69	396.45 (0.01)	−379.05(0.01)	−20.94	3.24	393.75 (0.02)	−369.22(0.03)
−21.30	7.04	394.38 (0.03)	−372.12(0.03)	−20.94	4.97	395.14 (0.03)	−378.76(0.03)

The observed SiO maser components in R13053A (2013-02-22) - (continued)

SiO (v=1 J=1−0)				SiO (v=2 J=1−0)			
$V_{\rm LSR}$ (km s^{-1})	I (Jy beam^{-1})	ΔRA (mas)	ΔDec (mas)	$V_{\rm LSR}$ (km s^{-1})	I (Jy beam^{-1})	ΔRA (mas)	ΔDec (mas)
−21.30	10.35	396.57 (0.01)	−379.05(0.02)	−20.94	2.67	396.13 (0.02)	−379.57(0.04)
−21.52	9.56	392.86 (0.01)	−365.97(0.02)	−21.16	8.33	393.95 (0.01)	−369.04(0.01)
−21.52	8.34	396.72 (0.02)	−379.08(0.01)	−21.16	2.14	393.96 (0.03)	−365.54(0.08)
−21.73	16.57	392.99 (0.01)	−365.98(0.01)	−21.16	3.60	395.35 (0.02)	−378.50(0.03)
−21.95	18.34	393.01 (0.00)	−365.93(0.01)	−21.38	4.12	392.32 (0.02)	−366.58(0.03)
−21.95	2.79	393.52 (0.02)	−365.38(0.02)	−21.38	6.33	393.99 (0.02)	−368.52(0.03)
−22.17	13.60	393.01 (0.01)	−365.87(0.01)	−21.60	3.25	392.43 (0.03)	−366.49(0.03)
−22.17	2.33	393.43 (0.02)	−365.28(0.03)	−21.60	9.08	394.08 (0.01)	−368.14(0.02)
−22.39	7.47	393.00 (0.01)	−365.86(0.01)	−21.82	15.86	394.25 (0.01)	−367.93(0.01)
−22.60	5.59	394.01 (0.02)	−369.67(0.02)	−22.04	19.98	394.32 (0.01)	−367.85(0.01)
−22.60	2.94	394.88 (0.03)	−370.61(0.06)	−22.25	16.68	394.33 (0.01)	−367.79(0.01)
−22.82	4.46	391.57 (0.02)	−369.20(0.03)	−22.47	11.23	394.31 (0.01)	−367.68(0.02)
−22.82	4.43	392.41 (0.02)	−370.35(0.03)	−22.69	5.15	394.32 (0.02)	−367.56(0.03)
−22.82	4.80	393.15 (0.03)	−368.56(0.03)	−22.69	6.00	395.07 (0.02)	−375.13(0.02)
−22.82	4.26	393.77 (0.03)	−373.09(0.03)	−22.91	3.60	393.67 (0.02)	−369.30(0.03)
−22.82	6.54	393.92 (0.02)	−369.75(0.02)	−22.91	5.08	394.52 (0.01)	−370.54(0.02)
−22.82	7.87	394.72 (0.01)	−370.81(0.02)	−22.91	5.94	394.99 (0.02)	−375.13(0.02)
−23.04	3.03	393.07 (0.03)	−368.67(0.04)	−22.91	4.17	395.24 (0.02)	−368.73(0.02)
−23.04	3.05	393.64 (0.03)	−373.15(0.04)	−22.91	3.53	395.25 (0.02)	−371.72(0.02)
−23.04	7.45	393.74 (0.01)	−369.89(0.02)	−22.91	3.91	395.90 (0.03)	−373.06(0.03)
−23.04	3.08	394.49 (0.03)	−371.03(0.05)	−22.91	3.75	396.58 (0.02)	−374.38(0.02)
−23.25	3.65	393.28 (0.02)	−370.27(0.02)	−22.91	3.84	396.60 (0.02)	−377.36(0.03)
−23.25	1.80	393.59 (0.03)	−367.00(0.03)	−22.91	3.66	397.31 (0.02)	−375.56(0.03)
−23.47	1.40	392.36 (0.03)	−369.25(0.04)	−23.13	2.90	393.76 (0.02)	−374.17(0.02)
−23.47	3.46	394.72 (0.01)	−376.35(0.02)	−23.13	2.63	394.52 (0.02)	−370.66(0.02)
−23.69	4.61	394.65 (0.01)	−376.46(0.01)	−23.13	2.37	394.85 (0.03)	−375.24(0.02)
−23.91	2.27	394.52 (0.01)	−376.50(0.02)	−23.13	2.67	395.18 (0.02)	−368.82(0.02)
−24.12	0.46	394.22 (0.06)	−376.57(0.06)	−23.35	1.27	393.44 (0.04)	−374.37(0.04)
−26.73	1.31	384.38 (0.02)	−391.87(0.03)	−23.35	2.67	394.13 (0.02)	−372.47(0.02)
−26.95	1.08	384.41 (0.03)	−391.66(0.04)	−23.35	1.41	395.20 (0.03)	−376.56(0.02)
−27.17	1.64	383.80 (0.03)	−390.76(0.03)	−23.35	1.43	396.08 (0.02)	−377.76(0.03)
−27.38	1.55	382.17 (0.02)	−388.36(0.02)	−23.57	1.31	393.99 (0.02)	−372.52(0.03)
−27.38	3.84	383.74 (0.01)	−390.71(0.01)	−23.57	1.02	394.20 (0.03)	−375.76(0.03)
−27.60	0.88	382.13 (0.05)	−388.26(0.04)	−23.79	0.72	394.19 (0.03)	−376.00(0.03)
−27.60	2.09	383.76 (0.02)	−390.64(0.02)				

The observed SiO maser components in R13093B (2013-04-03)

SiO (v=1 J=1−0)				SiO (v=2 J=1−0)			
$V_{\rm LSR}$ (km s^{-1})	I (Jy beam^{-1})	ΔRA (mas)	ΔDec (mas)	$V_{\rm LSR}$ (km s^{-1})	I (Jy beam^{-1})	ΔRA (mas)	ΔDec (mas)
−13.69	0.55	376.22 (0.03)	−386.74(0.05)	−12.84	1.06	373.73 (0.02)	−380.37(0.03)
−13.91	0.59	376.13 (0.03)	−386.82(0.05)	−13.06	1.56	373.74 (0.01)	−380.33(0.02)
−13.91	0.75	392.73 (0.02)	−379.14(0.04)	−13.28	1.65	373.76 (0.02)	−380.31(0.02)
−14.13	0.60	372.61 (0.03)	−381.31(0.05)	−13.50	1.02	373.80 (0.03)	−380.39(0.03)
−14.13	0.48	376.12 (0.05)	−386.83(0.06)	−13.72	0.63	373.69 (0.03)	−380.74(0.08)
−14.13	0.59	392.86 (0.03)	−379.20(0.05)	−14.16	0.53	373.45 (0.04)	−381.38(0.07)
−14.35	0.61	372.47 (0.03)	−381.44(0.06)	−14.16	0.50	387.55 (0.05)	−387.88(0.05)
−14.35	0.68	392.99 (0.03)	−379.15(0.04)	−14.38	0.66	387.74 (0.04)	−388.01(0.04)
−14.56	0.55	372.07 (0.03)	−381.19(0.08)	−14.60	0.70	374.18 (0.03)	−373.01(0.05)
−14.56	0.74	393.05 (0.03)	−379.14(0.03)	−14.81	0.83	374.16 (0.03)	−372.98(0.04)
−14.78	0.57	371.78 (0.03)	−381.10(0.07)	−15.03	0.56	374.06 (0.03)	−372.66(0.05)
−14.78	0.45	374.13 (0.04)	−372.88(0.05)	−15.25	0.81	390.36 (0.03)	−387.02(0.05)
−14.78	0.51	393.20 (0.04)	−379.16(0.05)	−15.47	0.74	373.99 (0.03)	−371.81(0.04)
−15.00	0.65	373.95 (0.03)	−372.64(0.04)	−15.47	1.26	390.62 (0.02)	−386.97(0.03)
−15.21	0.49	371.28 (0.05)	−381.22(0.08)	−15.69	1.57	374.07 (0.02)	−371.55(0.02)
−15.21	0.40	373.25 (0.04)	−374.25(0.08)	−15.69	2.77	390.73 (0.01)	−387.11(0.02)
−15.21	0.45	373.84 (0.04)	−372.19(0.07)	−15.91	2.69	374.02 (0.02)	−371.46(0.02)
−15.43	0.67	370.94 (0.03)	−381.21(0.05)	−15.91	4.83	390.88 (0.01)	−387.16(0.01)
−15.43	0.98	373.93 (0.02)	−371.87(0.03)	−16.13	3.33	373.96 (0.01)	−371.35(0.02)
−15.65	0.58	370.74 (0.03)	−381.33(0.06)	−16.13	1.41	390.54 (0.03)	−388.30(0.04)

The observed SiO maser components in R13093B (2013-04-03) - (continued)

SiO (v=1 J=1−0)				SiO (v=2 J=1−0)			
$V_{\rm LSR}$ (km s^{-1})	I (Jy beam^{-1})	ΔRA (mas)	ΔDec (mas)	$V_{\rm LSR}$ (km s^{-1})	I (Jy beam^{-1})	ΔRA (mas)	ΔDec (mas)
−15.65	1.64	373.96 (0.01)	−371.66(0.02)	−16.13	7.29	390.97 (0.01)	−387.34(0.01)
−15.87	0.53	370.44 (0.04)	−381.63(0.07)	−16.35	2.83	373.89 (0.02)	−371.20(0.03)
−15.87	2.53	373.96 (0.01)	−371.54(0.01)	−16.35	8.27	391.11 (0.01)	−387.54(0.01)
−15.87	0.67	390.98 (0.03)	−387.27(0.04)	−16.35	2.27	392.69 (0.03)	−386.01(0.03)
−16.08	0.69	373.31 (0.03)	−373.12(0.05)	−16.35	2.26	393.33 (0.03)	−384.17(0.03)
−16.08	3.08	373.94 (0.01)	−371.39(0.01)	−16.56	10.70	391.25 (0.01)	−387.76(0.01)
−16.08	1.30	391.16 (0.02)	−387.41(0.03)	−16.56	5.85	393.68 (0.02)	−383.95(0.02)
−16.30	0.73	373.26 (0.03)	−373.20(0.06)	−16.78	11.61	391.33 (0.01)	−388.01(0.01)
−16.30	2.91	373.88 (0.01)	−371.22(0.01)	−16.78	9.35	393.83 (0.01)	−383.95(0.02)
−16.30	1.97	391.26 (0.01)	−387.54(0.02)	−17.00	11.38	391.25 (0.01)	−388.40(0.01)
−16.30	1.13	393.40 (0.02)	−384.03(0.03)	−17.00	9.63	391.60 (0.01)	−388.00(0.01)
−16.52	1.57	373.81 (0.02)	−371.09(0.03)	−17.00	9.27	394.01 (0.01)	−383.97(0.02)
−16.52	2.46	391.43 (0.01)	−387.77(0.02)	−17.22	12.30	391.33 (0.01)	−388.56(0.01)
−16.52	3.15	393.52 (0.01)	−384.09(0.02)	−17.22	8.79	391.75 (0.01)	−388.23(0.01)
−16.74	1.58	391.06 (0.02)	−388.48(0.03)	−17.22	3.61	393.83 (0.02)	−385.01(0.03)
−16.74	2.32	391.53 (0.02)	−387.95(0.03)	−17.22	9.77	394.28 (0.01)	−384.03(0.01)
−16.74	4.34	393.64 (0.01)	−384.15(0.01)	−17.44	9.56	391.44 (0.01)	−388.74(0.01)
−16.95	1.97	390.65 (0.02)	−390.26(0.03)	−17.44	6.18	391.88 (0.01)	−388.49(0.02)
−16.95	1.85	391.77 (0.02)	−388.15(0.03)	−17.44	9.15	394.52 (0.01)	−384.10(0.01)
−16.95	3.06	393.74 (0.01)	−384.28(0.02)	−17.44	3.34	395.46 (0.04)	−382.65(0.04)
−16.95	1.25	394.85 (0.04)	−382.14(0.03)	−17.66	6.65	391.73 (0.02)	−388.97(0.02)
−17.17	1.09	391.07 (0.04)	−379.92(0.06)	−17.66	4.94	394.64 (0.02)	−384.13(0.02)
−17.17	2.56	391.42 (0.02)	−388.75(0.02)	−17.66	7.79	395.57 (0.01)	−382.83(0.02)
−17.17	1.95	391.93 (0.02)	−388.23(0.03)	−17.88	4.91	391.89 (0.02)	−389.16(0.02)
−17.17	1.21	393.73 (0.04)	−387.20(0.05)	−17.88	11.36	395.72 (0.01)	−382.98(0.01)
−17.17	1.20	394.11 (0.03)	−385.24(0.05)	−18.10	11.01	395.92 (0.01)	−383.14(0.01)
−17.39	1.50	391.05 (0.03)	−390.87(0.05)	−18.10	3.96	396.99 (0.03)	−381.64(0.03)
−17.39	2.13	391.57 (0.03)	−389.02(0.03)	−18.32	3.26	395.82 (0.02)	−383.32(0.04)
−17.39	1.64	393.57 (0.03)	−387.19(0.04)	−18.32	6.15	396.32 (0.01)	−383.24(0.01)
−17.39	1.72	394.24 (0.03)	−385.37(0.03)	−18.32	9.41	397.12 (0.01)	−381.56(0.01)
−17.39	3.31	395.28 (0.02)	−383.09(0.02)	−18.32	4.47	397.54 (0.01)	−380.56(0.02)
−17.60	2.32	391.25 (0.02)	−391.16(0.04)	−18.53	4.25	396.50 (0.03)	−383.43(0.03)
−17.60	1.45	391.79 (0.04)	−377.96(0.05)	−18.53	17.74	397.33 (0.01)	−381.36(0.01)
−17.60	1.51	394.29 (0.03)	−385.51(0.04)	−18.53	3.89	397.82 (0.02)	−380.50(0.02)
−17.60	7.15	395.49 (0.01)	−383.11(0.01)	−18.75	31.51	397.47 (0.00)	−381.32(0.01)
−17.82	2.36	391.43 (0.02)	−391.31(0.03)	−18.75	5.35	398.06 (0.03)	−380.64(0.04)
−17.82	1.73	391.94 (0.04)	−378.04(0.05)	−18.97	7.12	394.78 (0.02)	−387.32(0.03)
−17.82	9.02	395.64 (0.01)	−383.15(0.01)	−18.97	28.47	397.58 (0.01)	−381.31(0.01)
−17.82	1.48	396.25 (0.03)	−382.62(0.03)	−18.97	7.64	398.78 (0.03)	−379.16(0.02)
−18.04	2.19	391.56 (0.04)	−391.49(0.05)	−19.19	10.51	394.98 (0.01)	−387.51(0.02)
−18.04	5.11	395.78 (0.02)	−383.27(0.02)	−19.19	18.36	397.74 (0.01)	−381.30(0.01)
−18.04	1.95	396.83 (0.04)	−381.15(0.04)	−19.19	6.36	398.62 (0.02)	−380.76(0.02)
−18.26	2.45	395.90 (0.01)	−383.51(0.02)	−19.19	10.97	398.98 (0.01)	−379.25(0.01)
−18.26	2.98	396.42 (0.01)	−383.44(0.03)	−19.41	11.20	395.10 (0.01)	−387.62(0.02)
−18.26	2.70	397.18 (0.02)	−381.34(0.02)	−19.41	6.74	398.01 (0.02)	−381.29(0.02)
−18.47	1.83	394.61 (0.04)	−387.45(0.05)	−19.41	5.91	398.89 (0.03)	−380.82(0.02)
−18.47	2.70	396.65 (0.02)	−383.58(0.03)	−19.41	10.09	399.12 (0.01)	−379.33(0.02)
−18.47	6.37	397.36 (0.01)	−381.40(0.01)	−19.63	6.62	394.09 (0.03)	−391.06(0.04)
−18.69	4.55	394.68 (0.03)	−387.43(0.04)	−19.63	6.11	399.31 (0.03)	−380.90(0.03)
−18.69	2.84	397.01 (0.04)	−383.50(0.05)	−19.63	9.51	399.32 (0.02)	−379.45(0.02)
−18.69	8.32	397.57 (0.01)	−381.42(0.02)	−19.63	3.97	400.47 (0.03)	−376.97(0.05)
−18.69	3.51	398.48 (0.03)	−379.08(0.04)	−19.85	5.33	394.18 (0.05)	−391.16(0.06)
−18.91	7.65	394.95 (0.02)	−387.67(0.03)	−19.85	4.52	399.58 (0.03)	−379.68(0.05)
−18.91	4.31	397.05 (0.04)	−394.34(0.04)	−19.85	5.89	399.64 (0.03)	−373.07(0.03)
−18.91	7.41	397.90 (0.02)	−381.48(0.02)	−19.85	7.97	400.11 (0.02)	−378.16(0.05)
−19.13	8.49	395.20 (0.01)	−387.91(0.01)	−19.85	5.29	400.63 (0.02)	−376.83(0.04)
−19.13	2.39	397.28 (0.04)	−394.37(0.05)	−20.07	4.57	399.05 (0.03)	−372.18(0.04)
−19.13	7.43	398.31 (0.01)	−381.62(0.02)	−20.07	14.61	399.95 (0.01)	−380.54(0.02)
−19.13	3.61	399.29 (0.03)	−379.33(0.02)	−20.07	7.91	400.84 (0.02)	−376.50(0.03)
−19.34	4.45	394.05 (0.04)	−391.22(0.04)	−20.28	6.98	399.25 (0.03)	−372.12(0.03)
−19.34	4.81	395.45 (0.03)	−388.06(0.04)	−20.28	20.23	400.13 (0.01)	−380.55(0.01)
−19.34	5.10	398.80 (0.03)	−381.75(0.04)	−20.28	5.57	400.99 (0.03)	−376.37(0.04)
−19.56	2.49	373.97 (0.03)	−365.86(0.04)	−20.50	11.45	399.52 (0.02)	−372.14(0.02)

The observed SiO maser components in R13093B (2013-04-03) - (continued)

SiO (v=1 J=1−0)				SiO (v=2 J=1−0)			
$V_{\rm LSR}$ (km s^{-1})	I (Jy beam^{-1})	ΔRA (mas)	ΔDec (mas)	$V_{\rm LSR}$ (km s^{-1})	I (Jy beam^{-1})	ΔRA (mas)	ΔDec (mas)
−19.56	5.88	394.29 (0.02)	−391.39(0.02)	−20.50	22.37	400.33 (0.01)	−380.59(0.01)
−19.56	5.69	399.19 (0.02)	−381.87(0.02)	−20.72	14.17	399.83 (0.01)	−372.24(0.02)
−19.56	3.15	400.55 (0.02)	−377.17(0.03)	−20.72	9.14	400.14 (0.01)	−373.12(0.02)
−19.78	3.25	373.94 (0.04)	−365.78(0.05)	−20.72	8.42	400.25 (0.01)	−373.48(0.02)
−19.78	5.06	394.44 (0.02)	−391.53(0.04)	−20.72	23.76	400.54 (0.01)	−380.63(0.01)
−19.78	5.21	399.83 (0.03)	−382.16(0.02)	−20.94	12.83	400.05 (0.01)	−372.16(0.01)
−19.99	6.86	400.35 (0.02)	−382.34(0.02)	−20.94	16.10	400.69 (0.01)	−380.64(0.01)
−19.99	7.34	400.52 (0.02)	−380.74(0.02)	−20.94	7.66	401.76 (0.02)	−380.74(0.02)
−20.21	2.73	398.50 (0.02)	−370.81(0.03)	−21.16	13.22	400.35 (0.01)	−372.03(0.01)
−20.21	2.77	399.41 (0.02)	−371.90(0.03)	−21.16	4.99	400.69 (0.02)	−380.52(0.02)
−20.21	2.78	400.35 (0.03)	−372.96(0.03)	−21.16	7.40	401.90 (0.02)	−380.67(0.02)
−20.21	6.28	400.57 (0.02)	−382.43(0.01)	−21.38	6.80	372.12 (0.02)	−368.47(0.02)
−20.21	8.83	400.85 (0.01)	−380.85(0.01)	−21.38	5.13	399.92 (0.03)	−373.63(0.02)
−20.43	2.87	399.14 (0.02)	−373.29(0.03)	−21.38	7.47	400.42 (0.02)	−370.50(0.02)
−20.43	3.98	400.44 (0.02)	−373.09(0.02)	−21.38	10.92	400.59 (0.01)	−371.98(0.01)
−20.43	9.88	401.27 (0.01)	−380.87(0.01)	−21.38	5.21	401.09 (0.04)	−368.74(0.02)
−20.43	3.75	401.68 (0.02)	−376.05(0.03)	−21.60	8.29	372.08 (0.01)	−368.50(0.02)
−20.65	2.33	399.35 (0.02)	−373.25(0.03)	−21.60	4.52	398.89 (0.03)	−368.14(0.04)
−20.65	4.11	400.49 (0.02)	−373.17(0.02)	−21.60	13.47	400.57 (0.01)	−370.30(0.01)
−20.65	13.24	401.75 (0.01)	−380.88(0.01)	−21.82	7.22	372.01 (0.01)	−368.56(0.02)
−20.65	3.48	401.81 (0.02)	−376.02(0.02)	−21.82	13.04	400.60 (0.01)	−370.06(0.01)
−20.65	2.20	401.93 (0.02)	−379.01(0.03)	−21.82	7.40	401.20 (0.01)	−371.15(0.02)
−20.86	2.93	401.33 (0.02)	−382.56(0.02)	−22.03	4.56	371.96 (0.02)	−368.64(0.03)
−20.86	20.55	401.98 (0.00)	−380.88(0.00)	−22.03	9.52	400.62 (0.02)	−369.80(0.02)
−20.86	2.92	402.18 (0.02)	−379.18(0.02)	−22.03	16.47	401.31 (0.01)	−371.25(0.01)
−21.08	2.41	400.24 (0.04)	−373.95(0.03)	−22.25	5.31	400.67 (0.02)	−369.61(0.03)
−21.08	20.71	402.15 (0.00)	−380.91(0.00)	−22.25	19.41	401.38 (0.01)	−371.36(0.01)
−21.30	3.89	400.39 (0.04)	−373.88(0.03)	−22.25	4.00	402.30 (0.03)	−372.99(0.04)
−21.30	18.10	402.30 (0.01)	−380.96(0.01)	−22.47	2.93	399.54 (0.04)	−368.00(0.06)
−21.52	2.45	372.04 (0.03)	−368.58(0.04)	−22.47	4.82	400.61 (0.02)	−369.35(0.03)
−21.52	8.38	401.24 (0.01)	−370.74(0.01)	−22.47	3.00	401.44 (0.03)	−374.55(0.03)
−21.52	2.47	401.93 (0.05)	−382.95(0.04)	−22.47	10.50	401.44 (0.01)	−371.39(0.01)
−21.52	12.93	402.38 (0.01)	−380.96(0.01)	−22.47	2.92	402.54 (0.04)	−375.98(0.06)
−21.73	2.33	372.02 (0.02)	−368.64(0.03)	−22.69	4.92	400.57 (0.01)	−369.26(0.02)
−21.73	3.76	399.44 (0.01)	−367.77(0.02)	−22.69	2.81	401.18 (0.02)	−374.39(0.01)
−21.73	8.40	401.28 (0.01)	−370.46(0.01)	−22.69	1.93	401.25 (0.03)	−380.64(0.03)
−21.73	10.16	401.41 (0.00)	−371.27(0.01)	−22.69	2.60	401.39 (0.02)	−377.56(0.02)
−21.73	7.83	402.34 (0.01)	−380.84(0.01)	−22.69	2.01	401.43 (0.03)	−372.73(0.02)
−21.95	5.40	399.51 (0.02)	−367.65(0.04)	−22.69	2.02	401.56 (0.02)	−371.18(0.02)
−21.95	11.15	401.53 (0.01)	−371.32(0.02)	−22.69	1.94	402.15 (0.02)	−375.73(0.03)
−21.95	5.67	402.45 (0.02)	−372.72(0.03)	−22.69	1.90	402.43 (0.03)	−367.82(0.02)
−22.17	5.07	399.56 (0.02)	−367.67(0.03)	−22.91	2.10	400.60 (0.02)	−369.30(0.04)
−22.17	11.56	401.60 (0.01)	−371.42(0.01)	−22.91	2.91	400.90 (0.02)	−374.50(0.02)
−22.17	2.48	401.89 (0.03)	−374.37(0.05)	−22.91	1.79	401.19 (0.03)	−377.64(0.02)
−22.17	2.61	402.64 (0.03)	−378.91(0.04)	−22.91	1.77	401.33 (0.03)	−372.82(0.02)
−22.38	3.47	398.77 (0.03)	−366.26(0.04)	−22.91	1.81	401.68 (0.02)	−375.91(0.02)
−22.38	3.99	398.98 (0.02)	−369.34(0.03)	−23.13	5.08	400.60 (0.01)	−374.57(0.01)
−22.38	5.68	399.61 (0.02)	−367.65(0.03)	−23.13	2.42	400.76 (0.01)	−378.10(0.03)
−22.38	4.30	400.95 (0.02)	−373.11(0.03)	−23.35	6.47	400.43 (0.01)	−374.59(0.01)
−22.38	8.50	401.62 (0.01)	−371.41(0.01)	−23.35	3.10	400.69 (0.01)	−378.06(0.02)
−22.38	4.59	401.84 (0.02)	−374.46(0.02)	−23.57	3.87	400.31 (0.01)	−374.62(0.01)
−22.38	3.55	402.48 (0.02)	−372.76(0.03)	−23.57	1.10	400.58 (0.03)	−378.07(0.03)
−22.60	3.71	399.69 (0.01)	−367.74(0.02)	−23.79	0.81	400.12 (0.03)	−374.68(0.03)
−22.60	1.71	400.62 (0.03)	−369.37(0.04)				
−22.60	1.60	401.30 (0.04)	−372.77(0.03)				
−22.60	1.62	401.62 (0.04)	−380.62(0.03)				
−22.60	3.28	401.76 (0.02)	−371.14(0.02)				
−22.82	1.08	398.83 (0.03)	−366.24(0.05)				
−22.82	1.11	399.77 (0.03)	−367.81(0.04)				
−22.82	2.91	401.36 (0.01)	−372.84(0.02)				
−22.82	1.47	401.66 (0.02)	−377.55(0.03)				
−22.82	2.34	401.67 (0.02)	−374.24(0.02)				
−23.04	1.05	400.72 (0.03)	−376.14(0.02)				

The observed SiO maser components in R13093B (2013-04-03) - (continued)

SiO (v=1 J=1−0)				SiO (v=2 J=1−0)			
$V_{\rm LSR}$ (km s^{-1})	I (Jy beam^{-1})	ΔRA (mas)	ΔDec (mas)	$V_{\rm LSR}$ (km s^{-1})	I (Jy beam^{-1})	ΔRA (mas)	ΔDec (mas)
−23.04	2.16	401.45 (0.02)	−374.37(0.01)				
−23.04	2.10	401.58 (0.01)	−377.59(0.01)				
−23.04	1.07	401.78 (0.02)	−371.30(0.03)				
−23.25	0.70	400.83 (0.04)	−373.37(0.03)				
−23.25	1.66	401.01 (0.01)	−374.39(0.02)				
−23.25	0.79	401.57 (0.03)	−377.55(0.04)				
−23.25	0.84	401.59 (0.03)	−371.50(0.03)				
−23.47	0.52	400.94 (0.04)	−374.82(0.04)				
−23.47	0.78	401.81 (0.03)	−379.70(0.03)				
−23.69	1.10	400.77 (0.02)	−378.34(0.02)				
−23.91	0.70	400.58 (0.04)	−378.36(0.03)				
−24.12	0.41	400.30 (0.04)	−378.34(0.06)				
−26.73	0.76	390.74 (0.04)	−393.81(0.03)				
−26.95	1.45	390.18 (0.02)	−393.29(0.03)				
−26.95	1.00	391.07 (0.03)	−393.71(0.03)				
−27.16	1.14	389.46 (0.03)	−394.81(0.04)				
−27.16	3.52	390.11 (0.01)	−393.10(0.01)				
−27.38	1.34	389.53 (0.02)	−394.71(0.04)				
−27.38	3.85	390.09 (0.01)	−392.85(0.01)				
−27.60	0.94	389.54 (0.02)	−394.57(0.03)				
−27.60	2.65	390.17 (0.01)	−392.68(0.01)				
−27.82	0.81	390.22 (0.02)	−392.53(0.04)				

The observed SiO maser components in R13129B (2013-05-09)

SiO (v=1 J=1−0)				SiO (v=2 J=1−0)			
$V_{\rm LSR}$ (km s^{-1})	I (Jy beam^{-1})	ΔRA (mas)	ΔDec (mas)	$V_{\rm LSR}$ (km s^{-1})	I (Jy beam^{-1})	ΔRA (mas)	ΔDec (mas)
−15.00	0.31	379.05 (0.07)	−373.73(0.04)	−15.25	0.94	394.64 (0.02)	−388.70(0.03)
−15.21	0.55	378.83 (0.03)	−373.50(0.03)	−15.47	2.25	394.84 (0.01)	−388.73(0.01)
−15.43	0.76	378.71 (0.03)	−373.39(0.03)	−15.69	3.24	394.95 (0.01)	−388.80(0.01)
−15.65	0.85	378.64 (0.03)	−373.25(0.03)	−15.91	1.13	378.07 (0.03)	−373.01(0.03)
−15.87	0.65	378.53 (0.04)	−373.16(0.03)	−15.91	3.32	395.07 (0.01)	−388.99(0.01)
−15.87	0.49	395.29 (0.04)	−388.92(0.04)	−16.13	2.87	377.98 (0.01)	−372.87(0.02)
−16.08	0.51	378.14 (0.05)	−372.88(0.04)	−16.13	3.46	395.18 (0.01)	−389.26(0.02)
−16.08	0.50	395.48 (0.05)	−389.26(0.04)	−16.13	2.09	397.22 (0.02)	−385.75(0.02)
−16.08	0.59	397.35 (0.03)	−385.77(0.03)	−16.35	2.97	377.94 (0.02)	−372.83(0.02)
−16.30	0.77	395.53 (0.05)	−389.46(0.03)	−16.35	5.04	395.28 (0.01)	−389.54(0.01)
−16.30	1.03	397.36 (0.02)	−385.83(0.02)	−16.35	1.80	395.72 (0.03)	−391.02(0.02)
−16.52	0.90	395.62 (0.04)	−389.63(0.03)	−16.35	3.76	397.32 (0.01)	−385.86(0.02)
−16.52	0.90	397.40 (0.03)	−385.83(0.02)	−16.35	4.16	397.89 (0.01)	−385.47(0.01)
−16.74	1.11	395.78 (0.03)	−389.79(0.02)	−16.56	6.98	395.39 (0.01)	−389.73(0.01)
−16.95	1.02	395.98 (0.03)	−390.01(0.03)	−16.56	2.41	397.32 (0.02)	−385.94(0.02)
−17.17	0.91	396.22 (0.03)	−390.24(0.03)	−16.56	6.11	397.94 (0.01)	−385.60(0.01)
−17.39	1.11	397.08 (0.05)	−388.85(0.03)	−16.56	2.64	398.28 (0.02)	−387.14(0.02)
−17.39	1.09	399.36 (0.03)	−385.07(0.03)	−16.78	6.80	395.55 (0.01)	−389.89(0.01)
−17.60	1.49	397.24 (0.04)	−388.97(0.03)	−16.78	3.89	395.98 (0.01)	−388.37(0.02)
−17.60	1.38	399.53 (0.03)	−385.05(0.02)	−16.78	6.54	398.03 (0.01)	−385.67(0.01)
−17.82	1.26	397.41 (0.04)	−389.10(0.03)	−16.78	2.72	398.44 (0.02)	−387.18(0.02)
−17.82	1.20	399.70 (0.04)	−385.06(0.03)	−17.00	6.64	395.71 (0.01)	−390.06(0.01)
−18.04	0.70	399.93 (0.06)	−382.03(0.03)	−17.00	3.88	396.08 (0.01)	−388.47(0.01)
−18.26	0.91	400.38 (0.06)	−382.08(0.03)	−17.00	5.94	398.20 (0.01)	−385.76(0.01)
−18.26	0.92	401.36 (0.03)	−383.37(0.03)	−17.00	2.28	398.57 (0.02)	−387.28(0.02)
−18.47	1.05	398.67 (0.03)	−389.10(0.02)	−17.22	4.64	395.87 (0.01)	−390.23(0.01)
−18.47	1.61	401.65 (0.03)	−383.37(0.02)	−17.22	2.45	396.23 (0.03)	−388.53(0.02)
−18.69	1.38	398.86 (0.03)	−389.31(0.03)	−17.22	3.50	398.37 (0.01)	−385.91(0.02)
−18.69	1.78	402.00 (0.03)	−383.43(0.02)	−17.44	2.58	396.01 (0.03)	−390.41(0.02)
−18.91	1.52	398.17 (0.03)	−388.10(0.03)	−17.44	2.09	396.42 (0.03)	−388.72(0.02)
−18.91	1.16	399.06 (0.05)	−389.53(0.04)	−17.44	2.07	398.53 (0.03)	−383.15(0.02)
−18.91	1.73	402.35 (0.03)	−383.51(0.03)	−17.44	2.90	399.26 (0.02)	−384.94(0.02)
−19.13	1.51	398.39 (0.05)	−388.23(0.03)	−17.66	1.74	399.37 (0.03)	−391.46(0.02)

The observed SiO maser components in R13129B (2013-05-09) - (continued)

SiO (v=1 J=1−0)				SiO (v=2 J=1−0)			
$V_{\rm LSR}$ (km s^{-1})	I (Jy beam^{-1})	ΔRA (mas)	ΔDec (mas)	$V_{\rm LSR}$ (km s^{-1})	I (Jy beam^{-1})	ΔRA (mas)	ΔDec (mas)
−19.13	1.47	401.72 (0.04)	−382.18(0.04)	−17.66	5.25	399.39 (0.01)	−385.11(0.01)
−19.34	2.47	398.27 (0.02)	−393.08(0.02)	−17.66	6.55	399.79 (0.01)	−384.89(0.01)
−19.56	2.40	398.43 (0.03)	−393.20(0.04)	−17.88	2.43	398.61 (0.03)	−393.32(0.02)
−19.56	2.47	403.94 (0.04)	−382.53(0.02)	−17.88	10.07	399.84 (0.01)	−384.99(0.01)
−19.78	3.63	404.23 (0.03)	−382.51(0.02)	−17.88	2.50	401.62 (0.02)	−382.53(0.02)
−19.99	1.82	402.43 (0.04)	−377.06(0.03)	−18.10	3.56	397.99 (0.02)	−388.53(0.02)
−19.99	3.93	404.57 (0.02)	−382.56(0.02)	−18.10	11.75	400.15 (0.01)	−385.05(0.01)
−19.99	1.77	405.04 (0.04)	−384.32(0.04)	−18.10	3.12	400.88 (0.02)	−386.56(0.03)
−20.21	2.54	404.89 (0.03)	−376.29(0.02)	−18.10	3.21	400.89 (0.02)	−383.50(0.03)
−20.43	1.58	405.24 (0.04)	−373.14(0.03)	−18.10	4.87	401.65 (0.01)	−382.50(0.02)
−20.43	1.87	405.47 (0.02)	−382.56(0.02)	−18.31	5.75	398.17 (0.01)	−388.65(0.01)
−20.65	1.07	404.75 (0.04)	−375.02(0.03)	−18.31	10.74	400.43 (0.01)	−385.09(0.01)
−20.65	1.81	405.63 (0.03)	−382.61(0.02)	−18.31	3.11	400.97 (0.02)	−383.56(0.02)
−20.65	1.08	406.13 (0.04)	−377.84(0.03)	−18.31	5.43	401.79 (0.01)	−382.53(0.01)
−20.86	1.63	405.74 (0.02)	−379.53(0.02)	−18.53	6.03	398.38 (0.01)	−388.83(0.01)
−20.86	0.84	406.31 (0.02)	−379.55(0.03)	−18.53	6.59	400.66 (0.01)	−385.18(0.01)
−21.08	0.69	406.14 (0.06)	−379.52(0.04)	−18.53	4.90	401.91 (0.01)	−382.49(0.02)
−21.30	1.25	405.05 (0.02)	−372.67(0.02)	−18.53	2.87	402.50 (0.03)	−380.97(0.03)
−21.30	0.89	407.83 (0.04)	−381.31(0.03)	−18.75	5.69	398.57 (0.01)	−389.01(0.02)
−21.52	0.97	407.23 (0.04)	−379.57(0.03)	−18.75	5.33	401.67 (0.01)	−383.42(0.02)
−21.52	1.23	407.29 (0.03)	−382.84(0.02)	−18.75	2.60	402.06 (0.03)	−382.46(0.03)
−21.73	0.91	405.69 (0.03)	−373.21(0.03)	−18.75	2.91	402.57 (0.03)	−387.41(0.02)
−21.73	0.77	406.27 (0.06)	−382.80(0.05)	−18.75	5.11	402.62 (0.02)	−380.99(0.02)
−21.73	1.76	407.22 (0.03)	−382.68(0.02)	−18.97	4.56	398.76 (0.02)	−389.25(0.02)
−21.73	0.92	407.68 (0.04)	−384.38(0.03)	−18.97	9.73	401.86 (0.01)	−383.31(0.01)
−21.95	1.82	405.92 (0.02)	−373.23(0.02)	−18.97	6.65	402.50 (0.02)	−382.62(0.01)
−21.95	1.20	406.96 (0.03)	−373.07(0.02)	−18.97	2.58	402.80 (0.03)	−384.24(0.03)
−22.17	0.94	405.85 (0.04)	−370.17(0.03)	−19.19	3.98	378.55 (0.03)	−368.34(0.03)
−22.17	4.17	406.00 (0.01)	−373.38(0.01)	−19.19	9.03	402.03 (0.01)	−383.33(0.02)
−22.38	1.48	406.05 (0.01)	−373.41(0.02)	−19.19	9.84	402.69 (0.01)	−382.71(0.01)
−22.38	0.99	407.43 (0.03)	−381.89(0.02)	−19.41	7.89	378.43 (0.01)	−368.20(0.01)
−22.60	0.62	404.08 (0.03)	−369.37(0.04)	−19.41	3.63	398.01 (0.03)	−392.88(0.04)
−22.60	0.70	407.37 (0.03)	−381.88(0.03)	−19.41	4.90	402.12 (0.02)	−383.30(0.02)
−22.60	0.57	407.76 (0.05)	−377.04(0.04)	−19.41	9.78	402.84 (0.01)	−382.82(0.01)
−22.82	0.46	404.05 (0.04)	−369.32(0.04)	−19.41	4.93	403.72 (0.02)	−382.65(0.02)
−22.82	0.55	406.13 (0.04)	−377.66(0.03)	−19.63	8.47	378.42 (0.02)	−368.13(0.02)
−22.82	0.52	407.30 (0.04)	−381.80(0.03)	−19.63	6.38	398.27 (0.02)	−393.17(0.03)
−23.04	0.55	405.43 (0.03)	−376.05(0.03)	−19.63	5.72	402.83 (0.02)	−382.93(0.02)
−23.47	0.51	405.63 (0.05)	−374.98(0.03)	−19.63	8.59	403.60 (0.02)	−382.66(0.01)
−23.69	0.44	405.25 (0.03)	−375.08(0.03)	−19.85	5.14	378.48 (0.03)	−368.08(0.03)
−23.69	0.54	405.81 (0.03)	−374.88(0.03)	−19.85	4.89	398.50 (0.04)	−393.42(0.04)
−27.38	0.69	394.59 (0.02)	−394.65(0.02)	−19.85	13.18	403.73 (0.01)	−382.58(0.01)
−27.60	0.83	394.52 (0.02)	−394.49(0.02)	−19.85	4.69	404.98 (0.03)	−378.84(0.02)
				−20.07	15.93	403.91 (0.01)	−382.51(0.01)
				−20.07	4.25	405.96 (0.03)	−376.91(0.03)
				−20.28	2.86	402.73 (0.02)	−372.32(0.02)
				−20.28	17.44	404.10 (0.01)	−382.52(0.01)
				−20.28	3.24	404.27 (0.03)	−384.03(0.02)
				−20.28	3.01	406.15 (0.04)	−376.81(0.02)
				−20.50	4.99	402.88 (0.02)	−372.33(0.02)
				−20.50	13.08	404.24 (0.01)	−382.51(0.01)
				−20.50	4.14	404.65 (0.03)	−377.67(0.02)
				−20.72	2.83	403.06 (0.02)	−372.29(0.03)
				−20.72	10.65	404.22 (0.01)	−374.27(0.01)
				−20.72	4.45	404.26 (0.02)	−382.56(0.01)
				−20.72	3.43	405.04 (0.02)	−374.40(0.02)
				−20.72	2.58	405.24 (0.04)	−375.94(0.02)
				−20.94	2.26	403.39 (0.03)	−372.41(0.04)
				−20.94	16.78	404.29 (0.00)	−374.23(0.00)
				−20.94	2.18	405.03 (0.02)	−374.46(0.03)
				−21.16	4.18	403.56 (0.02)	−372.38(0.02)
				−21.16	3.51	404.23 (0.04)	−375.68(0.02)
				−21.16	3.71	404.32 (0.03)	−370.83(0.02)

The observed SiO maser components in R13129B (2013-05-09) - (continued)

SiO (v=1 J=1−0)				SiO (v=2 J=1−0)			
$V_{\rm LSR}$ (km s^{-1})	I (Jy beam^{-1})	ΔRA (mas)	ΔDec (mas)	$V_{\rm LSR}$ (km s^{-1})	I (Jy beam^{-1})	ΔRA (mas)	ΔDec (mas)
				−21.16	3.70	404.38 (0.03)	−377.28(0.02)
				−21.16	13.38	404.41 (0.01)	−374.04(0.01)
				−21.16	3.73	405.11 (0.02)	−372.30(0.02)
				−21.38	8.49	404.70 (0.01)	−373.77(0.01)
				−21.60	2.62	404.75 (0.02)	−372.11(0.02)
				−21.60	2.28	404.78 (0.04)	−375.22(0.02)
				−21.60	2.35	404.81 (0.04)	−380.03(0.02)
				−21.60	2.29	404.84 (0.04)	−376.83(0.02)
				−21.60	9.44	404.97 (0.01)	−373.55(0.01)
				−21.60	2.29	405.01 (0.03)	−370.38(0.02)
				−21.82	1.82	404.17 (0.01)	−370.33(0.03)
				−21.82	2.89	405.13 (0.01)	−371.71(0.02)
				−21.82	6.38	405.19 (0.01)	−373.38(0.01)
				−21.82	2.16	406.07 (0.02)	−373.06(0.02)
				−22.03	1.83	404.91 (0.03)	−368.33(0.02)
				−22.03	7.87	405.09 (0.01)	−371.54(0.01)
				−22.03	1.59	405.23 (0.04)	−378.05(0.02)
				−22.03	6.03	405.51 (0.01)	−373.27(0.01)
				−22.03	1.76	405.70 (0.03)	−376.44(0.02)
				−22.25	3.60	404.98 (0.02)	−368.27(0.02)
				−22.25	3.09	404.99 (0.03)	−369.88(0.02)
				−22.25	8.02	405.07 (0.01)	−371.47(0.01)
				−22.25	3.13	405.20 (0.02)	−374.79(0.02)
				−22.25	3.04	405.67 (0.02)	−382.92(0.02)
				−22.25	5.17	405.74 (0.01)	−373.33(0.01)
				−22.25	3.78	405.85 (0.02)	−376.48(0.01)
				−22.25	3.01	406.83 (0.02)	−374.94(0.02)
				−22.47	1.37	404.80 (0.02)	−382.24(0.03)
				−22.47	1.09	405.02 (0.02)	−372.84(0.02)
				−22.47	3.94	405.04 (0.01)	−371.31(0.01)
				−22.47	2.54	405.90 (0.01)	−373.36(0.02)
				−22.69	1.27	404.77 (0.03)	−382.24(0.03)
				−22.69	2.34	404.98 (0.01)	−371.05(0.01)
				−22.69	1.33	405.97 (0.02)	−377.79(0.02)
				−22.91	0.92	404.69 (0.03)	−382.10(0.05)
				−22.91	2.44	404.95 (0.01)	−376.25(0.01)
				−22.91	1.07	405.79 (0.03)	−377.78(0.03)
				−23.13	4.84	404.81 (0.01)	−376.34(0.01)
				−23.13	1.27	404.92 (0.03)	−379.56(0.02)
				−23.35	5.32	404.70 (0.01)	−376.37(0.01)
				−23.35	1.70	404.72 (0.02)	−379.65(0.02)
				−23.57	2.90	404.60 (0.01)	−376.45(0.01)
				−23.57	0.90	404.73 (0.03)	−381.21(0.02)
				−23.57	0.89	404.84 (0.04)	−378.05(0.03)
				−23.78	1.04	404.40 (0.03)	−376.50(0.02)
				−24.00	0.57	404.00 (0.04)	−381.41(0.04)

The observed SiO maser components in R13158D (2013-06-07)

SiO (v=1 J=1−0)				SiO (v=2 J=1−0)			
$V_{\rm LSR}$ (km s^{-1})	I (Jy beam^{-1})	ΔRA (mas)	ΔDec (mas)	$V_{\rm LSR}$ (km s^{-1})	I (Jy beam^{-1})	ΔRA (mas)	ΔDec (mas)
−14.56	0.90	383.12(0.05)	−376.33(0.06)	−13.94	0.89	397.52(0.04)	−390.20(0.06)
−14.78	3.50	382.99(0.02)	−376.17(0.03)	−14.16	0.96	397.59(0.04)	−390.46(0.05)
−15.00	5.94	382.91(0.02)	−376.14(0.03)	−14.38	1.21	397.77(0.03)	−390.70(0.04)
−15.21	6.78	382.81(0.02)	−376.07(0.03)	−14.59	1.15	397.98(0.03)	−390.93(0.05)
−15.43	5.96	382.72(0.02)	−375.97(0.03)	−14.81	0.88	383.08(0.05)	−376.21(0.05)
−15.65	4.04	382.65(0.03)	−375.80(0.04)	−14.81	2.32	398.17(0.02)	−391.11(0.02)
−15.87	2.73	382.62(0.03)	−375.55(0.04)	−15.03	2.38	382.92(0.02)	−376.17(0.03)
−16.08	1.76	382.69(0.06)	−375.20(0.08)	−15.03	4.61	398.26(0.01)	−391.22(0.02)
−16.08	2.03	398.95(0.05)	−392.39(0.06)	−15.25	3.82	382.84(0.01)	−376.07(0.02)

The observed SiO maser components in R13158D (2013-06-07) - (continued)

SiO (v=1 J=1−0)				SiO (v=2 J=1−0)			
$V_{\rm LSR}$ (km s^{-1})	I (Jy beam^{-1})	ΔRA (mas)	ΔDec (mas)	$V_{\rm LSR}$ (km s^{-1})	I (Jy beam^{-1})	ΔRA (mas)	ΔDec (mas)
−16.30	3.24	399.05(0.03)	−392.59(0.04)	−15.25	5.63	398.34(0.01)	−391.32(0.01)
−16.52	1.98	383.01(0.05)	−374.82(0.07)	−15.47	3.64	382.76(0.01)	−375.99(0.02)
−16.52	3.60	399.19(0.03)	−392.76(0.04)	−15.47	3.56	398.43(0.01)	−391.51(0.02)
−16.74	2.71	382.82(0.05)	−374.53(0.06)	−15.69	2.20	382.61(0.02)	−375.91(0.03)
−16.74	4.83	399.37(0.03)	−393.01(0.03)	−15.69	2.09	398.31(0.02)	−392.23(0.03)
−16.95	4.91	399.59(0.03)	−393.28(0.04)	−15.69	1.55	398.55(0.02)	−391.68(0.04)
−17.17	5.27	399.78(0.03)	−393.47(0.04)	−15.69	1.47	400.55(0.03)	−388.55(0.04)
−17.39	6.01	400.55(0.03)	−391.89(0.04)	−15.91	2.04	398.53(0.03)	−392.34(0.04)
−17.60	5.23	400.75(0.03)	−392.08(0.05)	−15.91	3.79	398.95(0.02)	−390.79(0.02)
−17.82	2.65	400.98(0.06)	−392.33(0.08)	−15.91	2.86	400.93(0.03)	−388.53(0.03)
−17.82	3.35	403.71(0.03)	−387.93(0.05)	−16.13	4.05	398.73(0.02)	−392.39(0.03)
−18.04	3.14	404.60(0.04)	−386.29(0.06)	−16.13	6.61	399.04(0.01)	−390.92(0.02)
−18.26	3.12	399.35(0.05)	−396.99(0.05)	−16.13	6.23	401.12(0.02)	−388.45(0.02)
−18.26	3.28	401.99(0.07)	−392.05(0.08)	−16.35	8.26	398.75(0.02)	−392.55(0.02)
−18.26	4.26	404.87(0.04)	−386.44(0.05)	−16.35	5.17	399.16(0.04)	−391.00(0.05)
−18.47	5.97	399.62(0.03)	−397.14(0.03)	−16.35	8.69	401.30(0.02)	−388.46(0.02)
−18.47	5.10	402.20(0.04)	−392.20(0.06)	−16.56	9.82	398.95(0.01)	−392.76(0.02)
−18.47	5.87	405.22(0.03)	−386.54(0.04)	−16.56	5.03	399.45(0.05)	−391.32(0.06)
−18.69	7.31	400.01(0.04)	−397.29(0.04)	−16.56	3.86	400.49(0.04)	−392.71(0.05)
−18.69	6.59	405.56(0.04)	−386.51(0.06)	−16.56	6.85	401.41(0.02)	−388.48(0.03)
−18.91	8.72	401.00(0.04)	−395.79(0.04)	−16.78	8.60	399.17(0.01)	−392.91(0.02)
−18.91	6.82	405.89(0.05)	−386.56(0.08)	−16.78	5.51	399.57(0.02)	−391.43(0.03)
−19.12	16.18	401.38(0.02)	−396.04(0.02)	−16.78	2.66	401.24(0.06)	−388.55(0.08)
−19.34	24.84	401.63(0.01)	−396.21(0.01)	−16.78	2.71	401.77(0.04)	−388.51(0.04)
−19.56	20.37	401.88(0.01)	−396.33(0.01)	−17.00	8.93	399.35(0.01)	−393.07(0.02)
−19.56	4.45	407.46(0.06)	−385.60(0.06)	−17.00	3.25	399.65(0.03)	−391.41(0.05)
−19.78	13.64	402.20(0.02)	−396.45(0.02)	−17.22	7.83	399.51(0.01)	−393.24(0.02)
−19.78	5.29	407.84(0.05)	−385.58(0.05)	−17.22	2.38	400.57(0.02)	−391.31(0.04)
−19.99	8.02	402.51(0.02)	−396.69(0.04)	−17.22	3.56	402.75(0.03)	−387.86(0.03)
−19.99	3.07	408.19(0.07)	−385.62(0.07)	−17.44	4.47	399.74(0.02)	−393.49(0.03)
−20.21	4.80	408.04(0.03)	−378.14(0.05)	−17.44	2.53	400.75(0.03)	−391.17(0.05)
−20.43	5.98	408.25(0.03)	−378.14(0.04)	−17.44	6.53	402.99(0.01)	−387.89(0.02)
−20.65	2.42	407.70(0.03)	−376.45(0.05)	−17.66	2.19	399.99(0.05)	−393.69(0.06)
−20.65	4.47	408.42(0.03)	−378.00(0.04)	−17.66	3.04	401.00(0.03)	−391.12(0.04)
−21.08	1.45	403.31(0.04)	−387.75(0.06)	−17.66	8.79	403.17(0.01)	−387.89(0.01)
−21.08	2.20	408.50(0.03)	−376.38(0.05)	−17.88	6.55	401.29(0.02)	−391.28(0.02)
−21.08	2.15	409.00(0.03)	−377.46(0.04)	−17.88	8.43	403.42(0.02)	−387.98(0.02)
−21.30	2.17	403.56(0.05)	−385.30(0.10)	−18.10	10.31	401.53(0.02)	−391.47(0.02)
−21.30	4.36	408.85(0.03)	−376.79(0.05)	−18.10	10.64	403.92(0.02)	−388.14(0.02)
−21.51	3.88	409.30(0.05)	−374.95(0.07)	−18.31	10.95	401.72(0.02)	−391.65(0.03)
−21.73	3.52	409.42(0.04)	−375.58(0.09)	−18.31	14.10	404.11(0.02)	−388.21(0.02)
−21.73	3.20	410.65(0.05)	−384.01(0.07)	−18.53	6.86	402.00(0.03)	−391.86(0.04)
−21.95	3.90	403.84(0.04)	−386.37(0.06)	−18.53	10.87	404.30(0.02)	−388.25(0.02)
−21.95	4.09	409.67(0.04)	−376.00(0.06)	−18.53	11.23	405.42(0.01)	−385.60(0.02)
−21.95	3.77	411.69(0.05)	−385.65(0.07)	−18.75	6.80	402.34(0.03)	−392.16(0.04)
−22.17	4.21	403.93(0.03)	−386.53(0.04)	−18.75	7.04	404.72(0.03)	−388.43(0.04)
−22.17	5.83	409.68(0.02)	−376.10(0.04)	−18.75	11.67	405.54(0.02)	−385.69(0.02)
−22.38	2.68	404.06(0.03)	−386.77(0.05)	−18.97	9.53	405.57(0.02)	−386.03(0.04)
−22.38	4.51	409.78(0.02)	−376.25(0.04)	−18.97	4.34	405.74(0.03)	−386.96(0.05)
−22.60	2.12	410.01(0.03)	−376.56(0.05)	−19.19	8.49	381.85(0.03)	−371.25(0.03)
−22.82	1.24	404.28(0.05)	−387.13(0.05)	−19.19	6.84	401.37(0.03)	−395.76(0.03)
−22.82	2.21	409.49(0.03)	−378.42(0.04)	−19.19	8.33	406.38(0.03)	−385.38(0.04)
−23.04	1.40	409.38(0.03)	−378.43(0.05)	−19.41	12.56	381.69(0.02)	−371.09(0.02)
−23.04	1.33	410.53(0.07)	−384.93(0.06)	−19.41	11.85	401.59(0.02)	−395.95(0.02)
−23.25	0.87	408.69(0.05)	−378.78(0.11)	−19.41	14.59	406.86(0.02)	−385.67(0.02)
−23.25	0.91	410.12(0.06)	−384.79(0.06)	−19.63	9.06	381.59(0.02)	−370.98(0.02)
−23.47	0.74	409.36(0.12)	−384.42(0.08)	−19.63	10.77	401.78(0.02)	−396.13(0.02)
−23.69	1.32	409.11(0.04)	−384.30(0.04)	−19.63	26.25	407.07(0.01)	−385.66(0.01)
−23.90	1.40	408.96(0.03)	−384.24(0.04)	−19.85	36.95	407.24(0.00)	−385.69(0.01)
−27.38	1.83	398.01(0.03)	−397.86(0.04)	−20.06	29.08	407.45(0.01)	−385.75(0.01)
−27.60	1.49	398.01(0.03)	−397.70(0.04)	−20.28	15.29	407.66(0.01)	−385.78(0.02)
				−20.28	3.63	408.06(0.04)	−377.88(0.06)
				−20.50	2.67	407.81(0.05)	−386.03(0.06)

The observed SiO maser components in R13158D (2013-06-07) - (continued)

SiO (v=1 J=1−0)				SiO (v=2 J=1−0)			
$V_{\rm LSR}$ (km s^{-1})	I (Jy beam^{-1})	ΔRA (mas)	ΔDec (mas)	$V_{\rm LSR}$ (km s^{-1})	I (Jy beam^{-1})	ΔRA (mas)	ΔDec (mas)
				−20.50	3.14	407.99(0.04)	−385.31(0.05)
				−20.72	2.59	407.09(0.03)	−375.66(0.02)
				−20.72	12.81	407.78(0.01)	−377.03(0.02)
				−20.94	20.29	407.85(0.01)	−376.97(0.01)
				−21.16	20.07	407.98(0.01)	−376.86(0.01)
				−21.38	20.54	408.17(0.01)	−376.77(0.01)
				−21.60	14.23	408.24(0.01)	−376.76(0.01)
				−21.60	11.37	408.70(0.01)	−376.38(0.01)
				−21.82	7.20	408.74(0.01)	−376.45(0.01)
				−21.82	2.91	409.03(0.03)	−374.79(0.03)
				−21.82	2.91	409.42(0.02)	−379.60(0.03)
				−22.03	1.73	409.44(0.03)	−379.55(0.05)
				−22.03	4.28	409.58(0.01)	−375.88(0.02)
				−22.25	9.56	409.62(0.01)	−376.04(0.01)
				−22.47	10.01	409.68(0.01)	−376.16(0.01)
				−22.69	2.67	408.66(0.03)	−379.28(0.04)
				−22.69	3.73	409.73(0.02)	−376.25(0.03)
				−22.91	7.26	408.53(0.01)	−379.25(0.01)
				−22.91	1.64	409.47(0.04)	−380.73(0.06)
				−23.13	11.78	408.46(0.01)	−379.25(0.01)
				−23.35	11.13	408.44(0.01)	−379.29(0.01)
				−23.35	3.60	408.50(0.03)	−384.24(0.04)
				−23.57	4.01	408.37(0.02)	−384.25(0.02)
				−23.57	5.29	408.43(0.01)	−379.30(0.01)
				−23.78	1.87	408.12(0.03)	−384.20(0.02)
				−24.00	0.98	407.83(0.04)	−384.08(0.05)
				−24.00	0.98	408.16(0.04)	−380.71(0.04)

The observed SiO maser components in R13255A (2013-09-12)

SiO (v=1 J=1−0)				SiO (v=2 J=1−0)			
$V_{\rm LSR}$ (km s^{-1})	I (Jy beam^{-1})	ΔRA (mas)	ΔDec (mas)	$V_{\rm LSR}$ (km s^{-1})	I (Jy beam^{-1})	ΔRA (mas)	ΔDec (mas)
−16.08	1.07	403.67(0.06)	−396.21(0.06)	−13.28	0.99	401.81(0.04)	−400.59(0.05)
−16.30	1.10	403.09(0.05)	−399.58(0.06)	−13.50	3.09	401.90(0.01)	−400.52(0.02)
−16.52	1.08	403.68(0.06)	−398.28(0.06)	−13.72	1.16	400.33(0.04)	−406.82(0.06)
−18.47	1.60	409.52(0.04)	−393.69(0.05)	−13.72	4.57	401.93(0.01)	−400.59(0.02)
−18.69	7.04	409.76(0.01)	−393.92(0.01)	−13.94	5.92	401.99(0.01)	−400.68(0.01)
−18.91	1.49	410.05(0.05)	−394.09(0.06)	−14.16	1.68	400.33(0.04)	−407.00(0.05)
−19.13	0.97	410.34(0.06)	−394.50(0.08)	−14.16	10.61	402.03(0.01)	−400.79(0.01)
				−14.38	6.19	402.12(0.01)	−400.82(0.02)
				−14.60	3.84	402.19(0.01)	−401.06(0.02)
				−14.60	3.55	402.48(0.01)	−400.33(0.02)
				−14.81	3.25	402.56(0.02)	−400.49(0.04)
				−15.03	3.19	402.62(0.01)	−400.49(0.02)
				−15.03	3.73	403.03(0.01)	−399.99(0.02)
				−15.25	2.52	402.76(0.01)	−400.56(0.03)
				−15.25	3.17	403.17(0.01)	−400.13(0.02)
				−15.47	2.02	402.82(0.02)	−400.55(0.03)
				−15.47	2.25	403.25(0.01)	−400.24(0.03)
				−15.69	1.36	403.22(0.04)	−400.51(0.05)
				−15.91	0.91	403.64(0.06)	−400.39(0.10)
				−16.13	1.44	403.83(0.03)	−400.21(0.07)
				−16.35	1.67	404.00(0.03)	−400.87(0.05)
				−16.56	1.45	404.28(0.03)	−401.11(0.07)
				−16.78	1.03	404.32(0.03)	−402.13(0.07)
				−16.78	2.02	404.69(0.02)	−400.96(0.04)
				−17.00	2.68	404.48(0.02)	−402.27(0.03)
				−17.00	3.17	404.89(0.02)	−401.17(0.03)
				−17.22	2.66	404.67(0.02)	−402.43(0.03)
				−17.22	3.02	405.12(0.02)	−401.26(0.03)

The observed SiO maser components in R13255A (2013-09-12) - (continued)

SiO (v=1 J=1−0)				SiO (v=2 J=1−0)			
$V_{\rm LSR}$ (km s^{-1})	I (Jy beam^{-1})	ΔRA (mas)	ΔDec (mas)	$V_{\rm LSR}$ (km s^{-1})	I (Jy beam^{-1})	ΔRA (mas)	ΔDec (mas)
				−17.44	4.37	405.50(0.02)	−401.32(0.02)
				−17.66	4.13	405.73(0.01)	−401.49(0.02)
				−17.88	2.63	406.03(0.02)	−401.76(0.03)
				−18.10	1.35	386.02(0.03)	−383.01(0.04)
				−18.10	1.65	386.32(0.02)	−382.63(0.04)
				−18.10	1.48	406.37(0.03)	−402.10(0.05)
				−18.10	1.13	409.61(0.04)	−395.90(0.06)
				−18.32	2.41	386.16(0.02)	−382.63(0.04)
				−18.32	3.44	409.76(0.02)	−395.83(0.02)
				−18.53	2.79	386.13(0.02)	−382.43(0.03)
				−18.53	4.72	409.94(0.02)	−395.80(0.02)
				−18.75	2.58	386.10(0.02)	−382.24(0.04)
				−18.75	3.44	410.12(0.02)	−395.82(0.02)
				−18.97	1.48	386.11(0.03)	−382.03(0.06)
				−18.97	2.87	405.34(0.02)	−406.75(0.04)
				−19.19	3.08	405.49(0.02)	−406.95(0.03)
				−19.41	1.43	405.75(0.03)	−407.41(0.06)
				−20.72	1.16	412.57(0.03)	−388.02(0.04)
				−20.94	1.46	412.17(0.02)	−386.24(0.04)
				−20.94	1.31	412.53(0.03)	−387.88(0.04)
				−21.16	1.97	412.31(0.02)	−386.37(0.04)
				−21.38	0.98	412.48(0.04)	−386.50(0.09)

The observed SiO maser components in R14026A (2014-01-26)

SiO (v=1 J=1−0)				SiO (v=2 J=1−0)			
$V_{\rm LSR}$ (km s^{-1})	I (Jy beam^{-1})	ΔRA (mas)	ΔDec (mas)	$V_{\rm LSR}$ (km s^{-1})	I (Jy beam^{-1})	ΔRA (mas)	ΔDec (mas)
−13.48	0.60	412.91(0.04)	−407.51(0.05)	−14.38	0.66	411.21(0.03)	−410.01(0.07)
−13.69	0.61	412.93(0.04)	−407.63(0.05)	−14.60	1.17	411.29(0.02)	−410.12(0.03)
−13.91	0.59	413.06(0.04)	−407.75(0.05)	−14.81	0.99	411.38(0.02)	−410.20(0.03)
−14.13	0.78	413.03(0.03)	−407.73(0.04)	−14.81	0.86	412.47(0.02)	−408.05(0.03)
−14.35	1.03	413.23(0.02)	−407.84(0.03)	−15.03	1.45	412.53(0.02)	−408.19(0.04)
−14.56	1.05	413.31(0.03)	−407.81(0.05)	−15.25	2.01	412.64(0.01)	−408.28(0.03)
−14.78	0.75	413.45(0.05)	−407.85(0.05)	−15.47	1.04	411.76(0.02)	−410.96(0.05)
−15.00	1.04	402.36(0.03)	−416.12(0.05)	−15.47	2.67	412.72(0.01)	−408.57(0.02)
−15.22	1.06	402.43(0.03)	−416.23(0.05)	−15.69	1.51	411.90(0.02)	−411.11(0.05)
−15.65	0.86	408.31(0.03)	−415.95(0.04)	−15.69	3.60	412.82(0.01)	−408.74(0.01)
−15.65	0.70	410.92(0.04)	−414.40(0.05)	−15.91	2.98	411.44(0.01)	−412.60(0.02)
−15.65	1.26	412.42(0.02)	−412.95(0.03)	−15.91	4.43	412.92(0.01)	−408.85(0.01)
−15.87	0.61	408.62(0.06)	−416.30(0.06)	−16.13	4.06	411.61(0.01)	−412.80(0.02)
−15.87	1.71	412.64(0.01)	−413.12(0.03)	−16.13	4.52	413.06(0.01)	−408.92(0.02)
−16.08	2.03	412.79(0.02)	−413.50(0.04)	−16.35	3.37	411.84(0.01)	−413.07(0.03)
−16.30	4.96	413.49(0.01)	−412.35(0.01)	−16.35	4.01	412.35(0.01)	−411.77(0.02)
−16.52	8.87	413.63(0.00)	−412.46(0.01)	−16.35	1.81	412.85(0.02)	−410.50(0.03)
−16.74	11.82	413.78(0.00)	−412.59(0.01)	−16.35	4.58	413.22(0.01)	−408.99(0.01)
−16.95	8.73	413.98(0.01)	−412.78(0.01)	−16.57	3.24	412.02(0.01)	−413.18(0.02)
−17.17	7.14	414.25(0.01)	−413.04(0.01)	−16.57	10.46	412.44(0.00)	−411.97(0.01)
−17.39	5.88	414.48(0.01)	−413.23(0.02)	−16.57	4.14	413.41(0.01)	−409.05(0.02)
−17.61	3.90	414.71(0.02)	−413.43(0.02)	−16.78	13.42	412.60(0.00)	−412.03(0.01)
−17.82	2.32	415.03(0.03)	−413.64(0.04)	−16.78	2.94	413.04(0.02)	−410.70(0.03)
−18.04	2.03	415.37(0.02)	−413.70(0.04)	−17.00	14.24	412.74(0.00)	−412.16(0.01)
−18.04	1.26	418.03(0.03)	−409.33(0.09)	−17.22	8.34	412.93(0.01)	−412.29(0.01)
−18.26	1.67	414.98(0.03)	−415.42(0.05)	−17.44	1.78	412.34(0.02)	−413.94(0.04)
−18.26	1.21	418.93(0.04)	−408.12(0.08)	−17.44	4.01	413.23(0.02)	−412.48(0.02)
−18.47	1.66	412.86(0.05)	−412.90(0.06)	−17.66	2.22	413.42(0.02)	−412.61(0.02)
−18.69	1.87	413.12(0.06)	−413.13(0.09)	−17.88	0.91	413.53(0.04)	−412.75(0.07)
−19.13	3.04	390.31(0.02)	−393.33(0.04)	−18.10	0.67	413.93(0.05)	−412.50(0.08)
−19.13	3.27	394.22(0.03)	−390.26(0.03)	−18.32	0.72	413.61(0.04)	−414.72(0.10)
−19.34	4.79	390.25(0.01)	−393.32(0.02)	−18.75	0.94	393.96(0.02)	−389.86(0.04)
−19.34	4.83	394.16(0.01)	−390.25(0.02)	−18.75	1.23	412.69(0.02)	−418.14(0.03)

The observed SiO maser components in R14026A (2014-01-26) - (continued)

SiO (v=1 J=1−0)				SiO (v=2 J=1−0)			
$V_{\rm LSR}$ (km s^{-1})	I (Jy beam^{-1})	ΔRA (mas)	ΔDec (mas)	$V_{\rm LSR}$ (km s^{-1})	I (Jy beam^{-1})	ΔRA (mas)	ΔDec (mas)
−19.56	2.89	390.22(0.02)	−393.32(0.03)	−18.97	1.67	393.71(0.03)	−389.86(0.03)
−19.56	4.52	391.99(0.01)	−391.73(0.02)	−18.97	3.06	412.93(0.01)	−418.44(0.02)
−19.56	2.86	394.14(0.02)	−390.25(0.03)	−19.19	2.05	393.49(0.05)	−389.83(0.04)
−19.56	2.06	422.86(0.05)	−406.85(0.04)	−19.19	3.74	413.28(0.02)	−418.93(0.03)
−19.78	7.00	391.95(0.01)	−391.71(0.02)	−19.41	3.92	413.76(0.03)	−419.54(0.04)
−19.78	4.19	423.28(0.03)	−407.01(0.02)	−19.63	2.10	414.13(0.03)	−419.98(0.04)
−20.00	6.12	391.91(0.01)	−391.72(0.02)	−19.85	1.55	390.87(0.03)	−391.09(0.05)
−20.00	5.05	423.74(0.02)	−407.11(0.02)	−19.85	2.70	421.95(0.03)	−406.59(0.02)
−20.21	4.28	391.85(0.01)	−391.73(0.02)	−20.07	1.44	390.82(0.04)	−391.05(0.05)
−20.21	2.81	424.07(0.02)	−407.21(0.02)	−20.07	4.51	422.50(0.02)	−406.75(0.02)
−20.43	2.35	391.76(0.02)	−391.73(0.02)	−20.29	1.98	419.29(0.03)	−402.37(0.04)
−20.43	1.13	422.71(0.04)	−397.50(0.05)	−20.29	3.59	422.75(0.02)	−406.97(0.02)
−20.65	1.00	391.67(0.03)	−391.63(0.04)	−20.29	1.62	423.59(0.04)	−405.21(0.05)
−20.65	0.95	422.79(0.04)	−397.53(0.06)	−20.50	3.97	419.27(0.01)	−402.40(0.02)
−20.86	0.96	422.18(0.02)	−397.65(0.04)	−20.50	3.30	419.90(0.02)	−401.88(0.02)
−20.86	0.58	422.86(0.03)	−397.44(0.07)	−20.72	1.56	407.89(0.03)	−415.52(0.04)
−21.08	2.41	422.07(0.01)	−397.76(0.02)	−20.72	4.22	418.93(0.01)	−403.46(0.02)
−21.08	0.86	422.71(0.03)	−396.15(0.04)	−20.94	1.62	407.90(0.03)	−415.52(0.04)
−21.30	2.33	422.06(0.01)	−397.79(0.02)	−20.94	2.69	418.94(0.02)	−403.41(0.02)
−21.52	1.22	422.26(0.02)	−402.71(0.03)	−20.94	2.79	419.37(0.01)	−402.22(0.03)
−21.73	3.41	422.23(0.01)	−402.62(0.01)	−21.16	1.63	417.79(0.03)	−403.44(0.03)
−21.95	4.42	422.24(0.01)	−402.59(0.01)	−21.16	2.05	419.43(0.01)	−402.07(0.03)
−22.17	3.41	422.27(0.01)	−402.54(0.01)	−21.38	1.46	417.73(0.03)	−403.35(0.03)
−22.39	1.64	422.36(0.01)	−402.38(0.02)	−21.38	1.06	419.58(0.03)	−402.44(0.09)
−22.39	0.81	422.94(0.02)	−401.86(0.05)	−21.60	0.98	417.58(0.04)	−403.31(0.04)
−22.60	0.61	422.70(0.04)	−402.11(0.06)	−21.82	0.90	421.05(0.02)	−402.04(0.04)
−22.60	0.64	422.99(0.04)	−401.41(0.10)	−22.04	1.88	421.06(0.01)	−402.03(0.02)
−23.04	0.62	416.25(0.03)	−388.11(0.05)	−22.25	1.30	421.06(0.02)	−402.00(0.03)
−23.25	0.68	403.58(0.03)	−387.83(0.05)	−22.47	0.65	419.69(0.05)	−400.66(0.04)
−23.25	0.76	416.22(0.03)	−388.29(0.04)	−22.69	0.81	419.68(0.03)	−400.58(0.04)
−23.47	1.32	403.53(0.02)	−387.83(0.03)	−22.91	1.00	419.66(0.02)	−400.42(0.03)
−23.69	1.28	403.53(0.02)	−387.86(0.03)	−23.13	0.86	419.64(0.03)	−400.23(0.06)
−23.91	0.80	403.67(0.03)	−387.89(0.04)	−23.35	1.09	405.76(0.02)	−388.11(0.04)
				−23.57	2.27	405.85(0.03)	−388.10(0.02)
				−23.79	4.29	403.83(0.01)	−388.70(0.02)
				−23.79	2.23	405.93(0.04)	−388.24(0.02)
				−24.01	8.05	403.85(0.01)	−388.75(0.01)
				−24.22	9.18	403.89(0.01)	−388.87(0.01)
				−24.22	5.09	404.65(0.01)	−388.67(0.02)
				−24.44	5.58	403.97(0.01)	−388.94(0.01)
				−24.44	3.02	404.72(0.01)	−388.71(0.02)
				−24.66	1.33	404.05(0.02)	−388.87(0.03)
				−24.88	1.06	415.55(0.02)	−389.44(0.04)
				−25.10	1.19	415.60(0.01)	−389.42(0.04)
				−25.10	0.90	415.75(0.02)	−390.62(0.02)
				−25.32	0.70	415.63(0.02)	−389.21(0.06)
				−25.54	0.47	415.72(0.03)	−389.02(0.05)

The observed SiO maser components in R14051A (2014-02-20)

SiO (v=1 J=1−0)				SiO (v=2 J=1−0)			
$V_{\rm LSR}$ (km s^{-1})	I (Jy beam^{-1})	ΔRA (mas)	ΔDec (mas)	$V_{\rm LSR}$ (km s^{-1})	I (Jy beam^{-1})	ΔRA (mas)	ΔDec (mas)
−13.69	0.78	416.01(0.02)	−409.76(0.03)	−15.03	0.58	416.92(0.03)	−410.70(0.06)
−13.91	1.07	416.07(0.02)	−409.75(0.02)	−15.25	0.78	417.02(0.03)	−410.82(0.05)
−14.13	0.92	416.13(0.02)	−409.80(0.03)	−15.47	1.03	416.98(0.02)	−411.34(0.04)
−14.35	0.77	405.49(0.03)	−417.86(0.04)	−15.69	0.98	416.63(0.02)	−412.83(0.05)
−14.35	0.70	416.25(0.03)	−409.77(0.04)	−15.69	1.33	417.08(0.02)	−411.58(0.04)
−14.56	2.29	405.50(0.01)	−417.90(0.02)	−15.91	1.37	416.78(0.02)	−412.84(0.05)
−14.78	3.18	405.52(0.01)	−417.99(0.02)	−15.91	2.01	417.23(0.02)	−411.57(0.03)
−15.00	3.00	405.58(0.01)	−418.15(0.02)	−16.13	1.64	416.38(0.03)	−414.53(0.04)

The observed SiO maser components in R14051A (2014-02-20) - (continued)

SiO (v=1 J=1−0)				SiO (v=2 J=1−0)			
$V_{\rm LSR}$ (km s^{-1})	I (Jy beam^{-1})	ΔRA (mas)	ΔDec (mas)	$V_{\rm LSR}$ (km s^{-1})	I (Jy beam^{-1})	ΔRA (mas)	ΔDec (mas)
−15.00	0.89	415.72(0.05)	−412.73(0.08)	−16.13	2.40	417.37(0.02)	−411.55(0.03)
−15.21	2.24	405.67(0.02)	−418.36(0.03)	−16.35	1.64	415.52(0.03)	−417.55(0.05)
−15.21	1.20	416.98(0.04)	−410.24(0.05)	−16.35	3.78	416.62(0.02)	−414.56(0.02)
−15.43	1.33	405.74(0.03)	−418.51(0.03)	−16.35	2.46	417.56(0.02)	−411.51(0.03)
−15.65	1.09	414.18(0.04)	−416.47(0.04)	−16.56	2.67	415.63(0.03)	−417.75(0.05)
−15.87	1.39	414.28(0.02)	−416.54(0.03)	−16.56	2.72	416.23(0.03)	−416.17(0.05)
−15.87	0.82	415.74(0.04)	−415.78(0.06)	−16.56	6.75	416.77(0.01)	−414.67(0.02)
−16.08	1.29	412.31(0.02)	−418.85(0.03)	−16.56	2.78	417.27(0.03)	−413.11(0.05)
−16.08	0.97	414.32(0.03)	−416.63(0.04)	−16.78	8.23	416.92(0.01)	−414.78(0.02)
−16.08	2.32	416.56(0.01)	−414.35(0.02)	−17.00	2.44	415.80(0.04)	−417.97(0.05)
−16.30	1.15	410.89(0.03)	−420.03(0.06)	−17.00	5.98	417.09(0.02)	−414.89(0.02)
−16.30	1.68	412.40(0.03)	−418.95(0.04)	−17.00	2.61	418.36(0.03)	−411.78(0.04)
−16.30	6.50	416.72(0.01)	−414.53(0.01)	−17.22	1.61	415.98(0.04)	−418.04(0.06)
−16.52	11.28	416.84(0.01)	−414.66(0.01)	−17.22	3.53	417.34(0.02)	−415.01(0.02)
−16.74	12.67	416.99(0.01)	−414.79(0.01)	−17.22	1.62	418.68(0.04)	−411.96(0.05)
−16.95	2.48	416.40(0.03)	−416.27(0.04)	−17.44	1.94	417.58(0.02)	−415.15(0.03)
−16.95	8.66	417.21(0.01)	−414.94(0.01)	−17.44	1.18	419.10(0.04)	−412.19(0.04)
−16.95	1.76	418.10(0.04)	−413.52(0.05)	−17.66	0.98	417.86(0.04)	−415.19(0.05)
−17.17	3.98	416.64(0.04)	−416.50(0.05)	−17.66	1.02	419.45(0.03)	−412.30(0.04)
−17.17	6.94	417.43(0.02)	−415.13(0.03)	−17.88	0.75	417.30(0.02)	−416.94(0.04)
−17.39	2.52	416.86(0.05)	−416.74(0.06)	−17.88	0.67	419.75(0.03)	−412.33(0.03)
−17.39	4.42	417.71(0.02)	−415.35(0.03)	−18.10	0.79	417.39(0.03)	−416.93(0.04)
−17.61	3.28	418.01(0.02)	−415.53(0.02)	−18.75	1.09	417.00(0.02)	−420.85(0.03)
−17.82	2.95	418.21(0.01)	−415.57(0.03)	−18.97	2.40	417.32(0.02)	−421.25(0.03)
−17.82	1.61	420.15(0.03)	−412.33(0.03)	−19.19	3.07	417.66(0.02)	−421.69(0.03)
−18.04	1.58	420.51(0.04)	−412.42(0.04)	−19.41	2.05	418.09(0.05)	−422.24(0.07)
−18.26	1.51	415.95(0.06)	−419.62(0.08)	−19.85	2.06	426.16(0.05)	−409.20(0.04)
−18.26	1.48	420.86(0.06)	−412.45(0.06)	−20.07	2.14	426.78(0.05)	−409.39(0.04)
−18.47	1.55	416.07(0.05)	−419.70(0.07)	−20.29	2.42	423.43(0.02)	−405.02(0.02)
−18.47	1.04	421.40(0.08)	−412.67(0.09)	−20.29	2.29	423.50(0.02)	−405.86(0.04)
−18.69	1.71	416.71(0.05)	−420.39(0.07)	−20.29	1.59	427.03(0.03)	−409.49(0.03)
−18.91	2.07	393.17(0.04)	−394.86(0.04)	−20.50	2.64	423.46(0.01)	−405.17(0.03)
−18.91	2.01	397.36(0.04)	−391.86(0.04)	−20.50	1.47	423.63(0.04)	−406.28(0.05)
−18.91	1.36	416.95(0.07)	−420.83(0.09)	−20.72	1.91	423.13(0.04)	−405.88(0.07)
−19.13	4.95	393.07(0.02)	−394.92(0.02)	−20.94	1.14	422.83(0.03)	−406.82(0.03)
−19.13	3.52	397.38(0.03)	−391.92(0.03)	−20.94	3.26	422.98(0.02)	−405.73(0.03)
−19.34	6.59	393.02(0.01)	−395.03(0.02)	−20.94	1.25	423.34(0.02)	−404.81(0.05)
−19.34	3.15	397.42(0.04)	−391.91(0.03)	−21.16	1.18	422.73(0.05)	−406.97(0.04)
−19.56	6.85	392.93(0.01)	−395.11(0.02)	−21.16	2.85	422.84(0.02)	−405.83(0.03)
−19.56	2.36	396.46(0.04)	−391.97(0.04)	−21.38	1.13	422.27(0.02)	−407.25(0.03)
−19.56	5.11	425.96(0.03)	−408.92(0.02)	−21.38	1.13	422.77(0.03)	−405.75(0.04)
−19.78	5.31	392.84(0.02)	−395.14(0.02)	−21.60	0.56	421.29(0.03)	−405.69(0.04)
−19.78	2.08	396.47(0.04)	−392.06(0.05)	−21.60	0.79	422.05(0.03)	−407.30(0.03)
−19.78	8.29	426.40(0.02)	−409.02(0.01)	−22.04	0.58	425.13(0.02)	−404.56(0.04)
−20.00	3.24	392.77(0.02)	−395.19(0.03)	−22.25	0.44	425.20(0.03)	−404.63(0.05)
−20.00	2.10	394.68(0.03)	−393.44(0.04)	−22.69	0.50	410.69(0.03)	−389.27(0.05)
−20.00	5.95	426.71(0.01)	−409.10(0.01)	−22.91	0.51	410.56(0.03)	−389.37(0.07)
−20.21	1.86	392.71(0.02)	−395.26(0.03)	−23.13	0.86	410.65(0.04)	−390.04(0.06)
−20.21	2.96	394.65(0.01)	−393.50(0.02)	−23.35	1.77	410.66(0.04)	−390.30(0.05)
−20.21	1.80	427.23(0.03)	−409.27(0.03)	−23.57	2.01	410.43(0.03)	−392.36(0.02)
−20.43	2.97	394.62(0.01)	−393.54(0.02)	−23.79	1.25	409.72(0.04)	−390.96(0.03)
−20.43	1.11	428.76(0.04)	−409.81(0.05)	−23.79	1.69	410.08(0.05)	−392.53(0.03)
−20.65	1.58	394.53(0.02)	−393.54(0.02)	−24.01	2.93	408.97(0.03)	−391.18(0.02)
−20.65	0.82	425.85(0.04)	−401.47(0.05)	−24.01	1.63	409.89(0.03)	−391.17(0.04)
−20.65	1.68	429.02(0.03)	−409.94(0.02)	−24.01	2.14	410.49(0.02)	−390.98(0.03)
−20.86	1.33	425.30(0.02)	−399.67(0.03)	−24.22	2.91	408.84(0.02)	−391.30(0.02)
−20.86	1.10	429.54(0.04)	−410.27(0.05)	−24.44	1.16	407.71(0.05)	−391.54(0.03)
−21.08	1.47	425.23(0.02)	−399.78(0.04)	−24.44	2.04	408.75(0.02)	−391.45(0.02)
−21.08	2.17	425.74(0.02)	−399.57(0.03)	−24.66	0.74	408.66(0.03)	−391.55(0.03)
−21.30	2.16	425.66(0.02)	−399.25(0.03)	−24.88	0.46	418.55(0.03)	−395.10(0.05)
−21.52	0.88	424.92(0.03)	−398.59(0.04)	−24.88	0.80	419.76(0.02)	−391.96(0.03)
−21.52	1.55	425.20(0.02)	−404.76(0.03)	−25.10	0.38	419.31(0.03)	−393.23(0.06)
−21.52	1.85	425.72(0.02)	−399.12(0.03)	−25.10	0.64	419.80(0.02)	−391.93(0.04)

The observed SiO maser components in R14051A (2014-02-20) - (continued)

SiO (v=1 J=1−0)				SiO (v=2 J=1−0)			
$V_{\rm LSR}$ (km s^{-1})	I (Jy beam^{-1})	ΔRA (mas)	ΔDec (mas)	$V_{\rm LSR}$ (km s^{-1})	I (Jy beam^{-1})	ΔRA (mas)	ΔDec (mas)
−21.73	2.25	425.22(0.01)	−404.78(0.02)	−25.32	0.42	418.66(0.03)	−394.93(0.04)
−21.73	1.09	425.83(0.02)	−399.04(0.04)	−25.32	0.70	419.89(0.02)	−391.81(0.03)
−21.95	1.69	425.25(0.01)	−404.76(0.03)	−25.54	0.52	419.90(0.02)	−391.72(0.04)
−21.95	0.76	426.34(0.02)	−402.08(0.04)				
−22.17	0.98	426.11(0.03)	−403.70(0.04)				
−22.39	2.41	426.17(0.01)	−403.82(0.02)				
−22.60	0.63	409.45(0.04)	−388.68(0.05)				
−22.60	2.18	426.19(0.01)	−403.78(0.02)				
−22.82	1.16	409.18(0.02)	−388.70(0.03)				
−22.82	0.96	426.20(0.02)	−403.64(0.03)				
−23.04	1.47	409.02(0.02)	−388.82(0.03)				
−23.04	1.10	419.27(0.03)	−390.24(0.04)				
−23.25	0.82	406.88(0.03)	−390.18(0.04)				
−23.25	0.85	407.43(0.03)	−388.43(0.04)				
−23.25	0.75	407.73(0.04)	−391.39(0.04)				
−23.25	0.82	408.26(0.03)	−389.72(0.04)				
−23.25	1.27	408.88(0.03)	−388.72(0.06)				
−23.25	1.27	419.27(0.02)	−390.35(0.03)				
−23.47	0.78	407.42(0.03)	−388.45(0.04)				
−23.47	2.25	408.21(0.01)	−389.84(0.02)				
−23.47	0.96	419.30(0.03)	−390.41(0.05)				
−23.69	0.74	406.90(0.03)	−390.16(0.04)				
−23.69	0.77	407.46(0.03)	−388.48(0.03)				
−23.69	2.60	408.21(0.01)	−389.89(0.01)				
−23.91	1.55	408.16(0.01)	−389.99(0.02)				
−24.12	0.61	408.01(0.04)	−390.10(0.03)				

The observed SiO maser components in R14086A (2014-03-27)

SiO (v=1 J=1−0)				SiO (v=2 J=1−0)			
$V_{\rm LSR}$ (km s^{-1})	I (Jy beam^{-1})	ΔRA (mas)	ΔDec (mas)	$V_{\rm LSR}$ (km s^{-1})	I (Jy beam^{-1})	ΔRA (mas)	ΔDec (mas)
−14.78	0.56	419.28(0.05)	−414.56(0.07)	−14.38	0.49	417.64(0.05)	−416.16(0.06)
−15.00	0.60	419.50(0.04)	−414.68(0.05)	−14.60	0.54	417.76(0.05)	−416.25(0.09)
−15.00	0.51	421.51(0.06)	−411.05(0.07)	−14.81	0.70	417.90(0.03)	−416.44(0.04)
−15.21	0.81	418.06(0.04)	−416.52(0.05)	−14.81	0.76	419.35(0.03)	−414.61(0.04)
−15.21	0.82	421.45(0.04)	−410.93(0.05)	−14.81	1.71	421.28(0.01)	−411.32(0.02)
−15.43	1.07	418.37(0.04)	−416.96(0.05)	−15.03	0.79	418.12(0.03)	−416.69(0.04)
−15.43	0.96	421.48(0.04)	−410.82(0.05)	−15.03	0.81	419.60(0.03)	−414.70(0.04)
−15.65	1.02	416.13(0.04)	−419.04(0.05)	−15.03	2.54	421.33(0.01)	−411.29(0.01)
−15.65	1.74	418.48(0.02)	−417.11(0.03)	−15.25	0.93	418.25(0.03)	−416.82(0.04)
−15.87	1.64	416.19(0.02)	−419.06(0.03)	−15.25	0.68	420.51(0.03)	−413.34(0.05)
−15.87	1.26	418.51(0.03)	−417.19(0.03)	−15.25	2.45	421.40(0.01)	−411.34(0.01)
−15.87	0.81	420.52(0.03)	−414.84(0.05)	−15.47	1.36	418.37(0.02)	−417.04(0.03)
−16.08	0.98	417.00(0.03)	−417.67(0.04)	−15.47	3.06	421.24(0.01)	−411.89(0.01)
−16.08	2.12	420.73(0.01)	−414.97(0.02)	−15.47	2.15	421.60(0.01)	−411.25(0.02)
−16.30	5.54	420.90(0.01)	−415.10(0.02)	−15.69	0.93	418.50(0.06)	−417.27(0.05)
−16.52	2.49	420.36(0.05)	−416.54(0.06)	−15.69	1.61	419.81(0.02)	−416.24(0.04)
−16.52	9.13	421.04(0.01)	−415.22(0.02)	−15.69	5.55	421.35(0.01)	−412.00(0.01)
−16.74	11.88	421.21(0.01)	−415.36(0.01)	−15.69	1.28	421.78(0.02)	−411.22(0.04)
−16.95	9.38	421.45(0.01)	−415.53(0.02)	−15.91	3.02	419.95(0.02)	−416.28(0.03)
−17.17	1.79	421.01(0.04)	−416.98(0.05)	−15.91	7.35	421.48(0.01)	−412.07(0.01)
−17.17	6.87	421.67(0.01)	−415.64(0.01)	−16.13	5.23	420.09(0.01)	−416.37(0.02)
−17.39	2.07	421.21(0.02)	−417.33(0.03)	−16.13	1.68	421.18(0.05)	−413.93(0.05)
−17.39	3.65	421.95(0.01)	−415.85(0.02)	−16.13	8.54	421.66(0.01)	−412.09(0.01)
−17.39	1.18	423.61(0.05)	−412.66(0.04)	−16.35	7.84	420.23(0.01)	−416.51(0.02)
−17.60	2.61	422.12(0.03)	−415.99(0.04)	−16.35	9.25	421.87(0.01)	−412.12(0.01)
−17.82	1.84	422.46(0.03)	−416.27(0.06)	−16.56	9.62	420.33(0.01)	−416.68(0.02)
−17.82	1.55	424.47(0.05)	−412.75(0.04)	−16.56	3.38	421.11(0.04)	−415.60(0.06)
−17.82	3.36	426.77(0.02)	−408.24(0.02)	−16.56	3.03	421.73(0.04)	−414.03(0.06)
−18.04	2.32	422.72(0.03)	−416.71(0.04)	−16.56	10.36	422.10(0.01)	−412.18(0.01)

The observed SiO maser components in R14086A (2014-03-27) - (continued)

SiO (v=1 J=1−0)				SiO (v=2 J=1−0)			
$V_{\rm LSR}$ (km s^{-1})	I (Jy beam^{-1})	ΔRA (mas)	ΔDec (mas)	$V_{\rm LSR}$ (km s^{-1})	I (Jy beam^{-1})	ΔRA (mas)	ΔDec (mas)
−18.04	2.79	426.97(0.03)	−408.21(0.03)	−16.78	6.88	420.46(0.01)	−416.81(0.02)
−18.26	1.82	421.71(0.04)	−419.55(0.05)	−16.78	4.73	421.21(0.03)	−415.63(0.04)
−18.26	1.78	422.93(0.03)	−416.90(0.05)	−16.78	2.71	421.97(0.04)	−414.24(0.06)
−18.26	2.03	427.50(0.04)	−408.19(0.04)	−16.78	10.54	422.34(0.01)	−412.29(0.01)
−18.47	1.59	420.57(0.04)	−420.74(0.05)	−17.00	2.56	420.67(0.03)	−416.74(0.03)
−18.47	2.09	421.90(0.03)	−419.69(0.04)	−17.00	7.79	421.36(0.01)	−415.69(0.01)
−18.47	1.81	427.87(0.04)	−408.22(0.05)	−17.00	7.83	422.64(0.01)	−412.42(0.01)
−18.69	1.79	420.81(0.04)	−421.04(0.05)	−17.22	2.54	420.91(0.02)	−416.86(0.03)
−18.69	1.92	422.15(0.03)	−420.00(0.05)	−17.22	5.31	421.54(0.01)	−415.80(0.02)
−18.91	1.46	398.63(0.04)	−393.15(0.05)	−17.22	6.79	422.98(0.01)	−412.53(0.01)
−18.91	1.68	421.27(0.05)	−421.75(0.06)	−17.44	2.96	421.05(0.01)	−417.01(0.02)
−18.91	2.38	422.99(0.03)	−418.88(0.05)	−17.44	2.06	421.74(0.02)	−416.05(0.03)
−18.91	1.99	428.63(0.03)	−409.04(0.03)	−17.44	6.83	423.27(0.01)	−412.66(0.01)
−19.13	2.91	398.68(0.04)	−393.07(0.05)	−17.66	2.64	421.13(0.01)	−417.11(0.02)
−19.13	3.53	428.87(0.04)	−409.13(0.04)	−17.66	1.35	421.97(0.03)	−416.23(0.04)
−19.34	2.12	396.48(0.04)	−395.22(0.05)	−17.66	6.51	423.55(0.01)	−412.76(0.01)
−19.34	2.83	398.60(0.02)	−393.14(0.03)	−17.88	1.25	421.24(0.03)	−417.44(0.06)
−19.34	4.54	428.66(0.02)	−407.28(0.02)	−17.88	1.10	422.25(0.04)	−416.53(0.05)
−19.34	4.96	429.33(0.03)	−409.25(0.02)	−17.88	3.69	423.83(0.01)	−412.85(0.01)
−19.56	5.06	428.73(0.03)	−407.38(0.03)	−17.88	1.35	426.61(0.03)	−408.39(0.03)
−19.56	4.44	429.28(0.03)	−405.86(0.03)	−18.10	1.54	422.53(0.02)	−416.85(0.03)
−19.56	7.66	429.85(0.02)	−409.40(0.03)	−18.10	1.44	424.19(0.03)	−412.94(0.03)
−19.56	3.60	430.68(0.05)	−411.10(0.05)	−18.10	3.55	426.86(0.01)	−408.39(0.01)
−19.78	3.61	429.25(0.03)	−405.94(0.03)	−18.32	1.45	422.72(0.02)	−417.06(0.04)
−19.78	5.42	430.16(0.03)	−409.47(0.02)	−18.32	3.97	427.06(0.01)	−408.39(0.01)
−19.99	4.13	428.30(0.02)	−404.79(0.03)	−18.53	1.00	420.87(0.03)	−421.20(0.04)
−19.99	4.17	430.69(0.03)	−409.55(0.03)	−18.53	0.85	422.17(0.03)	−420.03(0.04)
−20.21	6.21	428.33(0.01)	−404.91(0.03)	−18.53	0.80	422.96(0.03)	−417.26(0.05)
−20.21	1.95	428.84(0.03)	−406.16(0.03)	−18.53	2.95	427.35(0.01)	−408.38(0.01)
−20.43	5.65	428.44(0.02)	−405.25(0.03)	−18.75	3.22	421.21(0.02)	−421.62(0.03)
−20.65	4.49	428.55(0.01)	−405.63(0.03)	−18.75	1.55	422.20(0.04)	−420.16(0.05)
−20.65	3.39	433.03(0.03)	−410.42(0.02)	−18.75	1.76	427.60(0.04)	−408.39(0.03)
−20.86	4.16	428.42(0.01)	−405.70(0.02)	−18.97	5.43	421.58(0.01)	−422.01(0.01)
−20.86	3.08	430.16(0.02)	−400.46(0.02)	−18.97	1.52	423.54(0.03)	−420.27(0.04)
−20.86	5.31	433.42(0.01)	−410.63(0.02)	−19.19	5.12	421.95(0.01)	−422.43(0.01)
−21.08	4.36	428.29(0.01)	−405.75(0.02)	−19.19	4.71	423.82(0.01)	−420.78(0.02)
−21.08	4.37	430.10(0.01)	−400.43(0.02)	−19.41	3.01	422.40(0.03)	−422.88(0.03)
−21.08	1.91	433.57(0.03)	−410.65(0.04)	−19.41	7.34	424.14(0.01)	−421.12(0.01)
−21.08	1.82	434.50(0.04)	−411.82(0.06)	−19.41	1.78	429.30(0.04)	−409.47(0.05)
−21.30	3.40	428.30(0.01)	−405.77(0.02)	−19.63	2.64	423.27(0.03)	−423.65(0.04)
−21.30	3.96	430.02(0.01)	−400.24(0.02)	−19.63	7.79	424.47(0.01)	−421.47(0.01)
−21.52	1.10	428.48(0.04)	−405.97(0.05)	−19.63	2.83	427.07(0.02)	−405.92(0.04)
−21.52	2.62	429.98(0.01)	−399.96(0.02)	−19.63	4.12	429.76(0.02)	−409.65(0.02)
−21.73	1.01	429.85(0.06)	−404.40(0.08)	−19.85	6.60	424.85(0.01)	−421.88(0.01)
−21.73	1.15	430.01(0.03)	−399.83(0.04)	−19.85	5.69	427.19(0.01)	−405.83(0.02)
−21.95	0.63	429.46(0.03)	−406.57(0.05)	−19.85	3.12	429.97(0.03)	−409.91(0.03)
−21.95	1.58	430.01(0.02)	−404.54(0.02)	−19.85	3.26	430.48(0.03)	−409.93(0.03)
−22.17	2.28	430.17(0.02)	−404.50(0.02)	−20.07	2.63	425.07(0.02)	−422.06(0.03)
−22.38	3.73	430.32(0.01)	−404.45(0.02)	−20.07	9.99	427.40(0.00)	−405.70(0.01)
−22.60	4.09	430.35(0.01)	−404.35(0.02)	−20.07	3.68	430.82(0.02)	−410.30(0.03)
−22.82	2.15	413.33(0.02)	−389.52(0.02)	−20.28	18.59	427.54(0.00)	−405.66(0.00)
−22.82	2.17	414.42(0.02)	−389.70(0.02)	−20.50	25.21	427.58(0.00)	−405.72(0.00)
−22.82	2.56	430.33(0.01)	−404.24(0.02)	−20.72	23.45	427.61(0.00)	−405.80(0.00)
−23.04	2.90	413.17(0.02)	−389.60(0.02)	−20.94	20.73	427.64(0.00)	−405.84(0.00)
−23.04	2.18	414.46(0.02)	−389.89(0.02)	−21.16	3.84	426.51(0.01)	−406.12(0.01)
−23.04	0.78	430.38(0.04)	−404.09(0.07)	−21.16	14.16	427.70(0.00)	−405.87(0.00)
−23.25	3.60	413.02(0.01)	−389.70(0.02)	−21.38	5.42	426.42(0.01)	−406.16(0.01)
−23.25	1.53	414.37(0.03)	−390.19(0.04)	−21.38	6.32	427.86(0.01)	−405.91(0.01)
−23.47	2.13	412.95(0.03)	−389.68(0.04)	−21.60	4.63	426.36(0.01)	−406.14(0.01)
−23.47	3.71	414.43(0.02)	−391.02(0.02)	−21.60	2.67	428.10(0.01)	−406.00(0.01)
−23.47	1.36	415.16(0.05)	−389.23(0.07)	−21.82	2.49	426.34(0.01)	−406.09(0.02)
−23.69	5.94	414.46(0.02)	−391.17(0.02)	−22.03	0.86	426.32(0.02)	−405.94(0.03)
−23.91	4.86	414.54(0.01)	−391.36(0.01)	−22.25	2.36	426.07(0.01)	−407.52(0.01)

The observed SiO maser components in R14086A (2014-03-27) - (continued)

SiO (v=1 J=1−0)				SiO (v=2 J=1−0)			
$V_{\rm LSR}$ (km s^{-1})	I (Jy beam^{-1})	ΔRA (mas)	ΔDec (mas)	$V_{\rm LSR}$ (km s^{-1})	I (Jy beam^{-1})	ΔRA (mas)	ΔDec (mas)
−23.91	1.37	415.19(0.04)	−389.64(0.04)	−22.47	4.32	425.95(0.01)	−407.56(0.01)
−24.12	1.33	413.10(0.03)	−391.41(0.03)	−22.69	0.75	413.68(0.03)	−389.62(0.04)
−24.12	3.10	414.53(0.01)	−391.52(0.01)	−22.69	1.64	414.55(0.02)	−389.91(0.02)
−24.34	1.26	413.01(0.03)	−391.55(0.02)	−22.69	3.77	425.86(0.01)	−407.58(0.01)
−24.34	1.17	414.53(0.03)	−391.60(0.02)	−22.69	0.72	426.59(0.04)	−401.51(0.05)
−24.56	0.65	412.97(0.05)	−391.64(0.04)	−22.91	1.14	413.55(0.03)	−389.80(0.03)
−25.21	0.41	423.97(0.04)	−392.35(0.07)	−22.91	4.40	414.57(0.01)	−390.08(0.01)
−25.43	0.48	423.98(0.03)	−392.25(0.05)	−22.91	1.46	425.69(0.02)	−407.58(0.03)
				−22.91	2.23	426.62(0.01)	−401.73(0.02)
				−23.13	7.27	414.63(0.01)	−390.59(0.01)
				−23.13	4.10	426.47(0.01)	−401.76(0.02)
				−23.35	15.03	414.52(0.01)	−391.10(0.01)
				−23.35	3.00	416.40(0.03)	−391.42(0.04)
				−23.35	5.18	426.32(0.02)	−401.79(0.02)
				−23.57	22.73	414.44(0.00)	−391.31(0.01)
				−23.57	6.18	416.34(0.01)	−391.59(0.02)
				−23.57	4.77	426.20(0.03)	−401.80(0.03)
				−23.79	16.06	414.40(0.01)	−391.54(0.01)
				−23.79	5.24	416.35(0.02)	−391.70(0.03)
				−23.79	4.36	417.96(0.03)	−393.53(0.02)
				−23.79	3.71	418.95(0.03)	−394.73(0.03)
				−24.00	2.33	413.59(0.01)	−392.01(0.02)
				−24.00	12.06	414.43(0.01)	−391.84(0.01)
				−24.00	6.57	417.90(0.02)	−393.47(0.01)
				−24.22	2.17	413.43(0.01)	−392.09(0.02)
				−24.22	8.20	414.35(0.01)	−392.03(0.01)
				−24.22	5.57	417.69(0.01)	−393.44(0.01)
				−24.22	3.52	418.39(0.01)	−393.42(0.01)
				−24.44	1.28	412.69(0.02)	−392.33(0.02)
				−24.44	2.25	413.42(0.02)	−392.12(0.02)
				−24.44	3.20	414.30(0.01)	−392.13(0.01)
				−24.44	2.15	417.62(0.02)	−393.36(0.02)
				−24.44	1.12	418.40(0.03)	−393.35(0.03)
				−24.66	0.68	410.66(0.04)	−420.16(0.04)
				−24.66	0.88	413.04(0.06)	−390.62(0.04)
				−24.66	1.65	423.94(0.01)	−392.41(0.03)
				−24.88	0.81	408.99(0.03)	−392.93(0.04)
				−24.88	0.93	410.71(0.02)	−420.15(0.04)
				−24.88	2.64	423.92(0.01)	−392.41(0.01)
				−25.10	1.47	408.90(0.02)	−393.08(0.02)
				−25.10	0.59	410.77(0.04)	−420.00(0.05)
				−25.10	3.55	423.96(0.01)	−392.38(0.01)
				−25.32	1.10	408.86(0.02)	−393.22(0.03)
				−25.32	3.58	423.99(0.01)	−392.36(0.01)
				−25.54	2.74	424.01(0.01)	−392.36(0.01)
				−25.75	0.97	424.01(0.02)	−392.38(0.03)

The observed SiO maser components in R14116D (2014-04-26)

SiO (v=1 J=1−0)				SiO (v=2 J=1−0)			
$V_{\rm LSR}$ (km s^{-1})	I (Jy beam^{-1})	ΔRA (mas)	ΔDec (mas)	$V_{\rm LSR}$ (km s^{-1})	I (Jy beam^{-1})	ΔRA (mas)	ΔDec (mas)
−14.35	0.57	422.86(0.03)	−416.32(0.04)	−14.16	0.71	421.37(0.04)	−417.75(0.05)
−14.56	0.68	422.99(0.04)	−416.46(0.05)	−14.38	0.83	421.56(0.04)	−417.99(0.04)
−14.78	0.81	413.97(0.03)	−420.96(0.05)	−14.59	1.10	421.68(0.02)	−418.16(0.03)
−14.78	0.72	423.23(0.03)	−416.53(0.05)	−14.59	1.28	425.17(0.01)	−412.97(0.02)
−15.00	1.09	414.06(0.03)	−421.07(0.04)	−14.81	1.40	421.87(0.02)	−418.31(0.02)
−15.00	0.80	425.20(0.06)	−412.70(0.07)	−14.81	2.40	425.22(0.01)	−413.02(0.01)
−15.21	0.76	425.41(0.08)	−412.89(0.07)	−15.03	1.53	422.04(0.02)	−418.47(0.02)
−15.43	0.68	413.83(0.04)	−421.58(0.06)	−15.03	2.83	425.26(0.01)	−413.07(0.01)
−15.43	0.86	425.44(0.04)	−412.93(0.05)	−15.25	1.41	422.21(0.03)	−418.68(0.03)

The observed SiO maser components in R14116D (2014-04-26) - (continued)

SiO (v=1 J=1−0)				SiO (v=2 J=1−0)			
$V_{\rm LSR}$ (km s^{-1})	I (Jy beam^{-1})	ΔRA (mas)	ΔDec (mas)	$V_{\rm LSR}$ (km s^{-1})	I (Jy beam^{-1})	ΔRA (mas)	ΔDec (mas)
−15.65	1.06	413.76(0.02)	−421.70(0.04)	−15.25	3.12	425.33(0.01)	−413.16(0.01)
−15.65	0.81	420.07(0.04)	−420.93(0.06)	−15.47	3.03	425.34(0.01)	−413.29(0.02)
−15.87	0.88	413.77(0.03)	−421.86(0.05)	−15.69	1.61	423.70(0.02)	−417.89(0.04)
−15.87	1.02	420.22(0.03)	−421.05(0.04)	−15.69	4.17	425.30(0.01)	−413.57(0.02)
−15.87	1.21	424.45(0.02)	−416.65(0.04)	−15.91	1.27	421.96(0.02)	−419.41(0.04)
−16.08	3.16	424.66(0.02)	−416.78(0.03)	−15.91	3.75	423.83(0.01)	−418.06(0.02)
−16.30	5.80	424.83(0.01)	−416.92(0.02)	−15.91	2.52	424.84(0.02)	−415.63(0.02)
−16.52	7.31	425.00(0.01)	−417.07(0.02)	−15.91	4.92	425.43(0.01)	−413.74(0.01)
−16.74	9.85	425.19(0.01)	−417.23(0.01)	−16.13	6.23	423.96(0.01)	−418.19(0.01)
−16.95	6.65	425.38(0.01)	−417.38(0.02)	−16.13	3.41	425.00(0.02)	−415.83(0.02)
−16.95	1.90	426.88(0.04)	−414.43(0.05)	−16.13	5.21	425.59(0.01)	−413.80(0.01)
−17.17	4.79	425.58(0.01)	−417.56(0.02)	−16.35	9.10	424.10(0.01)	−418.31(0.01)
−17.17	1.76	427.12(0.03)	−414.53(0.04)	−16.35	4.03	425.21(0.01)	−416.03(0.02)
−17.39	3.16	425.86(0.02)	−417.88(0.03)	−16.35	5.86	425.81(0.01)	−413.91(0.01)
−17.60	2.84	426.09(0.02)	−418.21(0.03)	−16.56	9.56	424.21(0.01)	−418.36(0.01)
−17.60	2.50	430.36(0.02)	−410.04(0.03)	−16.56	4.35	425.36(0.01)	−416.13(0.01)
−17.82	3.07	426.33(0.02)	−418.54(0.03)	−16.56	6.65	426.04(0.01)	−414.00(0.01)
−17.82	3.37	430.65(0.02)	−410.12(0.03)	−16.78	6.60	424.36(0.01)	−418.48(0.01)
−18.04	2.23	425.43(0.04)	−421.35(0.05)	−16.78	2.71	425.55(0.02)	−416.20(0.02)
−18.04	2.67	426.53(0.02)	−418.81(0.04)	−16.78	6.93	426.27(0.01)	−414.10(0.01)
−18.04	4.71	431.08(0.02)	−410.15(0.02)	−17.00	3.76	424.58(0.01)	−418.64(0.02)
−18.26	3.40	425.57(0.02)	−421.52(0.04)	−17.00	1.50	425.30(0.02)	−417.51(0.04)
−18.26	3.55	431.36(0.03)	−410.19(0.03)	−17.00	6.53	426.56(0.01)	−414.23(0.01)
−18.47	2.88	425.78(0.03)	−421.72(0.04)	−17.00	1.23	426.98(0.03)	−411.59(0.05)
−18.69	2.12	426.68(0.04)	−420.83(0.07)	−17.22	2.19	424.79(0.02)	−418.89(0.03)
−18.91	2.23	426.98(0.04)	−421.21(0.07)	−17.22	1.71	425.50(0.02)	−417.48(0.04)
−18.91	1.82	432.65(0.05)	−410.96(0.04)	−17.22	6.68	426.88(0.01)	−414.36(0.01)
−19.13	3.86	432.96(0.03)	−411.06(0.03)	−17.44	2.98	425.68(0.01)	−417.70(0.03)
−19.34	6.33	433.22(0.02)	−411.20(0.02)	−17.44	6.36	427.17(0.01)	−414.46(0.01)
−19.56	5.86	433.42(0.03)	−411.31(0.02)	−17.66	3.31	425.88(0.01)	−418.06(0.02)
−19.78	3.70	432.96(0.04)	−407.96(0.04)	−17.66	4.20	427.49(0.01)	−414.51(0.01)
−19.99	1.91	431.87(0.03)	−402.53(0.03)	−17.88	2.95	426.09(0.01)	−418.36(0.02)
−19.99	2.60	432.82(0.03)	−407.77(0.03)	−17.88	2.47	427.80(0.02)	−414.55(0.02)
−19.99	2.01	434.96(0.04)	−411.51(0.03)	−17.88	1.36	430.50(0.03)	−410.14(0.03)
−20.21	2.39	432.39(0.03)	−401.10(0.03)	−18.10	2.78	426.31(0.01)	−418.70(0.02)
−20.21	2.26	435.22(0.03)	−411.68(0.03)	−18.10	0.88	427.16(0.04)	−416.15(0.04)
−20.43	2.07	432.20(0.05)	−407.68(0.04)	−18.10	2.48	430.87(0.01)	−410.18(0.02)
−20.43	1.84	432.39(0.04)	−401.04(0.04)	−18.31	1.93	426.53(0.02)	−418.84(0.03)
−20.43	2.83	436.10(0.03)	−411.80(0.02)	−18.31	3.37	431.11(0.01)	−410.18(0.01)
−20.65	2.51	432.26(0.05)	−407.50(0.04)	−18.53	1.34	424.86(0.02)	−406.95(0.03)
−20.65	3.60	436.56(0.03)	−412.07(0.03)	−18.53	1.17	425.75(0.02)	−421.60(0.04)
−20.86	2.81	432.47(0.02)	−407.29(0.04)	−18.53	1.79	431.21(0.02)	−410.17(0.02)
−20.86	3.47	437.06(0.02)	−412.46(0.03)	−18.75	1.74	424.87(0.02)	−406.75(0.03)
−21.08	1.89	432.50(0.02)	−407.20(0.03)	−18.75	1.86	425.18(0.03)	−423.51(0.03)
−21.08	1.17	433.93(0.03)	−402.39(0.04)	−18.97	1.10	424.88(0.02)	−406.55(0.03)
−21.08	1.56	437.29(0.03)	−412.54(0.04)	−18.97	2.52	425.60(0.02)	−423.92(0.02)
−21.30	0.64	433.01(0.03)	−405.62(0.07)	−18.97	2.78	427.29(0.01)	−422.12(0.02)
−21.30	0.61	433.82(0.04)	−402.17(0.07)	−19.19	2.05	425.96(0.03)	−424.32(0.03)
−21.52	1.66	432.19(0.01)	−407.96(0.02)	−19.19	5.50	427.70(0.01)	−422.56(0.02)
−21.73	3.13	432.22(0.01)	−407.92(0.01)	−19.41	2.17	426.79(0.03)	−425.01(0.03)
−21.95	2.81	432.23(0.01)	−407.88(0.01)	−19.41	7.21	428.06(0.01)	−423.05(0.01)
−22.17	1.23	432.26(0.02)	−407.84(0.03)	−19.63	2.00	427.09(0.03)	−425.42(0.03)
−22.38	0.57	432.40(0.04)	−407.83(0.05)	−19.63	8.41	428.36(0.01)	−423.39(0.01)
−22.38	0.92	433.70(0.03)	−407.72(0.03)	−19.63	2.72	430.77(0.02)	−407.64(0.03)
−22.38	1.09	434.25(0.02)	−406.46(0.04)	−19.85	4.17	428.55(0.01)	−423.53(0.01)
−22.60	1.22	417.60(0.03)	−391.40(0.03)	−19.85	6.85	431.00(0.01)	−407.61(0.01)
−22.60	1.32	434.33(0.02)	−406.39(0.04)	−20.07	12.41	431.10(0.00)	−407.62(0.01)
−22.82	0.66	417.39(0.03)	−391.58(0.06)	−20.28	15.34	431.17(0.00)	−407.62(0.00)
−22.82	1.62	417.94(0.03)	−391.66(0.02)	−20.50	17.75	431.22(0.00)	−407.62(0.00)
−22.82	0.86	434.42(0.03)	−406.29(0.05)	−20.72	12.57	431.29(0.00)	−407.65(0.01)
−23.04	1.50	417.18(0.02)	−391.81(0.03)	−20.94	9.00	431.46(0.00)	−407.76(0.01)
−23.04	2.44	418.16(0.02)	−391.97(0.02)	−20.94	1.40	432.39(0.03)	−407.21(0.02)
−23.25	2.01	417.07(0.03)	−391.93(0.03)	−21.16	7.87	431.54(0.00)	−407.86(0.01)

The observed SiO maser components in R14116D (2014-04-26) - (continued)

SiO (v=1 J=1−0)				SiO (v=2 J=1−0)			
$V_{\rm LSR}$ (km s^{-1})	I (Jy beam^{-1})	ΔRA (mas)	ΔDec (mas)	$V_{\rm LSR}$ (km s^{-1})	I (Jy beam^{-1})	ΔRA (mas)	ΔDec (mas)
−23.25	3.11	418.33(0.01)	−392.43(0.04)	−21.16	1.63	432.37(0.02)	−407.25(0.02)
−23.25	1.37	419.87(0.03)	−392.52(0.04)	−21.38	8.04	431.51(0.00)	−407.98(0.01)
−23.47	4.10	418.21(0.02)	−393.05(0.05)	−21.60	7.43	431.47(0.00)	−408.02(0.01)
−23.47	2.53	419.74(0.04)	−392.72(0.04)	−21.82	1.27	430.31(0.02)	−408.36(0.02)
−23.69	4.91	418.14(0.02)	−393.31(0.02)	−21.82	3.62	431.47(0.01)	−408.07(0.01)
−23.90	3.90	418.30(0.02)	−393.51(0.02)	−22.03	2.01	430.42(0.01)	−408.47(0.02)
−24.12	4.65	418.44(0.01)	−393.72(0.02)	−22.03	0.78	431.40(0.02)	−408.04(0.03)
−24.34	4.79	418.39(0.01)	−393.90(0.01)	−22.25	0.55	430.07(0.04)	−409.51(0.04)
−24.34	1.46	419.13(0.03)	−391.98(0.04)	−22.25	2.07	430.38(0.01)	−408.49(0.02)
−24.56	3.23	418.39(0.02)	−393.95(0.02)	−22.47	2.74	429.88(0.01)	−409.43(0.01)
−24.77	0.82	418.39(0.04)	−394.03(0.03)	−22.47	0.86	430.36(0.03)	−408.43(0.03)
−24.99	0.59	413.18(0.04)	−394.55(0.05)	−22.69	1.13	417.54(0.02)	−391.46(0.03)
−24.99	0.60	428.59(0.03)	−392.62(0.05)	−22.69	4.45	429.72(0.01)	−409.51(0.01)
−25.21	0.98	413.16(0.02)	−394.62(0.03)	−22.91	1.35	417.52(0.02)	−391.50(0.03)
−25.21	0.48	428.45(0.04)	−392.65(0.09)	−22.91	0.88	418.35(0.03)	−392.09(0.06)
−25.43	0.53	413.13(0.04)	−394.83(0.06)	−22.91	3.34	429.53(0.01)	−409.52(0.01)
				−23.13	5.23	418.30(0.01)	−392.47(0.02)
				−23.35	11.59	418.26(0.00)	−392.92(0.01)
				−23.35	3.91	429.83(0.02)	−403.75(0.02)
				−23.57	18.02	418.18(0.01)	−393.24(0.01)
				−23.57	6.43	429.77(0.02)	−403.74(0.02)
				−23.78	16.28	418.15(0.01)	−393.43(0.01)
				−23.78	7.07	429.74(0.02)	−403.79(0.02)
				−24.00	9.92	418.23(0.01)	−393.66(0.01)
				−24.00	2.87	420.98(0.02)	−394.91(0.04)
				−24.00	6.63	421.79(0.01)	−395.21(0.02)
				−24.00	5.25	429.69(0.02)	−403.88(0.02)
				−24.22	8.82	418.24(0.01)	−393.95(0.01)
				−24.22	2.96	420.91(0.02)	−394.91(0.03)
				−24.22	8.85	421.81(0.01)	−395.26(0.01)
				−24.22	2.41	429.64(0.03)	−403.97(0.04)
				−24.44	7.82	418.21(0.01)	−394.15(0.01)
				−24.44	1.88	420.73(0.03)	−394.92(0.03)
				−24.44	5.14	421.84(0.03)	−395.30(0.02)
				−24.66	1.19	414.59(0.02)	−421.78(0.04)
				−24.66	3.83	418.23(0.01)	−394.27(0.01)
				−24.66	1.73	420.72(0.02)	−395.09(0.02)
				−24.66	1.38	421.74(0.03)	−395.32(0.03)
				−24.66	1.48	427.76(0.02)	−394.21(0.03)
				−24.88	0.95	413.16(0.03)	−394.48(0.04)
				−24.88	1.67	414.56(0.01)	−421.61(0.03)
				−24.88	0.74	418.43(0.05)	−394.42(0.05)
				−24.88	0.87	420.39(0.03)	−395.04(0.03)
				−24.88	2.37	427.75(0.01)	−394.23(0.02)
				−25.10	1.62	413.17(0.02)	−394.73(0.02)
				−25.10	1.67	414.58(0.01)	−421.60(0.02)
				−25.10	3.20	427.76(0.01)	−394.16(0.01)
				−25.32	0.92	412.47(0.02)	−395.39(0.03)
				−25.32	1.23	413.15(0.03)	−394.93(0.03)
				−25.32	0.87	414.57(0.03)	−421.54(0.04)
				−25.32	2.70	427.78(0.01)	−394.16(0.01)
				−25.54	1.75	412.51(0.02)	−395.36(0.02)
				−25.54	0.78	413.36(0.03)	−395.05(0.04)
				−25.54	1.26	427.87(0.02)	−394.10(0.03)
				−25.75	1.75	412.47(0.01)	−395.47(0.01)
				−25.97	0.93	412.49(0.03)	−395.58(0.03)

The observed SiO maser components in R14164A (2014-06-13)

SiO (v=1 J=1−0)				SiO (v=2 J=1−0)			
$V_{\rm LSR}$ (km s^{-1})	I (Jy beam^{-1})	ΔRA (mas)	ΔDec (mas)	$V_{\rm LSR}$ (km s^{-1})	I (Jy beam^{-1})	ΔRA (mas)	ΔDec (mas)
−14.35	0.87	431.24(0.06)	−419.24(0.07)	−14.16	0.83	427.83(0.05)	−424.83(0.07)
−14.56	0.96	429.00(0.10)	−423.05(0.10)	−14.16	0.92	431.30(0.04)	−419.62(0.06)
−14.56	1.16	431.41(0.05)	−419.41(0.08)	−14.38	1.49	427.92(0.04)	−425.00(0.04)
−14.78	2.27	431.40(0.03)	−419.40(0.04)	−14.38	1.90	431.31(0.02)	−419.65(0.03)
−15.00	1.63	429.43(0.04)	−423.77(0.05)	−14.59	1.56	428.03(0.04)	−425.14(0.04)
−15.00	2.64	431.50(0.02)	−419.43(0.03)	−14.59	3.29	431.39(0.01)	−419.72(0.02)
−15.21	2.11	429.55(0.03)	−423.90(0.05)	−14.81	3.41	431.42(0.02)	−419.78(0.02)
−15.21	1.90	431.56(0.04)	−419.50(0.04)	−15.03	3.46	431.53(0.02)	−419.88(0.02)
−15.43	3.10	429.71(0.02)	−424.22(0.04)	−15.25	1.05	429.68(0.05)	−424.32(0.10)
−15.65	4.34	429.81(0.02)	−424.55(0.03)	−15.25	2.35	431.59(0.02)	−419.92(0.03)
−15.87	6.01	429.91(0.02)	−424.72(0.02)	−15.47	1.44	429.74(0.03)	−424.53(0.08)
−16.08	6.97	430.06(0.02)	−424.88(0.02)	−15.47	0.97	431.80(0.05)	−419.90(0.07)
−16.08	3.04	434.39(0.04)	−416.81(0.05)	−15.69	2.66	429.96(0.02)	−425.08(0.04)
−16.30	5.13	430.26(0.03)	−425.05(0.04)	−15.91	1.93	428.12(0.04)	−426.31(0.06)
−16.30	5.05	434.58(0.03)	−416.83(0.04)	−15.91	6.27	430.07(0.01)	−425.16(0.02)
−16.52	3.35	430.35(0.03)	−425.15(0.05)	−16.13	12.39	430.17(0.01)	−425.21(0.01)
−16.52	4.64	431.34(0.02)	−423.75(0.03)	−16.35	7.40	430.25(0.01)	−425.26(0.02)
−16.52	4.47	434.75(0.02)	−416.74(0.03)	−16.56	3.70	430.40(0.02)	−425.30(0.03)
−16.74	5.32	431.40(0.02)	−423.79(0.02)	−16.78	2.23	431.41(0.03)	−424.06(0.05)
−16.74	3.46	435.20(0.03)	−416.62(0.04)	−17.00	2.87	431.54(0.02)	−424.34(0.03)
−16.95	3.44	431.65(0.03)	−424.01(0.03)	−17.22	2.75	431.71(0.02)	−424.62(0.03)
−16.95	3.68	435.47(0.03)	−416.41(0.03)	−17.44	1.87	431.87(0.02)	−424.90(0.04)
−17.17	2.21	431.82(0.05)	−424.40(0.06)	−18.31	1.23	432.59(0.04)	−427.74(0.05)
−17.17	5.25	435.83(0.02)	−416.40(0.03)	−18.53	1.83	432.84(0.03)	−428.05(0.04)
−17.39	5.80	436.11(0.03)	−416.41(0.04)	−18.75	1.15	431.67(0.06)	−430.51(0.07)
−17.60	6.06	436.57(0.02)	−416.55(0.03)	−18.75	2.24	433.19(0.03)	−428.55(0.05)
−17.82	5.93	436.88(0.02)	−416.63(0.03)	−18.97	3.13	433.46(0.02)	−429.03(0.04)
−18.04	3.63	437.31(0.03)	−416.74(0.03)	−19.19	4.16	433.84(0.02)	−429.68(0.02)
−18.26	2.53	432.23(0.04)	−427.03(0.05)	−19.41	3.55	434.19(0.02)	−429.97(0.03)
−18.26	1.85	437.72(0.06)	−416.81(0.07)	−19.63	1.24	434.51(0.03)	−430.21(0.04)
−18.47	2.73	432.71(0.03)	−427.51(0.05)	−19.63	0.96	435.61(0.06)	−430.23(0.08)
−18.69	2.99	433.14(0.03)	−427.78(0.04)	−19.85	1.30	440.70(0.05)	−418.51(0.08)
−18.91	2.89	433.35(0.06)	−427.79(0.07)	−20.06	2.29	440.95(0.03)	−418.45(0.04)
−19.12	4.02	439.11(0.04)	−417.90(0.03)	−20.28	1.84	441.32(0.04)	−418.41(0.04)
−19.34	7.02	439.40(0.02)	−417.94(0.02)	−20.50	1.42	441.97(0.04)	−418.64(0.05)
−19.56	7.42	439.71(0.02)	−417.99(0.02)	−21.82	0.81	408.55(0.05)	−421.88(0.07)
−19.78	8.70	440.31(0.02)	−418.04(0.02)	−21.82	1.28	437.10(0.04)	−415.22(0.04)
−19.99	10.67	440.60(0.02)	−418.00(0.02)	−22.03	1.16	408.62(0.03)	−421.99(0.05)
−20.21	9.39	441.18(0.02)	−418.10(0.02)	−22.03	1.73	437.06(0.03)	−415.27(0.03)
−20.43	17.52	441.71(0.01)	−418.23(0.01)	−22.25	0.86	408.57(0.04)	−422.03(0.07)
−20.65	7.90	442.12(0.02)	−418.31(0.02)	−22.25	1.52	436.56(0.03)	−415.33(0.03)
−20.86	2.96	442.51(0.03)	−418.36(0.04)	−22.25	1.28	437.26(0.04)	−415.30(0.05)
−20.86	2.40	443.65(0.03)	−419.46(0.04)	−22.47	2.15	436.43(0.03)	−415.44(0.03)
−21.08	1.07	443.26(0.06)	−418.51(0.08)	−22.69	1.86	436.26(0.02)	−415.54(0.03)
−21.51	1.16	437.69(0.04)	−415.20(0.04)	−23.13	0.97	409.85(0.06)	−423.45(0.09)
−21.73	2.03	437.67(0.03)	−415.07(0.03)	−23.35	1.43	409.81(0.04)	−423.50(0.06)
−21.95	3.18	437.74(0.02)	−415.11(0.02)	−23.57	1.96	409.77(0.03)	−423.54(0.05)
−22.17	2.81	437.79(0.02)	−415.15(0.03)	−23.57	1.49	435.43(0.04)	−411.00(0.06)
−22.17	1.45	440.06(0.05)	−412.43(0.06)	−23.78	2.37	409.73(0.04)	−423.55(0.07)
−22.38	1.44	437.76(0.04)	−415.29(0.04)	−23.78	2.92	427.25(0.04)	−400.61(0.04)
−22.38	1.64	440.12(0.04)	−412.37(0.05)	−23.78	3.57	435.41(0.03)	−410.91(0.05)
−22.60	1.24	439.50(0.06)	−411.54(0.07)	−24.00	2.45	409.71(0.05)	−423.56(0.08)
−23.04	1.22	424.28(0.05)	−398.05(0.05)	−24.00	3.49	427.16(0.03)	−400.80(0.04)
−23.47	1.60	424.99(0.05)	−399.10(0.05)	−24.00	5.09	435.43(0.03)	−410.88(0.04)
−23.47	1.90	427.25(0.04)	−400.22(0.05)	−24.22	3.73	427.69(0.04)	−402.00(0.04)
−23.69	3.30	427.25(0.03)	−400.51(0.04)	−24.22	5.48	435.44(0.02)	−410.91(0.03)
−23.69	2.68	434.99(0.03)	−409.78(0.05)	−24.44	3.93	427.65(0.03)	−402.25(0.04)
−23.90	4.06	427.43(0.03)	−401.10(0.04)	−24.44	4.25	435.47(0.03)	−410.91(0.04)
−23.90	3.11	435.66(0.04)	−410.64(0.04)	−24.66	4.51	427.54(0.03)	−402.40(0.03)
−24.12	5.69	427.48(0.02)	−401.55(0.02)	−24.88	2.39	427.51(0.03)	−402.54(0.03)
−24.12	5.20	435.71(0.02)	−410.68(0.03)	−25.75	0.88	418.94(0.04)	−402.26(0.06)
−24.34	7.33	427.39(0.02)	−401.75(0.02)	−25.97	1.36	418.89(0.03)	−402.53(0.04)
−24.34	4.85	435.74(0.02)	−410.68(0.03)	−26.19	1.14	418.99(0.05)	−402.72(0.05)

The observed SiO maser components in R14164A (2014-06-13) - (continued)

SiO (v=1 J=1−0)				SiO (v=2 J=1−0)			
$V_{\rm LSR}$ (km s^{-1})	I (Jy beam^{-1})	ΔRA (mas)	ΔDec (mas)	$V_{\rm LSR}$ (km s^{-1})	I (Jy beam^{-1})	ΔRA (mas)	ΔDec (mas)
−24.56	2.23	426.62(0.06)	−404.11(0.08)	−26.41	0.82	418.96(0.04)	−402.81(0.09)
−24.56	7.54	427.27(0.02)	−401.84(0.02)	−26.41	0.85	419.60(0.04)	−403.03(0.07)
−24.56	2.76	435.73(0.04)	−410.62(0.05)	−26.63	0.83	420.09(0.05)	−403.47(0.07)
−24.77	5.31	427.17(0.02)	−401.91(0.02)	−26.85	1.10	420.09(0.04)	−403.60(0.05)
−24.99	1.88	426.90(0.05)	−401.94(0.04)				
−25.21	1.09	420.54(0.04)	−428.76(0.07)				
−25.21	0.86	434.63(0.06)	−399.58(0.08)				
−25.43	0.94	420.48(0.05)	−428.51(0.07)				